The Design and Testing of a Novel Compact Real-time Hybrid Compton and Neutron Scattering Instrument

Hajir Al Hamrashdi, MSc (Hons)

Submitted for the degree of Doctor of Philosophy at Lancaster University

February 2020

Declaration

I, Hajir Al Hamrashdi, hereby certify that this thesis has not been previously submitted in support of an application for another degree at this or any other university. It is the result of my own work and includes nothing that is the outcome of work done in collaboration except where specifically indicated. Many of the ideas in this thesis were the product of discussion with my supervisors Dr Stephen D. Monk and Dr David Cheneler. The work presented here was carried out at Lancaster University in the period between November 2015 and November 2019

Signature ………………………..Date…………………….

I, Dr Stephen D Monk, herby certify that the candidate has fulfilled the conditions of the resolution and regulations appropriate for the degree of Doctor of Philosophy in Lancaster University, and that the candidate is qualified to submit this thesis in application for that degree.

Signature ………………………..Date…………………….

I, Dr David Cheneler, herby certify that the candidate has fulfilled the conditions of the resolution and regulations appropriate for the degree of Doctor of Philosophy in Lancaster University, and that the candidate is qualified to submit this thesis in application for that degree.

Signature ………………………..Date…………………….

Abstract

The requirement for multiple-purpose imaging system occurs regularly within the field of radioactive materials safeguard and security applications. Current instrumentation utilised within the field of dual gamma-ray and neutron imaging systems suffer with limited portability, long scan times, and cover limited energy ranges. Conversely, the imaging system designed, built and tested in this work is not only capable of locating both gamma rays and neutrons, but is also capable of operating in near real time, covers a large energy range and is portable to a desktop degree. The imaging concept applied simultaneously combines Compton and neutron scattering techniques within a three-layer design comprising of a unique combination of scintillators backed with pixelated arrays of photodetectors in the form of 8 x 8 Silicon Photomultipliers (SiPMs).

The system features the organic scintillator EJ-204, neutron sensitive lithium glass and thallium doped caesium iodide utilised along with associated SiPMs and front-end electronics, all enclosed within a volume of 120 mm x 120 mm x 200 mm. Further back-end electronics is situated within a separate unit where each of the data channels are simultaneously interrogated in order to determine the location of the incident gamma rays and neutrons.

The validity of the instrument has been computationally verified using MCNP6 and Geant4 Monte Carlo simulation codes and experimentally tested using Cs-137 gamma sources of ~300 kBq and a Cf-252 neutron source featuring an emission rate of 10^6 neutrons per second. The developed instrument offers a real-time response with a scan time of 60 seconds and a further data analysis time of 60 seconds. The intrinsic efficiency of the instrument has been experimentally measured to be in the order of

10^{-4} for both gamma rays at 0.667 MeV and fast neutrons at average energy of 2.1 MeV, and 0.78 for thermal neutrons.

Acknowledgements

This research would have not been possible without the support and help of many people.

First and foremost, I would like to sincerely thank my supervisors, Dr Stephen Monk and Dr David Cheneler, who both have, regardless of their workloads, offered scientific guidance, continuous encouragement and genuine participation in the success of this project. I will always appreciate the support they both offered to me and the research skills they both taught me. I would like to thank my colleagues and the members of the nuclear research group at Lancaster University Engineering Department for their help and support. I would like to extend my thanks to the technical staff at the department for their help whenever it was needed.

Thanks go to my husband for his endless support, patience and non-stopping encouragement. To my little daughters; Maeen and Ayah, thank you for all your smiles, laughs, non-sense conversations and sleepless nights and for making this project at times a bit more challenging, I love you both. Thanks go to my family back in Oman.

Contents

List of Tables

List of Figures

List of Abbreviations and Acronyms

ACTL: Activation Library.

ADC: Analogue to digital converter.

ASCII: American Standard Code for Information Interchange.

CCM: Charge Comparison Method.

CLYC: $C_s2LiYCl_6$.

CVD: Chemical Vapour Deposition.

DAQ: Data Acquisition System.

d1: spacing between layers one and two in the design.

d2: spacing between layers two and three in the design.

E_n : Incident neutron energy.

E'_n: Scattered neutron energy.

E_p : Recoiled proton energy.

E_γ : Incident gamma-ray photon energy.

E'_γ : Scattered gamma-ray photon energy.

E_e: Recoil electron energy.

ENDF: Evaluated Nuclear Data Files.

ENDL: Evaluated Neutron Data Library

EPDL: Evaluated Photon Data Library.

EUROPL: European Police Office.

FGA: Frequency Gradient Analysis.

FOM: Figure of merit in pulse discrimination analysis.

FOM: Figure of merit in MCNP environment.

FPGA: Field-Programmable Gate Array.

GSO: Gadolinium oxyorthosilicate.

HEP: High Energy Physics.

HPHT: High Pressure, High Temperature.

IAEA: International Atomic Energy Agency.

ICSANT: International Convention for the Suppression of Acts of Nuclear Terrorism.

INTERPOL: The international criminal police organisation.

ITDB: Incident and Trafficking Database.

$FWHM_{\gamma}$: Gamma ray peak full width at half maximum value.

$FWHM_n$: Neutron peak full width at half maximum value.

FT: A keyword for pulse height tally in MCNP code.

Li-glass: Lithium glass.

m_n : Neutron mass.

m_e : Electron rest mass.

MFA: Mixed Field Analyser.

MCNP: Monte Carlo N-Particle code.

MISTI: Mobile Imaging and Spectroscopic Threat Identification.

MLEM: Maximum Likelihood Expectation Maximization.

MLEM: Maximum Likelihood Ratio.

NIST: National Institute of Standards and Technology.

PCB: Printed Circuit Board.

$Peak_\gamma$: Gamma-ray events peak position.

$Peak_n$: Neutron events peak position.

PDE: Photon detection efficiency.

PGA: Pulse gradient analysis.

PHA: Pulse height analysis.

PHL: A keyword for pulse height tally in MCNP code.

PMT: Photomultiplier tube.

PSD: Pulse shape discrimination.

PVT: Polyvinyltoluene polymer.

RID: Radionuclide Identification Devices.

RMC: Rotational Modulation Collimator.

RPM: Radiation Portal Monitors.

ROSD-RSD: Square Distance-based Radiation Source Detection.

SiPM: Silicon photomultiplier.

SNM: Special Nuclear Materials.

SPAD: Single Photon Avalanche Photodiode.

TDC: Time to Digital Converter.

TECMIPT: Test and evaluation capabilities and methodologies integrated process team.

TTOP: TECMIPT Test Operation procedures.

TOF: Time of flight.

V_{br} : Breakout voltage.

WCO: World Custom Organisation.

1 Introduction

Dual gamma-ray and neutron imaging systems have received a lot of attention in recent years due to their ability to locate radiation sources in complex environments, even in the presence of significant background radiation [1]. As such, these systems have been used in numerous practical applications in safeguarding and security [1, 2], radiography and tomography, [3] as well as in industrial gauging and monitoring [4, 5].

Safeguards and security applications are currently the central driver in the literature for the development of dual gamma-ray and neutron imaging systems. The ultimate concern is the potential harmful use of nuclear materials in dirty bombs or weapons of mass destruction. Since 1995, the IAEA annually publishes the Incident and Trafficking Database (ITDB), a report that monitors incidents and trafficking of radioactive sources and nuclear materials. This database shows there were 3,487 confirmed illicit trafficking incidents since the records begins [6]. This demonstrates the presence of potential threats related to this industry and hence proves the necessity of advanced radiation imaging systems with the ability to detect, locate and identify radioactive sources in complex environments, such at national borders and ports.

Current passive dual-particle imaging systems used for safeguarding and security applications, have limited portability, are bulky, and hence, have been mainly used at standoff distances [1, 2]. In addition, they cover a limited range of neutron energies, with some imaging systems focusing only on thermal neutrons (typically 0.025 eV) [7] while others focus only on fast neutrons (10 keV—10 MeV) [8]. Finally, yet importantly, limitations in detection speed and in real-time imaging is a key challenge not satisfied by the currently available imaging systems for border monitoring.

The goal of this research is therefore to design and built a real-time imaging system that is highly portable, compact in size and detects gamma-ray photons in the Compton energy range (~10 keV to ~10 MeV [9]) , thermal neutrons and fast neutrons. The work discussed in this thesis focuses on the design, build and experimental validation of a prototype imaging system with these characteristics. Ultimately, the work features a proof-of-concept study for designing an optimum imaging system that can be integrated in security systems and security checkpoints within controlled areas such as laboratories, border checkpoints, airports and nuclear sites.

The aims of this research were achieved in four stages:

- Stage I: a detailed review of the physics of radiation detection and current imaging systems targeting gamma rays, neutrons and dual gamma-ray and neutrons in literature.

- Stage II: an in-depth investigation of four different scintillation materials proposed as potential detectors in this multiple-layer design.

- Stage III: a full computational study into the optimum configuration of detectors and layers in the design.

- Stage IV: the build of the prototype design followed by experimental testing using Cs-137 source and Cf-252 source.

The detection and the imaging technique adopted in the proposed system followed a hybrid approach where Compton [10] and neutron scattering imaging [4] concepts were integrated into one system. The novelty in the proposed imaging system is found in the arrangement of scintillators within a three-layer design. The arrangement incorporates the combination of radiation hard lithium glass as the main scintillation material and plastic scintillator EJ-204 as a fast neutron scattering layer. The front-end of the system is portable with dimensions of 200 mm x 120 mm x 120 mm and a mass of 3 kg. The instrument offers fast data acquisition time with an experimentally measured scan time of 60-second for gamma sources of ~300 kBq and neutron sources of 10^6 neutrons per second (total) in close proximity (< 300 mm). Furthermore, the system covers wide energy ranges of gamma rays (energy range between 10 keV to 10 MeV), thermal neutrons and fast neutrons. In addition to these main features, the instrument utilises a bespoke application specific readout circuit (ASRC) designed to acquire signals from the 192 pixels (3 layers x 64 pixels) allowing an in depth investigation of the response of each silicon photomultiplier pixel and a thorough analysis of the different aspects involved in this proof-of-concept study. This circuit has been designed to acquire the time-of-flight (TOF) of neutrons between layers one and two (distance travelled between layers is 30 mm), hence allowing the detection of neutron scattering events with energies between 10 keV and 1 MeV. Unlike others in this field, the system utilises silicon photomultipliers instead of photomultiplier tubes (PMTs). The use of silicon photomultipliers in the design significantly reduces the size of the instrument, reduces the overall consumption of power compared to traditional PMTs, enhances the

robustness, and reduces the effect of external magnetic fields on the generated pulses. The research goes a step further in achieving the aims of the project by investigating the pulse discrimination abilities of the lithium glass scintillator (GS10) and the organic plastic scintillator (EJ-204).

1.1 Peer-reviewed publications

1. H. Al Hamrashdi, D. Cheneler, and S.D. Monk, *A fast and portable imager for neutron and gamma emitting radionuclides.* Nuclear Instruments and Methods in Physics Research, Section A: Accelerators, Spectrometers, Detectors and Associated Equipment, 2020. **953**.

2. H. Al Hamrashdi, S.D. Monk, and D. Cheneler, *Neutron/gamma pulse discrimination analysis of GS10 lithium glass and EJ-204 plastic scintillators.* Journal of Instrumentation, 2020. **15**(01): p. P01031-P01031.

3. H. Al Hamrashdi**,** S.D. Monk, and D. Cheneler, *Passive gamma-ray and neutron imaging systems for national security and nuclear non-proliferation in controlled and uncontrolled detection areas: review of past and current status.* Sensors, 2019. 19 (11): p. 2638.

4. H. Al Hamrashdi, D. Cheneler, and S.D. Monk, *Material optimization in dual particle detectors by comparing advanced scintillating materials using two Monte Carlo codes.* Nuclear Instruments and Methods in Physics Research Section A: Accelerators, Spectrometers, Detectors and Associated Equipment, 2017. **869** (Supplement C): p. 163-171.

5. S. D. Monk, B.A Shippen., B.R. Colling, D.C. Cheneler, H. Al Hamrashdi, T. Alton, *A comparison of MCNP6-1.0 and GEANT 4-10.1 when evaluating the neutron output of a complex real world nuclear environment: The thermal neutron facility at the Tri Universities Meson facility.* Nuclear Instruments and Methods in Physics Research, Section B: Beam Interactions with Materials and Atoms, 2017. 399: 48-61.

1.2 Conferences, meetings and awards

A list of the conferences and meetings attended as part of this research include:

- *Design and Optimisation of a Three Layers Thermal Neutron, Fast Neutron and Gamma-Ray Imaging System.* International conference on advancements in nuclear instrumentation measurement methods and their applications ANIMMA2019. Portoroz, Slovenia, 17-21 June 2019. (Oral Presentation and conference paper)

- *The Design and Development of a Real Time Neutron-Gamma Imaging System.* Universities' Nuclear Technology Forum 2018, Lancaster, United Kingdom, 10-11 July 2018. (Oral Presentation: runner-up award for best PhD student presentation)

- *Development of a Real Time Neutron-Gamma Imaging System.* The Engineering Department Postgraduate Research Conference, Lancaster, United Kingdom, 4-5 July 2018. (Oral Presentation)

- *The Feasibility of Neutron-Gamma Imaging with Hybrid Imaging Technique.* Topical meeting: Physics Innovation Nuclear, Manchester, United Kingdom, 1-2 November 2017. (Poster: best poster award)

- *Neutron-Gamma Imaging with Compton Camera and Coded Aperture.* Lancaster Security Meeting, Lancaster, United Kingdom, 27th July 2017. (Oral Presentation)

- *Neutron-Gamma Imaging with Compton Camera and Coded Aperture.* The Engineering Department Postgraduate Research Conference, Lancaster, United Kingdom, 5th June 2017. (Oral Presentation: runner-up award for best PhD student presentation)

- *The Feasibility of Dual Particle Imaging With Compton Camera Technique.* Neutron User's Club Meeting, NPL, Teddington, United Kingdom, (Oral Presentation)

- *Neutron-Gamma Imaging with Compton Camera and Coded Aperture.* Universities' Nuclear Technology Forum 2015, Sheffield, United Kingdom, 5-7 April 2016. (Oral Presentation)

1.3 Thesis structure and chapters outline

The structure of the thesis follows a collection-of-papers structure. In total, the thesis comprises of nine chapters, four of which have been published in respected journals. For consistency, the format and layout of the published papers follows the overall

format of the thesis. Apart from the current introduction chapter, the outlines of the eight chapters are:

- **Chapter 2: Background.**

This chapter reviews the underpinning background and theory of ionising radiation. It starts by discussing the fundamental definitions in ionising radiation and the interaction mechanisms of gamma-ray photons, neutrons and charged ionising particles. A review of common detection materials for gamma-ray photons, thermal neutrons and fast neutrons, along with the common definitions in radiation detection is given in the chapter.

- **Chapter 3: Passive Gamma-Ray and Neutrons Imaging Systems for National Security and Nuclear Non-proliferation in Controlled and Un-controlled Detections Areas: A Review of Past and Current Status.**

The chapter is the published review paper: H. Al Hamrashdi, S.D. Monk, and D. Cheneler, *Passive gamma-ray and neutron imaging systems for national security and nuclear non-proliferation in controlled and uncontrolled detection areas: review of past and current status.* Sensors, 2019. 19 (11): p. 2638. It presents the first stage in the research in which a comprehensive review of passive radioactive sources and nuclear materials detection and imaging systems was made. The review identified existing research in the field of passive detection and imaging of gamma rays and neutrons in safeguard and security applications and helped on recognising the gaps within this field. In addition, this chapter discusses the main definitions and classifications of detection and imaging systems in safeguard and security applications alongside the regulation and legislations bodies' requirements on detection and imaging system.

- **Chapter 4: Monte Carlo Simulations.**

This chapter reviews the basics of the Monte Carlo method, introduces the computational work made in this research. In addition, the chapter lists the main features of the simulation codes used in this work, namely MCNP6 and Geanr4, alongside their main physics models and data libraries. Ultimately, the chapter aims to establish a bridge between the theory behind Monte Carlo codes and the implementation of these codes in the chapters 5, 6 and 7.

- **Chapter 5: Material Optimisation in Dual Particle Detectors By Comparing Advanced Scintillating Materials Using Two Monte Carlo Codes.**

The chapter is the published paper: H. Al Hamrashdi, D. Cheneler, and S.D. Monk, *Material optimization in dual particle detectors by comparing advanced scintillating materials using two Monte Carlo codes.* Nuclear Instruments and Methods in Physics Research Section A: Accelerators, Spectrometers, Detectors and Associated Equipment, 2017. 869 (Supplement C): p. 163-171. It presents the second stage in this research were the optimum scintillation material for the proposed three layers imaging system is investigated. The investigation compares and contrasts the detection and attenuation abilities of thermal neutrons, fast neutrons and gamma rays of four different scintillators all with a common feature; dual sensitivity to gamma rays and neutrons. The results were used to propose the main scintillator in both the Compton scattering sub-system and the neutron scattering sub-system.

- **Chapter 6: Design and Optimisation of a Three Layers Thermal Neutron, Fast Neutron and Gamma-Ray Imaging System.**

This chapter is the conference paper: H. Al Hamrashdi, S.D.M., D. Cheneler. *Design and Optimisation of a Three Layers Thermal Neutron, Fast Neutron and Gamma-Ray Imaging System.* International conference on Advancements in Nuclear Instrumentation and Measurement Methods and their applications (ANIMMA), 2019. It presents the investigation conducted in the third stage of this research were the optimum design and configuration of the detectors and layers was computationally investigated using Monte Carlo simulations. The study included optimising the order of detectors in the design and optimising the separation distance between layers. The results of this chapter were directly implemented into building the prototype instrument.

- **Chapter 7: A Fast and Portable Imager for Neutron and Gamma Radiations.**

This chapter is the published paper: H. Al Hamrashdi, D. Cheneler, and S.D. Monk, *A fast and portable imager for neutron and gamma emitting radionuclides.* Nuclear Instruments and Methods in Physics Research, Section A: Accelerators, Spectrometers, Detectors and Associated Equipment, 2020. **953**. It presents the results of the computational and experimental work (stage four in the research) carried out to test the feasibility of the porotype design. The chapter describes in details the imaging concept of the design, the different components of the design, the experimental setup and the bespoke readout circuit. The results from this chapter proved the viability of the imaging concept and proved the capabilities of the prototype design in detecting and locating sources of gamma rays and neutrons in real-time.

- **Chapter 8: Neutron/Gamma-ray Pulse Discrimination Analysis of GS10 Lithium Glass and EJ-204 Plastic Scintillators.**

This chapter is the published paper: H. Al Hamrashdi, S.D. Monk, and D. Cheneler, *Neutron/Gamma-ray Pulse discrimination analysis of GS10 Lithium glass and EJ-204 plastic scintillators.* Journal of Instrumentation. 2020. **15**(01): p. P01031-P01031. The chapter discusses the pulse discrimination abilities of the glass scintillator GS10 and the organic plastic scintillator EJ-204. The investigation included using three different pulse discrimination methods and experimentally acquired pulses. The investigation presented the last part of this feasibility study and it mainly aimed to form a platform for further future investigation into the discrimination abilities of these two scintillation materials.

- **Chapter 9: Conclusions and recommendations.**

This chapter presents a summary of the work conducted in this the research with a discussion on the potential applications for the proposed design, followed by suggestions for future work.

1.4 References

1. Ayaz-Maierhafer, B., et al., *Angular resolution study of a combined gamma-neutron coded aperture imager for standoff detection.* Nuclear Instruments and Methods in Physics Research Section A: Accelerators, Spectrometers, Detectors and Associated Equipment, 2013. **712**: p. 120-125.

2. Polack, J.K., et al. *Dual-particle imager for standoff detection of special nuclear material.* in *2011 IEEE Nuclear Science Symposium Conference Record.* 2011. Valencia, Spain.

3. Rynes, J., et al., *Gamma-ray and neutron radiography as part of a pulsed fast neutron analysis inspection system.* Nuclear Instruments and Methods in

Physics Research Section A: Accelerators, Spectrometers, Detectors and Associated Equipment, 1999. **422**(1): p. 895-899.

4. Herzo, D., et al., *A Large Double Scatter Telescope for Gamma Rays and Neutrons.* Nuclear Instruments and Methods, 1975. **123**(3): p. 583-597.

5. Zych, A.D., et al., *Large Area Double Scattering Telescope for Balloon-Borne Studies of Neutrons and Gamma Rays.* Ieee Transactions on Nuclear Science, 1975. **NS22**(1): p. 605-610.

6. *IAEA incident and trafficking database fact sheet 2019.* 2019, International Atomic Energy Agency.

7. Baker, J.H., et al., *A combined NaI(Tl)+LiI(Eu) detector for environmental, geological and security applications.* Radiation Measurements, 2007. **42**(4): p. 937-940.

8. A. Enqvist, M. Flaska, and S. Pozzi, *Measurement and simulation of neutron/gamma-ray cross-correlation functions from spontaneous fission.* Nuclear Instruments and Methods in Physics Research Section A: Accelerators, Spectrometers, Detectors and Associated Equipment, 2008. **595**(2): p. 426-430.

9. Knoll, G.F., *Radiation detection and measurment.* Fourth ed. 2010, New York, NY, USA: John Wiley and Sons.

10. Everett, D.B., et al. *Gamma-radiation imaging system based on the Compton effect.* in *Proceedings of the Institution of Electrical Engineers-London.* 1977. IET Digital Library: London, UK.

2 Background

This chapter provides background information on gamma ray and neutron interaction mechanisms and detection methods. In addition, it briefly discuss photodetectors, noise and signal processing and common definitions in the field of radiation detection.

2.1 Principles of ionising radiation

There are two primary categories of ionising radiation: uncharged and charged. Uncharged ionising radiation categories include electromagnetic radiation in the form of X-rays, gamma rays and hadronic particles (mainly neutrons). The charged ionising radiation category includes high energetic electrons, heavy ions, such as alpha particles, protons and fission products. The ionising radiation of interest in this research are gamma rays and neutrons generated by atomic and nuclear processes. One of the key atomic and nuclear processes in generating ionising radiation is radioactivity or radioactive decay. Radioactivity refers to all forms of spontaneous emission of ionising radiation by unstable isotopes. It is measured in units of Becquerel (Bq), which corresponds to one transformation (disintegration or decay) per second. Radioactivity occurs naturally in unstable isotopes. Activation of materials can induce radioactivity

in nominally stable materials via the bombardment of stable isotopes with radiation. The exponential law of radioactive decay relates the parameters involved in governing the radioactivity process for a number of nuclei as follows:

$$N(t) = N_o \mathrm{e}^{-\frac{t}{t_{1/2}}(0.693)}$$
(2.1)

Where $N(t)$ is the number of nuclei at time t, N_o is the original number of nuclei and $t_{1/2}$ is the half-life of the radioactive isotope [1]. The IAEA defines radioactive materials as any material that is subject to regularity control because of their radioactivity that includes nuclear materials such as U-235 and artificially man-made radioactive sources [4].

Particle energy directly influences the ability of radiation quanta to travel through materials. Conventionally, radiation energy is described in units of electron volts (eV) which corresponds to the energy gained by an electron accelerates due a potential difference of 1 V (1.602×10^{-19} J). The following subsections review the fundamentals governing the interaction mechanisms of gamma-ray photons, neutrons and charged particles within a target material. In accordance with scope of this research, the energies of all particles of interest reviewed here are non-relativistic energies.

2.1.1 Gamma-ray interactions

The energy of a single photon is the product of Planck's constant, $h = 6.6262 \times 10^{-34}$ J.s, and the frequency of the electromagnetic radiation, f, and is described by the following equation [2]:

$$E_\gamma = \mathrm{h}f \qquad\qquad (2.2)$$

Gamma rays are emitted from excited nuclei while transitioning from an excited nuclear energy state to a lower nuclear energy state [3]. The emission of a gamma-ray photon almost always accompanies radioactive decay via beta⁻ particles, beta⁺ particles and alpha particles of a daughter nucleus in an excited state [3, 4]. Nuclear reactions are another source of gamma rays, such as activation reactions where the target nucleus is bombarded with high-energy particles resulting in it is transitioning to an excited nuclear energy state. Subsequently, a gamma-ray photon is emitted in an attempt to de-excite the nucleus to a lower nuclear energy levels. Another example of nuclear reactions is neutron capture reaction. In capture reactions, a neutron is captured by the nucleus of a target material. As a result, the nucleus is left in an excited nuclear energy state. Subsequently, the excited nucleus will decay and a gamma-ray photon is emitted as a result. Additionally, nuclear fission reactions are sources of as gamma-ray [5, 6]. Krane [1] defines fission reactions as the primary result of the competition between nuclear forces and Coulomb forces in a heavy nucleus resulting in the decay of the nucleus to a daughter nucleus in an excited state. Figure 2.1 illustrates three examples of gamma-ray photons sources.
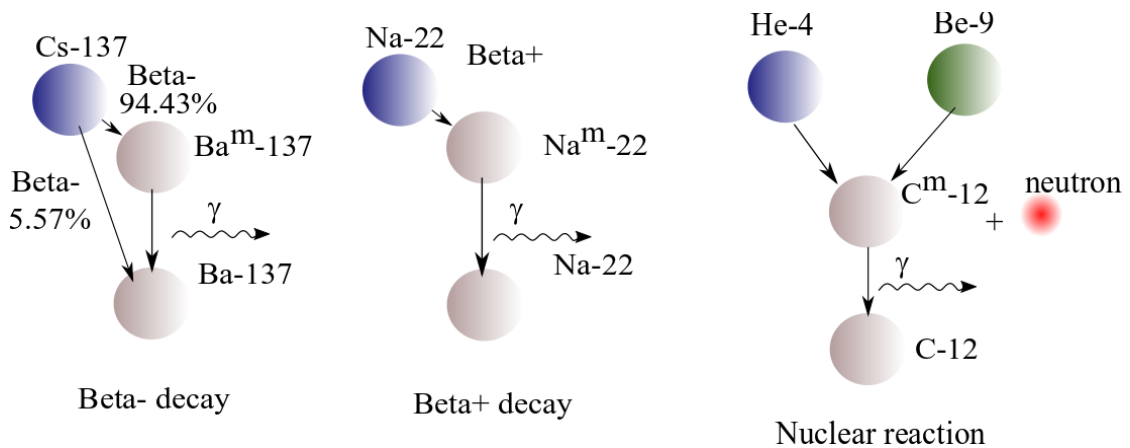
Figure 2.1: Examples of gamma-ray sources with the decay path of Cs-137 via beta- decay, Na-22 via beta+/electron conversion and nuclear reaction of Ba-9 with He-4 creating excited C-12 isotope and neutron. All excited nuclear state nuclei with very fast decay via gamma-ray emission to a lower energy state nuclear level [4, 7].

In gamma-ray detection applications, there are three interaction mechanisms of high importance, Compton scattering, photoelectric absorption and pair production. In Compton scattering, an incident photon loses part of its energy when interacting with a loosely bonded orbital electron consequently resulting in a free recoil electron and lower energy scattered photon. The amount of energy lost in Compton scattering depends on the energy of the incident photon and the scattering angle. Figure 2.2 illustrates the Compton scattering interaction mechanism.
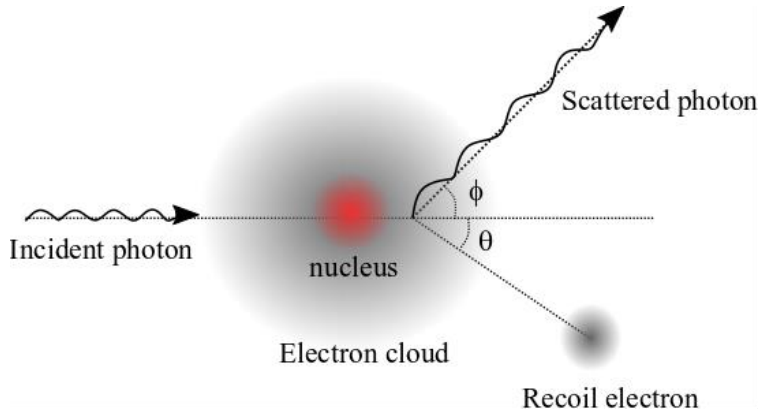
Figure 2.2: A schematic diagram of Compton scattering interaction between the incident photon and the orbital electron within the electron cloud, resulting in the scattering of the photon and a recoil electron (sizes illustrates the interaction components in the figure and do not reflect the relative actual sizes).

Within the Compton scattering interaction, energy and momentum are conserved. Hence, if a gamma-ray photon with initial energy E_γ undergoes a Compton scattering event and is scattered with an angle ϕ, the resulting final photon energy E_γ' can be calculated based on conservation of momentum and conservation of energy laws as following [3]:

$$E_\gamma' = \frac{E_\gamma}{1 + \frac{E_\gamma}{m_e c^2}(1 - \cos\phi)} \tag{2.3}$$

Where $m_e c^2$ is the electron rest mass energy (0.511 MeV).

Compton scattering interaction is dominant for photons with energies between approximately 0.5 MeV and 5 MeV, however, Compton scattering could occur at any energy within the path of a photon [4]. The probability of a Compton scattering interaction taking place depends on the number density of the target, which is proportionally related to the atomic number and the number of available electron scattering sites in the target material.

The photoelectric absorption interaction mechanism describes the predominant interaction mechanism for low energy photons in which the photon is completely absorbed by the atom. As a result, the atom will gain enough energy to emit a tightly bound electron from one of the bond shells surrounding the nucleus as shown in Figure 2.3.

Incident photon

nucleus

Electron cloud   Ejected
                      photoelectron
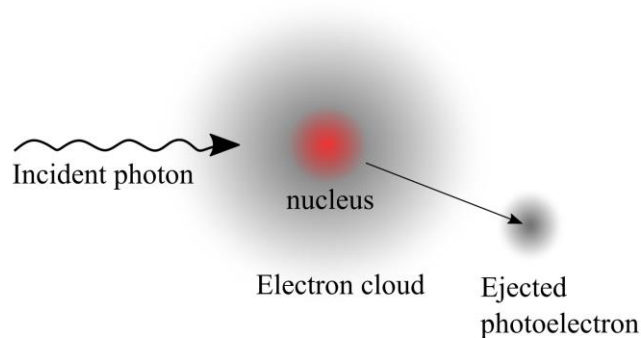
Figure 2.3: A schematic diagram of photoelectric absorption interaction mechanism between an incident photon and an atom in the electron cloud resulting in an ejected photoelectron (sizes illustrates the interaction components in the figure and do not reflect the relative actual sizes).

The photoelectric absorption interaction has a higher probability of occurring for low energy photons traversing a target comprised by high atomic number, *Z,* and high-density [4].

Pair production results in the disappearance of the incident photon and the creation of an electron-positron pair. [3]. The electron-positron pair is short-lived and subsequent annihilation gamma-ray photons are generated from the scene [3]. Pair production interaction mechanism dominates for incident photons with energies above 5 MeV and has threshold energy of 1.022 MeV [4].

For a beam of photons, the probability of a single photon being removed is described by the linear attenuation coefficient, μ. The loss in a photon beam per second or the intensity loss (ΔI) within a target thickness x can be computed using the formula [4]:

$$\Delta I = I_o - I = I_o \, (1-e^{-\mu x}) \tag{2.4}$$

Where I_o is the original intensity of the photon beam and I is the transmitted intensity through the target. μ can be partitioned into components based on the interaction mechanism:

$\mu =$ Pair production component + Compton scattering component + Photoelectric absorption component $\tag{2.5}$

2.1.2 Neutron interactions

Neutrons are an electrically neutral, highly penetrating, elementary hadronic particles comprised of one up spin quark and two down spin quarks held together with the strong nuclear force [1]. Neutrons are found in all nuclei with atomic mass number higher than the atomic mass number of hydrogen. Conventionally, free neutrons are classified based on their energies, as shown in Table 2.1, with thermal neutrons defined to be neutrons outside the nucleus in thermal equilibrium with their surroundings [1, 8].

Table 2.1: Classification of neutrons on the basis of energy.

Neutron type	Energy/Energy range
Cold	0 – 0.025 eV
Thermal	0.0253 eV*
Epithermal	0.2 eV – 10 eV
Slow	10 eV – 100 eV
Intermediate	100 eV – 10 keV
Fast	10 keV – 10 MeV
High-energy	>10MeV

* thermal neutron energy at 20°C

Neutron sources in nature and in industry emit neutrons at different energy ranges. Emitted neutrons are typically in the fast energy range such as neutrons emitted in fission reactions [9]. Neutrons at higher energy ranges can be found in Deuterium-Triton reactions and Triton-Triton reactions with typical energy of ~14 MeV [4]. Neutron at thermal energy are emitted from sources such as Sb-124/Be-9 photo-neutron source which is usually found in nuclear reactor sites [4].

Neutrons travel in straight lines and only a direct interaction with the nucleus of a target material can change their trajectory. The probability of any type of interaction taking place with a single nucleus is defined as the microscopic cross section σ. The microscopic cross section is conventionally expressed in units of barns (b) ($=10^{-28}$ m^{-2}). The total microscopic cross section is comprised of the sum of different individual microscopic interaction cross sections, such as the elastic scattering cross section, non-elastic cross section and capture cross section. The microscopic cross section is highly dependent on the energy of the incident neutron and the chemical composition of the

target. Figure 2.4 illustrates the dependency and variation of the total microscopic cross section with the energy of incident neutron for different nuclei including H-1 (comparable nucleus size to neutron), Li-6 and B-10 (intermediate size nuclei) and U-235 and Gd-157 (heavy target nuclei).
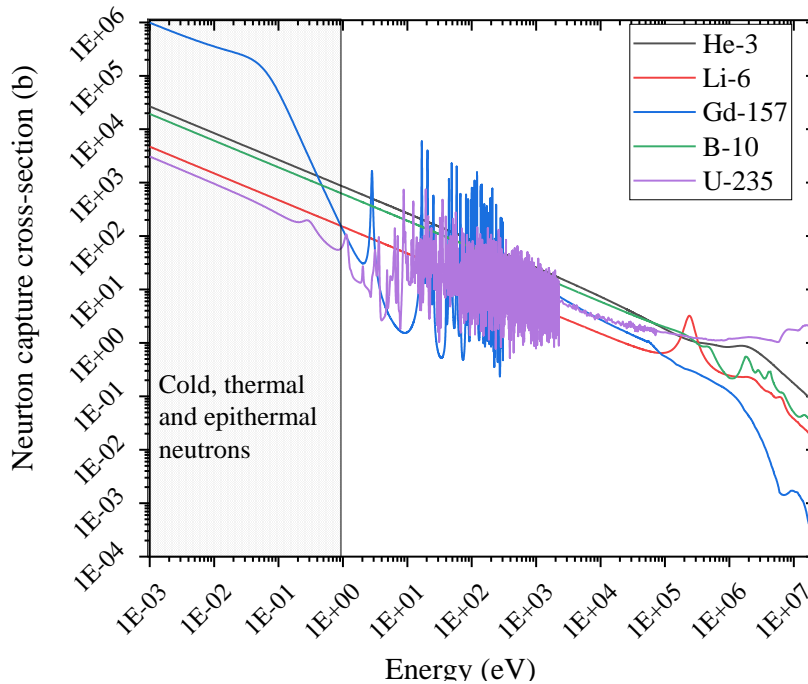
Figure 2.4: Total microscopic cross section variation with varying energy and varying target nucleus for H-1, Li-6, Gd-157, B-10 and U-235 [7].

The macroscopic cross section, Σ, is the product of the microscopic cross section and the number density of the target material, N_D. The macroscopic cross section describes the probability of interaction per unit length of track, x, in the target.

Neutrons traversing a target material can undergo scattering interactions. Generally, two types of neutron scattering interaction mechanisms are discussed in literature, elastic scattering and inelastic scattering [1, 10]. Elastic scattering is more common for fast neutrons interacting with low atomic number target Figure 2.5 illustrates the main

components in elastic scattering events for a neutron on a target nucleus in centre of mass frame and in laboratory frame.
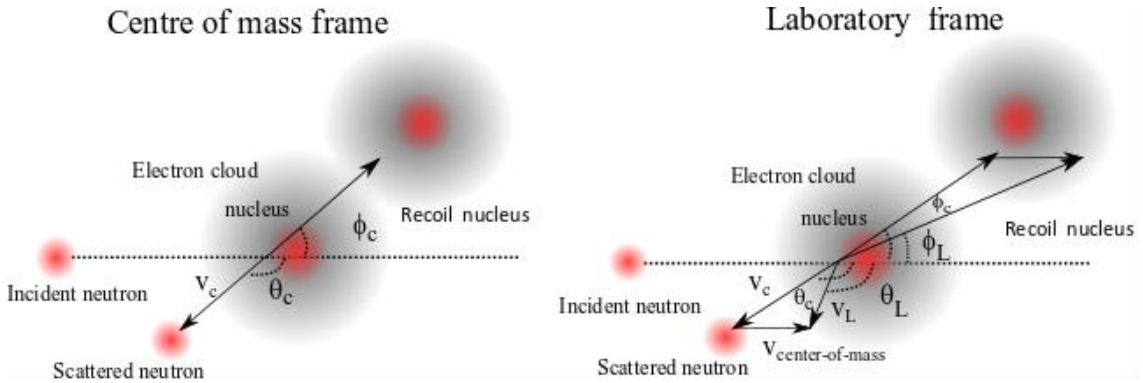
Figure 2.5: A schematic diagram of elastic scattering interaction of neutron and a target nucleus in the centre of mass frame (left) and in the laboratory frame (right) (sizes illustrates the interaction components in the figure and do not reflect the relative actual sizes).

In the centre of mass frame, the energy of the scattered neutron can be computed based on conservation of energy law and conservation of momentum law as [10]

$$E'_n = \frac{A^2 + 1 + 2A\cos\theta_c}{(A+1)^2} E_n \qquad (2.7)$$

Where E'_n is the energy of the scattered neutron, E_n is the energy of the incident neutron and θ_c is the scattering angle in the centre of mass frame. A equals $\frac{M+m_n}{m_n}$ where M is the atomic mass number of the target nucleus and m_n is the neutron mass. For M $>>m_n$, A is equal to atomic mass number of the target nucleus M. For head-on collisions with proton rich target, the scattering angle in the laboratory frame and the scattering angle in the centre of mass frame are related by the following formula [10]

$$\tan \theta_L = \frac{\sin \theta_c}{\frac{1}{A} + \cos \theta_c} \tag{2.8}$$

With $A \sim 1$, using the law of cosines further simplifies equation 2.8 to [11]:

$$E_p = E_n \sin^2 \theta_L \tag{2.9}$$

Here E_p is the recoil proton energy. The second scattering mechanism in which fast neutrons might undergo is inelastic scattering. Inelastic scattering events predominantly occur between high-energy neutrons and target nuclei with high atomic number. As a result, part of the neutrons energy is transferred to the target nucleus [12]. Therefore, energy and momentum quantities are not conserved in this interaction. With the intent energy range specified in this research and the aimed light target nuclei in the detector materials, elastic scattering is the scattering interaction mechanism of interest within this research.

Neutrons traversing target material can undergo capture reactions as well. For neutrons, capture reactions are a type of nuclear reaction in which the target nucleus absorbs a neutron. The target nucleus and the resultant nucleus from the capture reaction are isotopes of the same element. The probability of a capture interaction occurrence is highly dependent on the energy of the incident neutron and the type of the target nucleus. Secondary products such as gamma rays, alpha particles, triton and fission products are expected from thermal neutron capture reactions. Table 2.2 lists common thermal neutron capture reactions based on ENDF/B-VII data library[7].

Table 2.2: Thermal neutron capture cross sections.

Isotope	Capture cross section (b)	Secondary particles
H-1	0.3327	A photon per capture reaction with energy of 2.2 MeV
He-3	5317.591	A proton and a triton (Q = 0.765 MeV).
Li-6	938.3274	Alpha particle and triton (Q = 4.78 MeV). Photons with intensity >20% within energy range between 0.7 to 2.2 MeV
B-10	3845.509	Alpha particle and Li-7 (Q = 2.78 MeV). Photons emission with most probable energy of 0.478 MeV
Gd-155	60737.13	Photons with broad energy spectrum and maximum energy of 8 MeV
U-235	586.7371	Fission products

2.1.3 Charged ionising radiation interactions

Understanding the interaction mechanism of charged particles within this research is part of realising the fate of the secondary products in the interactions of the main ionising radiation understudy. Heavy charged particles such as protons, alpha particles and fission fragment directly ionise the target atoms via Coulomb interaction mechanism [3]. The Coulomb interaction mechanism allows the gradual and consistent loss of charged particles energy within the target. Conventionally, the linear stopping power, *–dE/dx,* of a material is used to describe the process via which charged particles transfer or lose energy and is commonly described in units of MeV/cm [3]. The linear stopping power is approximated by Bethe formula [4] and it relates the velocity of the charged particle to the characteristics of the target. The Bethe formula for a particle with a given charge is given as [4].

$$-dE/dx \;=\; \frac{4\pi e^4 z^2}{m_e v^2} \cdot N.\; Z.\; [\ln\frac{2m_e v^2}{I} -\ln (1- \frac{v^2}{c^2})-\frac{v^2}{c^2} \;] \tag{2.10}$$

Where e is the electron charge and z is the charge of the particle, c is the speed of light, v is to the velocity of the ionising particle, m_e is the electron rest mass and N is the number density if the target atomic number of the target. I is a characteristic parameter of the target and it describes the average excitation or ionisation potential of the atoms. Coulomb interactions are the most probable interaction mechanism of charged particles in matter. The Bremsstrahlung interaction mechanism occurs for light charged particles, such as electrons, in which high-energy charged particle decelerates within the electric field of the nucleus resulting in the emission of bremsstrahlung radiation. However, the occurrence of this interaction mechanism is significantly less likely compared to Coulomb interaction mechanism [3].

2.2 Detection methods of ionising radiation

2.2.1 Gamma-ray detection methods

Gamma-ray photons are charge-less and therefore the detection of these photons rely on the products of the interactions taking place. Three major material categories are considered as the main gamma-ray detection materials, gas detectors, scintillation materials and solid-state detectors. Gas-filled detectors for gamma-ray are very common in monitoring and gauging applications [13]. Examples of gas detectors are ion-chambers, proportional counters and Geiger-Muller counters all with the common structures of a gas-filled housing with applied voltage across it is electrodes. In gas-filled detectors, an incoming gamma-ray ionises the gas molecules via the photoelectric effect or Compton scattering interaction mechanisms generating electron-ion$^+$ pairs.

The voltage applied across the cavity will cause the electron and the ion$^+$ to travel across the gas towards the electrodes generating an electrical signal as a result.

Scintillation materials or scintillators operation principle is based on the scintillation process within the material in which the incident radiation field is absorbed or scattered and its energy is dissipated in the scintillator. The process results in luminescence emission of light (visible or ultraviolet). A light sensitive device then collects the scintillation photons. The manner via which energy is dissipated as ionisation or excitation in the scintillator fundamentally depends on the scintillation material. There are two main categories of scintillators; organic scintillators and inorganic scintillators. In organic scintillators, the conversion of radiation energy to luminescence is associated with the electronic structure of the organic molecules. In carbon based organic scintillators, the excited states of π-electrons are mainly responsible for luminescence emission. Within the π-electronic energy levels of organic scintillator molecules there are singlet states (S0, S1, S2 …) and triplet states (T0, T1, T2 …). Excitation or ionisation of electrons to singlet states and subsequently de-excitation to singlet states results in a prompt emission of scintillation light known as fluorescence. Fluorescence is characterised with short lifetime between 1 ns to 10 ns (S_1 level de-excitation). The excitation of electrons to singlet states followed by their immigration to and subsequently de-excitation from triplet state results in a delayed and slower emission of scintillation known as phosphorescence. This photon emission process forms the basis of scintillation light (signal carriers) production in organic scintillators. Organic scintillators can be found in vapour state, liquid state and crystalline state. Examples of organic scintillators utilised in gamma-ray detection in the literature are NE-213 and EJ-309 [14-16]. In inorganic scintillators, the interaction of gamma rays in the

scintillator causes changes in the energy level of the crystal lattice. Impurities (activators) are usually added to the crystal to reduce light self-absorption. Within the crystal lattice, electrons have only discrete energy bands to lie within. The energy bands have impurity sites in which electrons might emigrate to [17]. The absorption of energy from the interaction with ionising radiation excites the crystal lattice and raises the electrons from the valence band to the conduction band. Electrons eventually descend to the excited energy levels of the impurities and then de-excite to the ground energy level of the impurities. This de-excitation process results in the emission of scintillation light in the visible region or ultraviolet region. Figure 2.6 illustrates in a schematic of a crystal lattice the excitation and de-excitation process of electrons within inorganic scintillator and subsequently the production of scintillation light in the visible range.
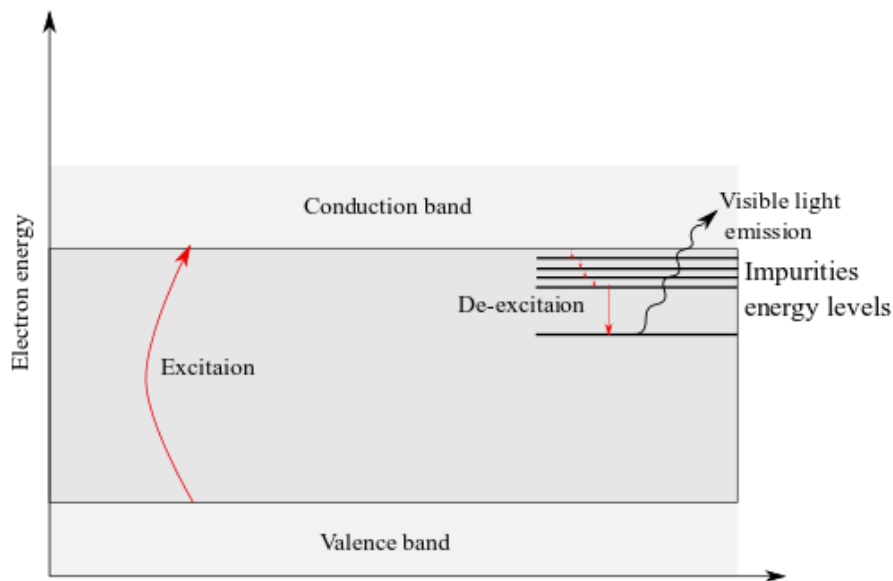
Figure 2.6: A schematic diagram of crystal lattice excitation and de-excitation process in doped inorganic scintillator.

 Typical gamma-ray inorganic scintillator crystals are alkali halides activated by metals such as NaI(Tl), CsI(Tl) and LiI(Eu) [17]. Inorganic glasses used in gamma-ray detection comprises typically of silicon oxides, boron, lithium, phosphors and

impurities such as Ce [18]. Other inorganic scintillator groups, including alkali earth Hilde such as $CaF_2(Eu)$ and BaF, transition metal scintillators such as $YAlO_3(Ce)$, post transition metal scintillators such as $Bi_4Ge_3O_{12}$ or BGO, rare-earth oxyorthosilicates such as $Gd_2SiO_5(Ce)$ or GSO(Ce) and elpasolite scintillators such as $Cs_2LiYCl_6(Ce)$ and $Cs_2LiLaBr_6(Ce)$ [19-21]. An important comparison feature between scintillators is their light yield, which is defined as the number of scintillation photons emitted per unit absorbed energy given in units of photon per unit mega electron volt [21].

Analogous to scintillators, in solid-state detectors the detection operation principle is based on absorbing gamma-ray photons and subsequently dissipating its energy in the crystal. Most common solid-state detectors are semiconductors with both pure and doped semiconductor configurations available in radiation detection applications. When sufficient reverse bias is applied across the semiconductor, the depletion region extends creating sufficient active detector area. The energy of the absorbed radiation creates free charges, an electron-hole pair. The amount of charge created in the semiconductor is proportional to the energy deposited by the radiation field. For both pure and doped semiconductor detectors, electron-hole pairs are collected through an applied electric field. Examples of gamma-ray semiconductor detectors include Si, Ge, CdZn, CdZnTe, HgI_2 and GaAs.

Gamma-ray radiation detection efficiency is a direct function of the detection materials atomic number [21]. This gives a huge advantage to scintillators and solid-state detectors with high density and high atomic number compared to gas detectors. In addition, gamma-ray spectrometry requires good discrimination abilities between different photon energies. Compared to scintillators, semiconductor detectors have higher energy discrimination abilities. This is mainly due to the higher number of signal

carriers per incident radiation generated in semiconductors compared to any other radiation detectors [3]. However, their small size and high cost might be disadvantageous in some applications.

2.2.2 Neutron detection methods

Neutrons detection is strongly dependent on their energy. This is due to the variation of the interaction cross section with neutron energy. At thermal energy and low energy ranges, detection through capture reactions (n, charged particles) is the most common detection technique. Capture reactions result in secondary charged particles whose combined kinetic energy equals the neutrons incident energy plus the Q value of the interaction. Neutron detection via capture reactions in gas detectors relies on nuclei with high neutron capture cross section such as He-3, B-10, and U-235 (Table 2.2). Proportional gas counters filled with gaseous detection materials such as He-3 gas (active gas component He-3) and BF_3 gas (active gas component B-10) are very common in radiation monitoring and gauging applications. Capture reactions of He-3 and BF_3 gas are written as [4]:

In He-3: $$^{3}_{2}He + ^{1}_{0}n \rightarrow ^{1}_{1}H + ^{3}_{1}H + 0.765 \text{ MeV}$$

In BF_3: $$^{10}_{5}B + ^{1}_{0}n \rightarrow ^{4}_{2}He + ^{7}_{3}Li + 2.78 \text{ MeV}$$
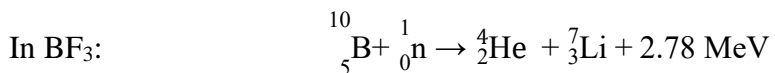
Within the proportional gas counter, charged particles generated from capture reactions will directly ionise the gas molecules resulting in the formation of electro-ion$^+$ pairs (signal carriers). Other examples of gas detectors including B-10 lined detector and fission chambers with fissionable nuclei such as U-235 coating the inner walls of the gas chamber [4].

Organic scintillators loaded with nuclei of high thermal neutron capture cross section exist in liquid state and in solid (plastic) state. Capture reactions in Li-6 nuclei are widely used in scintillation materials. The capture reaction in Li-6 can be written as [4]:

$$^{6}_{3}\text{Li} + ^{1}_{0}\text{n} \rightarrow ^{4}_{2}\text{He} + ^{3}_{1}\text{H} + 4.78\,\text{MeV}$$
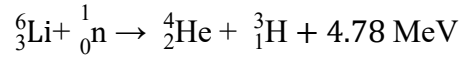
Capture reactions in Li-6 result in one of the highest Q-values among the reactions listed in Table 2.2. Li-6 loaded organic scintillators have been utilised and tested in literature for their background discrimination abilities [15]. The highly charged particles resultant from this interaction (i.e. alpha particle and triton) will deposit their energy in the scintillator. As a result, scintillation light will be generated indicating the detection of a neutron.

Li-6 based inorganic scintillators such as LiF(Ag), LiI(Eu), LiBaF$_3$ and LiCaAlF$_6$(Eu) in crystalline structure offer naturally high Li-6 macroscopic cross sections. Li-6 based glass scintillators containing Li$_2$O are by far the most widely used capture reaction based glass scintillators [3]. They exist in a variety of chemical combinations, Li-6 enrichment ratios and crystal thicknesses (usually between 0.5-25 mm) [3]. New Li-6 inorganic scintillator such as Cs$_2$LiYCl$_6$ and other elpasolite family detectors have been showing strong competition to conventional Li-6 based inorganic scintillators in the last two decades [22] , with some claiming higher detection characteristics compared to other conventional Li-6 based inorganic scintillators [20, 23]. Gd-157 based inorganic scintillation detectors such as Li$_6$Gd (BO$_3$)$_3$: Ce have also been suggested for capture reaction based detection methods [22].

The detection of neutrons via capture reactions in solid–state detectors is commonly approached through conversion layers. B-10 and Li-6 based conversion layers

combined with semiconductor-based detector are conventional choices in capture reaction solid-state detectors [4]. Other solid-state detectors such as [4]H-SiC and diamond have been suggested as solid-state detectors as well [4] . The charged ionisation particles generated from these capture reactions will travel from the conversion layer to the solid-state detector causing ionisation.

In the foil activation detection method, the capture of a neutron by the nucleus of the target transforms the element into a radioactive isotope [3]. The radioactive isotope eventually decays, some of which by emitting beta particles or gamma rays, and the emitted radiation is then detected by appropriate detectors indicating the capture of a neutron. Gold, Indium, Silver, Iron and Aluminium are examples of commonly used elements in activation foils. This method is utilised in neutron flux measurements and materials activation analysis with applications covering neutrons at broad energy range [3].

While it is possible to detect fast neutrons by their capture reactions, in most cases the detection efficiency of the instrument dramatically decrease with increasing neutrons energy. Moderating fast neutrons via elastic scattering is highly achievable in hydrogenous or carbon-based materials due to their high elastic cross section. Bonner spheres are good examples of the fast neutrons detection technique via moderation. They are frequently used in neutrons dose measurements and in neutron spectroscopy [24, 25]. In general, Bonner spheres offer high detection efficiency and good background rejection abilities, however, they are bulky and offer very poor energy resolution [25]. Another example of a fast neutron counter are long counters with cylindrical shaped moderator and gas proportional counter embedded within the

cylinder [26]. Two main shortcomings with this technique are, first, in most designs energy information is lost and second, the detection process is slow [4].

The scattering reactions of fast neutrons is a phenomenon that has been widely exploited for neutron detection. Elastic scattering of fast neutrons from light nuclei, such as hydrogen (proton) or carbon, transfers large amount of energy to the recoiled nuclei as shown through section 2.1.2. The limits of the recoil proton energy are $0 \leq E_p \leq E_n$ with zero energy is transferred in 90° collision scenario and total energy is transferred at head-on collision. The scattering angel of the recoil proton deduced from equation 2.9 is:

$$\sin^2\theta_L = E_p/E_n \qquad (2.11)$$

Conventionally, organic scintillators offer hydrogen rich detection medium with Stilbene, liquid and plastic scintillators all valid candidates for recoil proton fast neutron detection method. Gas filled detectors, mainly proportional counters, are used in recoil proton fast neutron detection method as well. However, gas filled detectors have inherently lower detection efficiency due to their lower density (hence lower macroscopic cross section compared to solid detectors). With the suitable response function of the detector in use, this method allows direct measurements of incident neutrons energy [27-29].

2.2.3 Photodetectors

The signal carriers generated by the interaction of ionising radiation in scintillators require further conversion to detectable electrical signals. A conventional technique of converting signal carriers in radiation detection is the use of Photomultiplier Tubes

(PMT). In an optically coupled PMT, the guided photons will traverse a photocathode conversion layer that converts photons into electrons via photoelectric effect. The body of the PMT is made with a series of electrodes amplifying the total number of electrons and therefore the electrical signal by a fixed factor. PMTs are the most common signal light converter and amplifier technique for scintillators in radiation detection. However, solid-state photodetectors are a rapidly emerging technology that has proven to be strong competitors to PMTs. Solid-state technology offers the characteristic missing from PMTs; the ability to operate under low voltage compared to PMTs. Solid state solutions also offer considerably less sensitivity to magnetic field effects, higher quantum efficiency, compactness, enhanced ruggedness and higher resistance to mechanical and physical stress [4]. Common conventional photodiodes utilises a semiconductor p-n junction configuration with a depletion region sandwiched in between the two. Within these photodiodes, signal carriers are directly converted into electron-hole pairs. The conversion efficiency of conventional photodiodes are between 60% and 80% [4]. Because there is no amplification however, electronic noise is a major problem with conventional photodiodes, especially when detecting low energy radiation fields. The avalanche photodiode concept is similar to that of conventional photodiodes, although the main difference between the two is their operation mode. While the voltage across conventional photodiodes is designed to only prohibit recombination of electron-hole pairs and to drive them to the corresponding electrode, in avalanche photodiode the voltage across the photodiode is designed to be large enough to accelerate electrons to very high velocities. The accelerated electrons cause further ionisation along their path in the photodiode creating more electron-hole pairs and causing an electron avalanche. The gain of the electric pulse generated from the electron avalanche increases with increasing applied voltage. Typically, the generated electrical signal is greater in

magnitude than the electrical noise level, hence an improved performance compared to conventional photodiodes [4]. If the applied voltage was sufficiently large enough to accelerate the holes, both electrons and holes will contribute in the generation of electron avalanche and avalanche breakdown appears in the semiconductor diode. Semiconductor photodiodes operating under this sufficiently high voltage are commonly known as Geiger mode avalanche photodiode [30]. An example of the voltage required to sustain an avalanched multiplication (breakdown voltage) for some semiconductor avalanche photodiodes is in the range between 16 V to 25 V [30]. Figure 2.7 illustrates the gain behaviour as function of applied bias voltage across the semiconductor based photodiode.
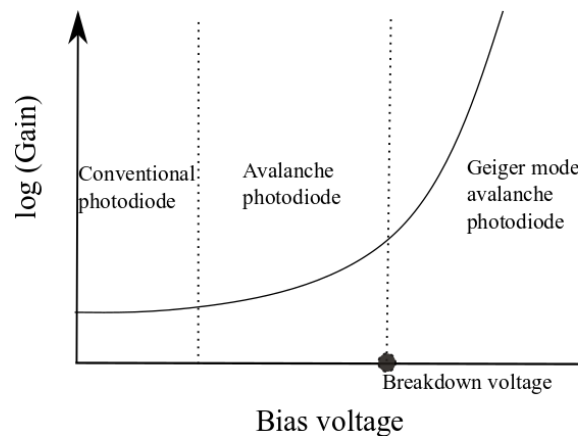
Figure 2.7: Photodiode gain as function of applied bias voltage for conventional photodiode, avalanche photodiode and Geiger mode photodiode.

Single photon avalanche photodiodes, SPAD, are the building blocks of many light sensing applications including silicon photomultipliers, SiPM. Because the size of each SPAD is small, the probability of a single photon creating an avalanche per SPAD is high enough to assume that the number of avalanches generated is proportional to the number of photons detected in the cell [4]. The photon detection efficiency, PDE, is a

measure of the efficiency of the SiPM in converting incident photons into a measurable signal with many commercial SiPMs offering PDE higher than traditional PMTs [4]. Some of the drawbacks in current SiPM models include dark pulses, electrical noise, performance dependency on operation temperature and applied voltage. The first two are tackled by setting a discrimination level to reject dark pulses and electrical noise from a single pixel. In addition, choosing a detector with peak light emission at short wavelengths (blue region) can considerably minimise thermally generated noise by restricting charge generation to be near the p-type region in the junction. Optical cross talk between SPADs may contribute to electrical noise generation as well. One approach to minimise cross talk is to minimise the size of the SPAD [31]. In addition, cooling the SiPM and eliminating any variations in the applied voltage can help reducing thermal and electrical noises. Because of their advantages and the ability of overcoming their drawbacks, SiPMs are the photodetectors utilised within the proposed design in this work.

2.2.4 Noise and signal processing

In the SiPMs, the standard output from a pixel is connected to a load resistor (~50 Ω) [32]. The pulse extracted beyond this point generally adopt transient pulse shape. Commonly, pulse shaping is the next step in signal processing. The first common objective of pulse shaping is to enhance the signal-to-noise ratio. Electrical noise is almost inevitable in radiation detection. Sources of electrical noise include thermal fluctuations and vibrational noise travelling through electrical power mains. Conventional passive noise filters such as high pass filters, low pass filters and band pass filters where combinations of resistor and capacitor are utilised as well as active op-amp based filters are all valid noise filter circuits. In the case of active filters the two

steps of pulse shaping and amplification is integrated into one-step as shown in Figure 2.8. The second objective of pulse shaping is to modify the shape of the pulse to facilitate meeting the target of the detection process, such as radiation counting applications, dual mode detection applications and spectroscopy applications [3]. Trans-impedance amplifiers and pulse amplification can be applied prior to or after pulse shaping. The aim is to convert the generated current to a measurable voltage pulse and hence an optimised coupling between the detection system and the processing unit and to further reduce any additional noise.
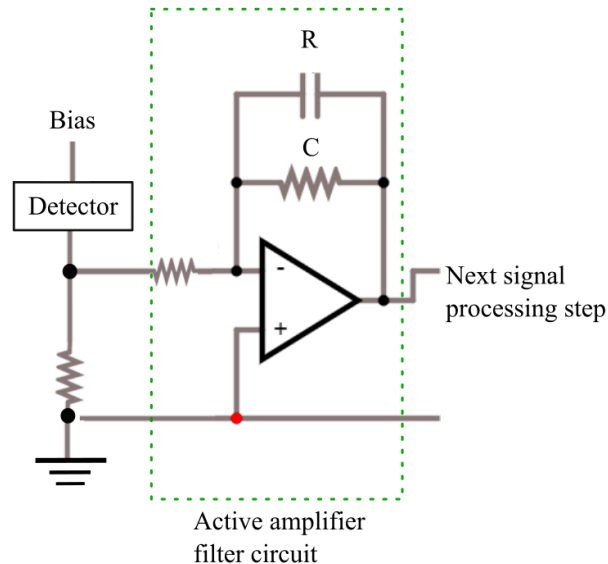
Figure 2.8: Example of combined filter-amplifier circuit utilised in pulse processing.

2.2.5 Common definitions and features of radiation detectors

Important aspects in ionising radiation detection are the characteristics of the detection medium. The main criteria upon which detectors are characterised are:

- Detection efficiency.

- Energy resolution.

- Spatial, angular and temporal resolutions.

- Shape, size and cost.

There are different definitions describing detection efficiency. However, a common feature between all of these definitions is that they all describe the conversion process of incident radiation particles into measurable signals. For a source-detector system, the ratio between the generated pulses in the detector and emitted radiation quanta from the source describes the absolute efficiency of the detector. Generally, absolute efficiency is defined using the formula [4]:

$$\text{Absolute efficiency} = \frac{\text{The number of measured pulses}}{\text{The number of radiation quanta emitted by the source}} \qquad (2.12)$$

Similarly, the ratio of the number of generated pulses and the incident radiation quanta on the detector describes intrinsic efficiency. Generally, intrinsic efficiency is defined using the formula [4]

$$\text{Intrinsic efficiency} = \frac{\text{The number of measured pulses}}{\text{The number of radiation quanta incident on the detector}} \qquad (2.13)$$

Statistical efficiency describes the pulse counting abilities of the system. Examples are total efficiency and peak efficiency. Total efficiency is related to the total number of pulses recorded in the instrument.

Energy resolution is an important characteristic of detection instrument especially in spectroscopy applications. The concept of energy resolution can be explained through a mono-energetic radiation source. For a pulse height spectrum generated with the differential number of pulses recorded in the system as function of the differential pulse height, the full width at half maximum (FWHM) of the differential pulse height

corresponding to the expected energy of the source divided by the pulse height is defined as the energy resolution [21]. Energy resolution measures the ability of the detection instrument to differentiate radiation quanta of different energies.

Spatial resolution is essential in describing the ability of the imaging system to accurately locate a radiation source. A number of definitions describes the spatial resolution in the literature, all of which seem to be field or application orientated. For a pixelated system, however, spatial resolution refers to the number and the size of the pixels utilised in creating the image. The quality of the generated image is proportionally related to the number of pixels in the system [33]. Angular resolution describes the ability of the system to differentiate between two closely spaced objects. This characteristic is conventionally described in units of radiant. For a scattering based imaging system, the angular resolution is a function of the parameters contributing in the formation of the probability cones such as the energy resolution of the system. These parameters are the measurements of position and the measurements of incident radiation energy [34]. Uncertainties in these measurements will cause spread around the predicted location of the radiation source. Temporal resolution is measure of the time required to acquire and reassess data. The shorter this time is the higher the temporal resolution and vice-versa. Dead-time is a related parameter to temporal resolution and is a measure of the time between two successful measurements [4]. Dead-time in an instrument is a crucial characteristic especially in high counting rate scenarios. A direct disadvantage of low temporal resolution or long dead time is the loss of real events and hence low detection efficiency. Shape and size are highly application dependent characteristics. Cost is undoubtedly a significant factor in selecting detectors especially in commercial application.

2.3 References

1. Krane, K.S., *Introductry nuclear physics*. 1988, New York, NY, USA: John Wiley and Sons.

2. *Photon*. 2019 25/10/2019]; Available from: https://www.britannica.com/science/photon.

3. Landsberger, N.T.a.S., *Measurement and Detection of Radiation* ed. F. edition. 2015, NY: CRC Press, Taylor & Francis Group.

4. Knoll, G.F., *Radiation detection and measurment*. Fourth ed. 2010, New York, NY, USA: John Wiley and Sons.

5. Schmitt, H.W., J.H. Neiler, and F.J. Walter, *Fragment energy correlation measurements for Cf252 spontaneous fission and U235 thermal-neutron fission.* Physical Review, 1966. **141**(3): p. 1146-1160.

6. Verbinski, V.V., H. Weber, and R.E. Sund, *Prompt gamma rays from U235(n,f), Pu239(n,f), and spontaneous fission of Cf252.* Physical Review C, 1973. **7**(3): p. 1173-1185.

7. NEA, O. *Java-based nuclear data information system*. 16/01/2016 [cited 2016 10/02/2016]; Available from: http://www.oecd-nea.org/janis/.

8. Reuss, P., *Neutron physics*. 2008: EDP Science.

9. TERRELL, J., *Distributions of Fission Neutron Numbers.* Physical Review, 1957. **108**(3).

10. Stacy, W.M., *Nuclear reactor physics*. Second ed. 2007, Fedral Republic of Germany: Wiley-VCH Verlag and Co.

11. Weinfurther, K., et al., *Model-based design evaluation of a compact, high-efficiency neutron scatter camera.* Nuclear Instruments and Methods in Physics Research, Section A: Accelerators, Spectrometers, Detectors and Associated Equipment, 2018. **883**: p. 115-135.

12. L'Annunziata, M.F., *Handbook of radioactivity analysis*. 2nd ed. ed. 2003: Academic.

13. Hubbell, J.H., *Survey of Industrial, Agricultural, and Medical Applications of Radiometric Gauging and Process Control.* Journal of research of the National Institute of Standards and Technology, 1990. **95**(6): p. 689-699.

14. Brooks, F.D., *A scintillation counter with neutron and gamma-ray discriminators.* Nuclear Instruments and Methods, 1959. **4**(3): p. 151-163.

15. Zaitseva, N., et al., *Plastic scintillators with efficient neutron/gamma pulse shape discrimination.* Nuclear Instruments and Methods in Physics Research, Section A: Accelerators, Spectrometers, Detectors and Associated Equipment, 2012. **668**: p. 88-93.

16. Polack, J.K., et al. *Dual-particle imager for standoff detection of special nuclear material*. in *2011 IEEE Nuclear Science Symposium Conference Record*. 2011. Valencia, Spain.

17. Birks, J.B., *The theory and practice of scintillation counting*. 1964: Pergamon Press, Macmillan, New York.

18. Guizhen, S., et al., *The preparation and properties of cerium-activated lithium glass scintillators.* Journal of Non-Crystalline Solids, 1986. **80**(1-3): p. 594-599.

19. Tanner, P.A., et al., *Absorption and emission spectra of Ce3+ in elpasolite lattices.* Journal of the American Chemical Society, 2003. **125**(43): p. 13225-13233.

20. Glodo, J., et al., *Selected Properties of Cs2LiYCl6, Cs2LiLaCl$_6$, and Cs$_2$LiLaYBr$_6$ Scintillators.* Ieee Transactions on Nuclear Science, 2011. **58**(1): p. 333-338.

21. McGregor, D.S., *Materials for Gamma-Ray Spectrometers: Inorganic Scintillators*, in *Annual Review of Materials Research*. 2018. p. 245-277.

22. van Eijk, C.W.E., A. Bessière, and P. Dorenbos, *Inorganic thermal-neutron scintillators.* Nuclear Instruments and Methods in Physics Research Section A: Accelerators, Spectrometers, Detectors and Associated Equipment, 2004. **529**(1): p. 260-267.

23. Giaz, A., et al., *The CLYC-6 and CLYC-7 response to gamma-rays, fast and thermal neutrons.* Nuclear Instruments & Methods in Physics Research Section a-Accelerators Spectrometers Detectors and Associated Equipment, 2016. **810**: p. 132-139.

24. Bramblett, R.L., R.I. Ewing, and T.W. Bonner, *A new type of neutron spectrometer.* Nuclear Instruments and Methods, 1960. **9**(1): p. 1-12.

25. Thomas, D.J. and A.V. Alevra, *Bonner sphere spectrometers—a critical review.* Nuclear Instruments and Methods in Physics Research Section A: Accelerators, Spectrometers, Detectors and Associated Equipment, 2002. **476**(1): p. 12-20.

26.   Hanson, A.O. and J.L. McKibben, *A neutron detector having uniform sensitivity from 10 Kev to 3 Mev.* Physical Review, 1947. **72**(8): p. 673-677.

27.   Lockwood, J.A., et al., *Response functions of organic scintillators to high energy neutrons.* Nuclear Instruments and Methods, 1976. **138**(2): p. 353-362.

28.   Enqvist, A., et al., *Neutron light output response and resolution functions in EJ-309 liquid scintillation detectors.* Nuclear Instruments & Methods in Physics Research Section a-Accelerators Spectrometers Detectors and Associated Equipment, 2013. **715**: p. 79-86.

29.   Pino, F., et al., *The light output and the detection efficiency of the liquid scintillator EJ-309.* Applied Radiation and Isotopes, 2014. **89**: p. 79-84.

30.   Spinelli, A. and A.L. Lacaita, *Physics and numerical simulation of single photon avalanche diodes.* IEEE Transactions on Electron Devices, 1997. **44**(11): p. 1931-1943.

31.   Piemonte, C., et al. *Development of an automatic procedure for the characterization of silicon photomultipliers.* in *IEEE Nuclear Science Symposium Conference Record.* 2012.

32.   *J-SERIES SIPM: Silicon Photomultiplier Sensors, J-Series (SiPM).* [cited 2019 15/05/2019]; Available from: https://www.onsemi.com/PowerSolutions/product.do?id=J-SERIES%20SIPM.

33.   Limousin, O., *New trends in CdTe and CdZnTe detectors for X- and gamma-ray applications.* Nuclear Instruments and Methods in Physics Research Section A: Accelerators, Spectrometers, Detectors and Associated Equipment, 2003. **504**(1): p. 24-37.

34.   Dogan, N. and D.K. Wehe, *Efficiency and Angular Resolution Calculations for A Prototype Multiple Compton Scatter Camera.* Nuclear Instruments & Methods in Physics Research Section a-Accelerators Spectrometers Detectors and Associated Equipment, 1994. **345**(2): p. 296-302.

3 Passive Gamma-ray and Neutron Imaging Systems for National Security and Nuclear Non-proliferation in Controlled and Uncontrolled Detection Areas: Review of Past and Current Status

H. Al Hamrashdi., S.D. Monk, and D. Cheneler,

3.1 Abstract

Global concern for the illicit transportation and trafficking of nuclear materials and other radioactive sources is on the rise, with efficient and rapid security and non-proliferation technologies are in more demand than ever. Many factors contribute to this issue, including the increasing number of terrorist cells, gaps in security networks, politically unstable states across the globe and the black-market trading of radioactive sources to unknown parties. The use of passive gamma-ray and neutron detection and imaging technologies in security-sensitive areas and ports has had more impact than most other techniques in detecting and deterring illicit transportation and trafficking of illegal radioactive materials. This work reviews and critically evaluates these techniques as currently utilised within national security and non-proliferation applications and proposes likely avenues of development.

3.2 Introduction

Due to the hazardous ionising and activating nature of neutron and gamma radiation, there is a requirement to control and monitor the radiological materials which produce them. Neutron and gamma-ray detection can directly lead to the identification of radiological sources in general, including nuclear materials. Due to the potential of these materials to be developed into nuclear weapons, these substances can pose direct threats to national security, and so are of great interest.

Illicit trafficking of nuclear materials and other radiological sources present a global threat that international organisations such as the IAEA are forced to tackle frequently [1, 2]. The IAEA Incident and trafficking database reported 3,235 confirmed incidents of nuclear and other radioactive materials out of regulatory control between 1993 and 2017.

Of these incidents, 278 were associated with trafficking or malicious use of materials such as highly-enriched uranium, plutonium and plutonium-beryllium neutron sources [2]. This issue highlights the importance of the effective control of nuclear and radiation materials at national and international cross points such as borders, ports and airports.

Effective application of radiation detection techniques requires knowledge of the environment in which the technology will be implemented, and the associated circumstances. In a controlled detection area such as an airport checkpoint, border line checkpoint, cargo inspection checkpoint or air cargo inspection, the space, and in most cases the physical contact time, allow for a reasonable level of flexibility. In an uncontrolled detection area such as buffer zones, airports terminals, train stations and public roads, space and physical contact time are less flexible and require more advanced detection technologies [3].

This review compares the various technologies utilised in radiation portal monitoring (RPM) of illicit radioactive materials including radiation sources, by-product materials and nuclear materials, with a view of identifying their advantages and limitations.

3.3 Radioactive materials, nuclear materials and radiation sources

Radioactive materials are defined by the IAEA as materials being designated in national law or by a regulatory body as being subject to regulatory control because of their radioactivity [4]. Nuclear material is similarly defined as:

- Any plutonium isotope concentration except that with 80% or more of Pu-238
- Uranium enriched in the isotopes U-233 or U-235

- Uranium containing the mixture of isotopes as occurring in nature other than in the form of ore or ore-residue

- Any material containing one or more of the above [4].

A radiation source is usually defined as artificially refined radioactive material produced outside the nuclear fuel cycles of research and power reactors [4, 5]. The choice of radiation detection technology employed is primarily based on the radiation type being emitted, the amount of radiation, the energy spectra and whether the radioactive isotope needs to be identified. Predominantly, nuclear security-based applications are interested in detecting either gamma rays (typically $E > 10$ keV), and/or neutrons [6-8]. Gamma rays are typically emitted from an excited nucleus going from a higher energy state to a lower energy state, usually following the decay of its parent nucleus. Several mechanisms, such as fission and fusion reactions, neutron capture reactions, annihilation reactions and activation processes, can all result in the emission of gamma rays. Because gamma-ray assay and spectra measurements are the easiest and most common technologies, they are of tensed to identify and differentiate different nuclear materials and their isotopic composition [7]. Figure 3.1 shows the gamma-ray intensity spectra and characteristic peaks for various nuclear material isotopes [7, 9, 10].
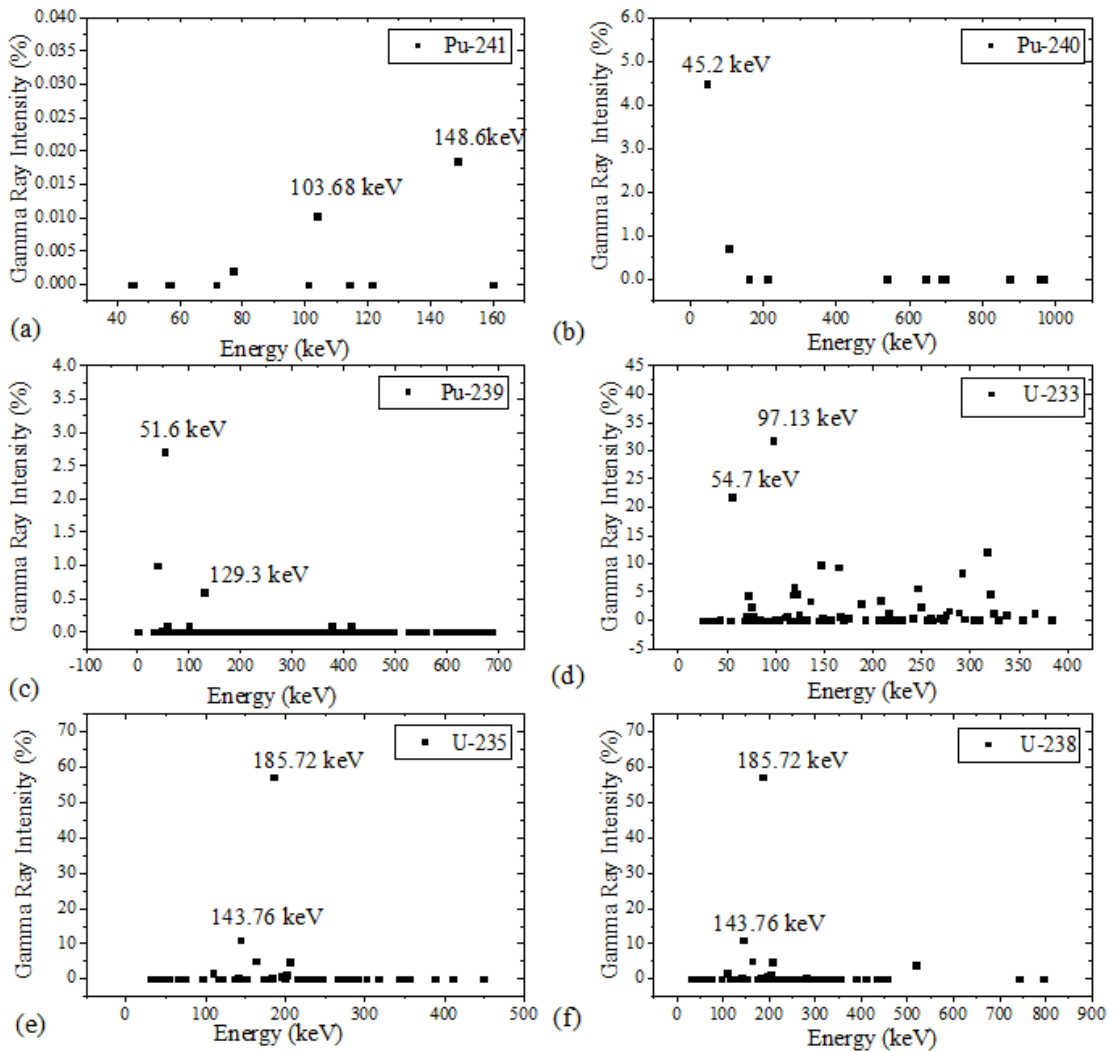
Figure 3.1: Characteristic gamma spectrum and gamma peaks of nuclear materials isotopes (a) Pu-241, (b) Pu-240, (c) Pu-239, (d) U-233, (e) U-235, (f) U-238 (Data source: Idaho National Engineering & Environmental Laboratory [9]).

Other gamma emitting radiation sources that are often found to be involved in illicit trafficking are Ir-192, Cs-137 and Am-241 [2]. Figure 3.2 shows gamma-ray characteristic peaks of these three isotopes.
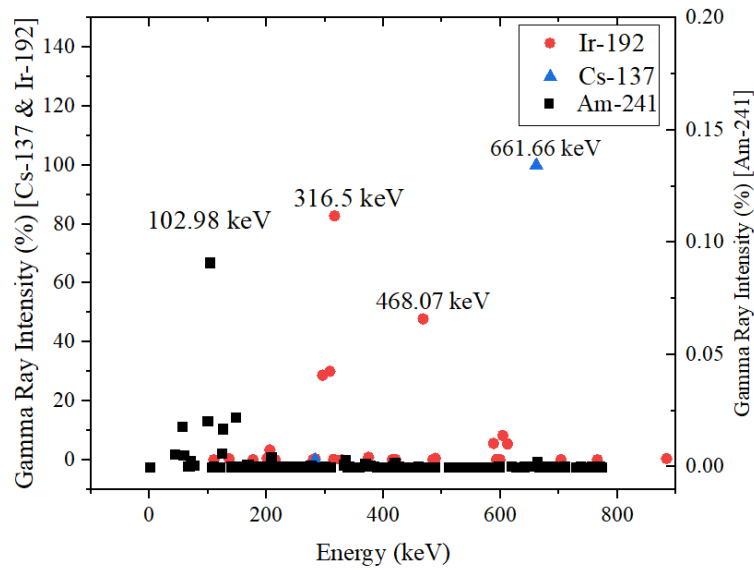
Figure 3.2: Gamma-ray characteristic energies and energy peaks of Ir-192, Cs-137 and Am-241.

Neutron emission detection and neutron assay is another common procedure used to detect and identify nuclear materials and radiation sources [6, 7]. Neutron sources in nature and industry can be categorised as spontaneous fission sources, reactor sources, alpha-neutron sources, photo-neutron (or gamma-neutron) sources and ion accelerator sources as shown in Table 3.1 [6, 11-13].

Table 3.1: Neutron sources and average energies.

Neutron Source	Neutron Source Type	Average Neutron Energy (MeV)	Half-Life (years)
Cf-252	Spontaneous fission	1– 3 (2.35 1)	2.645
Am-Be	Alpha-neutron source	4.2	432.2
Pu-Be	Alpha-neutron source	4 – 5	24,114 years
Sb-Be	Photo-neutron source	0.025 (close to mono-energetic)	0.164 (60 days)
D-D reaction	Accelerator source	2.4 (close to mono-energetic)	N/A
D-T reaction	Accelerator source	14.1 (close to mono-energetic)	12.32

Production of tritium from accelerator-based sources is effected by the closure of tritium-production reactors, non-proliferation policies and funding cuts. Other sources of tritium are breeding redactions in lithium blankets [14]. Other possible sources of neutron are D_Li-reactions [15] and spallation reactions [16]. Neutron multiplicity ṽ, or the number of neutrons emitted per fission, is a parameter obtained in the result of an analysis or measure. Table 3.2 gives a list of spontaneous fission isotopes commonly subjected to neutron multiplicity assays [6, 7, 10, 17].

---

[1] Reference [8], page 93.

Table 3.2: Spontaneous fission isotopes and neutron multiplicity.

Isotope	Neutron Number	Total Half-Life (years)	Average Spontaneous Fission Multiplicity
Cm-242	146	0.447	2.528
Bk-249	152	0.877	3.4
Cf-252	154	2.645	3.768
Cm-248	148	3.84	3.161
Pu-240	146	6.56	2.151
Pu-238	144	87.7	2.21
U-238	143	4.47E9	2.0
U-235	146	7.04E8	1.87

Induced fission multiplicity depends on the fission isotopes and the energy of the incident neutrons [17, 18]. Figure 3.3 illustrates neutron spectrum multiplicity for nuclear materials U-235 and Pu-239 as functions of energy.
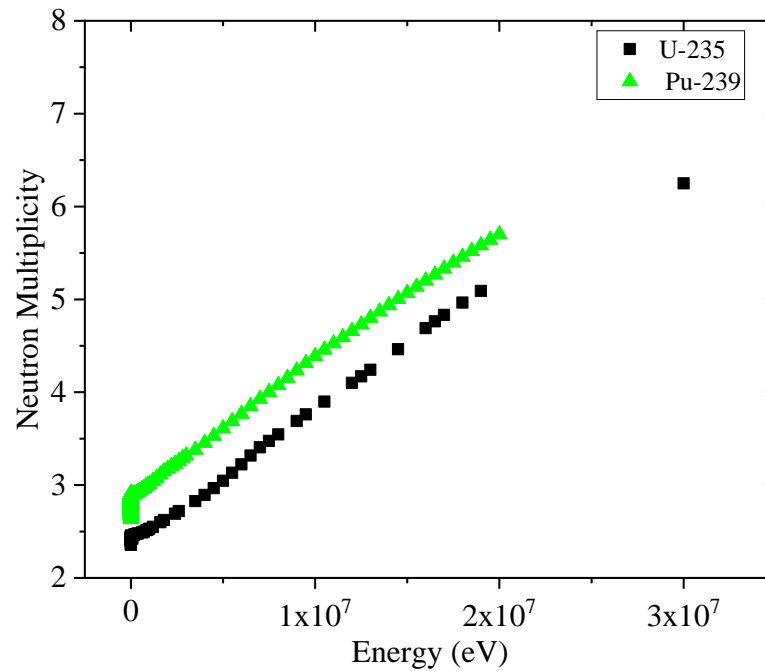
Figure 3.3: Neutron multiplicity as function of incident neutron energy for U-235 and Pu-239.

Unlike gamma rays, the wide energy spectrum of emitted neutrons and the change in their energy as they traverse materials, make source identification through the energy of emitted neutrons a less effective method of detection. However, the increasing volume of research in this field such as the research in the field of neutron scattering cameras may indicate the emergence of new technologies [19-23].

3.4 Problem definition and authorities' requirements

The major concern involving illicit trafficking and proliferation of nuclear materials is the threat of using these materials in criminal activities and terrorist acts. This concern has been gradually increasing during the last three decades and is becoming a definite threat in times of international instability and travel. The subject of illegal nuclear trafficking

and unlawful nuclear acts is becoming the primary concern of international and global agencies such as the IAEA [24], European Commission [25] and Interpol [26]. Other factors including the economic and political impacts of this illicit trafficking are also part of the multithreaded problem.

As with many illegal acts at the international level, security plans and prevention policies along with international legislation have been implemented to deter and prevent illicit trafficking and to promote nuclear non-proliferation. Examples of these plans and treaties are the Treaty on Non-proliferation of Nuclear Weapons in 1970 [27] and IAEA safeguards agreement and Code of Conduct on the Safety and Security of Radioactive Sources in 2004 [28]. Another example of international cooperation to deter illicit trafficking of nuclear materials is demonstrated by the adoption of the practices espoused in the Handbook of Nuclear Law produced by the IAEA [29]. This is the result of international organisations assisting legislation and regulatory bodies in member states in creating a strong and robust regulatory framework [29]. Other international, regional and cross continent agreements such as the International Convention for the Suppression of Acts of Nuclear Terrorism (ICSANT) [30] are part of the global effort to combat and prevent illicit trafficking of nuclear and radiological materials.

The safeguarding of radioactive materials in general is a continuous process, from the generation stage to the decommissioning stage, especially for nuclear materials. The uninterrupted tracking of these materials is the optimal method to safeguard and diminish the possibilities of illegal trafficking. While the situation norm is the controlled and legal transport of radioactive materials, incidents are still reported [2]. A series of protocols and procedures have been implemented at the national and international level to prevent these incidents. One of the most important factors in this process is the implementation of the

means of detecting, identifying and localising radioactive materials using radiation detection equipment and radiation imaging techniques.

The main purpose of implementing detection and imaging technologies in these applications is the timely and accurate identification of illegal acts and the generation of evidence to enforce legal proceedings to eliminate trafficking networks [24, 31]. The implementation of radiation detection and imaging technologies varies from state to state, but these technologies are generally implemented on sites where radioactive sources' life cycles are spent, such as nuclear reactors, hospitals, etc., and at national and international cross borders. Many parameters affect the efficacy of radioactive material detection [32], with the main factor being the performance of the technologies employed, especially their ability to identify and localise radioactive sources [24, 32]. Other directly related parameters that can influence the choice of technology employed are the field of view, the potential targets and the time constraints. The area of interest is the location where the detection or imaging instrument will be stationed and the zone that needs to be monitored. As implied in the Introduction, this area can be categorised as controlled or uncontrolled and varies in terms of the size of the area to be scanned, the detector to source distance, the number of people/vehicles/items to be monitored and the extent of the shielding or obstructions in the vicinity. The nature of the potential targets affects the choice of detection or imaging system due to their inherent shielding characteristics, i.e. nuclear material hidden inside the engine block of a large truck will be difficult to detect from a distance due to the significant shielding this environment affords. In addition, regulations that preclude the use of active interrogation systems on targets for health and safety reasons may also affects the selection process, if scanning pedestrians or queues of passengers, for instance. Timing is another parameter that affect the selection process.

Controlled areas such as airports and land ports are busy areas. For example, the daily average number of people at a busy airport like Heathrow Airport is over 200,000 passengers per day [33]. There will be a limit to how long passengers can be held for security checks for logistical reasons. Therefore, detection efficiency, data analysis speed and spatial resolution are key aspects of the specification of the technologies employed. The size of the detection or imaging system can as well be seen as a factor on the selection process. Pocket-type instruments are used to detect the presence of radioactive materials and in some cases the radiation level, usually to calculate personal dose. Hand-held instruments have higher sensitivity and can be used to detect, locate and characterise radioactive sources. Finally, fixed and vehicle-based devices are usually used at borders cross-points, seaports and similar controlled areas [32].

The IAEA suggests that there are over a hundred different forms of non-destructive analysis techniques available to be used in the process of identifying radioactive materials [31]. However, the most common detection and imaging devices utilise gamma rays and/or neutrons. The specification of suitable gamma-ray and neutron detection equipment varies according to legislation and the safeguarding abilities of states. A set of criteria have been recommended by the IAEA in a collaboration with World Custom Organization (WCO), EUROPOL and INTERPOL. The main components in this set of recommendations are [31, 34]:

Gamma-ray systems requirements:

- At a mean dose rate of 0.2 μSv/h, the alarm of the system should be activated when the dose rate increases in period of 1 second by 0.1μSv/h for a pocket size instrument, by 0.05μSv/h for a handheld instrument and 0.1μSv/h for a fixed-installation instrument, for duration of one second with 99% detection accuracy.

- False alarm rate should be minimal, with background measures of 0.2 μSv/h, with false alarms rate of less than 1 every 12 hours for pocket size instruments, less than 6 per hour for handheld instruments and less than 1 per day for fixed-installation instruments.

Neutron systems requirements:

- The alarm of the system should be activated above a threshold of 20,000 n/s with a source to detector distance of 0.25 m for handheld instruments and 20,000 n/s in 5s with source to detector distance of 2.0 m for fixed-installation instruments, using system with 99% detection accuracy.

- False alarm rate should be minimal with less than 6 per hour for handheld instruments and 1 per day for fixed-installation instruments.

Similarly, the American National Standard for Evaluation and Performance of Radiation Detection Portal Monitors for Use in Homeland Security have a set of criteria for gamma-ray and neutron equipment, however the set of requirements are relative to initial reference settings within the equipment [35]. Applying these requirements might limit direct implementation and might affect the response of the system. TECMIPT Test Operations Procedures (TTOP) For Radiation Detection Systems – Specific Methods specifies the minimum performance requirements for gamma-ray and neutron detection instruments [36]. These specifications have direct implementation and offer detailed requirements relative to the size category of the system.

Gamma-ray systems requirements:

- The alarm of the system should be activated when the count increases above background level by $0.5~\mu Sv/h$ in 2 s for Radionuclide Identification Devices (RIDs) in the pocket and handheld size categories.

- The alarm of the system should be activated with Th-232, Cs-137, and Ba-133, Co-60 and Co-57 sources moving past the system at a speed of 2.22 m/s and distance of closest approach of 3 m for RIDs in the fixed installation size category.

- False alarm rate should be minimal with less than 1 every 10 hours for pocket size and handheld instruments and less than one every two hours for fixed-installation size instruments.

Neutron systems requirements:

- The alarm of the system should be activated when the exposure is above the threshold of 20,000 n/s in 2 s with Cf-252 sources with a source to detector distance of 0.25 m for RIDs in the pocket size and handheld size categories.

- For a moving Cf source with activity of 20,000 n/s and moving past the system at a speed of 2.22 m/s at a distance of closest approach of 3 m, the system has to be able to detect the source with up to 1 cm steel or 0.5 cm of lead of shielding for RIDs in the fixed installation size category.

- False alarm rate should be minimal with less than 1 every 10 hours for pocket size and handheld instruments and less than one every two hours for fixed-installation size instruments.

3.5   Physical and electronic collimations

Neutrons and gamma rays are uncharged high-energy radiation fields. Conventional converging and diverging techniques, as well as other optical techniques, are not applicable in this case. A device is needed to precisely identify the lines along which detected radiation fields are generated. Collimation is the key word here. Collimation of incident radiation can be done physically and/or electronically. Physical collimation and electronic collimation are well-established imaging techniques in the field of radiation detection. The basic concepts of each of these two collimation techniques are discussed in this section.

3.5.1   Physical collimation

Physical collimators are patterns of highly attenuating materials positioned in front of a detector to limit the direction of incident radiation quanta to specific directions. As a result, a shadow image is formed on the detector resulting in greatly improved spatial resolution. However, this approach causes a noticeable decline in the efficiency of the system since it limits the number of detectable radiation quanta [37]. Physical collimation for gamma rays is more effective at lower energies as the probability of penetration through matter increases with gamma-ray energies above the energy peak of Compton scattering.

The simplest physical collimator design is the pinhole collimator, which consists of a single small aperture. This technique offers excellent angular resolution; however, it limits the geometrical efficiency of the system. Parallel holes collimator, converging and diverging collimators are arrays of opaque and transparent photon channels used in imaging where the system scans across the entire field of view. The technique improves

the angular resolution of the system and slightly increases the solid angle. Figure 3.4 shows schematics of physical collimators types.
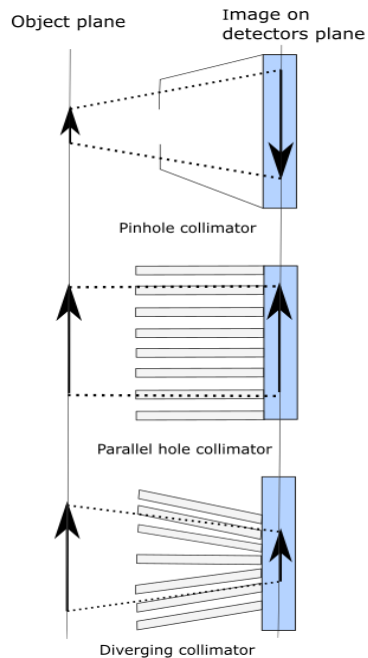
Figure 3.4: Schematic of physical collimator types.

A coded aperture is an alternative and popular form of physical collimation that was originally proposed for astrophysics measurements. It was first analytically proven effective for imaging systems in 1968 [38, 39]. Commonly based on a 50 % open mask with a large number of randomly distributed pinholes lying in a parallel plane with the detector, the technique offers higher efficiency compared to previously mentioned collimation techniques. Figure 3.5 illustrates the basic parameters of coded aperture imaging systems.
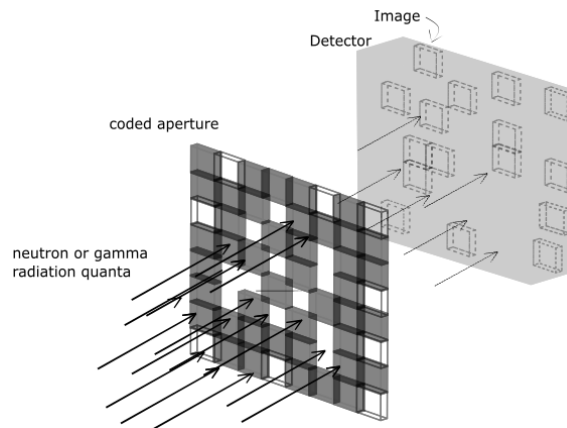
Figure 3.5: A schematic of coded aperture imaging system, with a coded aperture mask that is made with a pattern of opaque and open cells of highly attenuating materials followed by a radiation sensitive detector. Incident radiation field are attenuated in the coded aperture mask; with only a fraction of incident radiation is transmitted and detected on the system. (Based on reference [38]).

Coded aperture masks have greatly evolved since their inception, and in most cases, their design can be tailored to fit the application requirements. There are generally two types of coded apertures: passive masks and active masks. In the case of passive masks, a highly absorbing material is used to stop and eliminate non-normally directed radiation quanta from reaching the detector. The choice of materials in passive masks mainly depend on the type of target radiation. High density/atomic number materials such as lead, tungsten and depleted uranium are often used to block high energy photons, while neutron absorbing materials such as high-density polyethylene (HDPE) and Gadolinium are used in coded apertures for neutron detection [40, 41]. Passive physical collimation shows noticeable drawbacks over a considerable range of the energy spectrum, especially at high energies where radiation fields have enough energy to penetrate the opaque pattern of the mask [42-44]. On the other hand, active coded aperture designs use radiation sensitive

materials, such as B- and Gd-doped glass plates for detecting low energy neutrons, as part of the collimation and detection process, which allows the detection of radiation quanta with a wider energy range [45-48]. Most of these active collimation examples combine physical collimation and Compton scattering in one system by using a pattern of large area detectors. Physical collimation is mainly utilised for detection of low gamma-ray energies, while Compton scattering is utilised for higher energy gamma rays. Generally, the trade-off between angular resolution and detection efficiency is unavoidable in physical collimation. Higher activity sources or longer acquiring times (or both) are usually recommended to improve the efficiency of these systems.

3.5.2 Electronic collimation: Compton camera and neutron scattering camera

Electronic collimation (widely known as a Compton camera for gamma-ray detection and neutron scattering camera for fast neutron detection) is a well-studied collimation approach, especially utilised within gamma-ray detection. Gamma Compton cameras are comprised of two pixelated detectors and utilise the laws of conservation of momentum and energy to infer the most probable trajectories of the scattered and/or absorbed radiation fields. The first detector scatters the gamma photon, which results in an electron being emitted and its energy measured. The second detector absorbs the scattered gamma photon and measures its energy. The location of the pixels activated in each detector determines the angle of scattering and hence the probable origin; the energy of the initial gamma photon can be calculated from measured energies of the incident and scattered photons [43, 49]. The neutron scattering camera similarly utilises at least two detectors and the conservation of energy and momentum. However, in this instance the reaction is between an incident fast neutron and a proton present in the proton-rich detectors in order

to sense and localise the fast neutron source. The time-of-flight data of the scattered neutron is used to measure the energy of the incident neutron [19, 23]. Figure 3.6 shows the basic elements in two pixelated planes imaging system based on electronic collimation.
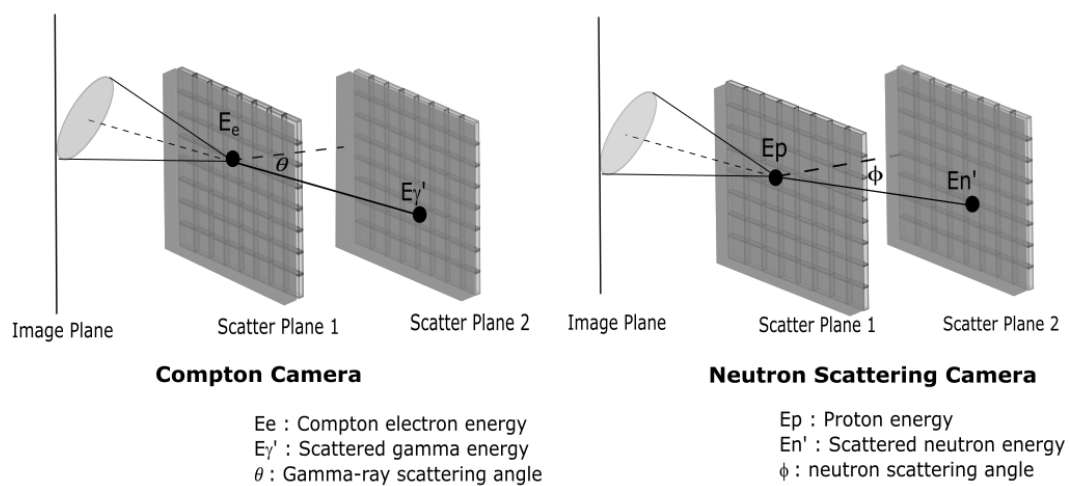
Figure 3.6: Schematics of basic parameters in Compton scattering camera (left) and neutron scattering camera (right).

3.6 Passive detection systems of illicit radioactive materials

The two modes of detecting nuclear materials and other radioactive sources are mainly active mode and passive mode. Active detection mode (not part of the work presented here) uses externally generated neutrons, gamma rays or X-rays to interrogate radioactive materials. This approach offers in-depth characterisation of target radioactive material, especially for fissile materials, although the major drawbacks are that it cannot be used in many circumstances, such as in proximity with humans and in uncontrolled detection areas [6, 50-53].

In passive detection, an imaging system is used to detect and characterise neutrons and gamma rays directly emitted from nuclear materials and radioactive sources. In contrast to active detection technique, passive detection requires less architecture arrangement and conceivably lower in cost. In Safeguards Techniques and Equipment series by IAEA, approximately all gamma-ray non-destructive equipment discussed in the report are in passive mode [31]. In the same report, the ratio of listed passive to active neutron assay equipment is 4:1. This clearly shows the impact of passive detection mode at the international level in safeguard and security applications. A common design is the Radiation Portal Monitor (RPM) which typically consists of several detectors designed in a rectangle shape located at a fixed site [5]. Some passive imaging systems can characterise the radioactive material, rejecting background radiation and estimating the source to system distance. Passive detection systems offer a safe and simple detection mode, although the drawback is that its absolute efficiency decreases with increasing shielding around the radioactive material [54]. Since passive detection depends exclusively on the radioactive source under investigation and the detection system used, the statistical quality of results and the time to detect a source of specified strength depends mainly on characteristics such as intrinsic efficiency, angular resolution, spatial resolution and time resolution, shielding, and source-detector distance.

In this work, passive detection and identification systems are categorised based on the target radiation field; gamma rays, neutrons and dual systems. In each category, the systems will be further classified into pocket-type instruments, hand-held instruments and large fixed or vehicle based instruments [32]. Another equally important classification factor is the purpose of detection instruments; summarised as detection, assessment and localisation, and identification [32]. The following review attempts to compare and appraise past and present passive detection systems and techniques found in the literature

that have been predominantly designed to detect and deter illicit trafficking, smuggling and transporting of nuclear materials and other radioactive sources.

3.6.1 Gamma-ray detection systems

Common single crystal inorganic gamma detectors such as NaI, CsI, $SrI_2(Eu)$ and PVT (organic scintillation detectors) or CdZnTe and HPGe (semiconductor detectors) are popular due to their stable performance, high efficiency and relatively low price [31, 55-58]. NaI(Tl) is by far the most studied and most commercially successful inorganic scintillator [8]. However, single crystal imaging systems are far more sensitive to background radiation and are more prone to false alarms [3, 59]. Pairing single crystal detector with signal analysers, such as multichannel analysers might widen the scope of applications for this group of detectors [31]. However, imaging is almost always desirable, alongside detection, to enhance a system's sensitivity, angular resolution, energy resolution and localisation of point-like sources [60, 61].

Physical collimation, in particular coded apertures, and Compton scattering techniques have both been adopted to enhance and improve the detection abilities of gamma imaging systems. Fixed installation coded aperture systems offer long distance and large area coverage with improved signal to background ratio [62, 63]. However, these systems are best implemented at border controls, as they require fixed or slowly moving targets. Problems and limitations, such as false alarms and timing issues, as well as proposed solutions for this technology, such as energy windows and baseline suppression, are frequently discussed in literature [64-70]. Hand-held coded aperture systems offer a flexible solution for detecting and localising of radioactive materials [71, 72]. In addition to the main goal of detecting and localising radioactive sources while scanning vehicles,

people, luggage and cargo, other applications such as monitoring the extent of nuclear related emergencies have been suggested. Many mechanically collimated systems have found success in this field [72-75]. Table 3.3 summarises coded aperture-based gamma imaging systems found in the literature, including their detection method, their size category and the purpose of application.

Table 3.3: Coded aperture-based gamma-imaging systems.

System size definition	Examples and Proposed application in literature	Detector/s	Industrial designation
Fixed installation	Detection and localisation [62] [63]	CsI(Na)	
Fixed installation	Detection, assessment and localisation [76]	HPGe & NaI	MISTI
Fixed installation	Detection, assessment and localisation [75]	CdZnTe	ORIGAMIX
Fixed installation/ hand-held	Detection and localisation [77]	NaI	RMC
Fixed installation/ hand-held	Detection and localisation [73]	CsI(Tl)	CARTOGAM
Fixed installation	Detection, assessment and localisation [78]	(GSO)	
Hand-held	Detection and localisation [71]	CdTe-Medpixi2	
hand-held	Detection and localisation [74]	CsI(Na)	RADCAM
hand-held	Detection and localisation [79]	CsI(Tl)	
hand-held	Detection and localisation[72]	CdZnTe-Timepix	GAMPIX

In the energy range of nuclear material gamma-ray sources (60 keV to 3.0 MeV) Compton scattering is the dominant photon interaction mechanism, that makes Compton scattering technique the most appropriate technique compared to other techniques [3]. Compton based systems feature a wide field of view with improved detection efficiency compared to mechanically collimated gamma imaging systems, especially for high-energy gamma rays [3, 80]. In addition, Compton systems offer the ability to detect, assess and localise a gamma-ray source with an associated reduction in background radiation [81]. Fixed

installation and portable Compton systems are the most common size categories [82-85]. The performance of these systems varies between detectors with some using low energy resolution, high sensitivity NaI(Tl) and CsI(Tl) scintillations [82, 83], while others use high resolution Si and HPGe semiconductor detectors [84]. Image reconstruction methods for Compton systems, such as Maximum Likelihood Expectation Maximization (MLEM), Maximum Likelihood Ratio (MLR) and stochastic origin ensembles, have been regularly studied and optimised for their direct impact on the performance of Compton system in this field [86, 87]. There are hybrid-imaging systems that utilise both Compton camera and coded aperture technology; examples include passive mask [88] and active mask [46, 89, 90] systems. The duality in imaging techniques aims to utilise the advantages of both physical collimation and Compton scattering. However, designs need to take into account the optimum arrangement of layers to avoid negating these advantages. Another promising technique in gamma-ray imaging are 3D systems that utilise coded apertures or Compton scattering. The 3D systems are used in assessing and localising smuggled and hidden sources by projecting a 3D image of the search scene, which allow faster and easier navigation in the area of interest [91, 92].

3.6.2 Neutron detection systems

Although most nuclear materials emit either or both neutrons and gamma rays, heavy shielding of gamma rays can greatly lower the efficiency of gamma-ray imaging systems, negatively impacting their efficacy in nuclear materials non-proliferation and safeguard applications. Neutrons are highly penetrating and nuclear materials emitting neutrons requires bulky shielding to completely conceal neutrons. Therefore, neutron-imaging systems are extensively used in nuclear materials imaging and they offer an excellent

alternative. Due to their high thermal neutron cross section (5,330 barns) and low gamma-ray sensitivity, He-3 gas filled counters have been the standard neutron monitoring technology for decades [31, 93]. Thermal neutrons detection efficiency for He-3 gas filled counters is a function of the amount of ^{3}He gas and increases with increasing pressure. For example, a 72 in in height and 2 in in diameter He-3 tube under in 3 atm pressure has efficiency of 3.05 cps/ng Cf-252. The main supply of He-3 is the H-3 purification process, which has seen a dramatic decrease in the last two decades [93, 94]. This has led to a continuous search for alternative neutron detection technologies. Direct gas filled counter alternatives such as BF_3 proportional counters, boron lined proportional counters and fission chambers have been commercially in use [31, 95-97], but they have shown to be significantly less efficient [94, 97, 98].

Neutron sensitive scintillation detectors and semiconductor detectors are frequently used in neutron detection. Neutron sensitive scintillation detectors include liquid and plastic organic scintillators [99-104], glass scintillators [105-108] scintillating fibres [109] and bubble chambers [110]. Bonner spheres are examples of radiation detectors embedded in a spherical moderator layer. Bonner spheres are well-established neutron spectrometer instruments in the field of nuclear dosimetry and inspection non-proliferation [111, 112]. However, Bonner spheres has inherently low energy resolution and inverse relationship between moderator thickness and detection efficiency. Semiconductor based detectors are a less popular means of neutron detection due to their lower efficiency compared to the scintillation detection materials in this field and the occasional requirement of having to use foils or coatings of conversion material to convert neutrons into a detectable signal, usually electrons [13, 113]. However, their ruggedness and high-speed response make them an interesting option for safeguarding and security applications [114, 115]. Semiconductor materials such as ^{4}H-SiC, diamond and CdZnTe have been investigated

in literature for their applications in neutron detection [116-119]. ^{4}H-SiC and SiC semiconductors are promoted for their abilities to work in high temperature and high radiation environments along with other desirable properties such as high energy band gap and lower production cost, compared to diamond that has similar properties [116]. Diamond materials, such as diamond high pressure, high temperature (HPHT) synthetic diamond or diamond grown using CVD, are mechanically durable and inherently radiation hard. Like SiC detectors, diamond detectors have a wide band gap, which makes them highly appealing for radiation detection applications at high temperatures [118, 120]. CdZnTe with neutron converting layer such as Gd are proposed for portable thermal neutron detection systems [119, 121]. Activation foils were suggested for safeguard applications as practical neutron flux measurement tool [122].

As for gamma-ray detection, collimation techniques in neutron detection are deployed to enhance detection efficiency, angular and energy resolutions, increase the field of view and decrease the acquisition time. In addition, for screening vehicles, cargo and large containers, the imaging systems should be accurate with a low probability of false alarms and low sensitivity to gamma rays [123]. A number of simulation-based studies discuss potential neutron imaging systems with physical collimation or neutron scattering/ToF based collimation [124-127]. An equally important aspect in nuclear materials detection is the discrimination method used to discriminate between neutrons and gamma rays [128]. Because gamma rays are almost always present in the background, discrimination methods are crucially important and has been extensively studied in literature [129-134]. A range of radiation detection and identification systems are commercially available from vehicles size [135] to handheld size [136-138]. For a more detailed review of portal

radiation monitors, Table 3.4 [2] lists all neutron-imaging systems discussed and experimentally evaluated in literature for safeguard and non-proliferation of nuclear materials. The categorisation of proposed applications and the size definitions are based on those mentioned in section 3.5.

Table 3.4: Examples of neutron imaging systems used in nuclear materials security, their collimation technique, properties and characteristics.

Author, year and reference	Proposed application	Collimation/ detection technique	System size definition	Main detection materials	Approximate Intrinsic efficiency (Thermal neutrons/ fast neutron Cf-252) (%)
Miller et al. (2003) [139]	Detection, assessment and localisation	Neutron scatter	Fixed installation	Plastic scintillator	NA/NA
Bravar et al. (2006) [140]	Detection and assessment	Neutron scatter	Fixed installation	BC-404 plastic scintillator	NA/NA
Vanier et al. (2007)[141]	Detection, assessment and localisation	Neutron scatter	Fixed installation	Plastic scintillator	NA/NA
Mascarenhas et al. (2009) [142]	Detection, assessment and localisation	Neutron scatter	Fixed installation	EJ-301	NA/NA

---

[2] The table extends from page 66 to page 69.

Table 3.4: Examples of neutron imaging systems used in nuclear materials security, their collimation technique, properties and characteristics.

Author, year and reference	Proposed application	Collimation/ detection technique	System size definition	Main detection materials	Approximate Intrinsic efficiency (Thermal neutrons/ fast neutron Cf-252) (%)
Siegmund et al. (2009) [143]	Detection	Coded aperture and Stack of microchannel plates	Fixed installation	B-10 doped microchannel plates	~20%/NA
Herbach et al. (2010) [144]	Detection and assessment	Null/gamma from neutron capture	Fixed installation	BGO with Cd converter	45% /NA
Ryzhikov et al. (2010) [145]	Detection and assessment	Null/gamma from neutron capture	Fixed installation	$CdWO_2$	67 % /42%
Marleau et al. (2010) [146]	Detection and assessment	Active coded aperture	Fixed installation	EJ-301	NA/NA
Nakae et al. (2011) [147]	Detection and assessment	Null/Array of liquid scintillator	Fixed installation	Organic liquid scintillator(not specified)	NA/~6% (absolute)
Bellinger et al. (2012) [148]	Detection and assessment	Null/array of slabs	Hand-held	Si diodes with ^{6}LiF	6.8% /NA

Table 3.4: Examples of neutron imaging systems used in nuclear materials security, their collimation technique, properties and characteristics.

Author, year and reference	Proposed application	Collimation/ detection technique	System size definition	Main detection materials	Approximate Intrinsic efficiency (Thermal neutrons/ fast neutron Cf-252) (%)
Ide et al. (2012)[149]	Detection, assessment and localisation	Neutron scatter	Fixed scintillator	EJ-309	NA/NA
Joyce et al. (2014) [150]	Detection and assessment	Null/Multiplicity assay	Fixed scintillator	EJ-309	NA/
Brennan et al. (2015)[151]	Detection, assessment and localisation	Coded aperture and Time-encoded imaging	Fixed installation	Organic liquid scintillator (not specified)	NA/NA
Fronk et al. (2015) [152]	Detection and assessment	Null/double sided Microstructure	Hand-held	Si diodes with ^{6}LiF	~29.48% / NA
Ianakiev et al. (2015) [153]	Detection and assessment	Null/Li-6 embedded in PVT	Fixed installation	Li-6 and PVT	NA /NA
Hoshor et al. (2015) [154]	Detection and assessment	Null/array of slabs	Hand-held	Si diodes with ^{6}LiF	~22% /~4.5%

Table 3.4: Examples of neutron imaging systems used in nuclear materials security, their collimation technique, properties and characteristics.

Author, year and reference	Proposed application	Collimation/ detection technique	System size definition	Main detection materials	Approximate Intrinsic efficiency (Thermal neutrons/ fast neutron Cf-252) (%)
Goldsmith et al. (2016) [155]	Detection, assessment and localisation	Neutron scatter	Fixed installation	EJ-309	NA/45%
Fulvio et al. (2017) [156]	Detection and assessment	Ring of multiplicity counters	Fixed installation	EJ-309	NA/
Cowles et al. (2018) [157]	Detection and assessment	Null/multiple panels	Fixed installation	LiF/ZnS	36% /NA
Ochs et al. (2019) [158]	Detection	Microstructure semiconductor	Wearable device	Si diode with ^{6}LiF	30%/NA

3.6.3 Dual gamma-ray and neutron detection systems

Dual particle imaging systems detect gamma rays and neutrons simultaneously and can differentiate between the two radiations. This method of imaging has an advantage over

single particle imaging methods because it allows the passive detection and identification of a wide range of nuclear materials and other radioactive sources.

There are two main groups of systems in the field of dual particle imaging. The first group are comprised of single materials that are sensitive to both gamma rays and neutrons. The second group uses multiple detection materials systems with detectors not necessarily sensitive to both particles. The later imaging technique offers reduction in system complexity as additional discrimination techniques are not necessarily required. In addition, this category offers higher design flexibility, as the parameters employed to enhance system response to one radiation field are usually independent of the other.

Materials sensitive to both gamma-ray and neutron have been investigated for their dual detection abilities since the 1950s [139, 140]. Examples of the list of detection materials range from inorganic scintillators [141-143], semiconductor detectors [144-146], glass organic scintillators [147], some classes of elpasolite scintillators [148, 149], some classes of liquid scintillators and plastic scintillators [150-154]. The common features between these detection materials is their superior ability to enable the distinguishing of gamma-ray signals from neutron signals by methods such as pulse shape discrimination and pulse height discrimination [133, 134, 150, 155]. A handful of fixed installation and portable monitoring systems are suggested for security and non-proliferation applications are found in the literature. The scintillation materials used in these systems vary dramatically with ^{6}Li(Eu) and Li-glass detectors, EJ-309 liquid scintillators and CLYC elpasolite detectors being popular [142, 156-158] with some also utilising coded aperture collimation to enhance imaging characteristics [159, 160]. A number of examples of hand-held and pocket size systems for monitoring purposes similarly exist; almost all detection materials in this size category are based on plastic scintillators or elpasolite

scintillation materials [99, 161-164]. These systems offer flexibility and fast response, albeit with a limited field of view.

Since 2004, the research on multiple detection materials imaging systems for security and non-proliferation applications has increased. Systems abilities varies according to the detection and collimation method and the size of the system. Table 3.5 presents a timeline of multiple detectors imaging systems discussed in literature along with their collimation and detection techniques between 2004 and 2016.

Table 3.5: Timeline of dual particle multiple detectors imaging system in security and non-proliferation applications.

YEAR	Author and reference	Collimation	Main detection materials
2004	Aryaeinejad, R. and Spencer, D. [165]	None	Li-6 and Li-7 loaded glass scintillators
2007	Baker et al. [166]	None	NaI(Tl) and LiI(Eu)
2008	Enqvist et al. [167]	None	Cross correlation BC-501A
2009	Runkle et al. [168]	None	NaI(Tl) and He-3
2011	Polack et al. [169]	Compton and neutron scattering	NaI(Tl) and EJ-309
2012	Cester et al. [170]	None	LaBr(Ce), NaI(Tl), NE-213 and ^{3}He
2013	Ayaz-Maierhafer et al [171]	Coded aperture	CsI and EJ-309
2014	Poitrasson-Rivière etal [172]	Compton and neutron scattering	NaI(Tl) and EJ-309
2016	Cester et al. [173]	Null	EJ-420, EJ-560 and EJ-299-33A

A number of research has been undertaken and investments have been made into large area coverage using a network of detectors. This concept has been around for over a decade [174-176], however, the realisation of the advantages of this technique along with the advances in network and communication fields will lead to new developments in this

area. Examples of network systems and algorithms in this field are RAdTrac network system for gamma detectors, particle filter algorithm for a network of gamma counters and the ROSD-RSD algorithm method [177-181]. Other systems like identiFINDER S900 [182] and SmartShieldTM v2.0 [183] are commercially available for radionuclides identification and tracking.

3.7 Conclusion

Illicit trafficking of nuclear materials and radioactive materials is a cross-border problem that must be tackled globally. Robust and efficient detection equipment and radiation detection systems stand on the front line of defence against the acts of illicit trafficking. However, understanding the different parameters that affect the choice of detection equipment and/or radiation detection systems can greatly help installing the most affective detection techniques. The parameters that have most effect are (more details in section 3.4):

- Security agencies and legislation bodies' requirements.

- Areas under surveillance and place of implementation.

- Image quality requirement.

- Timing and speed requirements.

Once the main requirements are established, the options can be then investigated within detection and/or imaging techniques of gamma-ray sensitive systems, neutron sensitive systems or dual gamma-ray and neutron sensitive systems. Each technique has its advantages over the others and the main stage in planning to install a detection system that will positively contribute in deterring illicit trafficking is to investigate and study each implementation site individually.

3.8 References

1.   Zaitseva, L. and K. Hand, *Nuclear smuggling chains. Suppliers, intermediaries, and end-users.* American Behavioral Scientist, 2003. **46**(6): p. 822-844.

2.   *IAEA Inicdents and Trafficking Database (ITDB) Incidents of nuclear and other radioactive material out of regulatory control*, in *2018 Fact Sheet*. 2018, International Atomic Energy Agency Vienna, Austria.

3.   Byrd, R.C., et al., *Nuclear detection to prevent or defeat clandestine nuclear attack.* IEEE Sensors Journal, 2005. **5**(4): p. 593-609.

4.   *IAEA Safety Glossary Terminology Used in Nuclear, Radiation, Radioactive Waste and Transport Safety Version 2.0*. 2006 Department of Nuclear Safety and Security, International Atomic Energy Agency Vienna, Austria.

5.   *Glossary of Terms for Nuclear, Biological, and Chemical Agents and Defense Equipment*. 2001, U.S. Army Medical Department and U.S. Army Medical Department, Army Public Health Center: Washington, DC, USA,.

6.   Gozani, T., *Active Nondestructive Assay of Nuclear Materials, Principles and Applications* 1981, Washington DC: US Nuclear Regulatory Commission.

7.   D. Reilly, N.E., H. Smith, and S. Kreiner, *Passive Nondestructive Assay of Nuclear Materials,* , N.E. D. Reilly, H. Smith, and S. Kreiner Editor. 1991: National Technical Information Service, U.S. Department of Commerce, Washington, DC,.

8.   Milbrath, B.D., et al., *Radiation detector materials: An overview.* Journal of Materials Research, 2008. **23**(10): p. 2561-2581.

9.   *Gamma-ray Spectrometry Catalog*. 1999, The Idaho National Laboratory: Idaho Falls, ID, USA.

10.   Gozani, T., *Fission signatures for nuclear material detection.* IEEE Transactions on Nuclear Science, 2009. **56**(3): p. 736-741.

11.   Stewart, L., *Neutron Spectrum and Absolute Yield of a Plutonium-Beryllium Source.* Physical Review, 1955. **98**(3): p. 740-743.

12.   Krane, K.S., *Introductry nuclear physics*. 1988, New York, NY, USA: John Wiley and Sons.

13.   Knoll, G.F., *Radiation detection and measurment*. Fourth ed. 2010, New York, NY, USA: John Wiley and Sons.

14.   Yapıcı, H., N. Şahin, and M. Bayrak, *Investigation of neutronic potential of a moderated (D–T) fusion driven hybrid reactor fueled with thorium to breed fissile fuel for LWRs.* Energy Conversion and Management, 2000. **41**(5): p. 435-447.

15.   Knaster, J., et al., *IFMIF, the European–Japanese efforts under the Broader Approach agreement towards a Li(d,xn) neutron source: Current status and future options.* Nuclear Materials and Energy, 2016. **9**: p. 46-54.

16.   Mansur, L.K., et al., *Materials needs for fusion, Generation IV fission reactors and spallation neutron sources – similarities and differences.* Journal of Nuclear Materials, 2004. **329-333**: p. 166-172.

17.   NEA, O. *Java-based nuclear data information system*. 16/01/2016 [cited 2016 10/02/2016]; Available from: http://www.oecd-nea.org/janis/.

18.   TERRELL, J., *Distributions of Fission Neutron Numbers.* Physical Review, 1957. **108**(3).

19.   Herzo, D., et al., *A Large Double Scatter Telescope for Gamma Rays and Neutrons.* Nuclear Instruments and Methods, 1975. **123**(3): p. 583-597.

20.   Wunderer, C.B., et al. *SONTRAC - a low background, large area solar neutron spectrometer*. in *Conference on the High Energy Radiation Background in Space, Proceedings*. 1997. Snowmass, CO, USA.

21.   Ryan, J.M., et al. *SONTRAC: An imaging spectrometer for solar neutrons*. in *Proceedings of SPIE - The International Society for Optical Engineering*. 2002. Waikoloa, HI, USA, .

22.   Marleau, P., et al. *Advances in imaging fission neutrons with a neutron scatter camera*. in *IEEE Nuclear Science Symposium Conference Record*. 2007. Honolulu, HI, USA.

23.   Mascarenhas, N., et al. *Development of a neutron scatter camera for fission neutrons*. in *IEEE Nuclear Science Symposium Conference Record*. 2007. San Diego, CA, USA.

24.   *Combating Ilicit Trafficking in Nuclear and Other Radioactive Materials*. 2007, International Atomic Energy Agency, IAEA: Vienna, Austria.

25.   *JRC: 20 years combating illicit trafficking of nuclear materials*. 2012 [cited 2019 07/03/2019]; Available from: https://ec.europa.eu/jrc/en/news/jrc-20-years-combating-illicit-trafficking-nuclear-materials-7023.

26.   *Radiological and nuclear prevention*. [cited 2019 07/03/2019]; Available from: https://www.interpol.int/en/Crimes/Terrorism/Radiological-and-Nuclear-terrorism/Radiological-and-nuclear-prevention.

27.   *Treaty on the Non-proliferation of Nuclear Weapons (NPT)*. [cited 2019 07/03/2019]; Available from: https://www.un.org/disarmament/wmd/nuclear/npt/text.

28.   IAEA, *Code of Conduct on The Safety and Secuirty of Radioactive Sources*. 2004, International Atomic Energy Agency. IAEA: Vienna, Austria.

29.   *Handbook on Nuclear Law*. 2003, International Atomic Energy Agency, IAEA: Vienna, Austria.

30.   *International Convention for the Suppression of Acts of Nuclear Terrorism*. 2005, Nucl. Terror. Conv.

31.   *Safeguards Techniques and Equipment*. 2011, International Atomic Energy Agency, IAEA.

32.   *Detection of Radioactive Material at Borders*, in *IAEA-TECDOC-1312*. 2002, International Atomic Energy Agency, IAEA: IAEA, Vienna

33.   *Heathrow Our Company: Facts and Figures*. [cited 2019 12/03/2019]; Available from: https://www.heathrow.com/company/company-news-and-information/company-information/facts-and-figures.

34.   *Detection of radioactive materials at borders* 2002, Radiation Safety Section, International Atomic Energy Agency , Jointly sponsored by IAEA, WCO,EUROPOL and INTERPOL: Vienna, Austria.

35.   *American National Standard for Evaluation and Performance of Radiation Detection Portal Monitors for Use in Homeland Security*, in *ANSI N42.35-2016 (Revision of ANSI N42.35-2006)*. 2016: Washington, DC, USA. p. 1-70.

36.   *TECMIPT Test Operations Procedures (TTOP) For Radiation Detection Systems – Specific Methods*. 2012: NIST: Gaithersburg, MD, USA.

37.   Gormley, J.E., et al., *Experimental comparison of mechanical and electronic gamma-ray collimation.* Nuclear Instruments & Methods in Physics Research

Section a-Accelerators Spectrometers Detectors and Associated Equipment, 1997. **397**(2-3): p. 440-447.

38. Dicke, R.H., *Scatter-Hole Cameras for X-Rays and Gamma Rays.* Astrophysical Journal, 1968. **153**(2P2): p. L101-&.

39. Ables, J.G. *Fourier transform photography: a new method for X-ray astronomy*. in *Astronomical Society of Australia*. 1968. Australia: Publ. Astron. Soc. .

40. Whitney, C.M., et al., *Gamma-neutron imaging system utilizing pulse shape discrimination with CLYC.* Nuclear Instruments & Methods in Physics Research Section A: Accelerators, Spectrometers, Detectors and Associated Equipment, 2015. **784**: p. 346-351.

41. Zou, Y.B., et al., *Coded source neutron imaging with a MURA mask.* Nuclear Instruments and Methods in Physics Research Section A: Accelerators, Spectrometers, Detectors and Associated Equipment, 2011. **651**(1): p. 192-196.

42. Todd, R.W., Nighting.Jm, and D.B. Everett, *Proposed Gamma Camera.* Nature, 1974. **251**(5471): p. 132-134.

43. Everett, D.B., et al. *Gamma-radiation imaging system based on the Compton effect*. in *Proceedings of the Institution of Electrical Engineers-London*. 1977. IET Digital Library: London, UK.

44. Singh, M. and R.R. Brechner, *Experimental Test-Object Study Of Electronically Collimated SPECT.* Journal of Nuclear Medicine, 1990. **31**(2): p. 178-186.

45. Cunningham, M.F., et al. *Active-mask coded-aperture imaging*. in *IEEE Nuclear Science Symposium/Medical Imaging Conference*. 2007. Honolulu, HI: Ieee.

46. Schultz, L.J., et al., *Hybrid coded aperture and Compton imaging using an active mask.* Nuclear Instruments & Methods in Physics Research Section a-Accelerators Spectrometers Detectors and Associated Equipment, 2009. **608**(2): p. 267-274.

47. Marleau, P., et al. *Active Coded Aperture Neutron Imaging*. in *2009 Ieee Nuclear Science Symposium Conference Record, Vols 1-5*. 2009. Orlando, FL, USA.

48.   Woolf, R.S., et al., *An Active Interrogation Detection System (ACTINIDES) Based on a Dual Fast Neutron/Gamma-Ray Coded Aperture Imager.* 2012 Ieee International Conference on Technologies for Homeland Security, 2012: p. 30-35.

49.   Singh, M., *An Electronically Collimated Gamma Camera for Single Photon Emission Computed Tomography. Part I: Theoretical Considerations and Design Criteria.* Medical Physics, 1983. **10**(4): p. 421-427.

50.   Runkle, R.C., D.L. Chichester, and S.J. Thompson, *Rattling nucleons: New developments in active interrogation of special nuclear material.* Nuclear Instruments and Methods in Physics Research Section A: Accelerators, Spectrometers, Detectors and Associated Equipment, 2012. **663**(1): p. 75-95.

51.   Norman, D.R., et al., *Active nuclear material detection and imaging*, in *2005 IEEE Nuclear Science Symposium Conference Record, Vols 1-5*, B. Yu, Editor. 2005. p. 1004-1008.

52.   Jones, J.L., et al., *Detection of shielded nuclear material in a cargo container.* Nuclear Instruments and Methods in Physics Research, Section A: Accelerators, Spectrometers, Detectors and Associated Equipment, 2006. **562**(2): p. 1085-1088.

53.   Chichester, D.L., J.D. Simpson, and M. Lemchak, *Advanced compact accelerator neutron generator technology for active neutron interrogation field work.* Journal of Radioanalytical and Nuclear Chemistry, 2007. **271**(3): p. 629-637.

54.   Runkle, R.C., L.E. Smith, and A.J. Peurrung, *The photon haystack and emerging radiation detection technology.* Journal of Applied Physics, 2009. **106**(4): p. 7.

55.   Guss, P., et al., *Size effect on nuclear gamma-ray energy spectra acquired by different-sized CeBr$_3$, LaBr$_3$:Ce, and NaI:Tl gamma-ray detectors.* Nuclear Technology, 2014. **185**(3): p. 309-321.

56.   Reinhard, M.I., et al. *Detection of illicit nuclear materials masked with other gamma-ray emitters*. in *IEEE Nuclear Science Symposium Conference Record*. 2007. San Diego, CA, USA.

57. Siciliano, E.R., et al., *Comparison of PVT and NaI(Tl) scintillators for vehicle portal monitor applications.* Nuclear Instruments and Methods in Physics Research, Section A: Accelerators, Spectrometers, Detectors and Associated Equipment, 2005. **550**(3): p. 647-674.

58. Mortreau, P. and R. Berndt, *Determination of 235U enrichment with a large volume CZT detector.* Nuclear Instruments and Methods in Physics Research Section A: Accelerators, Spectrometers, Detectors and Associated Equipment, 2006. **556**(1): p. 219-227.

59. Sjoden, G.E., et al., *Positive SNM gamma detection achieved through synthetic enhancement of sodium iodide detector spectra.* IEEE Transactions on Nuclear Science, 2009. **56**(3): p. 1329-1339.

60. Kim, K.H., et al., *Development of a car-mounted nuclear material monitoring system: A prototype system.* Nuclear Instruments and Methods in Physics Research, Section A: Accelerators, Spectrometers, Detectors and Associated Equipment, 2009. **607**(1): p. 154-157.

61. *TSA MD134.* [cited 2018 26/10/2018]; Available from: http://www.rapiscansystems.com/en/products/radiation_detection/rapiscan_mp100

62. Ziock, K.P., et al., *A Gamma-Ray Imager For Arms Control.* IEEE Transactions on Nuclear Science, 1992. **39**(4): p. 1046-1050.

63. Ziock, K.P., et al., *Autonomous radiation monitoring of small vessels.* Nuclear Instruments and Methods in Physics Research Section A: Accelerators, Spectrometers, Detectors and Associated Equipment, 2011. **652**(1): p. 10-15.

64. Ely, J., et al., *The use of energy windowing to discriminate SNM from NORM in radiation portal monitors.* Nuclear Instruments and Methods in Physics Research Section A: Accelerators, Spectrometers, Detectors and Associated Equipment, 2006. **560**(2): p. 373-387.

65. Hevener, R., M.-S. Yim, and K. Baird, *Investigation of energy windowing algorithms for effective cargo screening with radiation portal monitors.* Radiation Measurements, 2013. **58**: p. 113-120.

66. Lo Presti, C.A., et al., *Baseline suppression of vehicle portal monitor gamma count profiles: A characterization study.* Nuclear Instruments and Methods in

Physics Research Section A: Accelerators, Spectrometers, Detectors and Associated Equipment, 2006. **562**(1): p. 281-297.

67. Ziock, K.P. and W.H. Goldstein. *The lost source, varying backgrounds and why bigger may not be better*. in *Workshop on Unattended Radiation Sensor Systems for Remote Applications*. 2002. Washington, D.C.

68. Ziock, K.P., et al., *Performance of the Roadside Tracker Portal-Less Portal Monitor.* IEEE Transactions on Nuclear Science, 2013. **60**(3): p. 2237-2246.

69. Kouzes, R.T. and E.R. Siciliano, *The response of radiation portal monitors to medical radionuclides at border crossings.* Radiation Measurements, 2006. **41**(5): p. 499-512.

70. Robinson, S.M., et al., *Time Series Evaluation of Radiation Portal Monitor Data for Point Source Detection.* IEEE Transactions on Nuclear Science, 2009. **56**(6): p. 3688-3693.

71. Ivanov, O.P., et al. *Extra-light gamma-ray imager for safeguards and homeland security*. in *2015 4th International Conference on Advancements in Nuclear Instrumentation Measurement Methods and their Applications, ANIMMA 2015*. 2015. Lisbon, Portugal

72. Carrel, F., et al. *GAMPIX: A new gamma imaging system for radiological safety and Homeland Security Purposes*. in *2011 IEEE Nuclear Science Symposium Conference Record*. 2011.

73. Gal, O., et al., *CARTOGAM – a portable gamma camera for remote localisation of radioactive sources in nuclear facilities.* Nuclear Instruments and Methods in Physics Research Section A: Accelerators, Spectrometers, Detectors and Associated Equipment, 2001. **460**(1): p. 138-145.

74. Woodring, M., et al., *Advanced radiation imaging of low-intensity gamma-ray sources.* Nuclear Instruments and Methods in Physics Research Section A: Accelerators, Spectrometers, Detectors and Associated Equipment, 1999. **422**(1): p. 709-712.

75. Dubos, S., et al., *ORIGAMIX, a CdTe-based spectro-imager development for nuclear applications.* Nuclear Instruments & Methods in Physics Research Section a-Accelerators Spectrometers Detectors and Associated Equipment, 2015. **787**: p. 302-307.

76.   Wulf, E.A., et al. *MISTI imaging and source localization.* in *2008 IEEE Nuclear Science Symposium Conference Record.* 2008. Dresden, Germany.

77.   Kowash, B.R., D.K. Wehe, and J.A. Fessler, *A rotating modulation imager for locating mid-range point sources.* Nuclear Instruments & Methods in Physics Research Section a-Accelerators Spectrometers Detectors and Associated Equipment, 2009. **602**(2): p. 477-483.

78.   Vaska, P., et al. *A compact scintillator-based coded aperture imager for localizing illicit nuclear materials.* in *IEEE Nuclear Science Symposium Conference Record.* 2007. Honolulu, HI, USA

79.   Jeong, M., et al., *Scalable gamma-ray camera for wide-area search based on silicon photomultipliers array.* Review of Scientific Instruments, 2018. **89**(3): p. 033106.

80.   Ziock, K.P., *Principles and applications of gamma-ray imaging for arms control.* Nuclear Instruments and Methods in Physics Research Section A: Accelerators, Spectrometers, Detectors and Associated Equipment, 2018. **878**: p. 191-199.

81.   Kong, Y., et al., *A Prototype Compton Camera Array for Localization and Identification of Remote Radiation Sources.* IEEE Transactions on Nuclear Science, 2013. **60**(2): p. 1066-1071.

82.   Saull, P.R.B., et al. *SCoTSS modular survey spectrometer and Compton imager.* in *2016 IEEE Nuclear Science Symposium, Medical Imaging Conference and Room-Temperature Semiconductor Detector Workshop, NSS/MIC/RTSD 2016.* 2017. Strasbourg, France.

83.   MacLeod, A.M.L., et al., *Development of a Compton imager based on bars of scintillator.* Nuclear Instruments and Methods in Physics Research Section A: Accelerators, Spectrometers, Detectors and Associated Equipment, 2014. **767**: p. 397-406.

84.   Vetter, K., et al., *High-sensitivity Compton imaging with position-sensitive Si and Ge detectors.* Nuclear Instruments and Methods in Physics Research Section A: Accelerators, Spectrometers, Detectors and Associated Equipment, 2007. **579**(1): p. 363-366.

85.   M.V. Hynes, B.H., E.E. Lednum, M.S. Wallace, L.J. Schultz, D.M. Palmer, D.T. Wakeford, H.R. Andrews, R.C. Lanza, E.T.H. Clifford, et al., , *Multimodal Radiation Imager*. 2011.

86.   Andreyev, A., A. Sitek, and A. Celler, *Fast image reconstruction for Compton camera using stochastic origin ensemble approach.* Medical Physics, 2011. **38**(1): p. 429-438.

87.   Hoover, A.S., et al., *The LANL prototype Compton gamma-ray imager: design and image reconstruction techniques.* IEEE Transactions on Nuclear Science, 2005. **52**(6): p. 3047-3053.

88.   Montémont, G., et al. *NuVISION: a Portable Multimode Gamma Camera based on HiSPECT Imaging Module*. in *2017 IEEE Nuclear Science Symposium and Medical Imaging Conference (NSS/MIC)*. 2017. Atlanta, GA, USA.

89.   Penny, R.D., et al., *A dual-sided coded-aperture radiation detection system.* Nuclear Instruments & Methods in Physics Research Section a-Accelerators Spectrometers Detectors and Associated Equipment, 2011. **652**(1): p. 578-581.

90.   Zelakiewicz, S., et al., *SORIS-A standoff radiation imaging system.* Nuclear Instruments & Methods in Physics Research Section a-Accelerators Spectrometers Detectors and Associated Equipment, 2011. **652**(1): p. 5-9.

91.   Boehnen, C., et al. *Field trial of a highly portable coded aperture gamma ray and 3D imaging system*. in *2011 Future of Instrumentation International Workshop (FIIW) Proceedings*. 2011. Oak Ridge, TN, USA.

92.   Tornga, S.R., M.W.R. Sullivan, and J.P. Sullivan, *Three-Dimensional Compton Imaging Using List-Mode Maximum Likelihood Expectation Maximization.* IEEE Transactions on Nuclear Science, 2009. **56**(3): p. 1372-1376.

93.   Kouzes, R.T., et al., *Neutron detection alternatives to 3He for national security applications.* Nuclear Instruments and Methods in Physics Research Section A: Accelerators, Spectrometers, Detectors and Associated Equipment, 2010. **623**(3): p. 1035-1045.

94.   Peerani, P., et al., *Testing on novel neutron detectors as alternative to 3He for security applications.* Nuclear Instruments and Methods in Physics Research

Section A: Accelerators, Spectrometers, Detectors and Associated Equipment, 2012. **696**: p. 110-120.

95.   Lintereur, A.T., et al. *Alternatives to Helium-3 for Neutron Multiplicity Counters*. in *2012 Ieee Nuclear Science Symposium and Medical Imaging Conference Record*. 2012. Anaheim, CA, USA.

96.   Kouzes, R.T., A.T. Lintereur, and E.R. Siciliano, *Progress in alternative neutron detection to address the helium-3 shortage.* Nuclear Instruments and Methods in Physics Research Section A: Accelerators, Spectrometers, Detectors and Associated Equipment, 2015. **784**: p. 172-175.

97.   Zeitelhack, K., *Search for alternative techniques to helium-3 based detectors for neutron scattering applications.* Neutron News, 2012. **23**(4): p. 10-13.

98.   Lintereur, A., et al., *3He and BF3 neutron detector pressure effect and model comparison.* Nuclear Instruments and Methods in Physics Research Section A: Accelerators, Spectrometers, Detectors and Associated Equipment, 2011. **652**(1): p. 347-350.

99.   Flaska, M., S.A. Pozzi, and J.B. Czirr. *Use of an LGB detector in nuclear nonproliferation applications*. in *2008 IEEE Nuclear Science Symposium Conference Record*. 2008. Dresden, Germany.

100.   Tomanin, A., et al., *Characterization of a cubic EJ-309 liquid scintillator detector.* Nuclear Instruments & Methods in Physics Research Section a-Accelerators Spectrometers Detectors and Associated Equipment, 2014. **756**: p. 45-54.

101.   Pawełczak, I.A., et al., *Boron-loaded plastic scintillator with neutron-γ pulse shape discrimination capability.* Nuclear Instruments and Methods in Physics Research Section A: Accelerators, Spectrometers, Detectors and Associated Equipment, 2014. **751**: p. 62-69.

102.   Birch, J., et al., *(B4C)-B-10 Multi-Grid as an Alternative to He-3 for Large Area Neutron Detectors.* IEEE Transactions on Nuclear Science, 2013. **60**(2): p. 871-878.

103.   Swiderski, L., et al., *Boron-10 Loaded BC523A Liquid Scintillator for Neutron Detection in the Border Monitoring.* IEEE Transactions on Nuclear Science, 2008. **55**(6): p. 3710-3716.

104. Lawrence, C.C., et al., *Neutron response characterization for an EJ299-33 plastic scintillation detector.* Nuclear Instruments and Methods in Physics Research Section A: Accelerators, Spectrometers, Detectors and Associated Equipment, 2014. **759**: p. 16-22.

105. Mayer, M., et al., *Geometric optimization of a neutron detector based on a lithium glass–polymer composite.* Nuclear Instruments and Methods in Physics Research Section A: Accelerators, Spectrometers, Detectors and Associated Equipment, 2015. **784**: p. 168-171.

106. Ryzhikov, V., et al., *Detection of thermal and resonance neutrons using oxide scintillators.* IEEE Transactions on Nuclear Science, 2000. **47**(6): p. 2061-2064.

107. Haas, D.A., et al., *Actinide-loaded glass scintillators for fast neutron detection.* Nuclear Instruments and Methods in Physics Research Section A: Accelerators, Spectrometers, Detectors and Associated Equipment, 2011. **652**(1): p. 421-423.

108. van Eijk, C.W.E., *Inorganic Scintillators for Thermal Neutron Detection.* Ieee Transactions on Nuclear Science, 2012. **59**(5): p. 2242-2247.

109. Seymour, R.S., et al., *Scintillating-Glass-Fiber Neutron Sensors, their Application and Performance for Plutonium Detection and Monitoring.* Journal of Radioanalytical and Nuclear Chemistry, 2000. **243**(2): p. 387-388.

110. Jordan, D.V., et al., *Neutron detection via bubble chambers.* Applied Radiation and Isotopes, 2005. **63**(5): p. 645-653.

111. Bramblett, R.L., R.I. Ewing, and T.W. Bonner, *A new type of neutron spectrometer.* Nuclear Instruments and Methods, 1960. **9**(1): p. 1-12.

112. Thomas, D.J. and A.V. Alevra, *Bonner sphere spectrometers—a critical review.* Nuclear Instruments and Methods in Physics Research Section A: Accelerators, Spectrometers, Detectors and Associated Equipment, 2002. **476**(1): p. 12-20.

113. Caruso, A.N., *The physics of solid-state neutron detector materials and geometries.* Journal of Physics Condensed Matter, 2010. **22**(44).

114.   Peurrung, A.J., *Recent developments in neutron detection.* Nuclear Instruments and Methods in Physics Research Section A: Accelerators, Spectrometers, Detectors and Associated Equipment, 2000. **443**(2): p. 400-415.

115.   Runkle, R.C., A. Bernstein, and P.E. Vanier, *Securing special nuclear material: Recent advances in neutron detection and their role in nonproliferation.* Journal of Applied Physics, 2010. **108**(11).

116.   Szalkai, D., et al. *Detection of 14 MeV neutrons in high temperature environment up to 500 °C using 4H-SiC based diode detector.* in *2015 4th International Conference on Advancements in Nuclear Instrumentation Measurement Methods and their Applications (ANIMMA).* 2015. Lisbon, Portugal.

117.   Ha, J.H., et al., *A self-biased neutron detector based on an SiC semiconductor for a harsh environment.* Applied Radiation and Isotopes, 2009. **67**(7): p. 1204-1207.

118.   Balmer, R.S., et al., *Chemical vapour deposition synthetic diamond: Materials, technology and applications.* Journal of Physics Condensed Matter, 2009. **21**(36).

119.   Dumazert, J., et al., *Compensation scheme for online neutron detection using a Gd-covered CdZnTe sensor.* Nuclear Instruments and Methods in Physics Research, Section A: Accelerators, Spectrometers, Detectors and Associated Equipment, 2017. **857**: p. 7-15.

120.   Obraztsova, O., et al. *Comparison between Silicon-Carbide and diamond for fast neutron detection at room temperature.* in *5th International Conference on Advancements in Nuclear Instrumentation Measurement Methods and their Applications.* 2018. Palais des CongresLiege; Belgium.

121.   Streicher, M., et al., *Fast Neutron Detection Using Pixelated CdZnTe Spectrometers.* IEEE Transactions on Nuclear Science, 2017. **64**(7): p. 1920-1926.

122.   Janssens-Maenhout, G., F. De Roo, and W. Janssens, *Contributing to shipping container security: can passive sensors bring a solution?* Journal of Environmental Radioactivity, 2010. **101**(2): p. 95-105.

123.   Kouzes, R.T., et al., *Neutron detection gamma ray sensitivity criteria.* Nuclear Instruments and Methods in Physics Research Section A: Accelerators,

Spectrometers, Detectors and Associated Equipment, 2011. **654**(1): p. 412-416.

124.   Stave, S., et al., *LiF/ZnS neutron multiplicity counter.* Nuclear Instruments and Methods in Physics Research Section A: Accelerators, Spectrometers, Detectors and Associated Equipment, 2015. **784**: p. 208-212.

125.   Oakes, T.M., et al., *An accurate and portable solid state neutron rem meter.* Nuclear Instruments and Methods in Physics Research Section A: Accelerators, Spectrometers, Detectors and Associated Equipment, 2013. **719**: p. 6-12.

126.   Kouzes, R.T., et al., *Boron-10 based neutron coincidence counter for safeguards.* IEEE Transactions on Nuclear Science, 2014. **61**(5): p. 2608-2618.

127.   Littell, J., et al., *Coded moderator approach for fast neutron source detection and localization at standoff.* Nuclear Instruments and Methods in Physics Research Section A: Accelerators, Spectrometers, Detectors and Associated Equipment, 2015. **784**: p. 364-369.

128.   Runkle, R.C., *Neutron sensors and their role in nuclear nonproliferation.* Nuclear Instruments and Methods in Physics Research Section A: Accelerators, Spectrometers, Detectors and Associated Equipment, 2011. **652**(1): p. 37-40.

129.   Gamage, K.A.A., M.J. Joyce, and J.C. Adams, *Combined digital imaging of mixed-field radioactivity with a single detector.* Nuclear Instruments and Methods in Physics Research Section A: Accelerators, Spectrometers, Detectors and Associated Equipment, 2011. **635**(1): p. 74-77.

130.   Flaska, M. and S.A. Pozzi, *Digital pulse shape analysis for the capture-gated liquid scintillator BC-523A.* Nuclear Instruments and Methods in Physics Research, Section A: Accelerators, Spectrometers, Detectors and Associated Equipment, 2009. **599**(2-3): p. 221-225.

131.   Pausch, G. and J. Stein, *Application of6LiI(Eu) scintillators with photodiode readout for neutron counting in mixed gamma-neutron fields.* IEEE Transactions on Nuclear Science, 2008. **55**(3): p. 1413-1419.

132.   Joyce, M.J. and K.A.A. Gamage. *Real-time, digital imaging of fast neutrons and γ rays with a single fast liquid scintillation detector*. in *IEEE Nuclear Science Symposium Conference Record*. 2012. San Diego, CA, USA.

133.   Payne, C., et al. *Neutron/gamma pulse shape discrimination in EJ-299-34 at high flux*. in *2015 IEEE Nuclear Science Symposium and Medical Imaging Conference, NSS/MIC 2015*. 2016.

134.   Liu, G., et al., *A digital method for the discrimination of neutrons and γ rays with organic scintillation detectors using frequency gradient analysis*. IEEE Transactions on Nuclear Science, 2010. **57**(3 PART 3): p. 1682-1691.

135.   *UNSURPASSED MOBILE PRIMARY SCREENING*. [cited 2019 28/01/2019]; Available from: http://www.symetrica.com/mobile-rpm.

136.   *Fission Meter Portable Neutron Source Identification System*. [cited 2019 28/01/2019]; Available from: https://www.ortec-online.com/products/nuclear-security-and-safeguards/neutron-fission-systems/fission-meter.

137.   *SMITHS DETECTION RADSEEKER*. [cited 2019 28/01/2019]; Available from: http://www.symetrica.com/oem-sub-systems.

138.   *FLAT PANEL BACKPACK NEUTRON DETECTION (3HE FREE)*. [cited 2018 26/10/2018]; Available from: http://www.symetrica.com/backpack.

139.   Brooks, F.D., *A scintillation counter with neutron and gamma-ray discriminators*. Nuclear Instruments and Methods, 1959. **4**(3): p. 151-163.

140.   Adams, J.M. and G. White, *A versatile pulse shape discriminator for charged particle separation and its application to fast neutron time-of-flight spectroscopy*. Nuclear Instruments and Methods, 1978. **156**(3): p. 459-476.

141.   Yang, K., P.R. Menge, and V. Ouspenski, *Li Co-Doped NaI:Tl (NaIL)-A Large Volume Neutron-Gamma Scintillator with Exceptional Pulse Shape Discrimination*. IEEE Transactions on Nuclear Science, 2017. **64**(8): p. 2406-2413.

142.   Mukhopadhyay, S. and H.R. McHugh. *Portable gamma and thermal neutron detector using 6LiI(Eu) crystals*. in *Proceedings of SPIE - The International Society for Optical Engineering*. 2004. San Diego, CA, USA.

143.   Soundara-Pandian, L., et al., *Lithium Alkaline Halides—Next Generation of Dual Mode Scintillators*. IEEE Transactions on Nuclear Science, 2016. **63**(2): p. 490-496.

144.   McGregor, D.S., J.T. Lindsay, and R.W. Olsen, *Thermal neutron detection with cadmium1-x zincx telluride semiconductor detectors.* Nuclear Instruments and Methods in Physics Research, Section A: Accelerators, Spectrometers, Detectors and Associated Equipment, 1996. **381**(2-3): p. 498-501.

145.   Martín-Martín, A., et al., *Evaluation of CdZnTe as neutron detector around medical accelerators.* Radiation Protection Dosimetry, 2009. **133**(4): p. 193-199.

146.   Tupitsyn, E., et al., *Single crystal of LiInSe₂ semiconductor for neutron detector.* Applied Physics Letters, 2012. **101**(20).

147.   Coceva, C., *Pulse-shape discrimination with a glass scintillator.* Nuclear Instruments and Methods, 1963. **21**(C): p. 93-96.

148.   Combes, C.M., et al., *Optical and scintillation properties of pure and Ce3+-doped Cs2LiYCl6 and Li3YCl6 : Ce3+ crystals.* Journal of Luminescence, 1999. **82**(4): p. 299-305.

149.   Glodo, J., et al., *New Developments in Scintillators for Security Applications.* Physics Procedia, 2017. **90**: p. 285-290.

150.   Bell, Z.W., *Tests on a digital neutron-gamma pulse shape discriminator with NE213.* Nuclear Instruments and Methods in Physics Research, 1981. **188**(1): p. 105-109.

151.   Kaschuck, Y. and B. Esposito, *Neutron/γ-ray digital pulse shape discrimination with organic scintillators.* Nuclear Instruments and Methods in Physics Research Section A: Accelerators, Spectrometers, Detectors and Associated Equipment, 2005. **551**(2): p. 420-428.

152.   Pozzi, S.A., M.M. Bourne, and S.D. Clarke, *Pulse shape discrimination in the plastic scintillator EJ-299-33.* Nuclear Instruments and Methods in Physics Research, Section A: Accelerators, Spectrometers, Detectors and Associated Equipment, 2013. **723**: p. 19-23.

153.   Stevanato, L., et al., *Neutron detection in a high gamma-ray background with EJ-301 and EJ-309 liquid scintillators.* Nuclear Instruments and Methods in Physics Research Section A: Accelerators, Spectrometers, Detectors and Associated Equipment, 2012. **690**: p. 96-101.

154.   Al Hamrashdi, H., D. Cheneler, and S.D. Monk, *Material optimization in dual particle detectors by comparing advanced scintillating materials using two Monte Carlo codes.* Nuclear Instruments and Methods in Physics Research Section A: Accelerators, Spectrometers, Detectors and Associated Equipment, 2017. **869**(Supplement C): p. 163-171.

155.   Bell, Z.W., et al. *Wavelength-based neutron/gamma ray discrimination in CLYC.* in *2014 IEEE Nuclear Science Symposium and Medical Imaging Conference (NSS/MIC).* 2014. Seattle, WA, USA.

156.   Cester, D., et al., *A compact neutron–gamma spectrometer.* Nuclear Instruments and Methods in Physics Research Section A: Accelerators, Spectrometers, Detectors and Associated Equipment, 2013. **719**: p. 81-84.

157.   Paff, M.G., et al., *Organic liquid scintillation detectors for on-the-fly neutron/gamma alarming and radionuclide identification in a pedestrian radiation portal monitor.* Nuclear Instruments & Methods in Physics Research Section a-Accelerators Spectrometers Detectors and Associated Equipment, 2015. **789**: p. 16-27.

158.   Soundara-Pandian, L., et al., *Characterization of Large Volume CLYC Scintillators for Nuclear Security Applications.* IEEE Transactions on Nuclear Science, 2017. **64**(7): p. 1744-1748.

159.   Gamage, K.A.A., M.J. Joyce, and G.C. Taylor, *A digital approach to neutron–γ imaging with a narrow tungsten collimator aperture and a fast organic liquid scintillator detector.* Applied Radiation and Isotopes, 2012. **70**(7): p. 1223-1227.

160.   Soundara-Pandian, L., et al. *CLYC in gamma -Neutron imaging system.* in *IEEE Nuclear Science Symposium Conference Record.* 2012. Honolulu, HI, USA.

161.   McDonald, B.S., et al., *A wearable sensor based on CLYC scintillators.* Nuclear Instruments & Methods in Physics Research Section a-Accelerators Spectrometers Detectors and Associated Equipment, 2016. **821**: p. 73-80.

162.   Budden, B.S., et al., *A Cs2LiYCl6:Ce-based advanced radiation monitoring device.* Nuclear Instruments and Methods in Physics Research Section A: Accelerators, Spectrometers, Detectors and Associated Equipment, 2015. **784**: p. 97-104.

163. Glodo, J., et al. *Cs₂LiYCl₆: Ce Neutron gamma detection system*. in *2007 IEEE Nuclear Science Symposium Conference Record*. 2007. Honolulu, HI, USA.

164. Aryaeinejad, R., E.L. Reber, and D.F. Spencer, *Development of a handheld device for simultaneous monitoring of fast neutrons and gamma rays.* IEEE Transactions on Nuclear Science, 2002. **49**(4): p. 1909-1913.

165. Aryaeinejad, R. and D.F. Spencer, *Pocket dual neutron/gamma radiation detector.* IEEE Transactions on Nuclear Science, 2004. **51**(4): p. 1667-1671.

166. Baker, J.H., et al., *A combined NaI(Tl)+LiI(Eu) detector for environmental, geological and security applications.* Radiation Measurements, 2007. **42**(4): p. 937-940.

167. Enqvist, A., M. Flaska, and S. Pozzi, *Measurement and simulation of neutron/gamma-ray cross-correlation functions from spontaneous fission.* Nuclear Instruments and Methods in Physics Research Section A: Accelerators, Spectrometers, Detectors and Associated Equipment, 2008. **595**(2): p. 426-430.

168. Runkle, R.C., et al., *Lynx: An unattended sensor system for detection of gamma-ray and neutron emissions from special nuclear materials.* Nuclear Instruments and Methods in Physics Research Section A: Accelerators, Spectrometers, Detectors and Associated Equipment, 2009. **598**(3): p. 815-825.

169. Polack, J.K., et al. *Dual-particle imager for standoff detection of special nuclear material*. in *2011 IEEE Nuclear Science Symposium Conference Record*. 2011. Valencia, Spain.

170. Cester, D., et al., *Special nuclear material detection with a mobile multi-detector system.* Nuclear Instruments and Methods in Physics Research Section A: Accelerators, Spectrometers, Detectors and Associated Equipment, 2012. **663**(1): p. 55-63.

171. Ayaz-Maierhafer, B., et al., *Angular resolution study of a combined gamma-neutron coded aperture imager for standoff detection.* Nuclear Instruments and Methods in Physics Research Section A: Accelerators, Spectrometers, Detectors and Associated Equipment, 2013. **712**: p. 120-125.

172.   Poitrasson-Riviere, A., et al., *Dual-particle imaging system based on simultaneous detection of photon and neutron collision events.* Nuclear Instruments & Methods in Physics Research Section a-Accelerators Spectrometers Detectors and Associated Equipment, 2014. **760**: p. 40-45.

173.   Cester, D., et al., *A novel detector assembly for detecting thermal neutrons, fast neutrons and gamma rays.* Nuclear Instruments and Methods in Physics Research Section A: Accelerators, Spectrometers, Detectors and Associated Equipment, 2016. **830**: p. 191-196.

174.   Nemzek, R., et al., *SNM-DAT: Simulation of a heterogeneous network for nuclear border security.* Nuclear Instruments and Methods in Physics Research Section A: Accelerators, Spectrometers, Detectors and Associated Equipment, 2007. **579**(1): p. 414-417.

175.   Cooper, D.A., et al. *Intelligent radiation sensor system (IRSS) advanced technology demonstration (ATD).* in *2010 IEEE International Conference on Technologies for Homeland Security, HST 2010.* 2010. Waltham, MA, USA

176.   Klann, R., *RadTrac: A System for Detecting, Localizing, and Tracking Radioactive Sources in Real Time AU - Vilim, R.* Nuclear Technology, 2009. **168**(1): p. 61-73.

177.   Vilim, R. and R. Klann, *RadTrac: A System for Detecting, Localizing, and Tracking Radioactive Sources in Real Time.* Nuclear Technology, 2009. **168**(1): p. 61-73.

178.   Rao, N.S.V., et al., *Network algorithms for detection of radiation sources.* Nuclear Instruments and Methods in Physics Research Section A: Accelerators, Spectrometers, Detectors and Associated Equipment, 2015. **784**: p. 326-331.

179.   Wu, C.Q., et al. *Network detection of radiation sources using ROSD localization.* in *2015 IEEE Nuclear Science Symposium and Medical Imaging Conference (NSS/MIC).* 2015.

180.   Hite, J. and J. Mattingly, *Bayesian Metropolis methods for source localization in an urban environment.* Radiation Physics and Chemistry, 2019. **155**: p. 271-274.

181.   Wu, C.Q., et al., *Network Detection of Radiation Sources Using Localization-based Approaches.* IEEE Transactions on Industrial Informatics, 2019: p. 1-1.

182.   *identiFINDER S900 Radionuclide detection systems*. 2019 [cited 2019 28/04/2019]; Available from: https://www.southernscientific.co.uk/products-by-manufacturer/flir/radiation/stride-systems#overview.

183.   *Passport Releases SmartShield™ v2.0*. [cited 2019 28/04/2019].

4 Monte Carlo Simulations

This chapter introduces Monte Carlo methods and justifies the use of two well-known Monte Carlo simulation codes, namely MCNP and Geant4. In addition, the chapter provides a background on the features of these two Monte Carlo codes and discusses the areas in this project where they were implemented.

4.1 Monte Carlo method

Analysing the behaviour of gamma-ray photons and neutrons within the imaging system and subsequently proving the feasibility of the imaging system requires an adequate knowledge of the radiation transport theory that governs the transport of radiation particles through matter. The variation of gamma-ray and neutron fluxes through a system is a complex function that handles spatial, temporal, directional and energy variations. The Boltzmann transport equation is widely used to describe the transport of radiation within materials [1]. It relates the variables contributing to the variation of the radiation flux as it traverses through a target material. For neutrally charged particles, Boltzmann transport equation can be written as [1]:

$$\boldsymbol{\Omega}.\,\boldsymbol{\nabla}\phi\,(r,E,\boldsymbol{\Omega},t)+\frac{1}{\boldsymbol{v}}\frac{\partial\phi}{\partial t}(r,E,\boldsymbol{\Omega},t)+\Sigma_t\,\phi(r,E,\boldsymbol{\Omega},t)\;=$$

$$\int_{\boldsymbol{\Omega}'}\int_{E'}\Sigma_s\left(E'\rightarrow E,\boldsymbol{\Omega}'\rightarrow\boldsymbol{\Omega}\right)\phi(r,E',\boldsymbol{\Omega}',t)dE'd\boldsymbol{\Omega}'+S(r,E,\boldsymbol{\Omega},t) \qquad (4.1)$$

Where $\phi\,(r,E,\boldsymbol{\Omega},t)$ is the angular flux of the radiation quanta, r is the position vector of the radiation quanta in space, v is the velocity of radiation quanta, $\boldsymbol{\Omega}$ is the direction vector of the radiation quanta, and E is the energy of the radiation quanta. In addition, Σ_t is the total macroscopic cross section of the target material and Σ_s is the macroscopic scattering cross section of the target material.

The first term in the Boltzmann transport equation is $\boldsymbol{\Omega}.\,\boldsymbol{\nabla}\phi\,(r,E,\boldsymbol{\Omega},t)$. The term describes the flow of radiation quanta in the space they traverse. The second term in the equation is $\frac{1}{v}\frac{\partial\phi}{\partial t}(r,E,\boldsymbol{\Omega},t)$. The term describes the change in the radiation quanta's density in a volume element of space. The third term is $\Sigma_t\,\phi(r,E,\boldsymbol{\Omega},t)$, which presents the loss of radiation quanta to any possible interaction mechanism within the target. The term $\int_{\boldsymbol{\Omega}'}\int_{E'}\Sigma_s\left(E'\rightarrow E,\boldsymbol{\Omega}'\rightarrow\boldsymbol{\Omega}\right)\phi(r,E',\boldsymbol{\Omega}',t)dE'd\boldsymbol{\Omega}'$ is commonly known as the scattering term and it describes the change in energy and direction of radiation quanta in the target. The scattering of radiation quanta occur at energy E' to energy E and at direction $\boldsymbol{\Omega}'$ to direction $\boldsymbol{\Omega}$. The last term in the Boltzmann transport equation is the source term $S(r,E,\boldsymbol{\Omega},t)$. An additional acceleration term is added to this equation when charged radiation particles are investigated.

The number of variables in the Boltzmann transport equation necessitates indirect solving techniques. Generally, there are two methods of solutions, deterministic methods and Monte Carlo method. Deterministic methods such as energy variation simplification, angular variation simplifications, and space and time simplifications use

numerical approximations in an attempt to solve the Boltzmann transport equation. On the other hand, the Monte Carlo method stochastically models the Boltzmann transport equation and the problem under investigation. The Monte Carlo method offers an enhanced solution of the Boltzmann transport equation compared to deterministic methods because the later attempts to simplify the problem through approximations. In this work, Monte Carlo simulations were used to investigate the transport of gamma-ray photons and neutrons in the proposed design. In general, the Monte Carlo method is based on modelling the geometry and the setup of the system under investigation. A particle 'history' is followed through the system taking into account materials properties, interaction cross sections and interaction probabilities. The interaction cross sections and the interaction probabilities are based on data libraries and fundamental physics principles and laws. Conventionally, random number generators are used to start the parameters in the model. Some of the most commonly used codes are: Monte Carlo N-Particle transport code (MCNP®) for neutron and gamma-ray transport developed by Los Alamos National laboratory [2], Geant4 simulation toolkit by CERN [3-6], PENELOPE code for electron-photon transport by Nuclear Energy Agency[7], Particle and Heavy Ion Transport code System (PHITS) for particles and heavy ion transport by the Nuclear Energy Agency [8]. For the purpose of this work MCNP version 6.1.0 and Geant4 versions 10.2 —10.4, two widely known Monte Carlo codes for neutron and gamma-ray transport simulations, are utilised to investigate the propagation of these two radiation fields through the design. MCNP has been the main simulation code tool in various projects since the 1940s [9]. Geant4 simulation toolkit is a free licensing Monte Carlo simulation tool. It has been utilised in variety of radiation

detection applications including in high-energy physics, space radiation and medical imaging [4].

4.2 MCNP

MCNP is a multi-purpose, time dependent simulation code. It applies continuous energy presentation of data libraries and can be utilised in simulating neutrons, photons and electrons. The code covers neutrons with energies between 10^{-11} MeV and 20 MeV and photon and electron with energies between 1 keV and 1,000 MeV. In MCNP, each particle in the system is followed through a geometry from generation to termination. Take for example the journey of a neutron generated in a spontaneous fission reaction traversing through a highly scattering system. Figure 4.1 shows the first tracked point in the neutron's journey in MCNP (position 1) where the neutron is generated with energy E at position (x, y, z, u_x, u_y, u_z) in cell 1 with importance 1. Within MCNP environment the importance of a cell refers to the weight of the particle in a cell. The neutron then traverses the medium going through elastic scattering at position 2 with a scattering probability given by the chosen nuclear data library. The scattering angle of this interaction will be simulated in MCNP based on the physics of the interaction involved and the scattering cross section of the nucleus involved in the interaction. A gamma-ray photon is generated in the interaction scene and is temporarily banked while MCNP tracks the rest of the neutrons journey. At position 3, the neutron is captured and the neutron history is be terminated at this point. A secondary charged particle is generated in the scene of the last interaction. The gamma-ray photon generated at position 2 leaks to the void cell with zero importance zero (a cell beyond the volume of interest). The history of this gamma-ray photon will be terminated as a result. The secondary particle generated at position 3 ionises the matter and an electron is ejected

from the interaction scene at position 5. The electron will be absorbed in the medium, and its history is terminated at point 6.
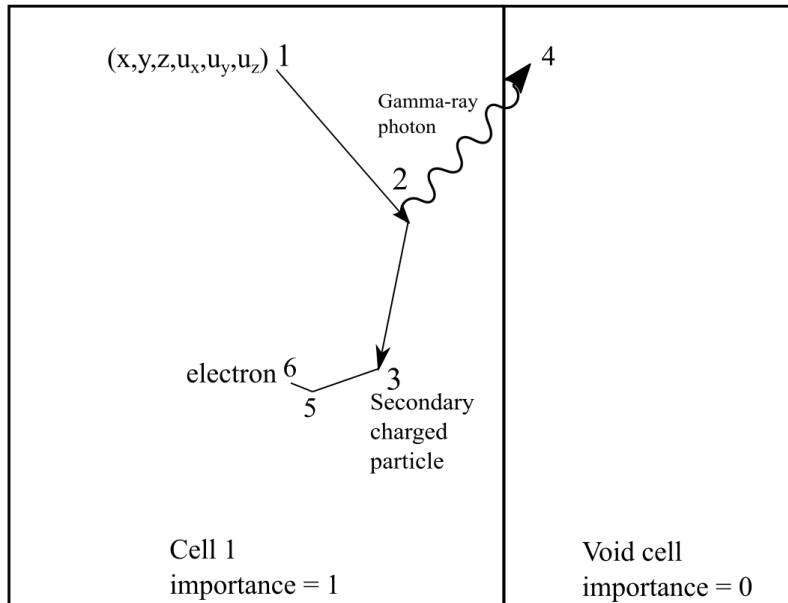
Figure 4.1: An example of neutron history tracking in MCNP code environment.

4.2.1 MCNP features

Probably one of the most notable features in MCNP is the use of continuous energy spectra from nuclear and data libraries in the simulations. There is a number of continuous neutron data libraries utilised in MCNP code, mainly the Evaluated Nuclear Data File (ENDF) [10, 11], the Evaluated Nuclear Data Library (ENDL), Activation Library (ACTL) and 100xs Neutron Cross Section Library [12]. In addition, there is a number of discrete data libraries utilised in MCNP including NEWXSD, DRMCCS and DRE5 [13]. Photon transport data libraries in MCNP comprise of MCNLIB versions 2, 3 and 4 some of which are based on ENF/B-VI.8 data library [13]. For electron transport simulations, EL03 is used as an electron data library [13]. In MCNP, each data table is

listed in directory file XDIR. Neutron interaction data tables are available for ~100 isotopes, whereas for photon interaction tables are available for atomic numbers between 1 and 94. Other specifications and features within MCNP include:

- Input file: the input file in MCNP has a fixed structure. The structure is featured with a title card, cell cards, surface cards, data cards and blank line delimiter lines between the cards.

- Geometry specifications: within MCNP environment, a combination of geometries are allowed which facilitates the simulation of complex and comprehensive geometries. The cell card defines the material involved in the geometry and the surfaces making up the boundary of the geometry [14, 15].

- Source definition: A source term or a source card in MCNP terminology specifies particles density from an external source. Source card allows defining spatial, angular, temporal and energy distributions of the generated particles. MCNP features a wide range of source geometries, configurations and conditions. In addition, there are several build-in source probability distribution functions in MCNP including Maxwellian and Watt spectra which are used to describe neutron spontaneous and induced fission energy spectra as well as fusion energy spectra [14, 15].

- Transport and collisions: The transport of neutral gamma-ray photons and neutrons in the MCNP environment is based on the assumption that both are effected by short-range forces from the atoms and nuclei in the medium they traverse. Therefore, gamma-ray photons and neutrons travel in a straight lines between interaction sites. While transporting across matter, particles are subject to different interaction scenarios 'collisions'. The process of collisions

continue through the transportation process of the particle until the history is terminated [1].

- A tally: A tally is specified in MCNP input file over a surface or a cell. A number of tallies are available in MCNP all identified by the letter F followed by the unique identifier of the tally. Table 4.1 lists the main standard tallies available in MCNP along with their description.

Table 4.1: MCNP main standard tallies [14].

Tally identifier	Unit (Fn)	Unit (*F)	Description
F1/*F1	Particles	MeV	Total current over a surface
F2/*F2	$\frac{particles}{cm^2}$	$\frac{MeV}{cm^2}$	Flux averaged over a surface
F4/*F4	$\frac{particles}{cm^2}$	$\frac{MeV}{cm^2}$	Flux averaged over a cell
F5a/*F5a	$\frac{particles}{cm^2}$	$\frac{MeV}{cm^2}$	Flux at a point or a ring detector
F6/*F6	$\frac{MeV}{g}$	$\frac{jerks}{g}$	Energy deposition over a cell
+F6	$\frac{MeV}{g}$	NA	Collision heating
F7	$\frac{MeV}{g}$	$\frac{jerks}{g}$	Fission energy deposition over a cell
F8/*F8	Pulses	MeV	Energy distribution of pulses in a detector
+F8	Charge	NA	Charge deposition

4.2.2 Mean, variance and standard deviation in MCNP

As discussed earlier, measurements and quantities are statistically estimated in MCNP environment. For example, the number of particles crossing a surface averaged over the

total number of histories provides an estimate of radiation field flux over a surface. In the MCNP environment, this process is known as tally scoring. Generally, in Monte Carlo techniques results are obtained via sampling random walks. A weighted score for a particle is generated for each random walk. The average score is maintained since it is the average result over all possible random walks. Therefore, an implicit sampling using the random walk technique is used to estimate the true mean through the sample mean. For a very large population, the law of large numbers attempts to evaluate the long-term behaviour of the mean of random walks and gives the assumption that the sample mean approaches the population mean as the number of random walks increases. Hence, the mean in the MCNP environment is presented as the sample mean and is given as [15]:

$$\bar{x} = \frac{1}{N}\sum_{i=1}^{N} x_i \qquad (4.2)$$

Where N is the total number of histories and x_i is the value of x for the ith history. The variance of a population,σ^2, is a measure of the spread of x for the total number of histories N. For a large population the variance can be estimated using the sample variance S^2.

$$S^2 = \frac{\sum_{i=1}^{N}(x_i - \bar{x})^2}{N\text{-}1} \sim \overline{x^2} - \bar{x}^2 \qquad (4.3)$$

The estimated variance of the mean $\bar{x}$ is given as [15]:

$$S_{\bar{x}}^2 = \frac{S^2}{N} \qquad (4.4)$$

S is the estimated standard deviation. As seen from equation 4.4, the standard deviation of the estimated mean is inversely proportional to $\sqrt{N}$.

4.2.3 The estimated relative error and the figure of merit in MCNP

A fixed feature in MCNP tallies is the normalisation of the tally output over the total number of histories (except for some criticality measurements). Every output reported in MCNP is associated with an estimated relative error R. In MCNP, the estimated relative error is defined as [15]:

$$R \equiv S_{\overline{x}}/\overline{x} \tag{4.5}$$

Based on equations 4.4 and 4.5, it can be seen that the estimated relative error R is proportional to $\sqrt{N}$. In addition, the estimated relative error R is always between zero and unity. In general, R represents the relative error at 1σ. A reliable tally output should be associated with R less than 0.1 (except for point detector tally where it is expected to be less than 0.05) [15].

The figure of merit in the MCNP environment describes the performance of MCNP code in calculating the tallies. It is defined as the inverse of the product of R^2 and the computing time T. R is proportional to $\sqrt{N}$ as discussed above and T is assumed to be proportional to N and hence R^2T should be constant through an MCNP run [15]. The figure of merit is an important indicator of the code performance and it reflects the reliability of the tally results. A plot of the figure of merit as function of histories should be constant plateau especially at the later stages in the simulation.

4.2.4 Variance reduction techniques in MCNP

Although increasing the number of particles histories in MCNP input file might improve the relative error of a scored tally, it can negatively affect the efficiency of the code by

increasing the computing time. In the MCNP environment, variance reduction techniques offer an alternative solution to improve relative error. Variance reduction techniques in MCNP enhance the number of particles in the tally region while terminating the number of particles in regions where no tallies are scored. A common variance reduction method in MCNP code, and one that has been frequently used throughout the simulations in this work, is the population control method. Russian roulette is one technique based on population control method. Geometry splitting, energy splitting and weight cut-off are all based on the Russian roulette technique. Geometry splitting is very popular the Russian roulette technique where the region of interest is split into smaller regions. The weight of particles must be modified as well here to boost and maintain the number of particles in the tally region and to avoid biasing. Particles moving away from the region of interest are killed off with a given probability. Truncation methods such as geometry truncation, energy cut-off and time cut-off are another examples of variance reduction techniques used to improve the statistics within simulations in MCNP. A less popular technique is the modified sampling method. Within this method, the sampling distribution is modified such that particles are forced into the regions of interest [15].

4.2.5 MCNP implementation

MCNP6^{TM} version 6.1[9] is the MCNP version utilised in this work. This version merges two MCNP predecessor codes; MCNP5^{TM} [16] and MCNPX^{TM} [17] such that it comprises all the features of the two codes. New characteristics in MCNP6 not found in the previous codes includes additional photon physics capabilities, time bins mesh tallies, surface flagging and cell flagging in FMESH tally. There are three major areas in this work where MCNP6 implementation was complementary to achieve the aims of

the project. First, MCNP6 was the key tool in studying the neutron source that was later

utilised in the experimental setup that is the Cf-252 source at the Faculty of Science and

Technology at Lancaster University (More details in chapter 6). Figure 4.2 shows an

image of the source housing while Figure 4.3 shows a sketch of the source housing with

dimensions included.

Figure 4.2: A photo showing the Cf-252 fission source housing in the Faculty of Science and Technology at Lancaster University.
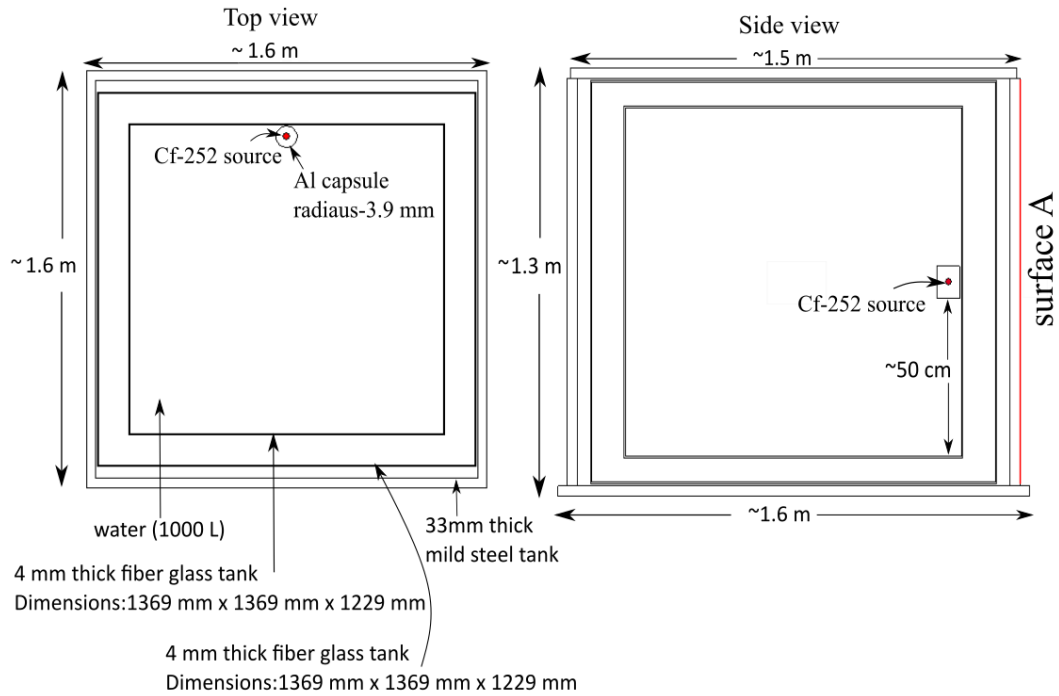
Figure 4.3: A sketch of the Cf-252 source tank showing the dimensions of the different layers surrounding the source when the source is at an exposed position.

Some of the fluxes and spectra measurements were made in parallel with the simulations using an EJ-309 liquid organic scintillator by Scionix, Netherlands (V94A94/3MEJ309E1XNEG) [18]. The scintillation volume of the EJ-309 detector was 10 cm x 10 cm x 11.8 cm and optically coupled with a PMT [19]. Measurements were analysed using Hybrid Instruments Ltd. MFA Mixed Field Analyser [20]. The system was first calibrated using a Cs-137 source with a total activity of 395 kBq at the time of use (more details in chapter 6). Through this part of the Cf-252 source experiment, the detector was located 50 cm away from surface A as indicated in Figure 4.3, at an angle of 45° relative to the source at the exposed position (detector is at the same level as the source). First, MCNP6 simulations estimated gamma-ray fluence over the EJ-309 scintillator using the F4 tally and 20,000,000 histories. The output of the tally was multiplied by the emission rate of gamma-ray from the Cf-252 source and the volume of the EJ-309 scintillator to estimate the number gamma-ray photons entering

the scintillator. Figure 4.4 shows the results of this simulation (fluence within the EJ-309 scintillator) alongside the experimental results of the gamma-ray energy deposition in the EJ-309 scintillator. The maximum relative error in the tally output was found to be 0.03 at 4.8 MeV. The error bars in the figure are caused by statistical errors in the results.
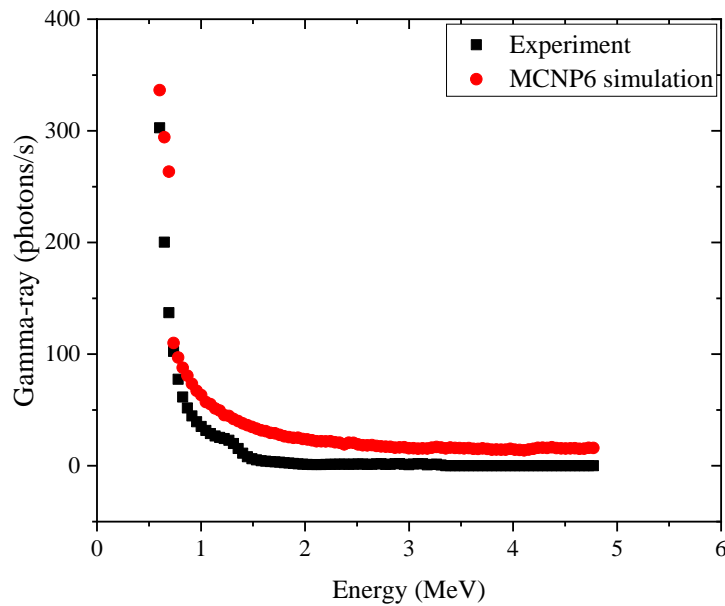
Figure 4.4: Gamma-ray count rate versus energy curve using experimental data and MCNP6 simulation.

The curves of gamma-ray count rate versus energy from the experimental results and from MCNP simulations shows a decaying gamma-ray photons count rate as function of energy. The differences in the two curves is due to the fact that F4 tally counts the number of photons entering the volume of the EJ-309 scintillator, whereas experimental results reflects the number of photons depositing their energy within the bulk of EJ-309. Similarly, MCNP6 simulations were utilised in investigating neutron count rate at surface A as indicated in Figure 4.3 using F2 tally and 20,000,000 histories (Note: this

is the same surface of the Cf-252 housing tank where the imaging system feasibility tests took place in this work and discussed in chapter 6). The output of this tally was multiplied by the neutrons emission rate from the Cf-252 source and the total area of surface A. Figure 4.5 shows neutron count rate across surface A as function of energy. The maximum relative error of the tally output was found to be 0.047 at 4.8 MeV. The error bars in the figure are caused by statistical errors in the results. The complete MCNP6 input file used in this investigation is given in Appendix A.1.
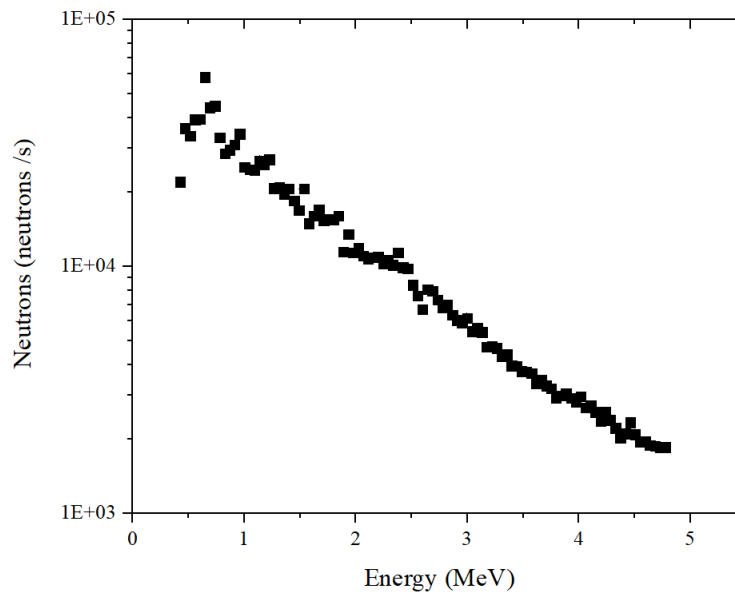
Figure 4.5: MCNP6 simulation of neutron count rate over one of the Cf-252 housing surfaces as function of energy.

The results in Figure 4.5 indicates that the neutron average energy is ~2.0 MeV and the most probable energy of emitted neutrons is ~ 0.7 MeV. These results fall within the range of the expected neutron energy spectrum characteristics from a Cf-252 [21-23]. All of these results were utilised in assessing the results during the feasibility experiments of the proposed imaging system in this work.

The second implementation of MCNP6 in this research was in studying the scintillation materials for the proposed three-layer design. Four materials were investigated here, lithium glass detector (GS10) [24], Cs_2LiYCl_6:Ce with two different Li-6 enrichments (95% and 6.6% enrichment percentages) [25] and EJ-309 liquid organic scintillator [18]. MCNP6 simulations investigated the detection and attenuation abilities of these materials and appraised their performance at different gamma-ray photon energies and different neutron energies. A dedicated MATLAB® program was designed to extract the desired information from MCNP6 PTRAC output files. The full program is attached in appendix A.3.1. A complete investigation on this published study is the subject of chapter 5.

A third implementation of the MCNP6 code within this research was in investigating the feasibility of the prototype design. First, the results were utilised to optimise the overall configuration of the system. An example of the MCNP6 code used in the analysis carried out in this part of the investigation is given in appendix A.1.2. A dedicated MATLAB® program was designed to extract the desired information form MCNP6 PTRAC output files. A flow diagram of the hierarchy followed in the MATLAB® program is shown in Figure 4.6. The full program is given in appendix A.3.2. The results of this investigation are part of the discussion in chapters 6 and 7.
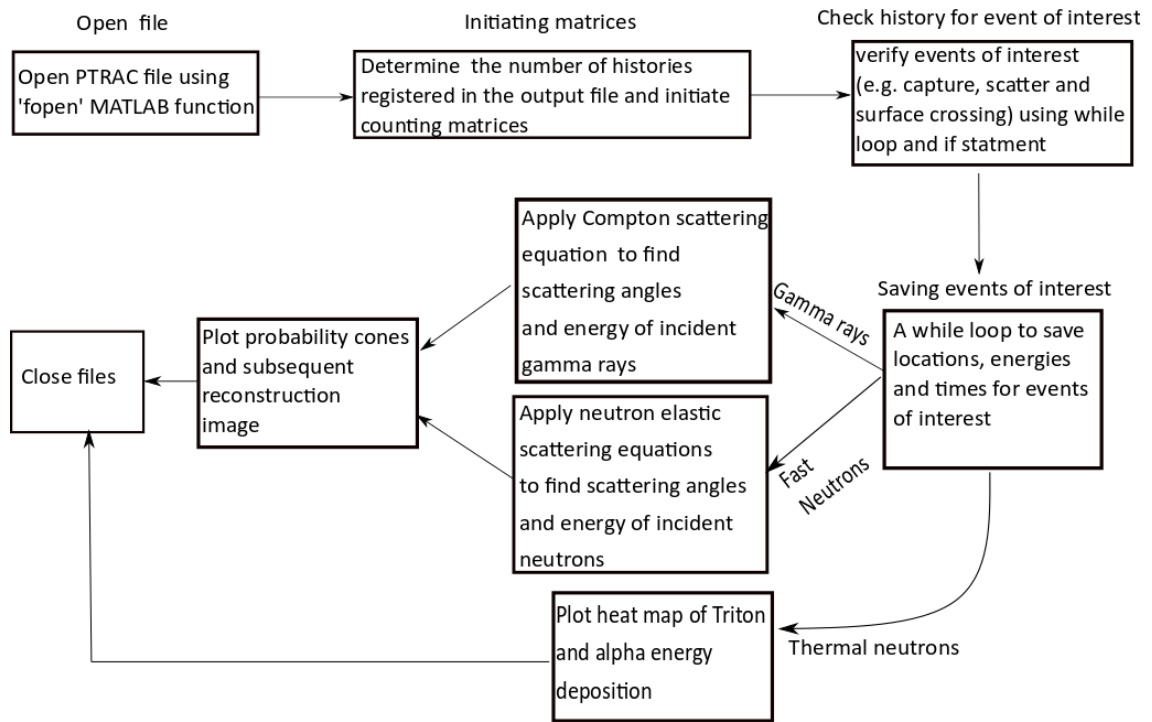
Figure 4.6: A flow diagram of the MATLAB® program used to analyse MCNP PTRAC file and to plot probability cones using the Monte Carlo simulation data.

4.3 Geant4

Geant4 is an object oriented simulation toolkit based on Monte Carlo method and is dedicated to study the transport of particles through matter. The version of Geant4 was constantly updated during the course of this project to ensure updated features and data tables were in use. As a Monte Carlo based method, Geant4 utilises statistical sampling with random numbers to solve the Boltzmann transport equation. Similar to MCNP method, Geant4 tracks the journey of the particle through the system. In addition, Geant4 transports the particle through the system based on the interaction probabilities with the materials in the system. A particle could lose energy, be absorbed or be captured in an interaction or terminated if it reaches the end of the world as it is conventionally known in the Geant4 environment [26,27]. Some of the fundamental

terminologies in Geant4 environment are a run, an event, a track and a step. A run sets the beam of particles on and generates events in the system. The parameters set in a run cannot be changed until the run is over. An event is a primary particle in the system that consists of a collection of tracks. A track describes the transportation of a particle within the system. A track consists of many steps. A step is the smallest unit used in describing the transportation of particles in Geant4. It consists of two points, a starting point and an end point, as well as energy and time of flight information [26,27].

The simulation process in Geant4 includes the geometry of the system, the materials of the system's components, the process of generating particles, the tracking of the generated particles and the physics process managing the interaction mechanisms of the particles in the system. The toolkit features built-in routines and classes that manages the tasks in the simulation. This include classes to manage the problem setup, the run of the simulation, the transportation of the particles and the tracking of the particles through the system. In addition, visualisation classes allow visual tracking of particles in the system. Some of the mandatory classes in Geant4 include detectors construction, physics lists and primary generator actions. Optional classes are essential features for a successful Geant4 code. In general, classes in the Geant4 toolkit are designed to be reusable by the user. The end user can modify, add and extend the classes to be application specific. A collection of physics models are available in the Geant4 toolkit allowing application specific design of simulation codes. The first level in understanding the physics models is to understand the different physics process categories. These processes cover a wide range of energies for electrons, photons, hadrons, muons and ions from 0.25 keV to several PeV. The interaction processes involved in the tracking of particles are electromagnetic, hadronic, transportation,

decay, optical, photo-lepton, hadron, and parameterisation processes. There are three main physics process categories; hadronic processes, standard electromagnetic processes for particles with energies above 1 keV and electromagnetic processes for lower energy particles. Physics processes combine data libraries and models to cover wide ranges of simulation applications. Depending on the type of the particles and the target energy range, physics models can be selected from a single physics process or a combination of physics processes [26-28].

A practical feature in Geant4 is multi-threading. Multithreaded applications share and combine data and information between threads while working independently. This allows a fast and an efficient execution of models. Geant4 follows general Monte Carlo methods in handling uncertainty analysis as described in section 4.2.2.

4.3.1 Geant4 implementation

Within this work, Geant4 was utilised in parallel with MCNP6 in investigating candidate detection materials, a task that Geant4 is greatly advertised for [26, 27]. All simulations were executed via VMware workstation 14 PRO[TM] [29]. Geant4-10.4.2 version virtual machine G4-10.04.p02 [6, 30] was installed and operated in the VMware workstation. Within the Geant4 environments, the following examples were utilised to build and create the application specific Geant4 code: Extended Electromagnetic TestEm14 and extended Hadr04. The Extended electromagnetic example utilises Standard Electromagnetic processes for studying gamma-ray photons transportation (at different energies varying from 1 keV to 10 MeV) in the detection materials under study. An additional desirable feature within this example is the restriction of scattering events to a single scatter. This allows exclusive studying of the material's ability to induce a single scatter photon event with no multiplications. The Extended Hadr04

example utilises class NeutronHPphysics with physical processes including neutronElastic, thermalScattering, neutronInelastic, nCapture and nFission. These processes are necessary for investigating fast neutron energies ranging from 1 keV to 10 MeV as well as thermal neutrons. During simulations, data tables used for Compton scattering interaction were the Lambda table from 100 eV to 1 MeV and the LambdaPrime table from 1 MeV to 10 TeV. Data tables utilised for photoelectric interaction in the simulations were the LambdaPrime table from 200 keV to 10 TeV. Modification and changes to DetectorConstruction.cc in both examples were necessary to create the geometry of interest (see appendix A.2 for Geant4 Detector class of Cs_2LiYCl_6:Ce detection material example). In addition, changes to TestEM14.in and hadr04.in were made to modify source specifications, varying source energy, and to set the level of verbose for step information on primary particles and secondary particles (see appendix A.2 for the macro files). A dedicated MATLAB® program was used to extract the desired information form Geant4 output files. The full program is given in appendix A.3.3. The results of this investigation was compared to the results from the MCNP6 simulations. The overall investigation and results are the subject of chapter 5.

In addition, the Geant4 toolkit was utilised in investigating the feasibility of the proposed design in detecting and localising gamma-ray photons. The simulation code was based on the OpNovice example from the Geant4 virtual machine and the modifications were made to DetectorConstruction.cc and OpNovice.in files. A modified version of the DetectorConstruction.cc is given in appendix A.2.3. The physics list utilised in this investigation included G4OpticalPhoton to define the particles in the simulations and G4Cerenkov, G4Scintillation, G4OpAbsorption, G4OpRayleigh and G4OpBoundaryProcess for defining the physical processes. Within simulations, the

data tables used for Compton scattering interactions were the Lambda table from 100 eV to 1 MeV and the LambdaPrime table from 1 MeV to 10 TeV. Data tables for the photoelectric interaction simulations were the LambdaPrime table from 200 keV to 10 TeV. In the OpNovice.in macro file, the modifications were made to the source description (see appendix A.2.4 for an example). A dedicated MATLAB® program is used to obtain the desired information from the Geant4 output files with a similar program hierarchy to the one shown in Figure 4.6. The full MATLAB® program is given in appendix A.3.4. Details on the results of this investigation are the subject of chapters 6.

4.4 References

1.   Stacy, W.M., *Nuclear reactor physics*. Second ed. 2007, Fedral Republic of Germany: Wiley-VCH Verlag and Co.

2.   *Monte Carlo Methods, Codes, & Applications Group*. [cited 2019 16/09/2019]; Available from: https://mcnp.lanl.gov/.

3.   Agostinelli, S., et al., *Geant4—a simulation toolkit.* Nuclear Instruments and Methods in Physics Research Section A: Accelerators, Spectrometers, Detectors and Associated Equipment, 2003. **506**(3): p. 250-303.

4.   Allison, J., et al., *Geant4 developments and applications.* IEEE Transactions on Nuclear Science, 2006. **53**(1): p. 270-278.

5.   Allison, J., et al., *Recent developments in Geant4.* Nuclear Instruments and Methods in Physics Research Section A: Accelerators, Spectrometers, Detectors and Associated Equipment, 2016. **835**: p. 186-225.

6.   INCERTI, S., et al., *THE GEANT4-DNA PROJECT.* International Journal of Modeling, Simulation, and Scientific Computing, 2010. **01**(02): p. 157-178.

7.   Baró, J., et al., *PENELOPE: An algorithm for Monte Carlo simulation of the penetration and energy loss of electrons and positrons in matter.* Nuclear Inst. and Methods in Physics Research, B, 1995. **100**(1): p. 31-46.

8.   Sato, T., et al., *Particle and heavy ion transport code system, PHITS, version 2.52.* Journal of Nuclear Science and Technology, 2013. **50**(9): p. 913-923.

9.   Goorley, J.T.J., Michael R.; Booth, Thomas E.; Brown, Forrest, et al., *Initial MCNP6 Release Overview - MCNP6 version 1.0*. 2012.

10.   Chadwick, M.B., et al., *ENDF/B-VII.1 Nuclear Data for Science and Technology: Cross Sections, Covariances, Fission Product Yields and Decay Data.* Nuclear Data Sheets, 2011. **112**(12): p. 2887-2996.

11.   Group, C.S.E.W. *Evaluated Nuclear Data File (ENDF)*. 2011 23rd February 2016   [cited   2016   23rd   February];   Available   from: http://www.nndc.bnl.gov/csewg/.

12.   *100XS Neutron Cross Section Library*. 1995 [cited 2019 16/09/2019]; Available from: https://www-xdiv.lanl.gov/projects/data/nuclear/mcnpdata/pdfs/la-ur-96-24.pdf.

13.   *ACE Libraries for Monte Carlo Transport Codes*. [cited 2019 16/09/2019]; Available   from: https://www-xdiv.lanl.gov/projects/data/nuclear/mcnpdata.html.

14.   *MCNP6^{TM} User's Manual*. Los Alamos National Laboratory

15.   *MCNP^{TM}–A General Monte Carlo N–Particle Transport Code*, J.F. Briesmeister, Editor. 2000: Los Alamos National Laboratory.

16.   *MCNP5*.   [cited   2019   18/09/2019];   Available   from: https://mcnp.lanl.gov/mcnp5.shtml.

17.   *MCNPX^{TM} User's Manual Version 2.7.0*, D.B. Pelowitz, Editor. April, 2011, Los Alamos National Laboratory

18. Technology, E. 18/02/2016]; Available from: EJ-309 URL 〈 http://www.eljentechnology.com/index.php/products/liquid-scintillators/73-ej-309〉 .

19. *9821B series data sheet*. [cited 2019 20/09/2019]; Available from: http://et-enterprises.com/images/data_sheets/9821B.pdf.

20. *The Mixed Field Analyser Suite*. [cited 2016 11/04/2016]; Available from: https://hybridinstruments.com/products/index.html.

21. Green, L., *TRANSMISSION MEASUREMENT OF CF-252 FISSION NEUTRON SPECTRUM.* Nuclear Science and Engineering, 1969. **37**(2): p. 232-242.

22. Mutone, G.A. and W. Meyer, *Neutron spectra estimation from proton recoil data.* Nuclear Instruments and Methods, 1973. **106**(3): p. 445-452.

23. Chyzh, A., et al., *Total prompt γ -ray emission in fission of U 235, Pu 239,241, and Cf 252.* Physical Review C - Nuclear Physics, 2014. **90**(1).

24. *6-lithium glass bespoke to your application*. [cited 2018; Available from: https://scintacor.com/products/6-lithium-glass/.

25. *CLYC scintillators*. [cited 2019 20/09/2019]; Available from: https://www.dynasil.com/product-category/scintillators/clyc-gamma-neutron-scintillators/.

26. Agostinelli, S., et al., *GEANT4-a simulation toolkit.* Nuclear Instruments & Methods in Physics Research Section a-Accelerators Spectrometers Detectors and Associated Equipment, 2003. **506**(3): p. 250-303.

27. Allison, J., et al., *Recent developments in GEANT4.* Nuclear Instruments & Methods in Physics Research Section a-Accelerators Spectrometers Detectors and Associated Equipment, 2016. **835**: p. 186-225.

28. Truscott, P., et al., *Geant4 - A new Monte Carlo toolkit for simulating space radiation shielding and effects*. 2000 Ieee Radiation Effects Data Workshop - Workshop Record. 2000. 147-152.

29.   *Workstation   Pro*.   [cited   2019   19/09/2019];   Available   from: https://www.vmware.com/products/workstation-pro.html.

30.   *Geant4   virtual   machine*.   [cited   2019   19/09/2019];   Available   from: http://geant4.in2p3.fr/spip.php?rubrique8&lang=en.

5 Material optimisation in dual particle detectors by comparing advanced scintillating materials using two Monte Carlo codes

H. Al Hamrashdi., D. Cheneler, and S.D. Monk

5.1 Abstract

A new generation of scintillating materials have been recently developed in the radiation-imaging field offering very promising dual particle detection abilities. Here, four different scintillating materials Cs_2LiYCl_6:Ce (CLYC), 95% Li-6 enriched Cs_2LiYCl_6:Ce (CLYC-6), natural Li-glass scintillator (GS10) and liquid scintillator EJ-309) have been characterised for their abilities to attenuate thermal neutrons, fast neutrons and gamma rays. Recent studies regarding these materials overlook these fundamental characteristics, which can directly affect the design process of advanced imaging systems such as Compton cameras and dual particle imaging systems. The response of each featured material to these three types of radiation fields was simulated with two different Monte Carlo codes, MCNP6 and Geant4. The results indicated that among these four materials, natural Li-glass scintillator (GS10) has the highest thermal neutron detection efficiency and the highest elastic scattering efficiencies. However, the attenuation of fast neutrons was found to be the most severe in EJ-309 liquid scintillator. When gamma rays are considered, it was found that the mass attenuation coefficient of CLYC and CLYC-6 is the highest of the four materials considered when energies lower than 1 MeV are incident. It is intended that this work will lead to the design and the build of an advanced prototype three stage Compton Camera which will be sensitive to both neutrons and gamma rays.

5.2 Introduction

Accurate localisation and characterisation of radiation sources is essential in many fields including border security, nuclear security, counter-terrorism, medical imaging as well as within nuclear site decommissioning. There are a number of materials and

detectors used in localizing and characterizing radiation sources that emit single mode radiation fields [1-3]. However, the real challenge in radiation detection research field is the development of an optimal detecting material that is capable of detecting both highly penetrating neutrons and gamma rays.

In the last two decades, the search for high performance scintillators has led to the discovery of new scintillating materials [3, 4], some of which are sensitive to both neutrons and gamma rays. Examples are Elpasolite scintillators [5-10], lithium based glass scintillators [11-16], some classes of liquid scintillators [11, 17-19] and plastic scintillators [20, 21]. An interesting example from the Elpasolite family is the Cs_2LiYCl_6:Ce (CLYC) scintillator, considered to be one of the most promising inorganic scintillators with an excellent energy resolution of less than 5% at 662 keV [4, 22]. The light yield photons of CLYC (with a Ce dopant concentration of 0.1%) is estimated to be 20,000 photons/MeV for gamma rays and 70,000 photons/n for thermal neutrons. In addition, the crystal is sensitive to both thermal and fast neutrons [4, 23, 24]. Enriching the crystal with the Li-6 isotope can tune the sensitivity of the detector towards thermal neutrons. 95% Li-6 enriched CLYC is commonly known as CLYC-6 [6, 25]. Within CLYC, thermal neutron detection is mainly due to $^6Li(n, \alpha)T$ interactions (thermal neutron $\sigma_{capture}\sim$940 barns, Q~4.8 MeV, negligible gamma emission). Fast neutrons mainly interact through elastic and inelastic scattering although capture reactions are possible as well via the $^{35}Cl(n,p)^{35}S$ and $^{35}Cl(n,\alpha)^{35}P$ reactions. Interaction of gamma rays in CLYC crystals results in a unique Core to Valence Luminescence (CVL) with a short decay time (~1 ns). This unique CVL is used to distinguish gamma rays from neutrons [4].

Lithium based glass (Li-6 glass) scintillators are another interesting example of dual particle scintillators. The light yield is estimated to be ~6,000 photons/n for neutrons and ~4,000 photons/MeV for gamma rays [3], with a decay time estimated to be around 75 ns for a Ce doped glass scintillator. Enriching the scintillating material with Li-6 can tune up the sensitivity towards thermal neutrons. Examples of Li-glass scintillators are Saint-Gobain developed Li-glass scintillators with 6.6% total lithium content. In this work, natural Li-glass scintillator, known as GS10, will be used in the simulations. This glass scintillator also contains varying amounts of Ce_2O_3, SiO_2, MgO, Al_2O_3, and Li_2O [26]. As in CLYC, thermal neutrons are mainly detected through $^6Li(n, \alpha)T$ interactions. However, in lithium glass, fast neutrons are mainly detected through scattering interactions. Pulse Shape Discrimination (PSD) is frequently used with these materials to differentiate between neutrons and gamma rays [27-29].

Some classes of liquid and plastic scintillators can also be utilised as multi-modal gamma/neutron detectors. The mixture of scintillator and solvent in any detector mainly depends on the application of the imaging system. This family of scintillators is usually found in applications where fast neutrons spectroscopy is required. In general, liquid scintillators have higher tendency to resist radiation and mechanical damages in comparison with plastic scintillators [17, 18]. An example of such a liquid scintillator might be EJ-309 (Eljen Technologies) which offers superior pulse shape discrimination (PSD) compared to some other liquid and plastic scintillators [30] . It also overcomes many drawbacks in other existing liquid scintillators, such as high toxicity [30]. EJ-309 is characterized by a scintillation efficiency of ~12,300 photons/MeV and decay time of ~ 3.5 ns [31]. In general, the light yield of EJ-309 depends on the size of the detector [32, 33]. The detection of fast neutrons in EJ-309 is mainly due to elastic scattering events with hydrogen and carbon nuclei. In general, liquid scintillators, including

EJ-309, can efficiently detect neutrons and gamma rays. However, at low (< 0.1 MeV) energies, the abilities of this class of scintillators to discriminate neutrons and gamma rays falls dramatically [11].

The ultimate aim of this research is the design of a dual particle imaging system where the characterising and quantifying detection abilities of some selected scintillation materials as function of energy and distance are essential. Most of the current studies on dual particle imaging discuss properties closely related to the application of interest [2-4, 23, 34, 35]. A. Giaz, et al. [4] compares the performance of CLYC-6 and CLYC-7 (99% Li-7 enriched CLYC) using the Time of Flight (TOF) and energy spectrum of fast neutrons. Similarly, C. W. E. van Eijk [34] compares the light yield, density and Ce concentration in different inorganic scintillators. In addition, he compares the scintillation properties of some neutron sensitive scintillators. Other studies discuss the detection properties of the integrated imaging system as one unit. For example, Alexis Poitrasson-Rivière et al. [35] find the angular resolution experimentally and using MCNP of liquid scintillators based dual particle imaging system. Ayaz-Maierhafer et al. [36] study the angular resolution of a combined neutron gamma imaging system. To this end, this work presents a detailed study on the detection efficiency and interaction probabilities of thermal neutrons, fast neutrons and gamma rays in four different scintillators: CLYC, CLYC-6, natural Li-glass (GS10) and EJ-309 liquid scintillator. This is undertaken using two Monte Carlo codes, MCNP6.1.0 and Geant4.10.2. These four scintillators where selected because they inherit the best scintillating characteristics of their class of materials while acquiring the most efficient detection abilities. In addition, the study aims to aid the design process of advanced neutron and gamma imaging systems, such as Compton cameras and elastic scattering cameras, using any one of these four scintillators. In section 5.6, a brief description of

the detectors arrangement in the design is provided using the design parameters determined within this work.

5.3 Materials and methods

5.3.1 MCNP6.1.0 simulations

MCNP6.1.0 is a general-purpose Monte Carlo radiation-transport code used to track radiation particles over a wide range of energies. The code finds applications in radiation shielding, radiation protection, medical physics, nuclear criticality safety and many others related fields. The code was created by merging two already established codes, MCNP5 and MCNPX, adding new features and capabilities. The models used in MCNP6.1.0 apply all possible nuclear interaction process in simulating real life experiments. In general, the MCNP code uses continuous-energy nuclear and atomic data libraries. For neutrons, the Evaluated Nuclear Data Files (ENDF) system is primarily used along with some other nuclear data libraries. In this work, the most updated version of ENDF (ENDF/B-VII.0) was primarily used. The neutrons data table energy range in MCNP6.1.0 starts from 10^{-11} MeV to 20 MeV for all isotopes and up to 150 MeV for some of them [37]. The Evaluated Photon Data Library (EPDL) and the Activation Library (ACTL) compilations from Livermore data libraries are mainly used in the simulation of gamma photon transport. In this work, EPDL is the primary source of data and interaction cross section. Data tables energy range for gamma-ray starts from 1eV to a few GeV [37].

5.3.2 Geant4 simulations

Geant4.10.2 is a CERN created Monte Carlo based toolkit used to simulate the transition of particles through matter [38], and finds applications wherever particle interaction in matter is considered important. It covers a wide range of parameters including physics models, geometry and particle tracking. Its comprehensive physics models allow it to be used in complex applications in the fields of nuclear physics, particle physics, medical physics and radiation shielding design. This C++ based open-source software undergoes continuous development by its international developer team [39, 40]. The most recent development in 2016 added a wide range of comprehensive improvements to Geant4 toolkit. The main features of this new version of Geant4 is the improved particle tracking and scoring capabilities along with some improvements in geometry models which allow more powerful simulations of real experimental setups. Neutron modelling in the Geant4 toolkit is done through the hadronic model. The main neutrons process listed in the hadronic model are high precision elastic, high precision inelastic, high precision capture and high precision fission. The original model is based on nine data libraries including ENDF/B-VI, JENDL-3 and JEF2.2 [40]. New versions of Geant4 have been utilizing more recent data libraries such as ENDF/B-VII.0 and JENDL-4.0 [40].The energy range for neutron simulation is limited to the available data on these libraries (up to 20 MeV for all isotopes and up to 150 MeV for some isotopes). Gamma modelling in Geant4 is done through Electromagnetic (EM) physics modelling which includes HEP (High Energy Physics) models. The model is based on the Livermore evaluated library [40]. The Geant4 toolkit covers a wide range of gamma energy from 250 eV up to the TeV range. The last update on the Geant4 toolkit added new physics and processes to the existing gamma models. Major parts of these modifications add specialized models to two major gamma photon interactions, pair

production and Compton scattering. The modifications were intended improve the models accuracy. The results of the new models are compared to NIST values and are reported to be within a tolerance of 10% [40].

5.4 Means of comparison and calculations of interest

Thermal neutron detection is mainly facilitated through capture reactions. Here, the capture efficiency of thermal neutrons in the four scintillators is studied via simulating the passage of thermal neutrons through the scintillating materials as a function of thickness. The definition of absolute efficiency for a particular interaction is the ratio of the number of counts to the number of particles which originated from the source. A sphere of each of the four scintillators with a point source at the centre was simulated using both the MCNP6 and GEANT4 codes. In MCNP6.1.0, the F8 tally with special treatment card was used to find the capture efficiency in each component in the four scintillators. The F8 tally provides the user with energy distribution of pulses in the detector region. In Geant4 the simulation was undertaken by counting the number of capture reactions relative to the total number of events.

The study of the response of the materials to fast neutrons was mainly done through investigating elastic scattering interaction probabilities and escaping event probabilities. This was done at four different neutron energies, 1 keV, 10 keV, 0.1 MeV and 1 MeV. The reaction rate for a flux of neutrons, φ, incident through a thin layer of matter per unit volume can be described with the following relation [41]:

$$\frac{Reaction\ Rate}{volume} = \Sigma \cdot \varphi \qquad (5.1)$$

Where Σ is the macroscopic cross section (m^{-1}). Table 5.1 shows the total cross section and the elastic scattering cross section of CLYC, CLYC-6, natural Li-glass scintillator (GS10) and EJ-309 liquid scintillator based on ENDF/B-VII.0 data library [42].

Table 5.1: Total and elastic scattering macroscopic cross sections of CLYC, CLYC-6, natural Li-glass scintillator (GS10) and EJ-309 liquid scintillator.

Energy (MeV)	CLYC		CLYC-6		Li-glass (GS10)		EJ-309 liquid scintillator	
	Total (cm^{-1})	Elastic scattering (cm^{-1})	Total (cm^{-1})	Elastic scattering (cm^{-1})	Total (cm^{-1})	Elastic scattering (cm^{-1})	Total (cm^{-1})	Elastic scattering (cm^{-1})
0.001	10.2	9.94	12.6	11.27	23.14	22.13	131.74	111.04
0.01	8.81	8.08	10.2	9.85	17.22	7.11	104.91	104.91
0.1	7.5	7.22	8.83	8.69	15.94	8.87	69.68	69.68
1	13.95	12.84	15.01	14.92	27.98	6.74	23.22	23.22

In the work presented here, the response of the material to incident neutrons was studied as a function of thickness. The geometry used in this set of simulations was a cylinder with an infinite radius compared to its length (thickness here) with a point source placed on the face of the cylinder to maximize the entrance dose of fast neutrons into the cylinder. This geometry was chosen to minimize the effect of multiple scattering events. In the MCNP6.1.0 simulations, the PTRAC file option was used in the analysis as in the case of neutrons, the type of interaction taking place in the material needs to be identified; a process which cannot be done using typical tallies. The PTRAC file option allows the user to track the particle of interest through the material. A number of keywords can be added to the PTRAC card that can help identifying the types of interaction along the particles trajectory.

The response of each material to incident gamma rays was mainly studied through the mass attenuation coefficient. Gamma interaction in matter mainly depends on the

energy of the incident photon, the density of the material and the effective atomic number. Therefore, in gamma photon analysis, CLYC and CLYC-6 were treated as one material. The effective atomic number according to the power law method is [43, 44]:

$$Z_{eff} = \sqrt[2.94]{\sum f_i Z_i^{2.94}} \tag{5.2}$$

Where f_i and Z_i are the relative electron fraction and the atomic number of the ith element respectively. The mass attenuation coefficient, μ_m (cm^2/g), measures the probability of interaction in a given material. The analysis of the mass attenuation coefficient is based on the attenuation law of gamma rays [45]:

$$\mu_m = \mu/\rho = \ln (I/I_o) / x \tag{5.3}$$

Where μ is the linear attenuation coefficient and ρ is the density of the material. I is the attenuated gamma-ray at x and I_o is the incident gamma-ray. The mass attenuation coefficient for each material as a function of energy can easily be found within the Geant4 simulation package.

The probability of Compton scattering in each material is calculated as a function of energy as well. For most target materials, the relative probability of Compton scattering occurrence is more dominant in the energy region between 0.1 MeV and 10 MeV. The photoelectric effect is more likely to occur at energies lower than 0.1 MeV, whereas, pair production dominates at energies higher than 10 MeV [45]. Comparing the probability of Compton scattering occurrence in these scintillators is vital in choosing which material is best utilized in Compton scattering based imaging systems.

5.5 Results and discussion

5.5.1 Thermal neutrons

Thermal neutron interaction in the four organic scintillators was modelled using MCNP6.1.0 and Geant4.10.2. In the design process of scintillation based neutron detectors, thermal neutron absorption is the interaction process of major interest, and it is this factor that is compared here over the four scintillators. Figure 5.1 shows the thermal neutron intrinsic capture efficiency of thermal neutrons as function of thickness for CLYC, CLYC6, natural Li-glass and an EJ-309 liquid scintillator. The results indicate that intrinsic thermal neutron capturing efficiency increases steadily as a function of thickness before saturating for all four materials. Lithium-based scintillators, CLYC, CLYC-6 and Li-glass, require less than 5 cm of transport through the material in question to reach their maximum intrinsic efficiency.
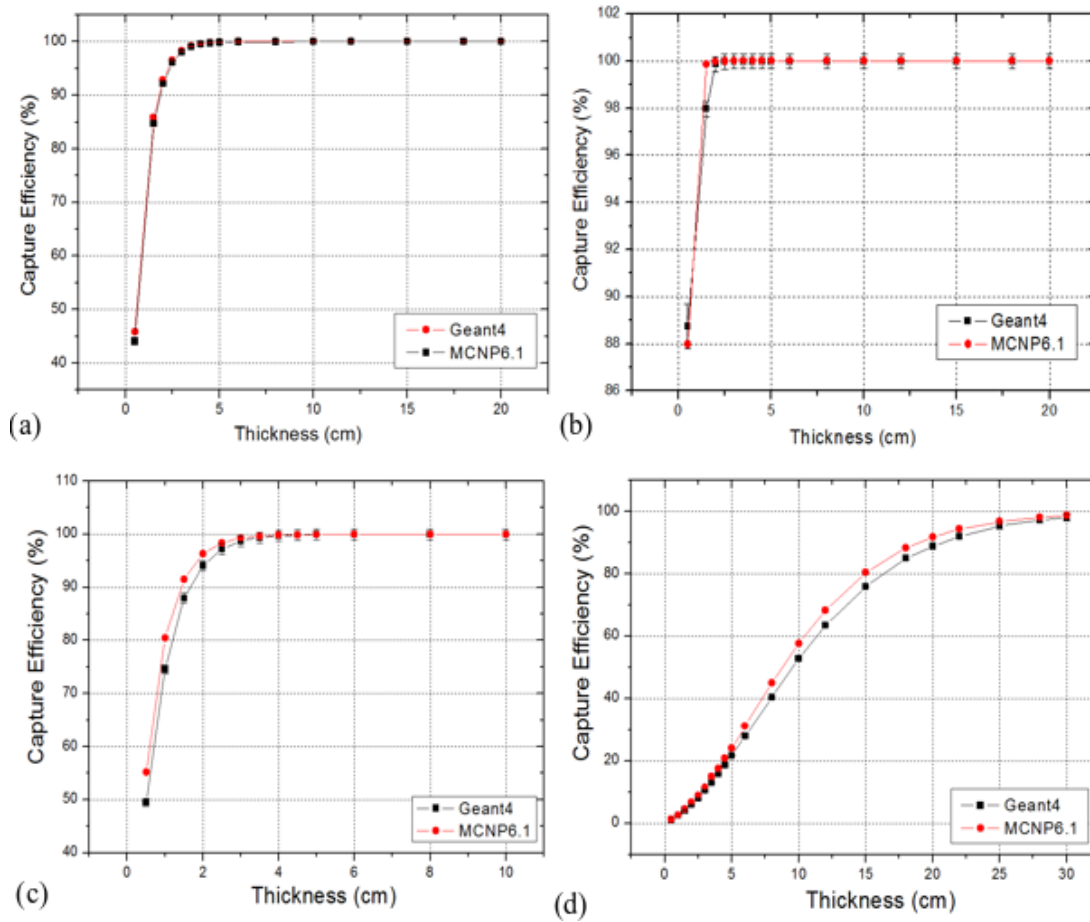
Figure 5.1: Thermal neutron capturing efficiency as function of thickness of (a) CLYC, (b) CLYC-6, (c) natural Li-glass (GS10) (d) EJ-309 liquid scintillator.

The maximum difference between MCNP6.1.0 and Geant4.10.2 simulations for the four scintillators is less than 5%. These differences are mainly due to differences in cross sections libraries used by MCNP6.1.0 and Geant4.10.2 [46-50]. Table 5.2 compares thermal neutron capture efficiency of the four scintillators at a thickness of 2 cm, 5 cm and 10 cm respectively.

Table 5.2: MCNP6.1.0 simulations of thermal neutron capture efficiency in CLYC, CLYC-6, natural Li-glass and EJ-309 liquid scintillator.

Thickness (cm)	CLYC Efficiency (%) (capture in Li-6)	CLYC-6 Efficiency (%) (capture in Li-6)	Natural Li-glass efficiency (%) (capture in Li-6)	Liquid scintillator efficiency (EJ-309) (%)
2	92.86 ± 0.03 (19.89 ± 0.04)	99.98 ± 0.01 (77.67 ± 0.04)	96.33 ± 0.01 (96.10 ± 0.05)	5.95 ± 0.08
5	99.90 ± 0.02 (21.40 ± 0.04)	100.01 ± 0.01 (77.68 ± 0.04)	99.92 ±0.01 (96.69 ± 0.01)	21.7 ± 0.5
10	100.00 ± 0.01 (21.42 ± 0.04)	100.00 ± 0.01 (77.68 ± 0.04)	99.95 ± 0.01 (99.71 ± 0.01)	52.8 ± 0.2

Table 5.3: Geant4.10.2 simulations of thermal neutron capture efficiency in CLYC, CLYC-6, natural Li-glass and EJ-309 liquid scintillator.

Thickness (cm)	CLYC Efficiency (%) (capture in ^{6}Li)	CLYC-6 Efficiency (%) (capture in ^{6}Li)	Natural Li-glass efficiency (%) (capture in ^{6}Li)	Liquid scintillator efficiency (EJ-309) (%)
2	92.1 ± 0.3 (23.2 ± 0.5)	99.9 ± 0.3 (79.7 ±0.3)	94 ±1 (93.9 ±0.3)	6.0 ± 0.3
5	99.8 ± 0.3 (25.5 ± 0.5)	100.0 ± 0.3 (79.8 ±0.3)	100 ± 1 (99.7 ± 0.3)	21.6 ± 0.5
10	100.0 ± 0.3 (25.5 ± 0.5)	100.0 ± 0.3 (79.8 ± 0.3)	100 ± 1 (99.7 ± 0.3)	52.8 ± 0.7

Table 5.2 and Table 5.3 illustrate that CLYC-6 has higher intrinsic capture efficiency of thermal neutrons compared to the other three scintillators followed by CLYC.

However, for detection purposes, Li-glass showed higher capture efficiency in Li-6. Compared to CLYC and CLYC-6, Li-glass has higher atomic density of Li-6 atoms, 1.81×10^{22} atoms/cm^3 compared to 1.58×10^{20} atoms/cm^3 in CLYC and 1.97×10^{21} atoms/cm^3 in CLYC-6.

5.5.2 Fast neutrons

Fast neutron interaction in the four scintillators was simulated at four different energies (1 keV, 10 keV, 0.1 MeV and 1 MeV). The results of elastic scattering efficiency, from single interaction events, as well as the escaping percentages as function of thickness are shown from Figure 5.2 to Figure 5.5. As above, MCNP6.1.0 simulations agree with Geant4.10.2 simulations with discrepancies of less than 5 %. A common trend in all graphs is the exponential decrease of the escaping probability as a function of thickness in all four materials. As energy increases, the probability of escape and elastic scattering slightly vary with thickness. That is mainly because the macroscopic cross section slightly varies over these energies. In general, in CLYC and CLYC-6 the elastic scattering cross section slightly decreases as function of energy. However, at each energy the probability of single elastic scattering slowly increases as function of thickness before starting to decrease again as other types of interaction occur.

Natural Li-glass scintillator exhibits higher attenuation for fast neutrons as compared to CLYC and CLYC-6. This is mainly due to the higher total cross section of Li-glass. The single scattering abilities of fast neutrons is the highest in Li-glass compared to the other three materials for similar reasons. The EJ-309 liquid scintillator exhibits the highest attenuating ability in fast neutrons as a function of thickness across the four specified energies. This is mainly due to the high scattering cross section of the

hydrogen atom, which causes multiple scattering events, which has the effect of slowing down neutrons while they travel through the scintillator. Single scattering probability and escaping probability slightly varies across the four energies. Unlike the CLYC, CLYC-6 and Li-glass based scintillators, the abilities of EJ-309 to cause single elastic scattering decreases exponentially with increasing thickness. This is because other attenuation mechanisms, such as multiple scattering, increase as the thickness of as thickness of the material increases.
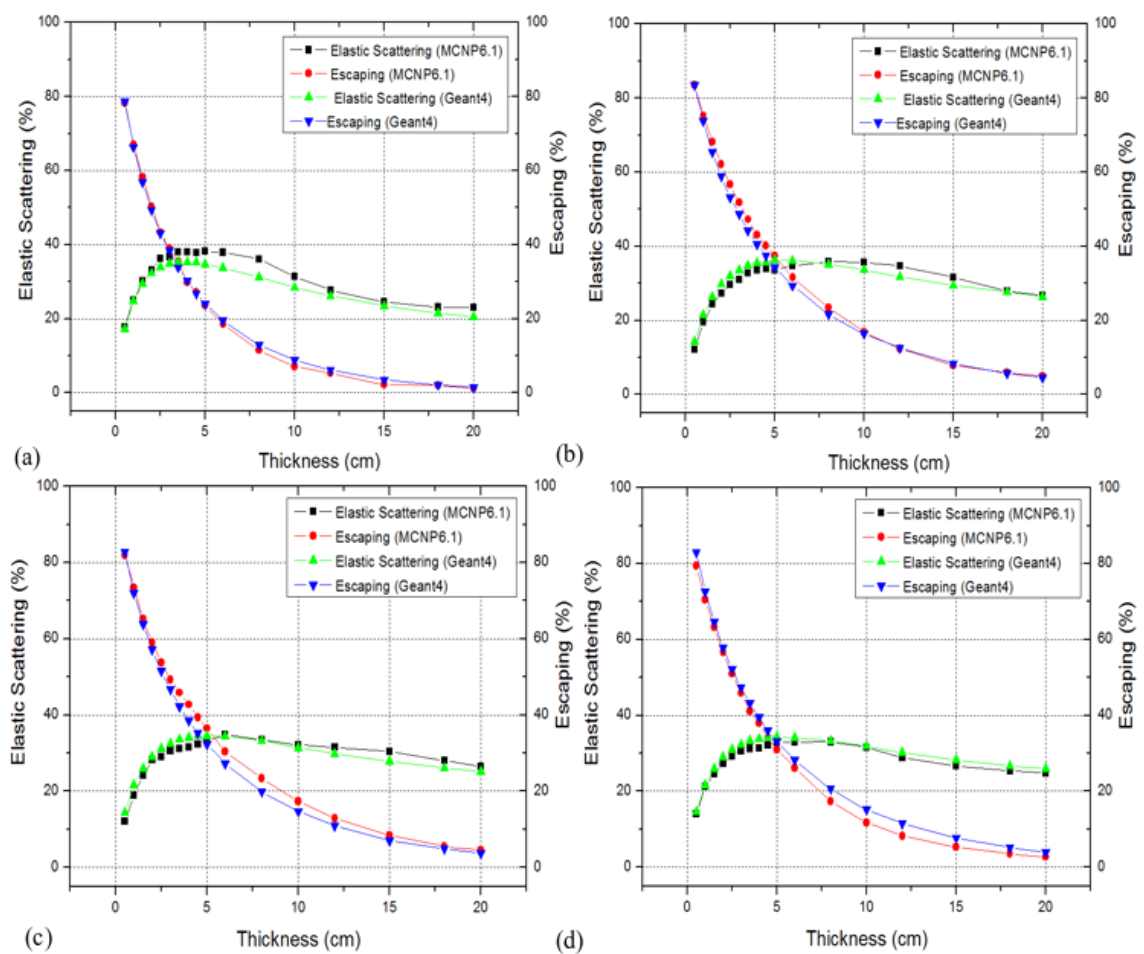
Figure 5.2: Elastic scattering probability and escaping probability in CLYC at (a) 1 MeV, (b) 0.1 MeV, (c) 10 keV and (d) 1 keV.
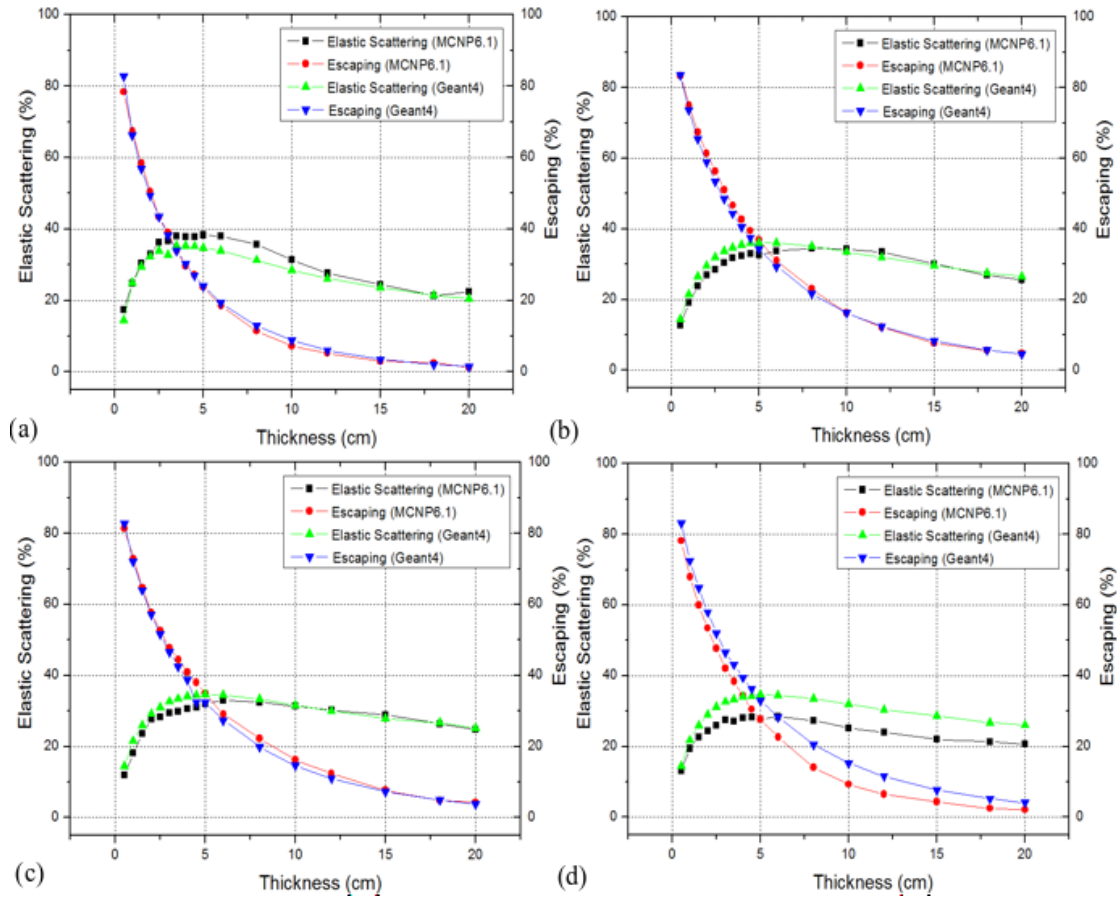
Figure 5.3: Elastic scattering probability and escaping probability in CLYC-6 at

(a) 1 MeV, (b) 0.1 MeV, (c) 10 keV and (d) 1 keV.
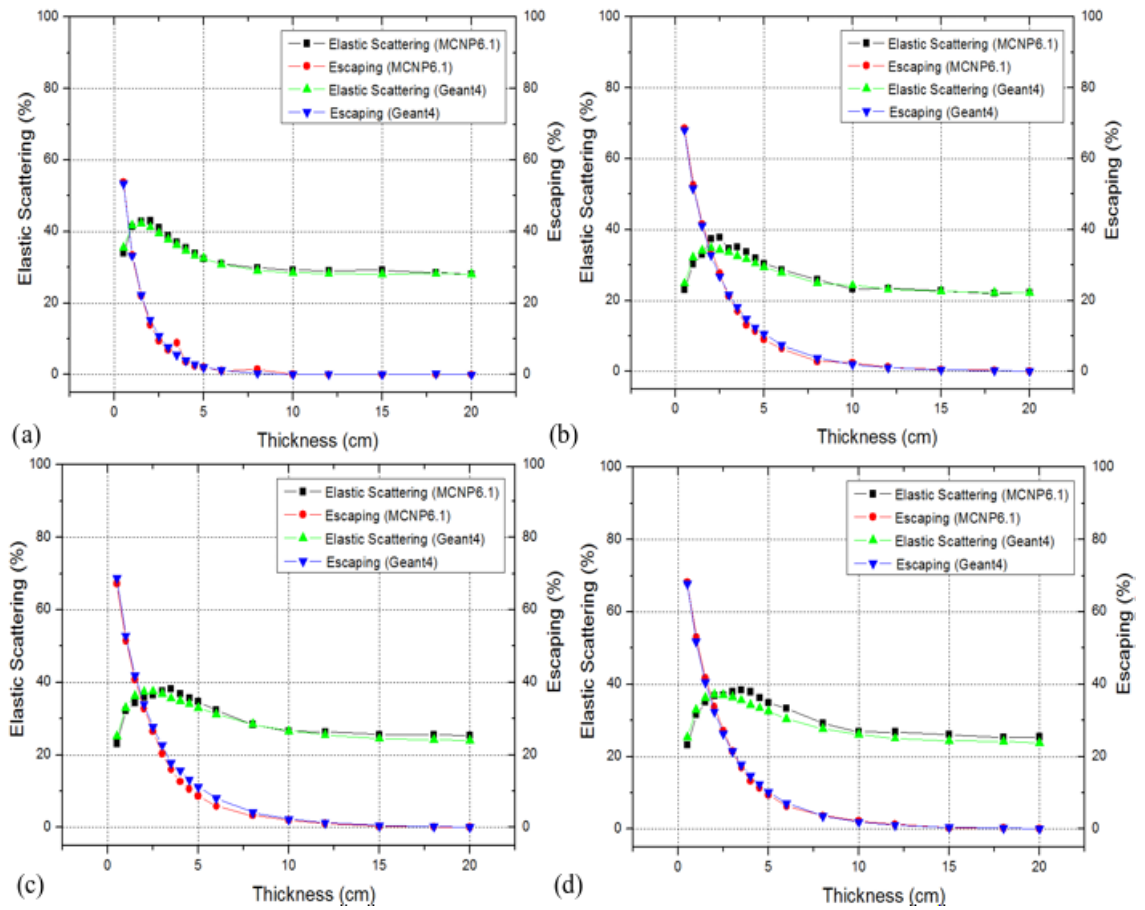
Figure 5.4: Elastic scattering probability and escaping probability in GS10 natural Li-glass (GS10) at (a) 1 MeV, (b) 0.1 MeV, (c) 10 keV and (d) 1 keV.
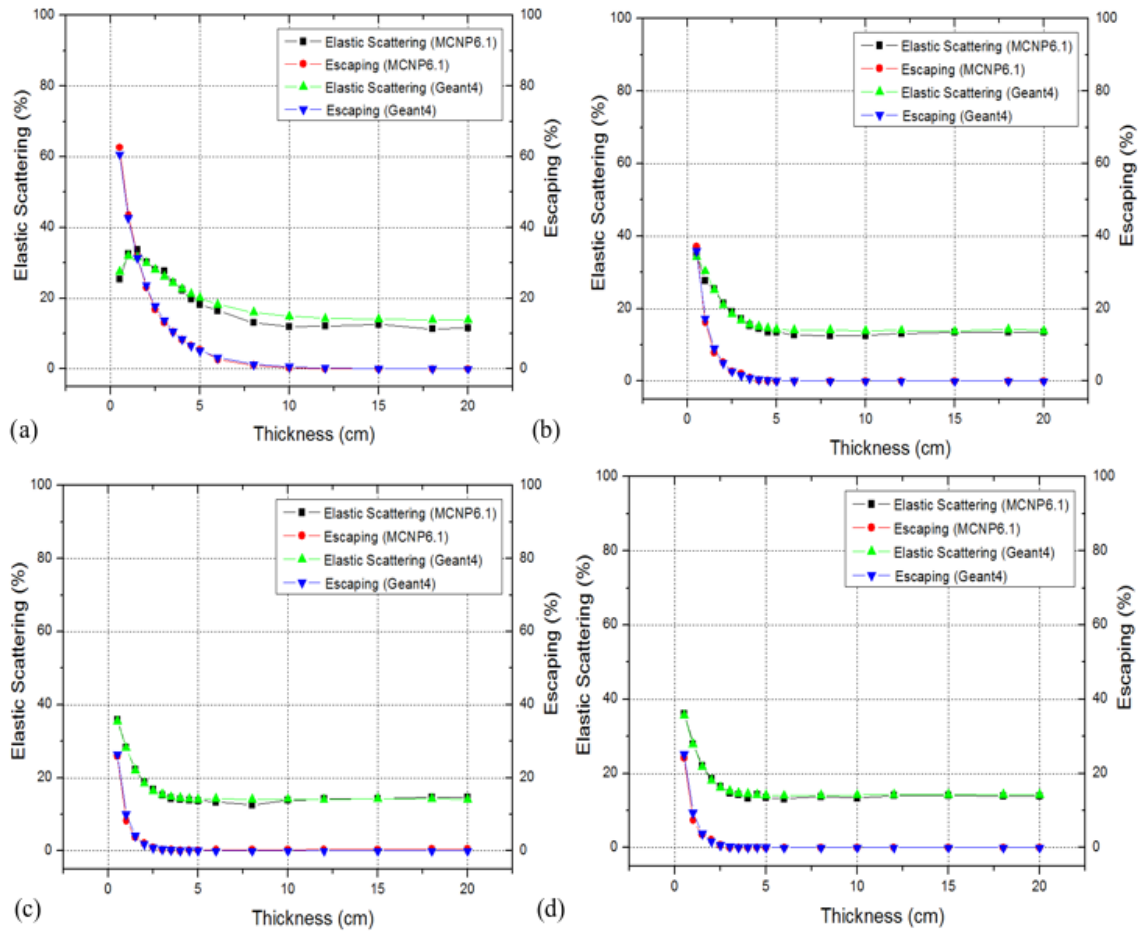
Figure 5.5: Elastic scattering probability and escaping probability in EJ-309 liquid scintillator at (a) 1 MeV, (b) 0.1 MeV, (c) 10 keV and (d) 1 keV.

Figure 5.6 compares single elastic scattering abilities over 2 cm considering four different neutron energies; 1 MeV, 0.1MeV, 10 keV and 1 keV. The figure splits elastic scattering events into backscattering efficiency and forward scattering efficiency. The natural Li-glass shows higher elastic scattering abilities in general, with higher backscattering efficiency compared to forward scattering across all four listed energies. CLYC and CLYC-6 show similar elastic scattering abilities with slightly higher forward scattering efficiency compared to backscattering efficiency. Finally, the EJ-309 liquid scintillator exhibits higher backscattering efficiency compared to forward scattering

efficiency except at 1 MeV. In general, the results of MCNP6.1.0 and Geant4.10.2 simulations agree with attenuation cross sections as reported in table 5.1.
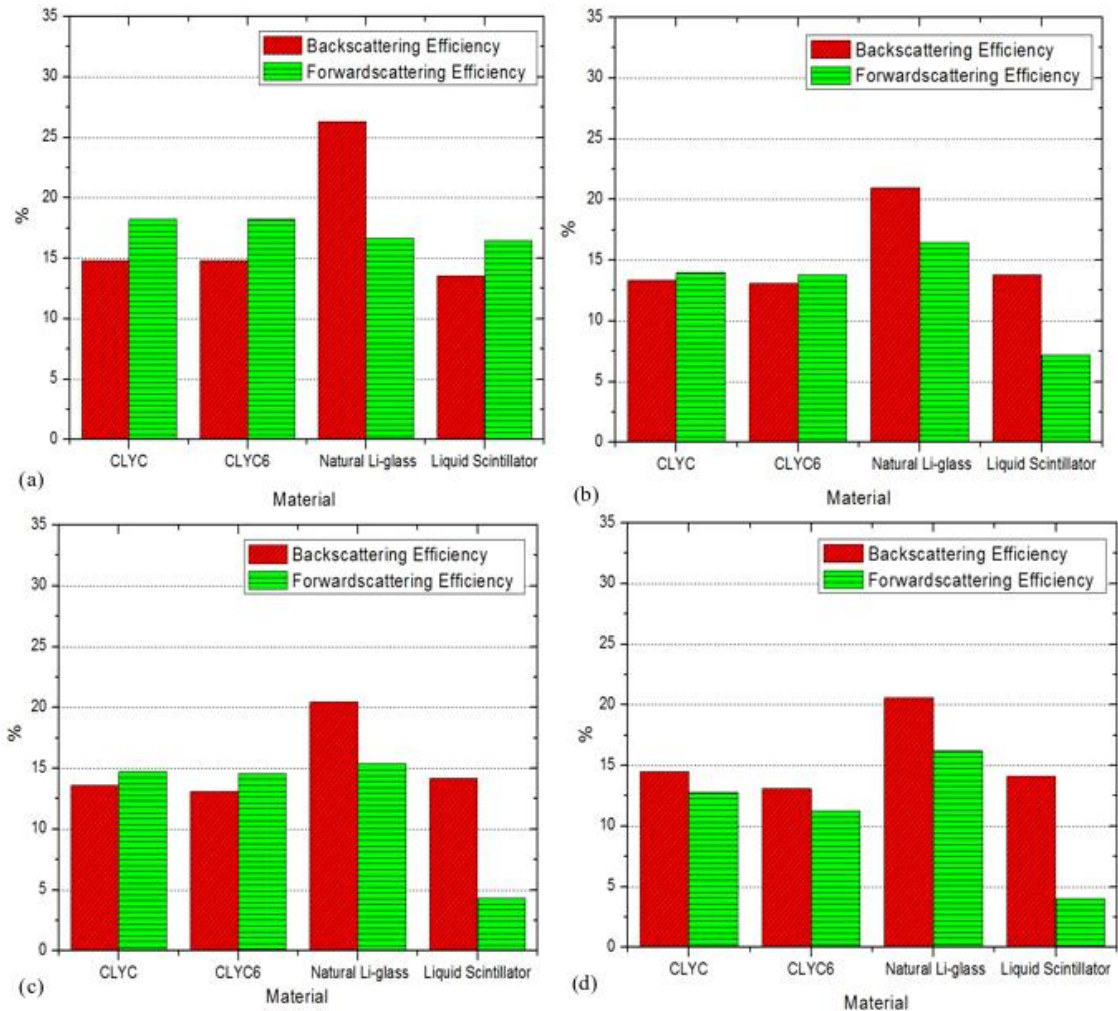
Figure 5.6: Comparison between backscattering efficiency and forward scattering efficiency of MCNP6.1.0 simulations at (a) 1 MeV, (b) 0.1 MeV, (C) 10 keV (d) 1 keV.

5.5.3   Gamma-ray

Using equation 5.3, the mass attenuation coefficient was calculated for each of the four materials. The total mass attenuation coefficients determined by the Geant4 simulations are shown in Figure 5.7. NIST values were extracted using XCOM version 3.1 [51].

Geant4 simulation results are in good agreement with the NIST values. A common feature in all three graphs is the decreasing total mass attenuation coefficient with increasing incident photon energy, which clearly indicated the dependency of the mass attenuation coefficient on energy. This is mainly due to the decrease in the interaction probability between the incident photon and the target material.
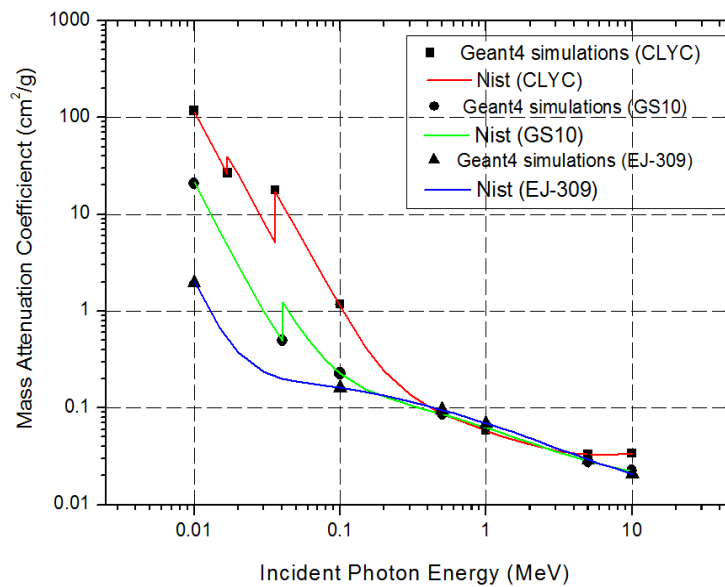
Figure 5.7: Mass attenuation coefficient as function of energy for CLYC, natural Li-glass (GS10) and EJ-309 liquid scintillator from Geant4 simulations and NIST values.

The attenuation abilities of the four listed materials are compared in Table 5.4. At energies lower than 0.1 MeV the total mass attenuation coefficient of CLYC and CLYC-6 crystals is higher compared to GS10 and EJ-309. At this energy range, photoelectric absorption is the most common interaction mechanism between gamma rays and matter. The higher density and the higher effective atomic number of CLYC/CLYC-6 causes a noticeable effect on its attenuation ability compared to the

other materials. At higher energies, the total mass attenuation coefficients of the three scintillators decreases as the probability of interaction decreases.

Table 5.4: Comparison of the total mass attenuation coefficient of CLYC/CLYC-6, natural Li-glass (GS10) and liquid scintillator estimated using Geant4.

Energy (MeV)	CLYC/CLYC-6 ($z_{eff} = 42.50$) ($\rho = 3.31$ g/cm^3)	Natural Li-glass ($z_{eff} = 11.81$) ($\rho = 2.5$ g/cm^3)	Liquid scintillator (EJ-309) ($z_{eff} = 7.62$) ($\rho = 0.964$ g/cm^3)
0.01	117.6 ± 0.8	21.04 ± 0.03	2.00 ± 0.01
0.1	1.179 ± 0.003	0.227 ± 0.0003	0.162 ± 0.001
1	0.0592 ± 0.0004	0.06240 ± 0.00005	0.06950 ± 0.00009
10	0.03414 ± 0.0004	0.02240 ± 0.00005	0.0207 ± 0.0001

The abilities of the scintillators to cause Compton scattering on gamma rays as a function of incident photon energy is shown in Figure 5.8. The thickness of the scintillators used in this set of simulations was fixed at 2.0 cm. Compton scattering probability rises dramatically in the energy region 0.1 MeV – 1 MeV, before starting to fall again. The decrease in Compton scattering probability with increasing incident gamma-ray (> 1 MeV) is likely due to the decrease in the overall interaction probability.
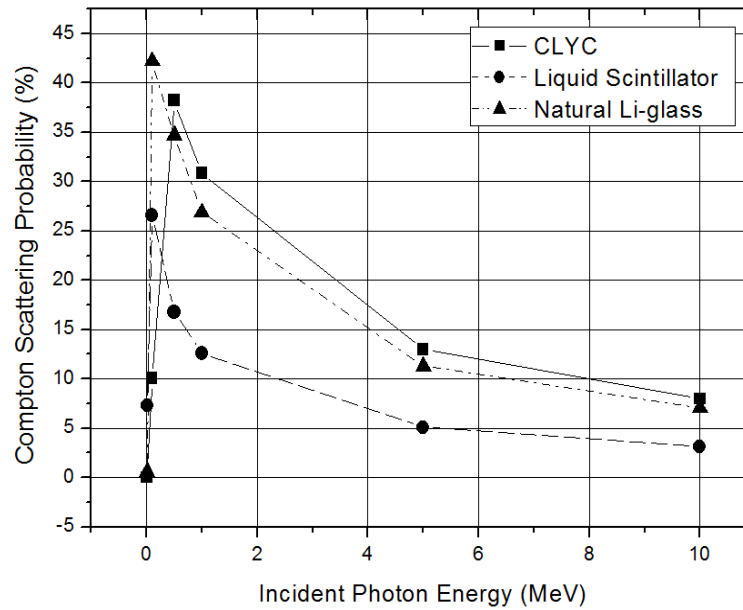
Figure 5.8: Comparison of Compton scattering probability as function of energy between CLYC, GS10 natural Li-glass (GS10) and EJ-309 liquid scintillator.

5.6 Designing a dual particle imaging system

The results of the simulations in this work have been utilised in the designing process of a multi-layered neutron/gamma imaging system. The simulations were used to find the scintillator material, which exhibited optimum detection and attenuation capabilities for thermal neutrons, fast neutrons and gamma rays. Moreover, the results were used to determine the optimum thickness of each layer in the design. Natural Li-glass (GS10) was found to be the optimum detector material for the design. The dimensions of the Li-glass (GS10) are the optimal design parameters derived from the data presented in Figure 5.1 and Figure 5.4. From the results, 10 mm thickness of Li-glass can capture up to 80% thermal neutrons while transmitting 92% of high-energy gamma rays. A 20 mm thick layer of a plastic scintillator (EJ-204) was added to the system to solely detect scattered fast neutrons, while having minimum influence on gamma –rays. The

thickness of the second layer was selected to be 15 mm. This layer will serve as a second interaction plane of fast neutrons and a scattering plane of transmitted gamma rays. A monolithic layer of a scintillator material, such as caesium iodide is added to the system to detect scattered gamma rays. SiPM arrays will be used to detect resultant photons. The arrangement of the detectors and an early estimated configuration of the system is shown in Figure 5.9.
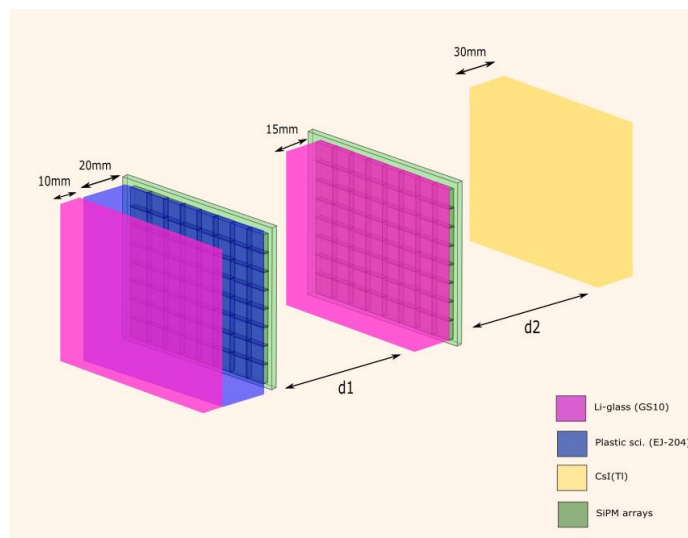
Figure 5.9: Configuration and dimensions of detectors in the novel design of a neutron/gamma imaging system.

MCNP6.1.0 and Geant4 simulations showed that for this particular configuration, the system can detect up to 80% of thermal neutrons and up to 50% of gamma photons. Further investigations and experimental work are in progress.

5.7 Conclusion

In this work CLYC, CLYC-6, natural Li-glass and EJ-309 scintillators were characterized by studying thermal neutron capture efficiency, fast neutron single elastic scattering abilities and gamma-ray attenuating abilities using two simulation toolkits,

MCNP6.1.0 and Geant4.10.2. CLYC-6, and to a slightly lesser extent CLYC, showed impressive capturing efficiency of thermal neutrons with a maximum of 100 %. For thermal neutron detection efficiency, however, Li-glass scintillator exhibited the highest efficiency compared to the other three scintillators due to its higher atomic density of Li-6. The maximum capture efficiency of natural Li-glass was found to be around 99.95 %. EJ-309 liquid scintillator showed the lowest attenuation abilities at thicknesses lower than 5 cm with around 21.6 %. The Li-glass scintillator had the highest attenuation abilities of neutrons at 1 keV although EJ-309 showed higher attenuation abilities at higher energies (>10 keV). The probability of single scattering events for natural Li-glass is the highest of the three scintillators. CLYC and CLYC-6 showed the highest attenuation abilities of gamma-ray at energies lower than 1 MeV mainly due to its high effective atomic number. At higher energies, the attenuation abilities of the four materials slightly varies when compared to one another. Natural Li-glass scintillators and both elpasolite scintillators demonstrate good Compton scattering efficiency of gamma rays with natural Li-glass acquiring slightly higher scattering efficiencies at energies lower than 1 MeV. The results achieved were used in designing a basic neutron/gamma imaging system, which will be built and tested in work to follow on.

5.8 References

1. Katagiri, M., et al., *Scintillation materials for neutron imaging detectors.* Nuclear Instruments & Methods in Physics Research Section a-Accelerators Spectrometers Detectors and Associated Equipment, 2004. **529**(1-3): p. 274-279.

2. Weber, M.J., *Inorganic scintillators: today and tomorrow.* Journal of Luminescence, 2002. **100**(1-4): p. 35-45.

3.   van Eijk, C.W.E., *Inorganic Scintillators for Thermal Neutron Detection.* Ieee Transactions on Nuclear Science, 2012. **59**(5): p. 2242-2247.

4.   Giaz, A., et al., *The CLYC-6 and CLYC-7 response to gamma-rays, fast and thermal neutrons.* Nuclear Instruments & Methods in Physics Research Section a-Accelerators Spectrometers Detectors and Associated Equipment, 2016. **810**: p. 132-139.

5.   Yang, P., et al., *The Synthesis and Structures of Elpasolite Halide Scintillators*, in *Nuclear Radiation Detection Materials-2009*, M. Fiederle, et al., Editors. 2010. p. 185-192.

6.   Glodo, J., et al., *Selected Properties of Cs$_2$LiYCl$_6$, Cs$_2$LiLaCl$_6$, and Cs2LiLaYBr6 Scintillators.* Ieee Transactions on Nuclear Science, 2011. **58**(1): p. 333-338.

7.   Tanner, P.A., et al., *Absorption and emission spectra of Ce3+ in elpasolite lattices.* Journal of the American Chemical Society, 2003. **125**(43): p. 13225-13233.

8.   Gundiah, G., et al., *Structure and scintillation properties of Ce3+ -activated Cs$_2$NaLaCl$_6$, Cs$_3$LaCl$_6$, Cs$_2$NaLaBr$_6$, Cs$_3$LaBr$_6$, Cs$_2$NaLaI$_6$ and Cs$_3$LaI$_6$.* Journal of Luminescence, 2014. **149**: p. 374-384.

9.   Samulon, E.C., et al., *Luminescence and scintillation properties of Ce3+-activated Cs$_2$NaGdCl$_6$, Cs$_3$GdCl$_6$, Cs$_2$NaGdBr$_6$ and Cs$_3$GdBr$_6$.* Journal of Luminescence, 2014. **153**: p. 64-72.

10.   Kim, H.J., et al., *Tl2LiYCl6 (Ce3+): New Tl-based Elpasolite Scintillation Material.* Ieee Transactions on Nuclear Science, 2016. **63**(2): p. 439-442.

11.   Nattress, J., et al., *Capture-gated Spectroscopic Measurements of Monoenergetic Neutrons with a Composite Scintillation Detector.* Ieee Transactions on Nuclear Science, 2016. **63**(2): p. 1227-1235.

12.   Wang, C.L. and R.A. Riedel, *Improved neutron-gamma discrimination for a Li-6-glass neutron detector using digital signal analysis methods.* Review of Scientific Instruments, 2016. **87**(1).

13. CHEN Yan-Ping, L.D.-L., *Development of Containing ⁶Li Glass Scintillators for Neutron Detection.* Journal of Inorganic Materials, 2012. **27**(11): p. 1121-1128.

14. Lee, H.Y., et al., *Li-glass detector response study with a Cf-252 source for low-energy prompt fission neutrons.* Nuclear Instruments & Methods in Physics Research Section a-Accelerators Spectrometers Detectors and Associated Equipment, 2013. **703**: p. 213-219.

15. Arikawa, Y., et al., *Multichannel down-scattered neutron detector for areal density measurement*, in *Ifsa 2011 - Seventh International Conference on Inertial Fusion Sciences and Applications*, P. Mora, K.A. Tanaka, and E. Moses, Editors. 2013.

16. Lampoudis, C., et al., *Neutron transmission and capture cross section measurements for Am-241 at the GELINA facility.* European Physical Journal Plus, 2013. **128**(8).

17. Polack, J.K., et al., *Dual-Particle Imager for Standoff Detection of Special Nuclear Material*, in *2011 Ieee Nuclear Science Symposium and Medical Imaging Conference*. 2011. p. 1494-1500.

18. Poitrasson-Riviere, A., et al., *Dual-particle imaging system based on simultaneous detection of photon and neutron collision events.* Nuclear Instruments & Methods in Physics Research Section a-Accelerators Spectrometers Detectors and Associated Equipment, 2014. **760**: p. 40-45.

19. Klix, A., et al., *Fast neutron and gamma-ray spectra measurements with a NE-213 spectrometer in the FNG Copper Benchmark Experiment.* Fusion Engineering and Design, 2016. **109**: p. 309-314.

20. Blanc, P., et al., *Neutron/gamma pulse shape discrimination in plastic scintillators: Preparation and characterization of various compositions.* Nuclear Instruments & Methods in Physics Research Section a-Accelerators Spectrometers Detectors and Associated Equipment, 2014. **750**: p. 1-11.

21. Bertrand, G.H.V., et al., *Pulse shape discrimination between (fast or thermal) neutrons and gamma rays with plastic scintillators: State of the art.* Nuclear

Instruments & Methods in Physics Research Section a-Accelerators Spectrometers Detectors and Associated Equipment, 2015. **776**: p. 114-128.

22.   Pellegri, L., et al., *Performances of a 1 " x1 " Cs₂LiYCl₆ scintillator detector.* 2013 Ieee Nuclear Science Symposium and Medical Imaging Conference (Nss/Mic), 2013.

23.   Giaz, A., et al., *Fast neutron measurements with Li-7 and Li-6 enriched CLYC scintillators.* Nuclear Instruments & Methods in Physics Research Section a-Accelerators Spectrometers Detectors and Associated Equipment, 2016. **825**: p. 51-61.

24.   Whitney, C.M., et al., *Gamma-neutron imaging system utilizing pulse shape discrimination with CLYC.* Nuclear Instruments & Methods in Physics Research Section a-Accelerators Spectrometers Detectors and Associated Equipment, 2015. **784**: p. 346-351.

25.   Glodo, J., R. Hawrami, and K.S. Shah, *Development of Cs₂LiYCl₆ scintillator.* Journal of Crystal Growth, 2013. **379**: p. 73-78.

26.   Ban, G., et al., *First tests of Li-6 doped glass scintillators for ultracold neutron detection.* Journal of Research of the National Institute of Standards and Technology, 2005. **110**(3): p. 283-288.

27.   Popov, V., P. Degtiarenko, and Ieee, *Lithium Glass Scintillator Neutron Detector as an Improved Alternative to the Standard He-3 Proportional Counter*, in *2010 Ieee Nuclear Science Symposium Conference Record*. 2010. p. 1819-1822.

28.   Rich, G.C., et al., *Fabrication and characterization of a lithium-glass-based composite neutron detector.* Nuclear Instruments & Methods in Physics Research Section a-Accelerators Spectrometers Detectors and Associated Equipment, 2015. **794**: p. 15-24.

29.   Yamazaki, A., et al., *Neutron-gamma discrimination based on pulse shape discrimination in a Ce:LiCaAlF6 scintillator.* Nuclear Instruments & Methods in Physics Research Section a-Accelerators Spectrometers Detectors and Associated Equipment, 2011. **652**(1): p. 435-438.

30. Tomanin, A., et al., *Characterization of a cubic EJ-309 liquid scintillator detector.* Nuclear Instruments & Methods in Physics Research Section a-Accelerators Spectrometers Detectors and Associated Equipment, 2014. **756**: p. 45-54.

31. Technology, E.   18/02/2016]; Available from: EJ-309 URL ⟨http://www.eljentechnology.com/index.php/products/liquid-scintillators/73-ej-309⟩.

32. Enqvist, A., et al., *Neutron light output response and resolution functions in EJ-309 liquid scintillation detectors.* Nuclear Instruments & Methods in Physics Research Section a-Accelerators Spectrometers Detectors and Associated Equipment, 2013. **715**: p. 79-86.

33. Pino, F., et al., *The light output and the detection efficiency of the liquid scintillator EJ-309.* Applied Radiation and Isotopes, 2014. **89**: p. 79-84.

34. van Eijk, C.W.E., *Inorganic-scintillator development.* Nuclear Instruments & Methods in Physics Research Section a-Accelerators Spectrometers Detectors and Associated Equipment, 2001. **460**(1): p. 1-14.

35. Poitrasson-Riviere, A., et al., *Angular-resolution and material-characterization measurements for a dual-particle imaging system with mixed-oxide fuel.* Nuclear Instruments & Methods in Physics Research Section a-Accelerators Spectrometers Detectors and Associated Equipment, 2015. **797**: p. 278-284.

36. Ayaz-Maierhafer, B., et al., *Angular resolution study of a combined gamma-neutron coded aperture imager for standoff detection.* Nuclear Instruments & Methods in Physics Research Section a-Accelerators Spectrometers Detectors and Associated Equipment, 2013. **712**: p. 120-125.

37. Goorley, J.T.J., Michael R.; Booth, Thomas E.; Brown, Forrest, et al., *Initial MCNP6 Release Overview - MCNP6 version 1.0.* 2012.

38. Agostinelli, S., et al., *GEANT4-a simulation toolkit.* Nuclear Instruments & Methods in Physics Research Section a-Accelerators Spectrometers Detectors and Associated Equipment, 2003. **506**(3): p. 250-303.

39. Allison, J., et al., *Geant4 developments and applications.* Ieee Transactions on Nuclear Science, 2006. **53**(1): p. 270-278.

40. Allison, J., et al., *Recent developments in GEANT4.* Nuclear Instruments & Methods in Physics Research Section a-Accelerators Spectrometers Detectors and Associated Equipment, 2016. **835**: p. 186-225.

41. Reuss, P., *Neutron physics*. 2008, France: EDP Science.

42. NEA, O. *Java-based nuclear data information system*. 16/01/2016 [cited 2016 10/02/2016]; Available from: http://www.oecd-nea.org/janis/.

43. Kahn, F., *The physics of radiation therpy*. 3rd ed. 2003: Lippincott Williams & Wilkins, Philadelphia USA.

44. Taylor, M.L., et al., *The effective atomic number of dosimetric gels.* Australasian Physical & Engineering Sciences in Medicine, 2008. **31**(2): p. 131-138.

45. Knoll, G.F., *Radiation detection and measurment*. Fourth ed. 2010, United States of America: John Wiley and Sons.

46. Colonna, N. and S. Altieri, *Simulations of neutron transport at low energy: A comparison between GEANT and MCNP.* Health Physics, 2002. **82**(6): p. 840-846.

47. Enger, S.A., et al., *Monte Carlo calculations of thermal neutron capture in gadolinium: A comparison of GEANT4 and MCNP with measurements.* Medical Physics, 2006. **33**(2): p. 337-341.

48. Yeh, Y.S., et al., *Simulating neutron propagations with FLUKA, GEANT4 and MCNP*, in *2007 Ieee Nuclear Science Symposium Conference Record, Vols 1-11*. 2007. p. 2016-+.

49. Guardiola, C., et al., *Geant4 and MCNPX simulations of thermal neutron detection with planar silicon detectors.* Journal of Instrumentation, 2011. **6**.

50. Monk, S.D., et al., *A comparison of MCNP6-1.0 and GEANT 4-10.1 when evaluating the neutron output of a complex real world nuclear environment: The thermal neutron facility at the Tri Universities Meson facility.* Nuclear

Instruments and Methods in Physics Research, Section B: Beam Interactions with Materials and Atoms, 2017. **399**: p. 48-61.

51.   Berger, J., Hubbell, J.H. , Seltzer, S.M. , Chang, J., Coursey, J.S. Sukumar, R., Zucker, D.S. and Olsen, K. *XCOM: Photon Cross Sections Database*. 2009 19/03/2015   [cited   2016   08/02/2016];   Available   from: http://www.nist.gov/pml/data/xcom/index.cfm.

6 Design and Optimisation of a Three Layers Thermal Neutron, Fast Neutron and Gamma-Ray Imaging System

H. Al Hamrashdi, S.D. Monk, and D. Cheneler,

6.1 Abstract

The design and configuration of a multi-layered imaging system with the ability to detect thermal neutrons, fast neutrons and gamma rays has been developed and its efficacy demonstrated. The work presented here numerically determines the systems efficiency and spatial resolution, using Cf -252 and Cs-137 as a case study. The novelty of this

detection system lies in the use of small form factor detectors in a three-layer design, which utilises neutron elastic scattering and Compton scattering simultaneously. The current configuration consists of 10 mm thick natural lithium glass (GS10) scintillator integrated with a 20 mm thick plastic scintillator (EJ-204) in the first layer, a 15 mm thick lithium glass (GS10) scintillator in the second and a 30 mm thick CsI(Tl) scintillator forming the final layer. Each of these layers is backed with an 8 x 8 silicon photomultiplier diode (SiPM) array. The overall size of the imaging system is 27 mm x 27 mm x 135 mm. MCNPv6.1 and Geant4-10.04 were alternatively used to optimise the overall configuration and to investigate detection modalities. Results show promising performance with high precision source localisation and characterisation abilities. Measurements were virtually obtained of two gamma-ray sources within steel enclosures at angles of 15°, 30° and 50° separation in order to test spatial resolution ability of the system. With the current active size of the system and the 8 x 8 SiPM configuration, the results estimate the spatial resolution to be close to 30°. The ability of the system to characterise and identify sources based on the type and energy of the radiation emitted, has been investigated and results show that for all radiation types the system can identify the source energy within the energy range of typical reported sources in literature.

6.2 Introduction

The detection and localisation of special nuclear materials (SNM) and radioactive materials in general, is a significant problem for national security agencies across the globe and international organisations such as the IAEA [1, 2]. Over the last two decades, much research has involved the investigation of the design and the build of passive neutron/gamma mobile detection systems for safeguard and security applications [3]. The size of these systems range from vehicle scale down to wearable technology scale

[4-10]. Many vehicle size systems, such as [4-6], are designed to detect strong-orphaned sources at long distances with a very wide field of view, although these systems have limited portability. Handheld devices offer an efficient solution for personal and luggage inspection at security checking points and within potentially crowded areas such as airports, but current systems have limited functionality. Commercially available handheld devices, such as Thermo Scientific[TM], PackEye Radiation Detection Backpack [11] and The Bruker Radiation Backpack Sentry [12] offer localisation abilities for gamma sources only, and have a relatively narrow field of view. To enhance systems abilities to identify and characterise radioactive materials and SNM, the focus on simultaneous detection of both neutrons and gamma rays has grown noticeably in the last decade. An example of a handheld device that employs the characteristics of modern scintillation materials with dual particle detection abilities is a Cs_2LiYCl_6:Ce (CLYC) based monitoring device [7] which claims radioisotope identification and localisation of thermal neutron and gamma–ray sources. Some coded aperture based imaging systems that are related to homeland security and safeguard applications with dual-mode capability offer enhanced sensitivity and source localisation abilities. Examples include the three-dimensional localisation of radioactive sources using liquid scintillators [8] and the CLYC based RadCam imaging system which are based on the RadCam gamma imaging system [9]. Multi-layered dual-particle imaging systems use neutron scattering and Compton scattering techniques to offer a better field of view and higher detection efficiency [10, 13]. For example, the dual-particle imager by Polack et al. [10] allows for accurate detection and source localisation even in the presence of shielding. This offers a larger range of detection materials, shorter acquisition time and a wider range of targets.

The aim of the work here is to design and optimise an innovative handheld, real-time dual-particle imaging system that is capable of simultaneously detecting thermal neutrons, fast neutrons and gamma rays using Monte Carlo simulations. The design utilises multi-layered system techniques to enhance the spectral and temporal abilities of the system, while keeping the weight and size flexible. The proposed design will allow the system to image, localise and characterise a wide range of radioactive sources and SNM in a real time frame. The system is capable of detecting three different types of radiation, allowing a wider range of radioactive sources and SNMs monitoring capabilities.

6.3 Imaging system concept

The multi-layered imaging system described here is based on the combination of three different modes of radiation detection in one handheld device: thermal neutron capture reactions in ^{6}Li nuclei, neutron scattering physics for fast neutrons detection and Compton scattering physics for gamma-ray detection. Scintillation crystal candidates, along with their interaction probabilities and proposed thicknesses for a multi-particle detection system were extensively studied in previous work [14]. The work presented here goes beyond this earlier study in order to better understand the interaction of these detection sub-systems and to verify the efficacy of their combination to form a more comprehensive radiation detection system.

The first layer consists of a 10 mm thick lithium glass (GS10) scintillator (Scintacor Ltd) combined with a 20 mm thick EJ-204 plastic scintillator. The second layer features a 15 mm thick lithium glass (GS10) scintillator (Scintacor Ltd), with a 30 mm thick CsI(Tl) scintillator forming the final absorption layer. The rational behind the use of

GS10 (natural lithium content) rather than GS20 (95% ^{6}Li content) in the first and second layers is mainly due to technical and financial reasons. GS10 will serve the purpose of proving the ability of the system to capture thermal neutrons with 10 mm thick crystal [15] and sufficiently scatter fast neutrons and gamma rays [14]. Secondly, GS10 was found to be more practical in the current prototype due to financial restrictions. It is assumed here that SensL's ArrayJ-30035-64P-PCB 8 x 8 SiPM is to be used as the photodetector throughout the design [16]. SiPMs are compact in size and require a relatively low operating voltage (~30V), offering a solution for small size imaging systems. This 64-pixel avalanche photodiode offers a segmented detection of pulses generated on the area covered by the detector. Hence, the geometry used to define the pixels in the simulation were based on these SiPMs. A schematic of the system arrangement is shown in Figure 6.1.
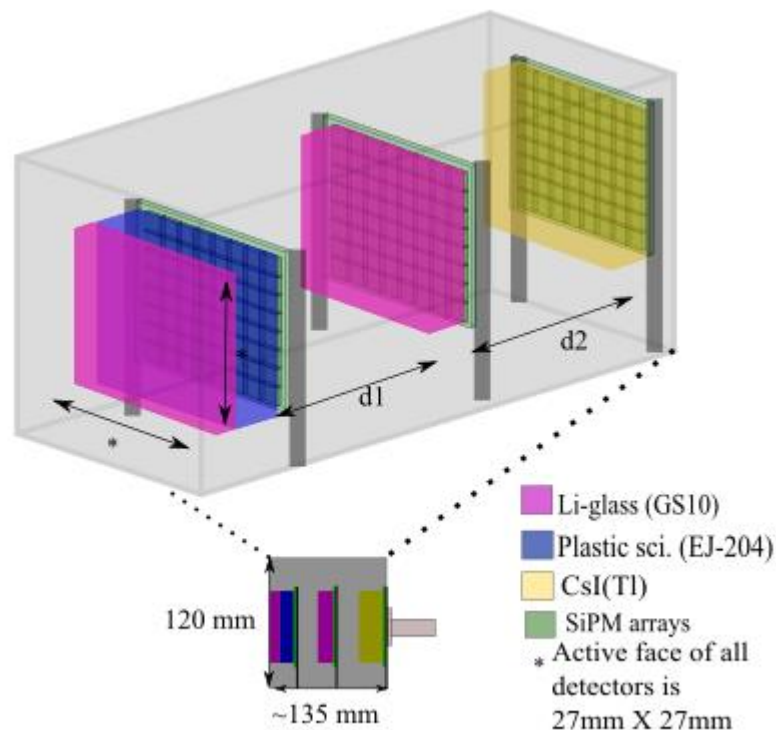
Figure 6.1: Schematic of the multi-layered system configuration.

The thermal neutron detection mechanism in this imaging system is based on the ^{6}Li(n,α)^{3}H capture reaction in the first layer lithium glass detector, releasing alpha and triton particles. Lithium glass will emit detectable light as a result of the energy deposited by the resultant ionising particles [17]. The thermal capture cross section for this particular reaction is 940 barns with a Q value of +4.78 MeV. The aim of adding thermal neutron detection in the first layer is to enhance the energy range of detected neutron sources. Although most SNM are characterised with neutrons in the fast energy range (>1 keV), shielding around smuggled or hidden sources can moderate the energy of these fast neutrons to be in the thermal neutron energy range.

Fast neutron imaging in the system is based on the physics of neutron elastic scattering in hydrogen rich EJ-204, followed by a second elastic scattering event in the Li-glass detector. The principle of fast neutron imaging in scattering cameras is thoroughly discussed within the literature [10, 13, 18-20]. The elastic scattering physics proportionally relates the neutron scattered angle in the first detector, θ, with the energy of the recoil proton, Ep, and the energy of the scattered neutron, E'_n:

$$\tan^2\theta = Ep/E'_n: \tag{6.1}$$

The energy of the recoiled proton is measured in the first scattering plane. The energy of the scattered neutron is calculated using the time-of-flight (TOF) between the two neutron scattering planes as illustrated in equation 6.2.

$$E'_n = \frac{1}{2}\, m_n \left[\frac{d_1}{\text{TOF}}\right]^2 \tag{6.2}$$

Where m_n is the mass of the neutron and d_1 is the separation between the two scattering planes. The probability cone of the location of the source can be reconstructed using the

scattering angle of each incident neutron. The intersection of the cones generated by all incident neutrons will form an image of the neutron source. Figure 6.2, shows a schematic of a neutron scattering event in the system.

En

Ep

θ

E'n

d1

Image plane   Scatter plane 1   Scatter plane 2
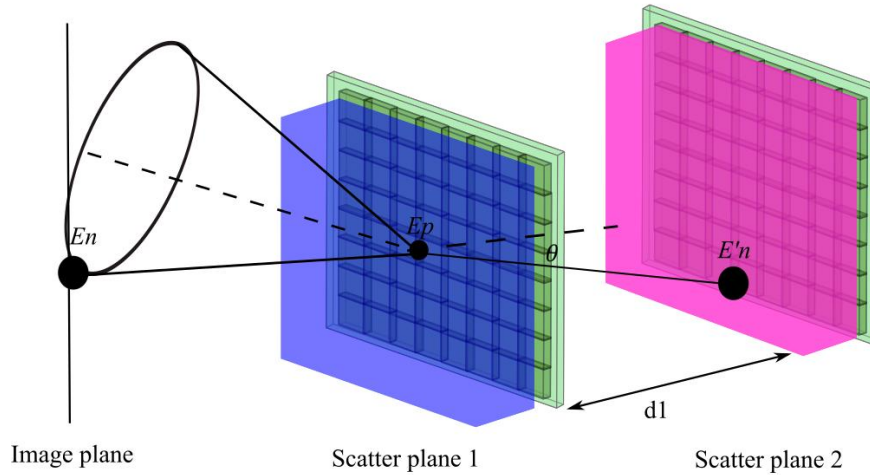
Figure 6.2: Schematic of a neutron scattering system, with monolithic detectors and segmented photodetectors.

Gamma-ray detection in this system is based on Compton scattering kinematics; examples of the analysis of Compton cameras in literature can be found abundantly [21, 22]. This method of gamma-ray detection has been studied extensively for the last four decades and has proved to offer a wider field of view and improved sensitivity over conventional mechanically collimated systems [23-25]. In principle, and as illustrated in Figure 6.3, gamma rays scatter in the first plane depositing part of their energy before undergoing photoelectric absorption in a second high-density scintillator. The energy and position of the two interactions are then utilised to find the angle between the incident and scattered gamma rays, φ. Compton kinematics relate these parameters and allows the calculation of φ as in equation 6.3:

$$\cos \varphi = 1 - 0.511\text{MeV} \left[\frac{1}{E_2} - \frac{1}{E_2 + E_1} \right] \qquad (6.3)$$
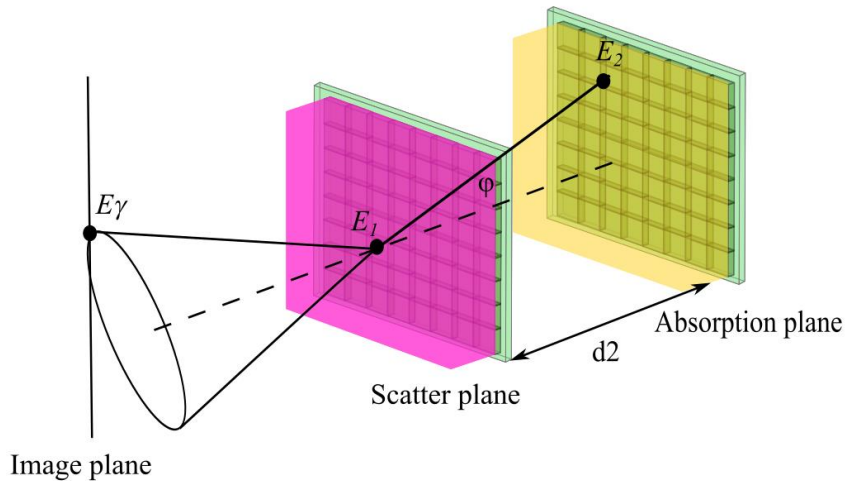
Figure 6.3: Schematic of Compton scattering system with monolithic detectors and segmented photodetectors.

Where d2 is the separation between layers two and three. This will allow the generation of a probability cone of the incident gamma-ray location. The intersection of the cones created by all detected Compton scattering events is used to obtain the source location.

6.4 Prototype setup

MCNPv6.1 [26] and Geant4-10.04 [27] Monte Carlo codes have been used to investigate the optimum configuration of detectors and layers and then to test the feasibility and efficacy of this design. In the MCNP environment, neutron simulations utilised data from the ENDF70a file which is based on the ENDF/B-VII cross section data [26]. The Evaluated Photon Data Library (EPDL) and the Activation Library (ACTL) compilations from Livermore data libraries were mainly used in the simulation of gamma photon transport [26]. All default options in physics cards are applied except for the neutrons physics card where analogue capture is invoked. In Geant4, additional gamma simulations used the Electromagnetic (EM) physics package. The model is based on the emstandard physics list with the Livermore evaluated library [27]. For all

simulations, a point source configuration was used in testing the response of the system. The exact position and energy of the point sources used in the simulations is investigation specific and details are discussed during each investigation in the following sections.

In the current design and for all simulations, all layers have the same active front face size of 27 mm x 27 mm. Simulations were first used to investigate the effect of increasing the separation distance between detection layers, d1 and d2, and detection efficiency of the system. For the neutron scattering layers, a bare Cf-252 source 1 cm away from the system was used in MCNP6.1.0 simulations with no intervening materials and no scattering objects. Although simulations started at separation distance d1=10 mm, 30 mm is the minimum d1 in the current porotype configuration because of the physical size of the SiPM array and the associated breakout board. The relationship between the numbers of successive scattering events relative to the total number of fast neutrons entering the system and the separation distance is shown in Figure 6.4. The efficiency decreases with increasing plane separation, with the maximum efficiency observed at a 30 mm plane separation.
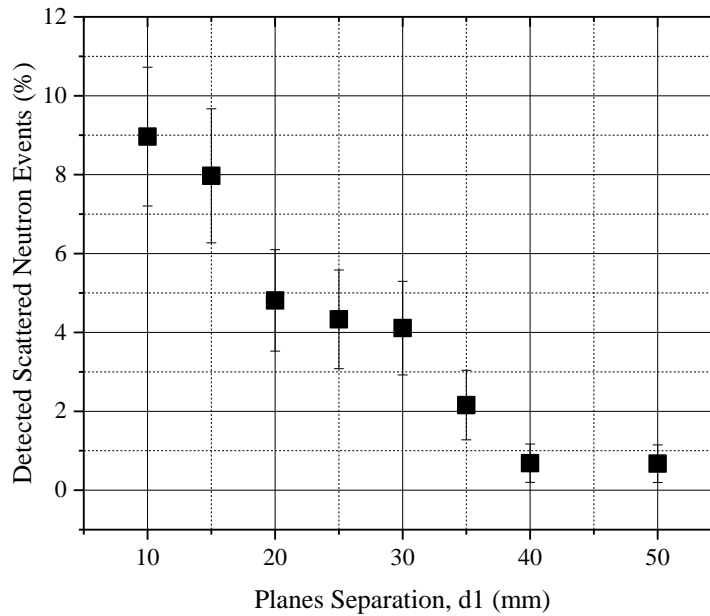
Figure 6.4: Detected fast neutron scattering events as function of planes separation for Cf-252 source.

Optimising the value of d2 in the Compton camera sub-system was based on Geant4-10.04 simulations of four different gamma-ray energies in point source configuration with no intervening materials and no scattering objects. The relation between the fractions of Compton scattering events relevant to the total number of gamma rays entering the system was plotted in Figure 6.5 as function of the plane separation. As above, in reality the minimum plane separation starts at 30 mm because of the physical size of the SiPM and the associated breakout board in the current configuration. The efficiency decreases with increasing planes separation with maximum efficiency at 30 mm.
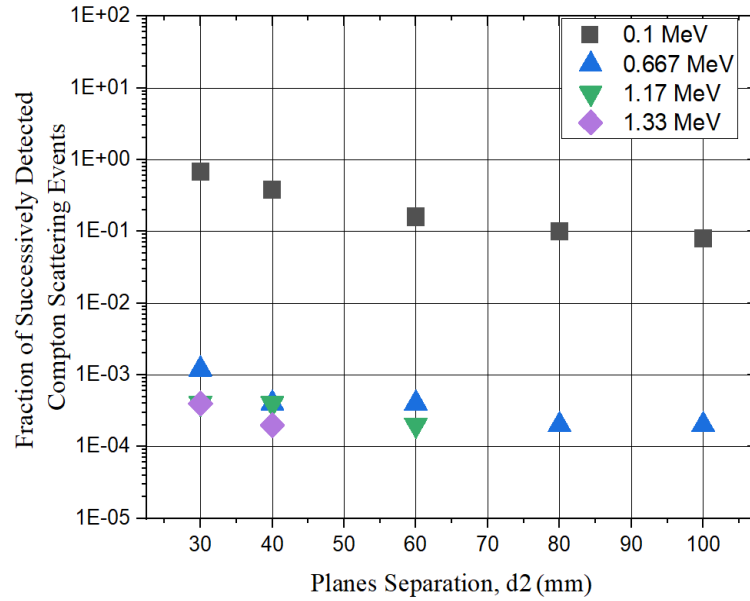
Figure 6.5: Fraction of successively detected Compton events as function of planes separation.

The overall trend of the results shows that increasing the intra-plane distance between detectors for this multi-layered system decreases the probability of successively detected scattering events especially for fast neutrons. However, this flexible prototype configuration allows changing the size of the front face of layers, which can consequently increases detection probabilities and improves geometric efficiency.

6.5 Systems Response and Detection characteristics

6.5.1 Systems response to a thermal neutron source

Here, the ability of the system to locate and identify thermal neutron point sources in a 10 cm x 10 cm carbon steel enclosure was investigated. The source was located 1 cm away from the system at the centre of the detector with no intervening materials and no scattering objects. An example of the simulation made in the MCNPv6.1 environment

is shown in Figure 6.6. The 2D figure shows a top down view of thermal neutrons tracks inside the box and their trajectory in the detector. The 3D right hand figure shows the distribution of particles inside the carbon steel box.
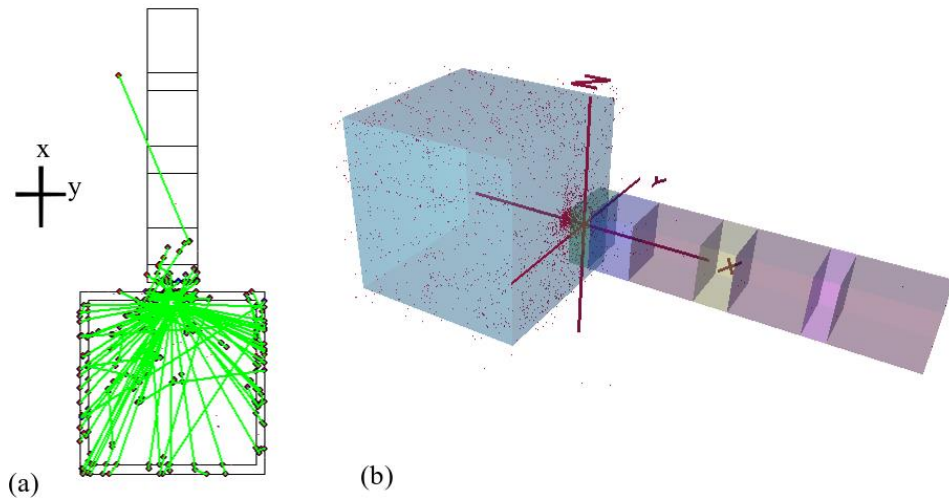
Figure 6.6: (a) 2D and (b) 3D representation of the MCNPv6.1 simulation of a bare thermal neutrons source.

The results in this section are mainly presented as reconstruction images of the system response in an 8 x 8 array format (the size of the SiPM photodetector utilised in the design), which epitomises the configure of light output of each layer.

Figure 6.7 shows an image reconstruction of the signal generated in the lithium glass detector in the first layer (MCNPv6.1.0). The calculated intrinsic efficiency was found to be (79 ± 3) %.
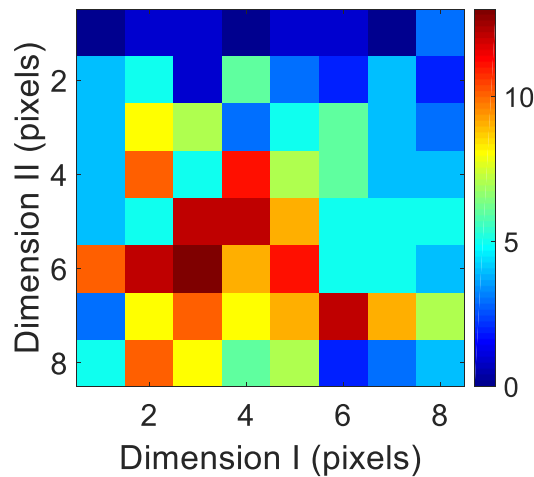
Figure 6.7: System response to thermal neutron source located at pixels (4 ,4). Colour bar shows pixel intensity in arbitrary units.

6.5.2 Systems response to fast neutron sources

The response of the system to fast neutrons is based on neutron scattering kinematics in the EJ-204 within the first layer and the lithium glass (15mm) in the second layer. Using the PTRAC file generated in MCNPv6.1 simulations, energies of the scattered fast neutrons and TOF in these two layers was found. Based on equations (6.1) and (6.2), an estimation of the source location was obtained. In the first testing scenario, the response of the system to a bare Cf-252 source placed at different positions was investigated in order to evaluate the detection ability of the system as well as the spatial resolution of the system. The source-to-detector distance was 1 cm with no intervening materials and no scattering objects. The results in Figure 6.8 illustrate the ability of the system to identify the direction of incident radiation using neutron scattering kinematics.
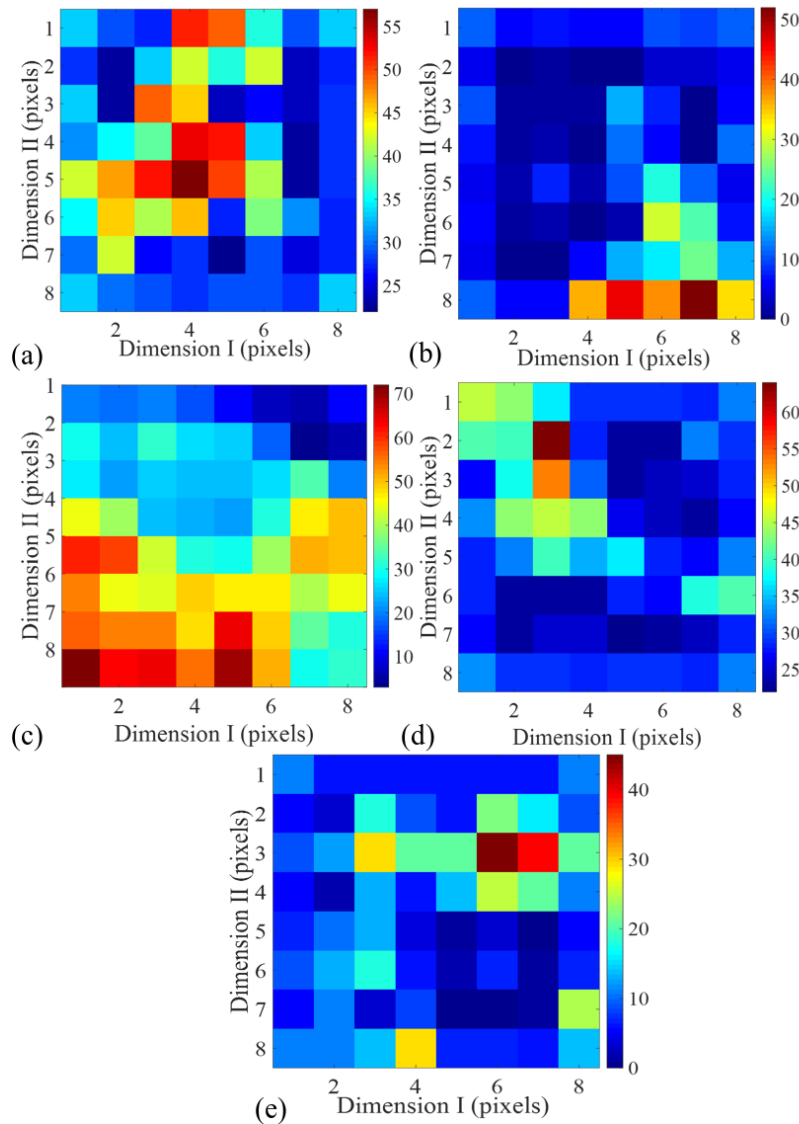
Figure 6.8: The response of the system to a Cf-252 source located at five different positions at pixels (a) (4, 4), (b) (2, 7), (c) (2, 2), (d) (7, 7) and (e) (7, 2) (Colour bars indicate image intensity in arbitrary units).

The second test involved simulations utilising Cf-252 and AmBe sources located 1cm from the detection plane, in order to test the ability of the system to identify two fast neutron sources based on their energies. Table 6.1 lists reported average energies and calculated average energies of these two sources. These results illustrate the system's ability to identify different neutron sources based on their energies.

Table 6.1: System's average energy calculations for different fast neutron sources [17, 28].

Source	Average energy in literature (MeV)	Average energy calculated from simulations (MeV)
AmBe	4.2	4.2 ± 1.3
Cf-252	2.35	2.0 ± 0.8

6.5.3 Systems response to a gamma source

The ability of the system to identify the location of gamma sources was investigated using a bare Cs-137 point source. In the simulations (Geant4), the source was positioned 30 cm away from the system, with no intervening materials and no scattering objects. Using equation 6.3 where E_1 and E_2 are the energies deposited in Li-glass and CsI(Tl) respectively, probability cones were constructed and the image intensities map of SiPM was constructed as illustrated in Figure 6.9. The results in this figure show a high ability to precisely locate the position of a gamma-ray source.
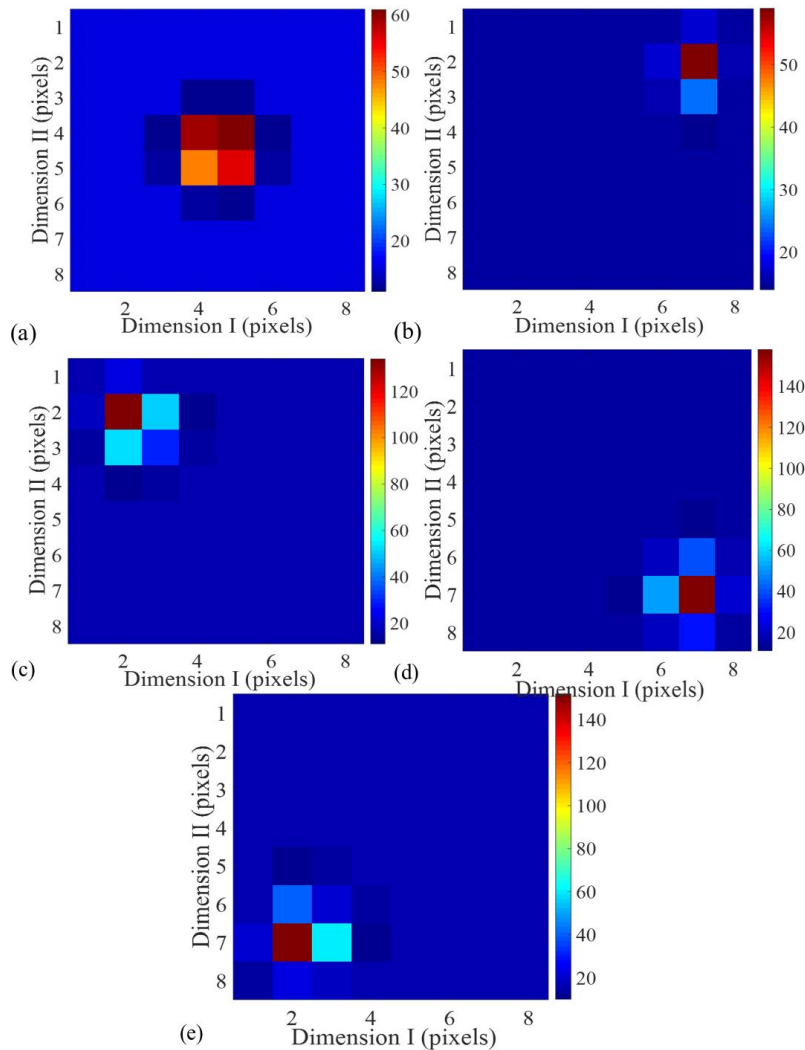
Figure 6.9: The response of the system to a Cs-137 source located at five different pixel positions (a) (5,5), (b) (7, 2), (c) (2,2) (d) (7,7) and (e) (2,7) (Colour bars indicate image intensity in arbitrary units).

In addition, the ability of the system to differentiate between closely spaced sources was investigated using two Cs-137 sources. The sources were placed 1 mm away from the imaging system. The results of this investigation are shown in Figure 6.10 for 15º, 30º and 50º sources separation, with spatial resolution close to 30º.
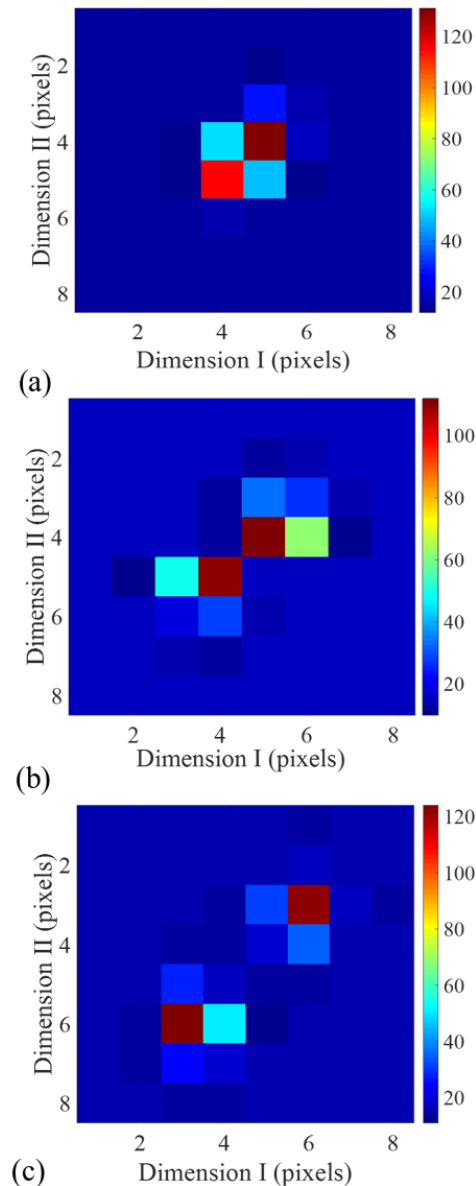
Figure 6.10: System's response to two Cs-137 sources at a. 15º and b. 30º and c. 50º separation distance (Colour bars indicate image intensity in arbitrary units).

The system's capability to identify and characterise gamma-ray sources according to their energy was investigated using the simulations of Cs-137 and Co-60 point sources. The sources were placed 1 mm away from the system. Using equation 6.3 with E_1 and E_2 being the energies deposited in Li-glass and CsI(Tl) respectively, the average

gamma-ray energy peaks were calculated. Table 6.2 shows calculated average energies from simulations and reported average energies in literature.

Table 6.2: Calculated average energies from simulations and reported average energies in the literature for Cs-137 and Co-60 [17, 28].

Source	Average energy in literature (MeV)	Average energy calculated from simulations (MeV)
Cs-137	0.667	0.669 ± 0.006
Co-60	(1) 1.17	1.17 ± 0.01
	(2) 1.33	1.33 ± 0.05

6.6 Conclusion

This work discusses briefly the designing parameters and computational testing of the feasibility of a multi-particle imaging system that is based on three detection layers. Results show the prototype configuration is capable of detecting and localising thermal neutrons, fast neutrons and gamma-ray sources. The results from this study have been directly implemented to build the prototype imaging system, which is now under experimental investigation.

6.7 References

1. IAEA, *IAEA Inicdents and Trafficking Database (ITDB) Incidents of nuclear and other radioactive material out of regulatory control*, in *2018 Fact Sheet*. 2018, International Atomic Energy Agency Vienna, Austria.

2. D. Reilly, N.E., H. Smith, and S. Kreiner, *Passive Nondestructive Assay of Nuclear Materials,* , N.E. D. Reilly, H. Smith, and S. Kreiner Editor. 1991:

National Technical Information Service, U.S. Department of Commerce, Washington, DC,.

3. Al Hamrashdi, H., S.D. Monk, and D. Cheneler, *Passive Gamma-Ray and Neutron Imaging Systems for National Security and Nuclear Non-Proliferation in Controlled and Uncontrolled Detection Areas: Review of Past and Current Status.* Sensors, 2019. **19**(11): p. 2638.

4. Zelakiewicz, S., et al., *SORIS—A standoff radiation imaging system.* Nuclear Instruments and Methods in Physics Research Section A: Accelerators, Spectrometers, Detectors and Associated Equipment, 2011. **652**(1): p. 5-9.

5. Ziock, K.P., et al. *Source-search sensitivity of a large-area, coded-aperture, gamma-ray imager*. in *Nuclear Science Symposium/Medical Imaging Conference*. 2004. Rome, ITALY.

6. Christian, J.F., et al. *Nuclear material detection techniques*. in *SPIE Defense and Security Symposium*. 2008. SPIE.

7. Budden, B.S., et al., *A Cs2LiYCl6:Ce-based advanced radiation monitoring device.* Nuclear Instruments and Methods in Physics Research Section A: Accelerators, Spectrometers, Detectors and Associated Equipment, 2015. **784**: p. 97-104.

8. Gamage, K.A.A., M.J. Joyce, and G.C. Taylor, *Investigation of three-dimensional localisation of radioactive sources using a fast organic liquid scintillator detector.* Nuclear Instruments and Methods in Physics Research Section A: Accelerators, Spectrometers, Detectors and Associated Equipment, 2013. **707**: p. 123-126.

9. Soundara-Pandian, L., et al., *Characterization of Large Volume CLYC Scintillators for Nuclear Security Applications.* IEEE Transactions on Nuclear Science, 2017. **64**(7): p. 1744-1748.

10. Polack, J.K., et al. *Dual-particle imager for standoff detection of special nuclear material*. in *2011 IEEE Nuclear Science Symposium Conference Record*. 2011. Valencia, Spain.

11. *PackEye Radiation Detection Backpack*. [cited 2018 26/10/2018]; Available from: https://www.thermofisher.com/order/catalog/product/FHT1377.

12. *Radiation Backpack Sentry*. 2012   [cited 2018 26/10/2018]; Available from: https://www.bruker.com/fileadmin/user_upload/8-PDF-Docs/CBRNE_Detection/Literature/Backpack-Brochure-en.pdf.

13. Mascarenhas, N., et al., *Results With the Neutron Scatter Camera.* IEEE Transactions on Nuclear Science, 2009. **56**(3): p. 1269-1273.

14. Al Hamrashdi, H., D. Cheneler, and S.D. Monk, *Material optimization in dual particle detectors by comparing advanced scintillating materials using two Monte Carlo codes.* Nuclear Instruments and Methods in Physics Research Section A: Accelerators, Spectrometers, Detectors and Associated Equipment, 2017. **869**(Supplement C): p. 163-171.

15. Wraight, L.A., D.H.C. Harris, and P.A. Egelstaff, *Improvements in thermal neutron scintillation detectors for time-of-flight studies.* Nuclear Instruments and Methods, 1965. **33**(2): p. 181-193.

16. *SensL J-series*.   [cited 2018 01/11/2018]; Available from: https://sensl.com/products/j-series/

17. Knoll, G.F., *Radiation detection and measurment*. Fourth ed. 2010, New York, NY, USA: John Wiley and Sons.

18. Vanier, P.E. and L. Forman. *Demonstration of a directional fast neutron detector*. in *IEEE Nuclear Science Symposium Conference Record, 2005*. 2005.

19. Vanier, P.E., et al. *Calibration and testing of a large-area fast-neutron directional detector*. in *2007 IEEE Nuclear Science Symposium Conference Record*. 2007. Honolulu, HI, USA.

20. Macri, J.R., et al. *The Fast Neutron Imaging Telescope (FNIT) - hardware development and prototype testing*. in *2007 IEEE Nuclear Science Symposium Conference Record*. 2007.

21. Todd, R.W., Nighting.Jm, and D.B. Everett, *Proposed Gamma Camera.* Nature, 1974. **251**(5471): p. 132-134.

22. Herzo, D., et al., *A Large Double Scatter Telescope for Gamma Rays and Neutrons.* Nuclear Instruments and Methods, 1975. **123**(3): p. 583-597.

23. Kamae, T., N. Hanada, and R. Enomoto, *PROTOTYPE DESIGN OF MULTIPLE COMPTON GAMMA-RAY CAMERA.* Ieee Transactions on Nuclear Science, 1988. **35**(1): p. 352-355.

24. Everett, D.B., et al. *Gamma-radiation imaging system based on the Compton effect*. in *Proceedings of the Institution of Electrical Engineers-London*. 1977. IET Digital Library: London, UK.

25. Singh, M. and R.R. Brechner, *Experimental Test-Object Study Of Electronically Collimated SPECT*. Journal of Nuclear Medicine, 1990. **31**(2): p. 178-186.

26. Goorley, J.T.J., Michael R.; Booth, Thomas E.; Brown, Forrest, et al., *Initial MCNP6 Release Overview - MCNP6 version 1.0*. 2012.

27. Allison, J., et al., *Recent developments in GEANT4*. Nuclear Instruments & Methods in Physics Research Section a-Accelerators Spectrometers Detectors and Associated Equipment, 2016. **835**: p. 186-225.

28. Gozani, T., *Active Nondestructive Assay of Nuclear Materials, Principles and Applications* 1981, Washington DC: US Nuclear Regulatory Commission.

7 A fast and portable imager for neutron and gamma emitting radionuclides

H. Al Hamrashdi, D. Cheneler, and S.D. Monk.

7.1 Abstract

Here a novel, real-time, highly-compact imaging system capable of detecting and localising gamma rays, thermal and fast neutrons is reported. The imaging system presented in this research comprises of a front-end containing three detection layers with a unique combination of scintillators optimised for multi-particle detection, and backed with silicon photomultiplier diode arrays to enable source localisation and to maximise efficiency. The system exploits Compton and neutron scattering techniques simultaneously to constitute a dual-mode radiation camera. Application-specific

software algorithms are implemented here to process the numerous signals from the system and to reconstruct the location of radioactive sources using a back-projection technique. The three front-end detection layers fit within a volume of 120 mm × 120 mm × 200 mm, offering a uniquely compact imaging solution. A prototype of the instrument and the associated electronics have been designed using Monte Carlo simulations, and tested with Cs-137 (given its singular gamma-ray component) and Cf-252 (for its mixed neutron and gamma-ray emission). Experimental results indicate that the system can detect and localise both gamma-ray and neutron sources successfully, with intrinsic efficiencies in the order of 10^{-4}. All results have been achieved within a scan time of 60 seconds and with a further data processing time of less than 60 seconds, for gamma sources of ~300 kBq and neutron sources of 10^6 neutrons per second (total) in close proximity (< 300 mm). Whilst high-speed, mixed-field, particle-imaging systems have numerous applications within both nuclear and non-nuclear fields; this particular system has been optimised for use within the areas of nuclear materials assay and proliferation prevention.

7.2 Introduction

Global imperatives to decarbonise electricity supplies have resulted in a variety of new nuclear build programmes and related developments in nuclear fuel technology. These developments have the potential to generate new challenges at national and international levels [1, 2]. The diversion of nuclear materials deemed unlawful under international regulations might involve several different stages, starting with for example: the acquisition of safeguarded material, its transportation and eventual deposition at a point where non-peaceful use might be the intent and concern. Of key strategic importance in

this regard is the deployment of detection technologies capable of identifying and tracking special nuclear materials at national and international cross points, ports and borders [3, 4]. These areas can be either controlled (e.g., associated with secure areas within airports, border and cargo inspection points etc.) or uncontrolled (e.g., at airport terminals, train stations and so forth). The latter scenario is associated typically with a complex environment where innovative detection technologies are required [4]. In particular, these technologies usually need to be mobile (so they can be placed as required and offer flexibility when closer inspection is required) and offer fast data acquisition times (to ensure that the materials in question can be identified rapidly and tracked within what can be dynamic environments).

General radiation cameras have been utilised widely as thoroughly reviewed by H. Al Hamrashdi et al. [4], with some systems finding industrial designation such as RadCam [5] GAMPIX [6-8], GeGi [9] and Cartogam [10]. Systems that detect gamma rays and neutrons both passively and simultaneously are widely described and utilised within the literature [4, 11-15]. Such multi-mode systems possess an obvious advantage over single particle detection for security applications as it permits the location of a wider range of radioactive and nuclear materials. Compton and neutron scattering are physical interaction phenomena that are well-established, with Compton scattering being especially popular in the medical industry [16-18] and possessing intrinsic detection efficiencies typically between 10^{-6} to 10^{-3} [19, 20]. The concept of combining neutron and Compton scattering techniques to detect fast neutrons and gamma rays in safeguarding applications was first suggested by Polack et al. [21] in 2011 and experimentally investigated by Poitrasson-Riviere et al. in 2014 [22]. The system described by Poitrasson-Riviere et al. consists of three detection arrays, each with sixteen, relatively large EJ-309 and NaI(Tl) scintillation detectors, and offer comparable

detection and localisation abilities to standard multilayer designs. Designed as a lab-based proof-of-concept study, the configuration is not practical for many security applications due to the sheer bulk of the system. This paper describes the design, construction and testing of a portable and real-time, compact neutron and gamma-ray detection and imaging instrument, along with the assessment of its detection abilities and characteristics. The main features of this design are:

- The prototype front-end is highly compact, having dimensions of 200 mm x 120 mm x 120 mm and a mass of 3 kg. When battery powered, this allows the instrument to be utilised at any stage during the monitoring protocols of radioactive and nuclear materials at national and international cross points, ports and borders.

- The design targets gamma rays in the Compton energy range (~10 keV to ~10 MeV), thermal and fast neutrons, and is capable of simultaneous detection of all three.

- The instrument features fast data acquisition techniques leading to a 60-second scan time, short compared to most other imaging cameras. This allows rapid creation of a source position probability map that can be used to identify potential radiological sources. (The scan time is achieved for gamma sources of ~300 kBq and neutron sources of 10^6 neutrons per second (total) in close proximity < 300 mm).

The main target application for this system is border security, although it is anticipated that a more mature version of the design could be applied within alternative fields such as medical and industrial imaging. Previous work by the authors [23, 24] concerned the determination of aspects such as the materials used in the front end of the instrument

and the optimal distances between layers. The work described here describes the physical construction of the front end, the electronics used in the instrument and the software utilised to extract and present the data generated. For reasons of brevity, the development of Pulse Shape Discrimination (PSD) techniques to be used with this instrument are to be discussed in future work.

7.3 Imaging concept

Within this imaging system, Compton scattering is exploited to detect gamma rays with energies between ~10 keV and ~10 MeV [25]. Similarly, neutron scattering technology is used here to detect fast neutrons with energies higher than 1 keV, with additional capture technologies also integrated to detect low-energy neutrons; the detection system is shown in Figure 7.1. Each of the four scintillators used have an active detection area of 27 mm × 27 mm. The materials selected and the particular thicknesses used are the result of an earlier, in-depth Monte Carlo-based optimisation study by the authors [23].
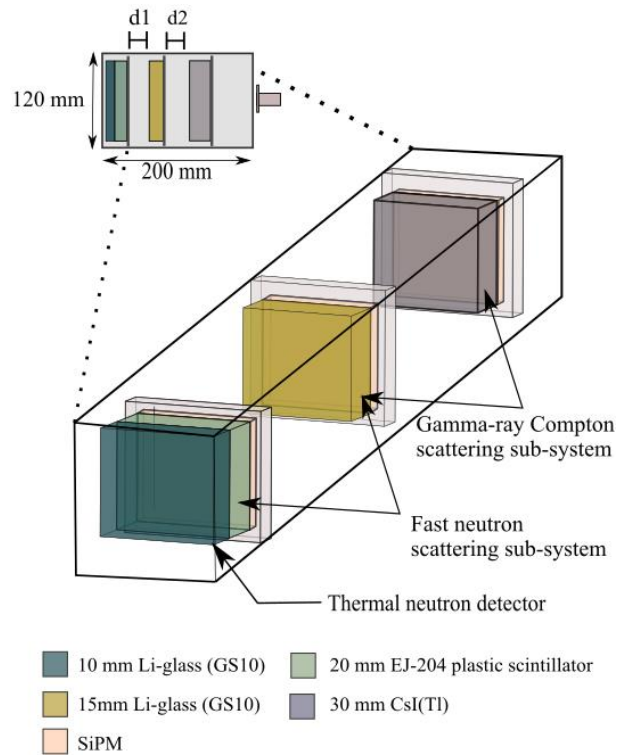
Figure 7.1: A schematic of the imaging system comprising of scintillators and silicon photomultipliers (SiPMs). The upper diagram representing a side elevation of the system and the lower diagram representation a front elevation of the system. Here, d1 and d2 in the side elevation view are the separation distances between layers. The values of d1 and d2 were both 30 mm.

The three layers are constructed from a unique combination of scintillators optimised for multi-particle detection. Each of the layers is backed by a segmented (8×8 array) silicon-based photomultiplier (SiPM), and a compact, photon-counting transducer device that is used to localise and quantify photons produced in the scintillation layers, as described below:

- The first layer consists of two detectors coupled via optical gel. The first is a 10 mm thick, natural lithium glass scintillator (i.e. 6.6% of the lithium content is Li-6; GS10 from Scintacor Ltd., Cambridge, UK [26]) which captures thermal

neutrons, whilst it is anticipated that fast neutrons and gamma rays generally pass through without interaction. The second is a 20 mm thick EJ-204 plastic scintillator (Eljen Technology, Sweetwater, TX, USA) [27]) that serves as the fast neutron scattering media within the neutron-scattering sub-system, again without significantly affecting the gamma-ray flux. This particular thickness of lithium glass detector in this layer has been selected to optimise thermal neutron detection while minimising gamma-ray interaction probability in the detector [23].

- The second layer comprises a 15-mm thick lithium glass scintillator (GS10 from Scintacor Ltd. as in the first layer) which captures the neutrons scattered and thermalised by the plastic scintillator in the first layer. The same crystal serves as the first Compton scattering layer in the Compton scattering sub-system.

- The third layer is a 30 mm thick thallium-doped, caesium iodide (CsI(Tl)) scintillator (John Caunt Scientific Ltd., UK [28]) which forms the final gamma-ray detection layer in the Compton scattering sub-system.

The lithium glass used in the imaging system is a cerium-activated, silicate glass with lithium content in its natural isotopic abundance. As shown in the previously-mentioned material characteristics optimisation study (Al Hamrashdi et al. [23]), the GS10 lithium glass exhibits superior scattering capabilities compared to other scintillation materials that are sensitive to both neutrons and gamma rays. EJ-204 is a general-purpose, plastic scintillator which possesses a 1.1 H:C ratio and demonstrates sensitivity to both fast neutrons and photons with energy of less than 100 keV. Indeed, EJ-204 (also known as NE-104 and BC-404) possesses one of the highest scintillation efficiencies amongst all plastic detectors with 10,400 photons generated per MeV of incident electrons. CsI(Tl) is a widely-utilised, inorganic scintillator renowned for its larger gamma-ray absorption

coefficient compared to sodium iodide and a higher absolute light yield of 65,000 photons/MeV compared to 38,000 photons/MeV for NaI(Tl) [25].

Thermal neutron detection is achieved in the first lithium glass layer via the ^{6}Li(n,α)^{3}H thermal neutron capture reaction. The alpha and triton products of this reaction are highly ionising, with energies of 2.73 MeV and 2.05 MeV respectively [25], and transfer their energy to the cerium-activated lithium glass. Pulses generated in this layer are of consistent height and shape characteristics albeit with slight variations due discrepancies in photon transport and photodetector response. Fast neutron detection is the result of neutrons undergoing elastic scattering whilst interacting with the protons within the EJ-204 plastic scintillator located in the first layer, followed by the detection of the scattered neutrons in the second layer. The scattered protons in the EJ-204 deposit most of their energy within this volume (the range of a 10 MeV proton in general PVT plastic scintillators is c.a. 1.2 mm [29]) generating visible photons, which are detected by a SiPM. Within the second layer of the system, some of the lower energy scattered neutrons will interact with the lithium glass through capture reactions or elastic scattering, with both reactions producing visible photons. The pulses generated from these interactions are utilised to measure the time-of-flight (TOF) of the neutrons between the two layers. Figure 7.2 shows a schematic of the components used in the neutron-scattering technique, and the parameters used in the analysis.
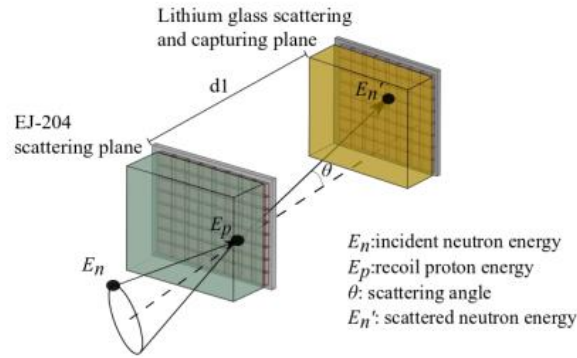
Figure 7.2: A schematic of the neutron scattering sub-system components. The schematic illustrates a successful neutron scattering event within the system in which the neutron will first interact in EJ-204 detector, producing a proton that will eventually generate scintillation photons in the scintillator. The scintillation photons will then be collected in the SiPM of that layer. The scattered neutron then interacts in the lithium glass layer. Secondary particles from this interaction will then generate scintillation photons that will be collected in the SiPM of that layer.

The scattering angles and incident trajectories can be calculated from the relative positions of the detected pulses via the position of activated pixels in the SiPM array. The energy of an incident neutron is assumed to be the sum of the energy of the scattered proton, E_p, and of the energy of the scattered neutron, E'_n [30, 31]. These energies are related to the scattering angle, θ, through equation 7.1:

$$\tan^2\theta = E_p/E'_n \qquad (7.1)$$

The energy of the scattered neutron can be calculated using the time-of-flight (TOF) measurement between the two SiPMs, as shown in equation 7.2.

$$E'_n = 0.5\ m_n\ (d1^2/TOF^2) \tag{7.2}$$

Where d1 is the separation distance between the two SiPM arrays, and m_n is the rest mass of a neutron. The probable origin of the neutron source is formed by creating probability cones coincident on the plane defined by the scattering angle. The compound images of the intersection areas of all of the resultant ellipses can then be used to estimate the most likely location of the incident neutron source.

The Compton detection technique is used here to overcome the drawbacks of conventional physical collimation, the most significant of which concerns the narrow range of incidence angle, which has a direct effect on detection efficiency [16, 17]. Two layers of scintillators are utilised in this Compton scattering sub-system: the second lithium glass scintillator operating as the photon-scattering layer with the CsI(Tl) scintillator operating as the photon detection layer. The scattering angles and incident trajectories can be related using conservation of energy and conservation of momentum equations as shown in equation 7.3 and Figure 7.3. It is assumed that the energy of the incident gamma-ray photon is the sum of the measured energy of the recoil electron E_e and the measured, absorbed, scattering photon energy E'_γ.

The high fill-factor J-series SiPM sensor array (ArrayJ-30035-64P-PCB 8 x 8 SiPM, SensL, Cork, Ireland [28]) is used as the photodetector within each of the three detection layers of the design described in this paper. The typical breakdown voltage (V_{br}) of this particular array is 24.5 V, with a sensitive spectral range between 200 nm and 900 nm; a limit that comfortably spans the wavelength of maximum emission for lithium glass (395 nm), EJ-204 (408 nm) and CsI(Tl) (550 nm) [25]. The main features of the J-series SiPM array are the low dark count rate (typically 50 kHz/mm^2 at 2.5 V above V_{br} and 80 kHz/mm^2 at 5V above V_{br}) and the high photon detection efficiency (38% at 2.5V

above V_{br} and 51% at 5V above V_{br}). The photon detection efficiency extends into the blue range of the electromagnetic spectrum, matching the wavelength range of the lithium glass and EJ-204 emission spectra [32]. This latter feature contributes directly to the reduction of dark current as the penetration of light in the blue region is shallow in a silicon wafer, minimising the depth of the generated electric field and subsequent spontaneous generation of electrons [25]. The main physical feature of the ArrayJ-30035-64P-PCB 8 x 8 SiPM is the efficient use of space within the active area of the array. The arrays used here feature 64 individual pixels (each with a total number of 5,676 SPAD microcells) with each pixel featuring a pitch of 3.16 mm equating to a total size of 26.68 mm $\times$ 26.68 mm, offering high-resolution 2D-mapping of incident and locally-generated pulses [32].
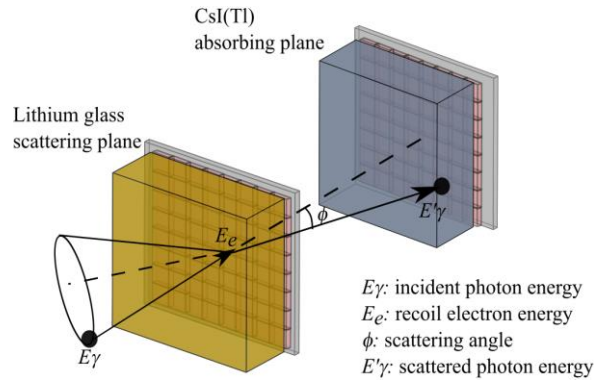
Figure 7.3: Gamma particle collides with an atom in the lithium glass via the Compton Effect, the electron producing visible photons in the volume, which are collected in the SiPM. The photon scattered in this volume then enters the CsI(Tl) scintillator with the electron produced via the photoelectric effect producing visible photons which are collected in the associated SiPM.

$$\cos\phi = 1 - mc^2 \left[\left(\frac{1}{E'\gamma}\right) - \left(\frac{1}{E'\gamma + E_e}\right)\right] \tag{7.3}$$

7.4 Experimental set-up

The experimental system consists of three 'zones'. The measurement zone features the three-layer detectors assembly as described above, the front-end electronics associated with the detection layers, and the three power supplies that provide the 29.4 V DC required by the SiPMs. The 192 channels of data generated in this zone are fed into the readout circuit zone, which comprises of a large volume of bespoke electronics designed to process the data from the SiPM pixels and utilising a ±12 V, 10 A power supply. Finally, the control zone, incorporates the software used to collect and process the data produced by the instrument.

7.4.1 Measurement zone

The scintillator detectors are orientated vertically in a stainless steel enclosure with a wall thickness of 4 mm to simultaneously reduce the influence of background radiation while offering structural integrity and machinability. The enclosure has external dimensions of 120 mm × 120 mm × 200 mm, reflecting the small form factor of the imaging system. The 8 × 8 SiPM arrays are placed in optical contact with the scintillators within each layer, and are mounted on ARRAYJ-BOB3-64P (SensL) breakout boards. Each SiPM pixel has a dedicated simple current-to-voltage converter consisting of a 47 Ω resistor in series with the diode. Off-the-shelf benchtop power supplies were used to provide 29.4 V of reverse bias, which was applied across the resistor and diode, with the output, read across the diode and transmitted via ribbon cable to the readout circuit. Figure 7.4 shows the SiPM array with the front-end electronics.
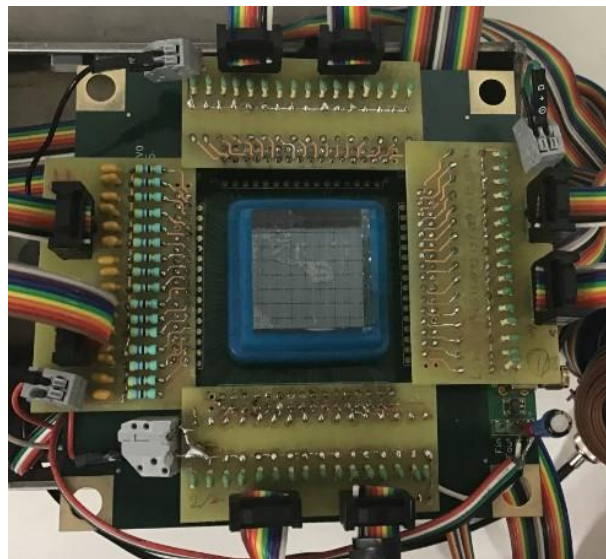
Figure 7.4: A photograph of the SiPM array with the front-end electronics used in this research.

The characteristic equation describing an output current pulse from the SiPM has been discussed previously by A. Spinelli and A. L. Lacaita [33], and by R. Turchetta [34]. The shape of the raw pulses from a single SPAD (or microcell) is commonly described as a Dirac's delta pulse ($Q\delta(t-c)$). The total charge Q generated by each SPAD in the SiPM array being equal to $\Delta V(C_q+C_d)$; where ΔV is the overvoltage, C_q is the quenching capacitor value and C_d is the depletion region capacitance in the SiPM cell. The anode-cathode (standard) output of the SiPM module used in this design has a total capacitance of 1000 pF. Figure 7.5 showcases the processed and normalised output pulses from the SiPM when lithium glass, EJ-204 and CsI(Tl) detectors are utilised. The data were acquired using Agilent 54845A Infiniium Oscilloscope with a sampling speed of 8 GSa/s and bandwidth of 1.5 GHz.
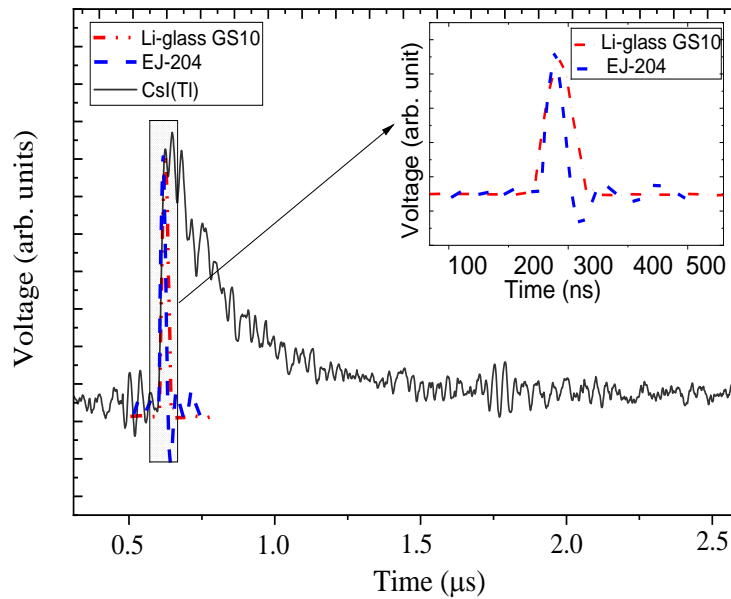
Figure 7.5: Pulses generated from an SiPM and front-end electronics (current-to-voltage converter) for lithium glass (Li-glass), EJ-204 and CsI(Tl) detectors, using a Cf-252 source (the inset figure is an enlarged proportion of the figure comprising close-ups of the lithium glass and EJ-204 short pulses).

Table 7.1 provides a list of the average rise and fall times of the three types of pulse featured in Figure 7.5. The rise time in the table refers to the time required for the leading edge of the pulse to rise from 10% to 90% of its maximum value, whereas fall time is the time required for the decaying edge of the pulse to fall from 90% to 10%.

Table 7.1: Rise time and fall time of SiPMs pulses for lithium glass, CsI(Tl) and EJ-204 (Note that measurements here are limited by the sampling speed of the oscilloscope utilised in this part of the experiment)

Detector	Maximum emission wavelength (nm)	Radiation source	Average rise time (ns)		Average fall time (ns)	
			Measured	Reported	Measured	Reported
Lithium glass	395	mixed	50.4 ± 0.9	NA	70 ± 3	$70^{(1)}$
CsI(Tl)	550	gamma-ray	67 ± 2	NA	1600 ± 30	600 (fast component) /3340 (slow component)
EJ-204	408	mixed	NA	$0.7^{(b)}$	NA	$1.8^{(b)}$

(q) van Ejik et. al, 2012[35]

(b) https://eljentechnology.com/images/products/data_sheets/EJ-200_EJ-204_EJ-208_EJ-212.pdf [27]

EJ-204 is an appropriate scintillator choice within counting applications that require a fast response, as the material boasts a pulse rise and fall time of less than 3 ns and a pulse width at FWHM of 2.2 ns. While this is of great advantage in the TOF measurements, an issue occurs when sampling the pulse with conventional instrumentation, such as the oscilloscope. The high sampling speed of the Agilent 54845A Infiniium Oscilloscope allows the digitising of EJ-204 pulses and hence the plotting of the pulses shown in Figure 7.5, although the low input impedance (1 MΩ) can cause the undershooting observed in the EJ-204 pulse, which might affect further analysis on pulse shape discrimination.

7.4.2 Readout circuit zone

An application-specific readout circuit (ASRC) was designed in order to process each of the 192 pixels from the three SiPM arrays individually. There are three main levels of circuitry within the ASRC: (i) filtering and amplification, (ii) pulse comparison, and (iii) time-of-flight (TOF) measurement. The DAQ used here was the USB-2633 (Measurement Computing Corporation, USA) [36] which operates at a sampling rate of 1 MSa/s with 64 single-ended analogue inputs (1 GΩ input impedance) and three 8-bit digital inputs. Figure 7.6 shows a block diagram of the readout circuit with an example of the different stages in the ASRC for two channels. It should be noted that whilst this also features the current-to-voltage stage for completeness, this component is physically in the measurement zone as opposed to being in the application-specific readout circuit zone.
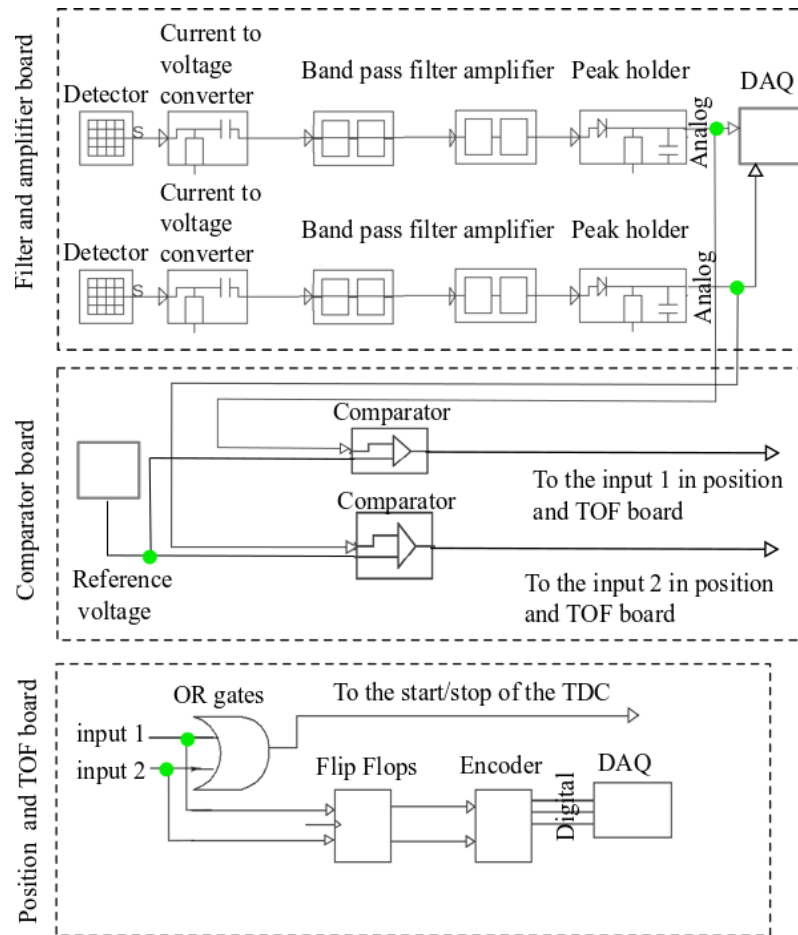
Figure 7.6: Block diagram of the ASRC showing, as an example, the transition of pulses within two of the channels.

The function of the first stage of the circuit is to filter and amplify the voltage pulses from each of the SiPM pixels via a high-pass filter and two inverting amplifiers (also acting as active low-pass filters). This features a cut off frequency of 10 GHz and a gain of 100 (shown in Figure 7.7). The amplifier used is the low-noise and high-speed LT1226 (Linear Technology, USA) which features a gain bandwidth product of 1 GHz at ±12 V and a slew rate of 400 V/ms.
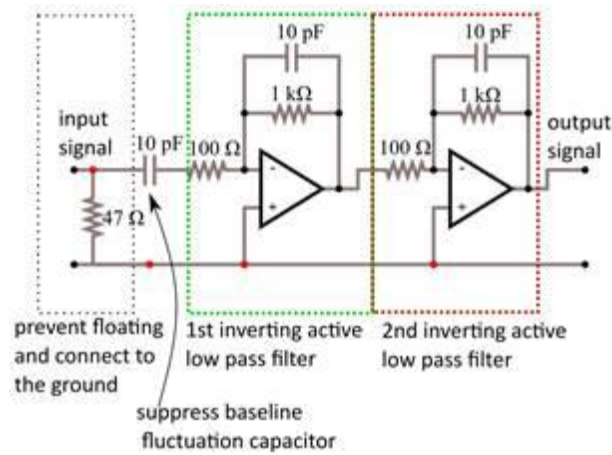
Figure 7.7: Schematic diagram of the double-inverting amplifier, active low-pass filters in the filter and amplifier boards.

An input pulse to this circuit, with a peak height of 80 mV and decay time of 1.6 µs, was found to correspond to an output pulse with a peak height of 5,000 mV and a decay time of 200 µs. This allows for a longer time for digitisation and analysis of the signal as well as reducing the likelihood of pulses being lost while being read in the DAQ. Each of these processed signals are input to a LM319MX dual high-speed comparator (Texas Instruments, USA [37]), where the peak amplitude of the pulse is compared to a user-adjustable reference voltage, which is set above the electrical noise and background levels. When the input voltage is above this reference threshold, it is treated as an 'event'. For each layer in the imaging system, there is a PCB featuring 32 LM319MX dual comparators (±12 V) which can compare 64 analogue signals, simultaneously, in 80 ns. The output is sent to a voltage divider, comprising two 10-kΩ resistors (shown in Figure 7.8), resulting in a 'high' output pulse of 6 V.
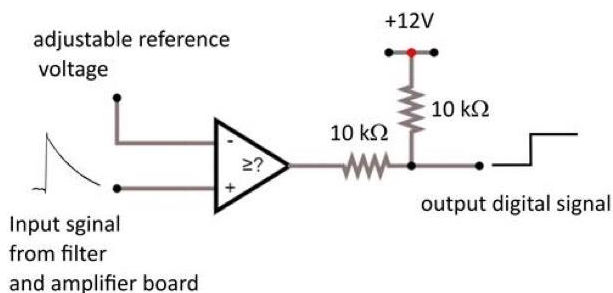
Figure 7.8: Main building block circuit for the comparator PCB.

These digital signals are then sent to the TOF circuit, which generates digital pulses to trigger a time-to-digital Converter (TDC) module via the start/stop input. The TOF circuit uses a series of rising-edge, trigger logic OR gates which determine whether any of the outputs from the comparators are non-zero at time 't'. This output is sent to the TDC7200EVM (Texas Instruments) evaluation module (used to operate and evaluate the TDC7200 TDC) to trigger the start/stop clock. This module possesses an input measurement range between 12 ns and 500 ns, with a resolution of 30 ps - a range that roughly matches that of the scattered neutron TOF anticipated in these experiments. Within the measurement range of the TDC7200EVM (12 ns to 500 ns) and the separation distance between layers 1 and 2 (30 mm), it would be rational to evaluate the minimum and the maximum TOF time boundaries of the circuit. Using the kinetic energy equation (equation 7.2), one can find the TOF for a scattered neutron losing 50%, 90% and 99% of its energy to a proton in EJ-204. Table 7.2 shows the TOF calculations for a scattered neutron with original kinetic energies of 0.001 MeV, 0.01 MeV, 0.1 MeV and 1 MeV. The examples are used to illustrate the relation between the incident neutron energies, percentages of energy losses in the scattering reactions and the corresponding TOFs. Based on this, one can estimate neutrons TOF that can be successfully detected in the TOF circuit and hence the minimum and maximum neutron energies that can be measured by the imaging system. The table indicates that within the current TOF circuit,

scattered neutrons with energies equal to or above 0.1 MeV will fall outside the TDC7200EVM measurement range if they lose 50% or less of their initial energies. Similarly, neutrons with incident energies lower than 0.001 MeV will not be detected by the TOF circuit if they lose 99% of their initial energy in the scattering reaction.

Table 7.2: Estimated neutron TOFs and velocities measured in the current prototype configuration.

	Neutron Energy (MeV)			
	1	0.1	0.01	0.001
Energy (MeV) and TOF after 50% energy loss after scattering (ns) (velocity m/s)	3.1 (9.8×10^6)	9.7 (3.1×10^6)	31 (9.8×10^5)	97 (3.1×10^5)
TOF after 90% energy loss after scattering (ns) (velocity m/s)	6.9 (4.4×10^6)	22 (1.4×10^6)	69 (4.4×10^5)	220 (1.4×10^5)
TOF after 99% energy loss after scattering (ns) (velocity m/s)	22 (1.4×10^6)	69 (4.4×10^5)	220 (1.4×10^5)	690 (4.4×10^4)

In addition, the TOF circuit generates a list of the digital addresses of all SiPM pixels that are activated, based on the first arrived/first recorded approach. This list will facilitate data reconstruction of the Compton camera and the neutron scattering sub-system since events generated in the SiPM array are time correlated according to their order of arrival. Figure 7.9 shows the direction of logical operations in the TOF board starting with arrival of pulses from the comparator board to the transmission of the activated 8-bit address to the USB2633 DAQ digital port.

The pulses from each comparator are simultaneously sent to a D-type flip-flop (MC14174M, ON Semiconductors) which will store a value of 1 when the corresponding comparator has a high output, at the same time as the clock (given by the output of the OR gate in level 3 – see Figure 7.9) is at a rising edge. The output of the flip-flop will return to 0 when the corresponding comparator has a low output at the next rising edge of the clock input. Note that the clear input pin on the flip-flop is always high, as this input is connected directly to a constant +12 V supply. The flip-flops are in groups of 8 and the outputs of the flip-flops in each group are sent to an 8-input 8-bit priority encoder (CD4532B, Texas Instrument) which encodes the location of whichever flip-flop has a high output to a 3-bit binary code output. This output represents the address of the corresponding SiPM pixel that has registered an event. Each encoder also has another output, GS, which goes high if any of the inputs are high, i.e. if an event was registered by any of the corresponding flip-flops. As 8 of these encoders are needed to encode the address of the 64 pixels, it is necessary to discriminate between the output of each encoder to acquire a unique complete address. The three binary outputs from each encoder (Q1, Q2 and Q3) are consolidated using three 8-input OR gates, resulting in a single 3-bit address. Furthermore, the GS outputs from each encoder are fed into another 8-input 8-bit priority encoder. The output of this encoder gives the address of the other encoders (0-7) that had registered an event. These two 3-bit addresses therefore uniquely identify the pixel that registered an event as it occurs. These six values are eventually saved in a .csv file, the data transferred via the digital input of the USB2633 DAQ. While each SiPM array has a corresponding TOF circuit, for the third layer it is only used to generate the digital address list. That is, there is not a TDC board connected to the third layer.
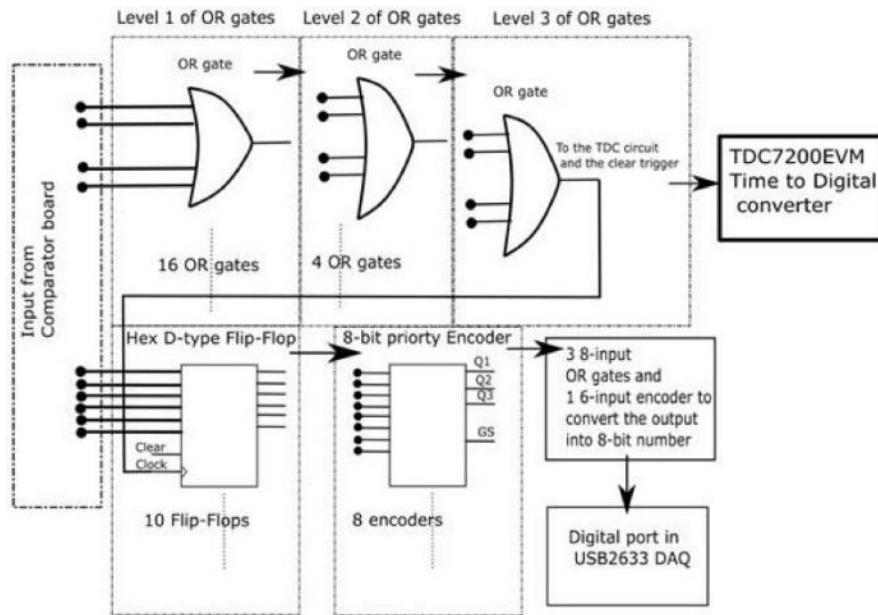
Figure 7.9: Architecture of the TOF board.

7.4.3 Control zone

In order to process the data coming from the ASRC, three pieces of software are used in this system. A Python code (v3.6.5) is first used to serially acquire the data from the 64 analogue ports and 1 digital port from each of the three DAQs utilised. The code utilises the mcculw module [38] to communicate and read the data from the DAQs before saving the data from each layer in individual .csv files. The digital port in each DAQ reads the 8-bit digital data stream that contains the addresses of the pixels that have been activated and saves this in another.csv file. Also acquired here is the analogue TOF data stream generated from the TDC7200EVM module which utilises a LABVIEW GUI [39] to interact with the user and generate more .csv files in which TOFs are saved in general number format. In total, seven .csv output files are generated after the 60-second data acquisition cycle for the activity of the sources described in the next section (section 7.4.4). Six of these output files use the Python code interface, while the TOF data is instead relayed to the computer via a LabVIEW™ interface. A

MATLAB® [40] script has been developed for analysing and reconstructing the data from these seven .csv files. For each layer, the 8-bit addresses are converted into channel numbers and then using a while loop, the voltage is read from the analogue output files of the corresponding layer and assigned to the channel number. Depending on the type of event, the measured voltages are converted into energy, probability cones are created and the image plane reconstructed. The flowchart shown in Figure 7.10 illustrates the steps taken within the MATLAB® algorithm.

Open files using csvread function

3 Analog output csv files containing the voltage recorded from each SiPM pixel/
3 Digital output csv files containing addresses of all channels where the threshold has been exceeded alongside time order.
1 ToF csv file containing the time of flight data

Initiating matrices

Determine the number of channels registered in each of the digital output files for each layer using the 'ischar' MATLAB function to create matrices which data will be saved to.

Saving digital addresses into matrices

Use a while loop to read and store channel numbers from the digital output files for each layer

Within a 'for' loop. find all possible Compton scattering event combinations and then find the scattering angles using equation 1

Within a 'For' loop, convert the analog voltages into energy using an energy calibration curve

Gamma rays

Assign voltage values to digital addresses

Use a while loop to find the corresponding voltage from the analog output files f or each digital address.

Close files

Plot probability cones and reconstruction image

Find all possible neutron scattering event combinations falling within a 500 ns time window (set based on the ToF between layers 1 and 2 calculated for a 1keV neutron (fast neutron cut off) after losing 99% of it is energy which is by default the maximum time window for the TDC7200 circuit)

Fast Neutrons

Within a 'for' loop: 1. convert voltage into energy using energy calibration curve 2. finding scattering angles using equations 2 and 3

Plot heat map of triton and alpha energy deposition

Within a 'for' loop, convert voltage into energy using energy calibration curve

Thermal neutrons

Figure 7.10: Flow diagram illustrating how the MATLAB® algorithm creates the probability cones and constructs source image.

7.4.4 Radioactive source details

Two sealed radioactive sources have been used for the testing of the device; Cs-137 and Cf-252. The Cs-137 used had a total activity of 315 kBq at the time of use. A high proportion (94.7%) of the beta particles produced during its decay lead to Cs-137 disintegrating to an excited state of barium, which decays subsequently via a 662 keV gamma-ray, corresponding on this basis to a total of 300,000 gamma rays emitted by this source each second. The Cf-252 source at Lancaster University is encapsulated with aluminium and had an activity of 18.8 MBq at the time of use. This source is held inside a double-walled, fibreglass tank of water of volume ~1 m^3 that, in turn, is located inside a mild-steel enclosure. Cf-252 decays via either α emission or spontaneous fission, with a branching ratio of 96.91% and 3.09%, respectively [41]. 3.759 neutrons on average are emitted per spontaneous fission event, thus yielding a total number of 2.18 x 10^6 n/s into 4π with an average energy of *c.a.* 2.1 MeV, and most probable energy of *c.a.* 0.7 MeV [42]. The average energy of the associated gamma-ray component is 0.8 MeV with average prompt fission multiplicity of 8.3 gamma rays per fission event [43].

7.5 Experimental Setup

Figure 7.11 shows the experimental setup with detector enclosure assembly (front-end), voltage supplies and the readout electronics ASRC. Using a Gaussian fit of the counts against voltage, the 662 keV gamma-ray photo-peak was detected in the lithium glass at 0.36 V and resolution in terms of a FWHM of (0.23 ± 0.02) V. Similarly within CsI(Tl), the 662 keV gamma-ray photo-peak was detected at 0.44 V and resolution in terms of a FWHM of (0.37 ± 0.01) V. Figure 7.12 shows a plan schematic of the experimental setup used for the neutron measurements. The source-to-detector enclosure distance can

be broken down into several components. First, there is the 50 mm distance between the detector enclosure and the source tank, and then there is a 242 mm gap between the Cf-252 source and the edge of the tank. This equates to a total source-to-detector distance of 292 mm. However, for simplicity, the source tank to detector enclosure distance (50 ± 1) mm is defined for the rest of this paper as the source-to-detector distance.
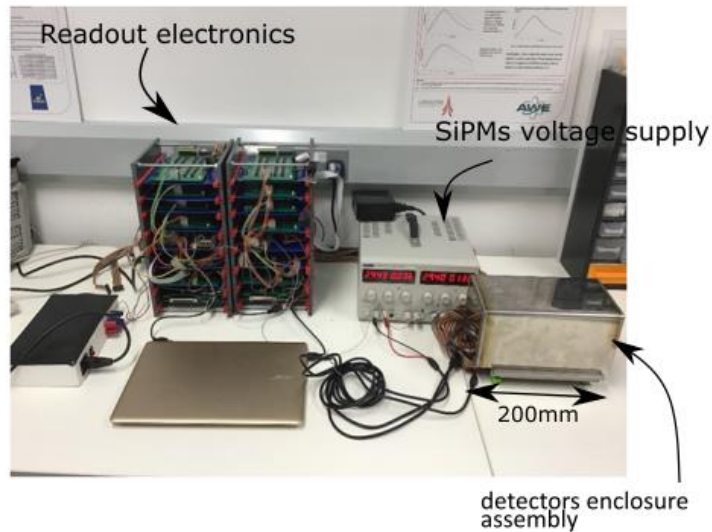
Figure 7.11: A photograph of the gamma-ray detection experiment setup. The sealed Cs-137 gamma source will be positioned just out of view of this photograph, on the right-hand side.
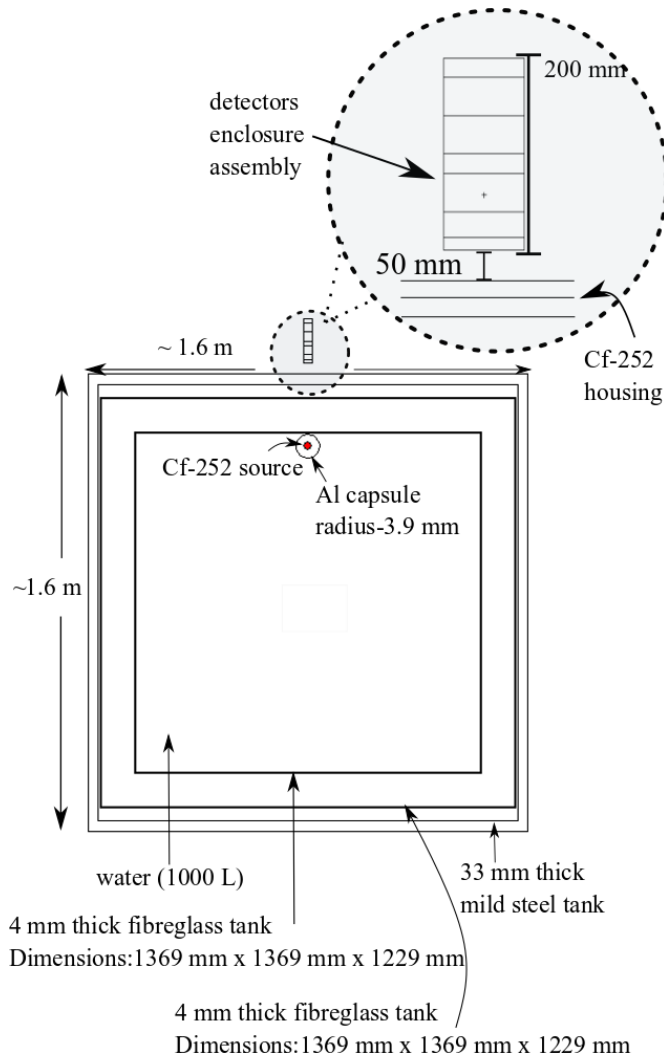
Figure 7.12: A plan view (schematic) of the experimental setup for the neutron measurements performed in this research.

7.6 Monte Carlo Simulations

The system was designed and verified using Monte Carlo simulations in MCNPv6.1.0 [44]. The cross sections used in this work for neutrons simulations are from the ENDF/B-VII.1 library, with room temperature assumed throughout (293K). For gamma-ray analysis, the Evaluated Photon Data Library (EPDL) and the Activation Library (ACTL) compilations from Livermore data libraries were used [44]. In all subsequent simulations, the geometry of the detection system and material

characteristics were as defined in section 7.2. In addition, the absence of significant levels of background radiation within the experimental setup allows the comparison of experimental measurements with simulation results and enables the verification of experimental results. The analysis for all radiation types described here is based on the output of the PTRAC card, FMESH tally and F8 pulse height tally. Adding the PTRAC card to an MCNP input file creates an output file detailing particle tracks through the system with complete information of collisions and interactions depending on the keywords added to the input card. An overview of the cards used in the PTRAC file, FMESH card and F8 tally are shown in Figure 7.12, illustrating the layout of the output files with brief highlights of the main elements. The PTRAC input file includes the output control keyword FILE=ASC that instructs the software to generate an ASCII output file type, with the command WRITE=ALL indicating that the location in Cartesian coordinates and directional cosines of the particle should be written to the output file along with the particle energy for each interaction, the weight and the time. The control keyword TYPE=n, p, t, a, h specifies the particle types in the PTRAC output file (denoting neutrons, photons, tritons, alpha particles and protons, respectively). Furthermore, the control keyword MAX=100000 controls the maximum number of events to be written within the PTRAC file. The output file generated by the use of the PTRAC card is subsequently analysed in MATLAB®.

The FMESH card generates a user-defined mesh tally laying over the surface or cell of interest with Cartesian geometry used throughout the FMESH based simulations. For the Monte Carlo simulations used in this research, the main facets of the scintillators in the detector module are defined in the y-z plane, and hence the locations of the fine mesh points are specified in these two directions, with keywords JINTS=60 and KINTS=60 defining 60 fine mesh points in each orientation. The F8 tally is defined in

MCNP6 as a pulse-height tally, and thus the output of this tally is a register of the energy distribution of pulses within a cell by the defined radiation particle and any subsequent secondary particles. In contrast to the case of photons, when neutrons are evaluated using the F8 tally, an inconsistency can arise because of differences in the way neutrons transport through matter. To overcome this error, the F6 MCNP energy deposition tally (in units of MeV/g) is used to determine the secondary particles generated by a neutron interaction. For example, the triton and alpha generated as a result of neutron capture in Li-6, is used in coincidence with the F8 tally with a pulse-height light tally with the anticoincidence (PHL) option added to the tally specification card (FT). The following MCNP code is an example of an F8 tally card executed to generate a distribution of pulses from neutrons capture reactions in lithium glass through the interactions of the secondary particles:

- F6:a (cell number)

- F16:t (cell number)

- F8:a (cell number)

- FT8 PHL 1 6 1 LIG-1

- F18:t (cell number)

- FT18 PHL 1 16 1 LIG-1

LIG-1 and CSI-1 are keywords for the lithium glass and CsI(Tl) scintillators that enable the use of a special tally treatment used when scintillators are selected. The numbers following the tally number, FT and PHL are the F6 tally number for this detector region followed by the pairing numbers of the tally number (6 or 16) and the tally bin number, which is the one in the example given here. More details of these keywords is available in the MCNP manual [45]. The way the cones are plotted can be described in several stages:

1) The PTRAC file is imported into the MATLAB environment.

2) The number of histories is ascertained in order to initiate counting matrices.

3) Using a 'while' loop and 'If' statement, events of interest are determined.

4) The appropriate equations are used to find scattering angles and energies of gamma rays and neutrons (see section 7.2).

5) Cones are plotted leading to probability map generation.
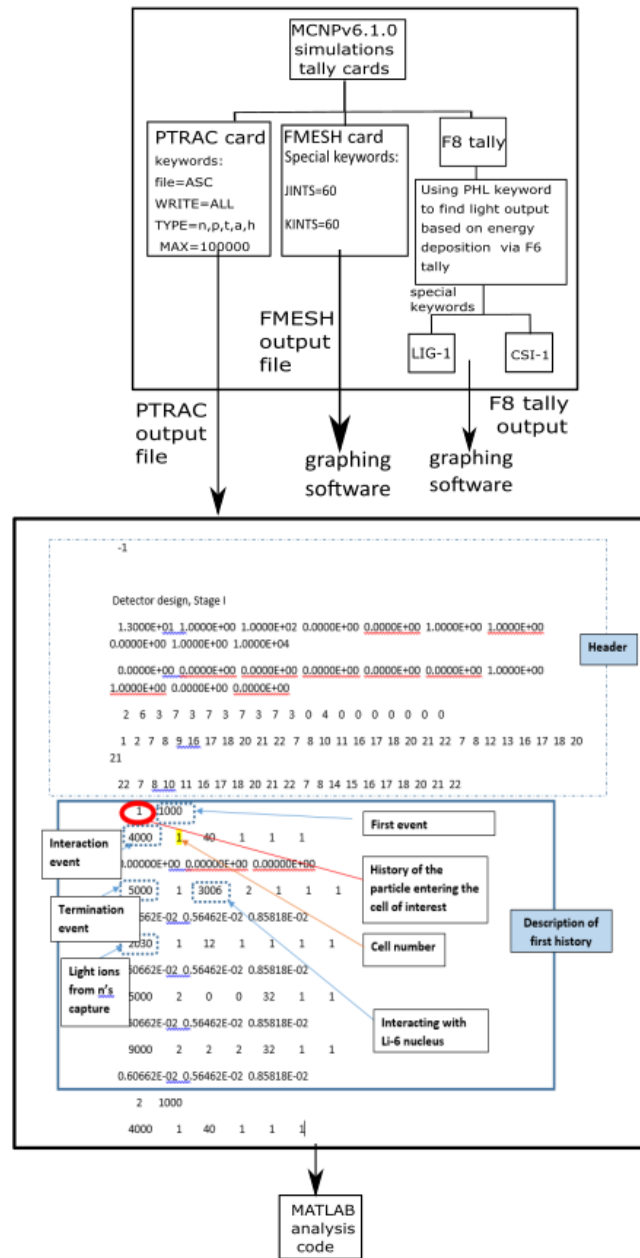
Figure 7.13: A schematic diagram illustrating MCNPv6.1.0 input parameters and simulation output analysis.

7.6.1 Simulation results for the gamma-ray detection sub-system

7.6.1.1 Detection efficiency of the Compton-scattering sub-system and the localisation of a gamma-ray source

Simulations of the complete front-end system exposed to a single Cs-137 source (as defined in section 7.4.4) were conducted. The number of particles specified in the MCNPv6.1.0 environment was 298,305, with 1,106 of these events registered in the PTRAC output file. The positions, the energy deposited by gamma-ray interactions and the associated scattering angles were determined within the layer 2 15-mm lithium glass and layer 3 CsI(Tl), using a combination of the MATLAB® code described above and equation 7.3. The output is illustrated in Figure 7.14 with the source located centrally 50 mm in front of the first detection layer; denoted here with an 'X'. It can be observed visually here that the pixel located at (3, 5) shows the highest probability of source location, a position within one pixel of the actual location; a distance of 3.375 mm. Due to the statistical nature of this technique, it is necessary to consider the surrounding pixels of the actual source position. The intensity in the pixel of the actual source location and the 16 pixels surrounding it combined is (31.2 ± 0.5) % of the total predicted fluence – an average of 1.95% in each pixel. The pixels outside this area receive on average 1.43% of the total predicted fluence each. Thus, there is a rise of 36% in the pixels around the correct source location. The intrinsic efficiency has been simulated too indicating the total number of radiation quanta detected in the Compton scattering sub-system of 13 events per second (a figure verified using repeated simulations). Given the detector cross sectional area (7.29 cm^2), an estimate of the geometric efficiency of the detector of 0.023 follows. Given the activity of the Cs-137 source, 6,861 photons would be expected to reach the active detector surface in the specified period of time.

Thirteen events were recorded indicating an intrinsic efficiency of 1.89 x 10^{-3} at 0.662 MeV.
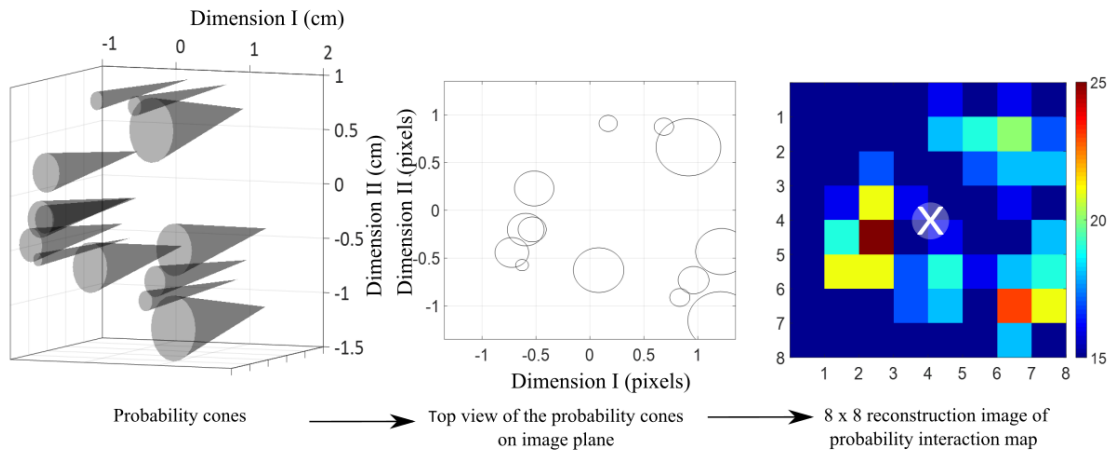
Figure 7.14: A schematic diagram illustrating the steps of image reconstruction applied to yield the response of the system to a gamma-ray source ('X' indicates the source location in simulations). The intensity units are arbitrary.

7.6.1.2   Source localisation ability of the Compton scattering sub-system

The source localisation ability of the Compton scattering sub-system was determined using the Cs-137 source placed at four different locations, relative to the front of the detector system, as illustrated in Figure 7.15, with the results shown in Figure 7.16. The pixel corresponding to the real location of the source, along with the 8 surrounding pixels, represents 63.9% of the total fluence recorded by the camera, an average of 7.1 ± 0.1 % per pixel compared to 0.7% of the total fluence on average per pixel outside of this area. Similarly, Figure 7.16 (b) indicates 69.3% of the fluence in the nine pixels around the real source location (7.7 ± 0.2 % per pixel compared to 0.9% outside of it), Figure 7.16 (c) shows 60.3% of the fluence in the nine pixels (6.7 ± 0.1 % compared to 0.7% outside of this) and finally Figure 7.16 (d) shows 71.1% of the fluence observed

from within the nine pixels surrounding the real source location (7.9 ± 0.1 % compared to 0.9% outside of this area).
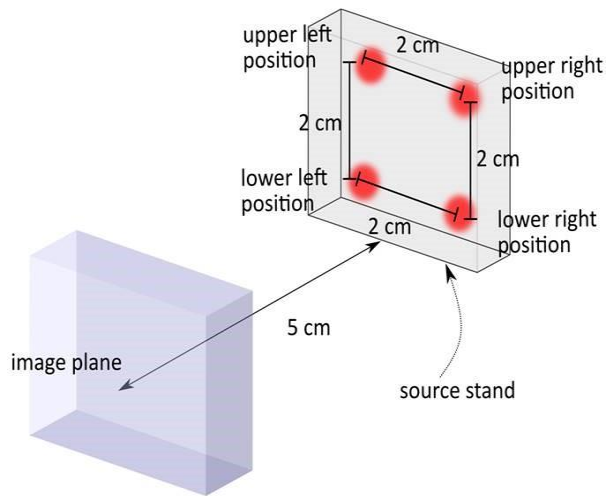
Figure 7.15: A schematic diagram of the four different locations of the Cs-137 source relevant to the image plane.
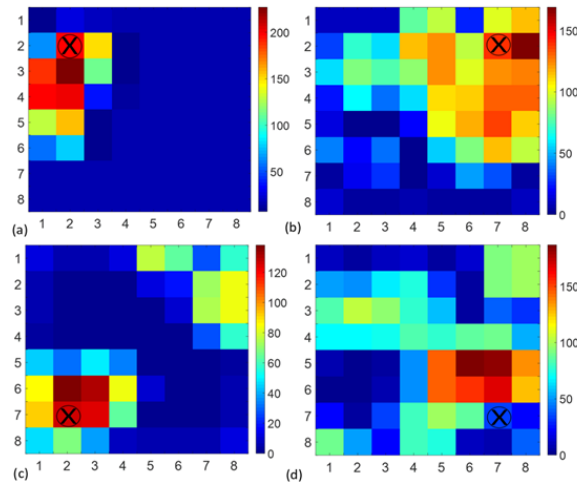
Figure 7.16: The reconstructed images derived from the results of simulations of the response of the system to changing the position of the Cs-137 source (a) upper left, (b) upper right, (c) lower left and (d) lower right. The colour map indicates image intensity and $\otimes$ the source position in the simulations relative to the imaging system.

7.6.1.3 Angular resolution of the Compton scattering sub-system

The ability of the system to differentiate between two, closely-spaced gamma-ray sources was investigated in order to estimate the angular resolution of the system. Three different angular spacing scenarios were explored, namely 40º, 15º and 5º. The resulting reconstructed images with two Cs-137 sources 40º (29 mm) apart, 15º (10.5 mm) apart and 5º (5 mm) apart are shown in Figure 7.17. The number of PTRAC events recorded was 1736. In Figure 7.17 (a), the points at which the ellipses intersect appears to be shifted upward relative to the location of the source defined in the simulation geometry. Nonetheless, these results indicates that the system can differentiate between two sources with a minimum angular spacing of 15º.
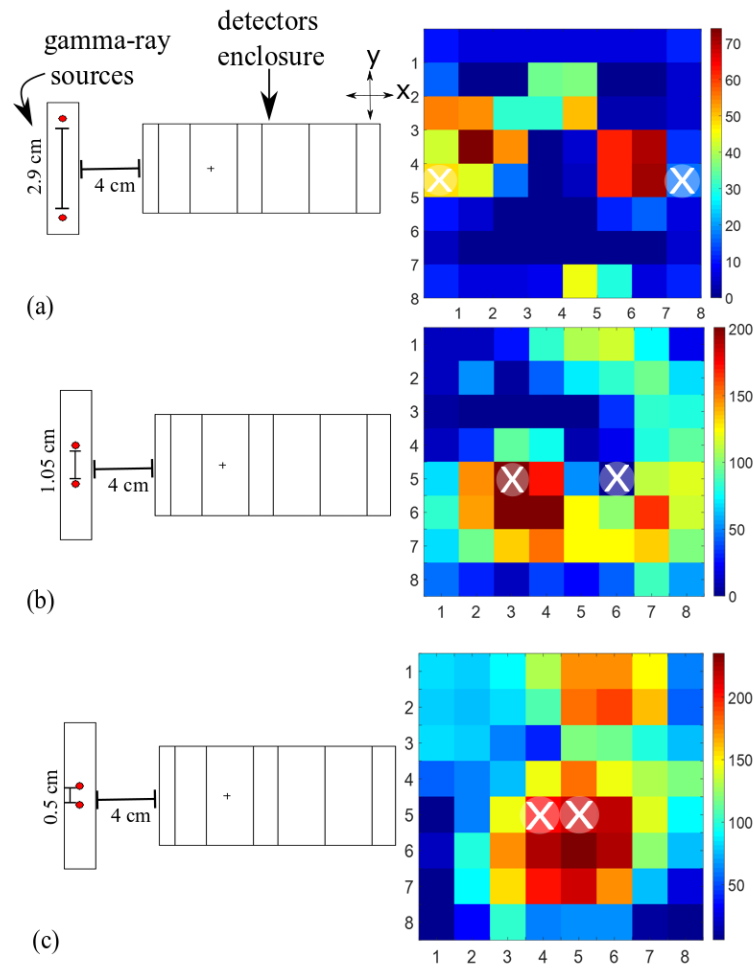
Figure 7.17: A schematic diagram of source position with respect to detector enclosure and the reconstructed images of the computational analysis of two Cs-137 sources 40º (29 mm) apart, 15º (10.5 mm) apart and 5º (5 mm) apart (colour map shows image intensity and $\otimes$ indicates source location specified in the simulation geometry).

7.6.2 Simulated results of the thermal neutron detection system

The response of the system exposed to thermal neutrons was simulated using the Cf-252 source set-up as illustrated in Figure 7.12. The Cf-252 source is defined using the Watt approximation of the corresponding fission spectrum using the Spontaneous

Fission (SP) keyword with appropriate constants in the source card [33]. In order to generate a high proportion of thermal neutrons, an 11-mm thick polyethylene slab was included in the simulation geometry between the instrument and the source tank to act as a moderator. The F2 card was utilised in the MCNPv6.1.0 input file to estimate the number of thermal neutrons incident on the instrument. Considering the number of neutrons output from the polyethylene slab is 4.16×10^{-6} per initial neutron, the thermal neutron fluence was determined to be 81 n/cm^2 over the 60 s period. Therefore, the expected number of thermal neutrons is 591 over the whole of the 2.7 cm × 2.7 cm detector area. The F8 tally card was added to the MCNPv6.1.0 input file which was used to investigate the number of triton particles generated by the thermal neutrons capture reactions and subsequent energy pulse height generation in the lithium glass detector. The details of the F8 tally card used in the input file are indicated in section 7.6. In the Monte Carlo environment, 478 tritons are simulated as being generated within the lithium glass layer indicating a simulated intrinsic efficiency of $(81 \pm 4)\%$.

7.6.3 Simulation results for fast neutron detection system

7.6.3.1 Detection efficiency of the neutron scattering sub-system and localisation of the neutron source

The response of the system when located 50 mm from the front of the Cf-252 neutron source tank was simulated using the PTRAC card to generate the data required in equations 7.2 and 7.3, using the keywords listed in Figure 7.13. The parameters registered in the PTRAC output file included interaction positions, energy depositions and TOF data. Equations 7.2 and 7.3 were then used to find the scattering angles and to

generate the probability cones, as shown in Figure 7.18. Based on these simulations, 8177 neutrons reached the detectors enclosure, 50 of which were recorded in the system as neutrons scattering events. This indicates an intrinsic detection efficiency of 6.1 x10^{-3} at 2.1 MeV (the average energy of neutrons from Cf-252 source).
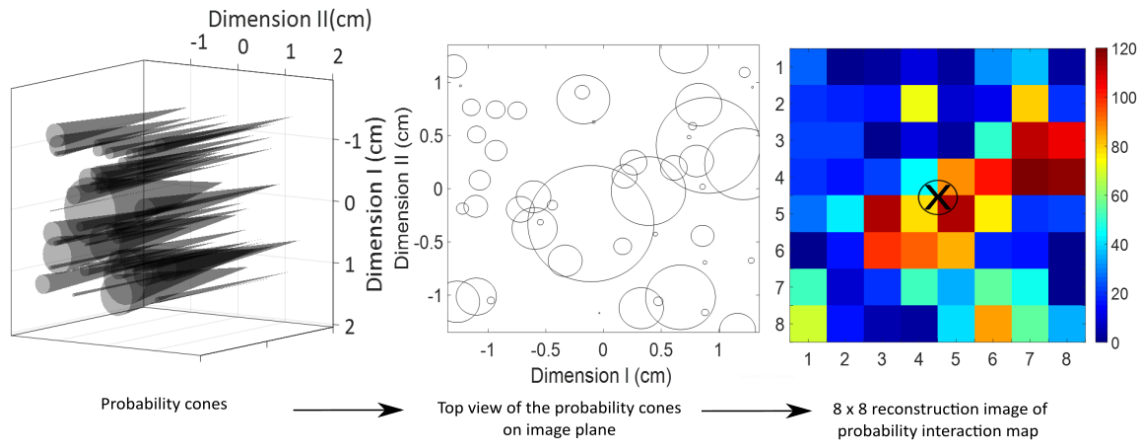
Figure 7.18: A schematic diagram illustrating the steps taken in image reconstruction to extract the response of the system to the neutron source ($\otimes$ is source location defined in the simulation geometry).

Figure 7.18 would suggest that the source is a scattered source with only 27.2% of the neutron flux predicted to be within one pixel of the real source location in this result. This can be compared to Figure 7.14, which illustrated a Monte Carlo simulation of the probability map achieved when the Cs-137 source was located 50 mm in front of the instrument. As expected, the Cs-137 results illustrate a point source as oppose to a scattered source. Based on these simulations, 8177 neutrons reached the detectors enclosure, 50 of which were recorded in the system as neutrons scattering events. This indicates an intrinsic detection efficiency of 6.1 x10^{-3} at 2.1 MeV (the average energy of neutrons from Cf-252 source).

7.7 Experimental results and discussion

7.7.1 Gamma-ray results

The experimental gamma-ray results are divided into three sets: the first two sets focus on the validation of the system exploiting Compton scattering to detect and locate gamma rays, and the third set on the abilities of the system to locate and differentiate different gamma-ray sources. Keeping in mind the activity of the gamma-ray source describe in section 7.4.4, all measurements (unless specified) were made over a 60 s time interval and repeated three times to yield an average. The uncertainties depicted by the error bars were determined in each case on the basis of one standard deviation of the mean in these results. The usual compromise, i.e. longer scan times yield more statistics and thus reduce uncertainties, has been sought. However, shorter scan times may be desirable in some applications where a faster camera may be preferable to one offering greater accuracy.

7.7.1.1 Compton events as function of time

The probability of Compton scattering events as a function of time was determined experimentally to determine the efficiency of the system. Figure 7.19 indicates the total number of Compton scattering events, which occur in the system as a function of time when the Cs-137 source is 50 mm away from the front detector plane. An average of 2.03 ± 0.01 events were observed per second whereas; the geometrical efficiency of 0.023 implies 6,900 gamma-ray photons were incident on the detector surface. The figure of 1.98 thus indicates an intrinsic efficiency of $(2.89 \pm 0.07) \times 10^{-4}$ at 0.662 MeV. This figure is consistent with the experimental reported value in the work done by

Poitrasson-Rivier et al. [22] who also reported an efficiency in the order of 10^{-4}. This measured efficiency is 15 % lower than the MCNPv6.1.0 results in section 7.6.1.1.
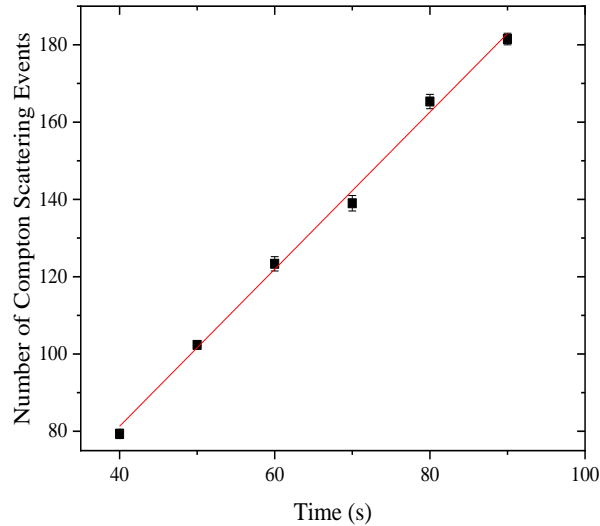
Figure 7.19: Number of Compton-scattered events versus time for the Compton scattering sub-system. The fit of the points indicates a linear relationship between the number of Compton scattering events and time with a slope of (2.03 ± 0.01) counts per second and R^2 value of 1.0

7.7.1.2 Compton events as a function of distance

For further confirmation of the successful operation of the system, a graph of the count rate as a function of distance is provided in Figure 7.20. The inverse-square law would suggest that the exponent in the fit line would be -2 instead of -2.28 ± 0.01.
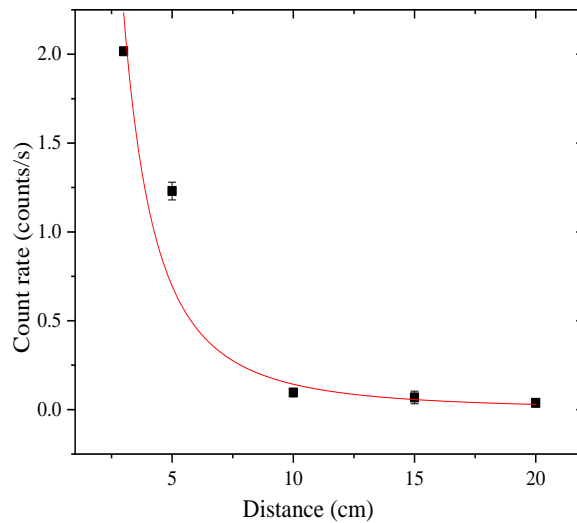
Figure 7.20: Count rate vs. distance for Compton camera sub-system. The fit display an exponential decay with decay constant of (-2.28 ± 0.001) counts/cm and R^2 value of 0.99.

7.7.1.3 Source localisation ability of the Compton scattering sub-system

In order to verify the ability of the system to identify individual sources and to locate the source position, the Cs-137 source was moved to four different locations close to the four different corners of the active area of the system, and 50 mm from the image plane, as illustrated in Figure 7.15. The system responds to this change in source position with relatively high accuracy as illustrated in Figure 7.21, in which reconstructed images as a function of changing source position are presented. It can be seen that the location of the source is identified successfully in each scenario. Figure 7.21(a) shows that 26.0% of the predicted flux is within one pixel of the real source location. The corresponding value is 35.4% in Figure 7.21(b), 43.3% in Figure 7.21(c), and 34.2% in Figure 7.21(d). This appears to indicate relative consistency across all four locations with between 26.0% and 43.3% of the flux correctly predicting the source location to within a pixel. Another way to quantify these results is to compare the peak-to-average values. In (a)

the maximum value is 25, compared to a total fluence over the 64 pixels of 600, an average of 9.2. This indicates a peak-to-average figure of 2.7, with corresponding figures of 7.8, 5.7 and 2.8 for results (b), (c) and (d) respectively. The equivalent simulated results shown in Figure 7.16 indicated that between 46% and 64% of the total predicted fluence was within one pixel of the real source.
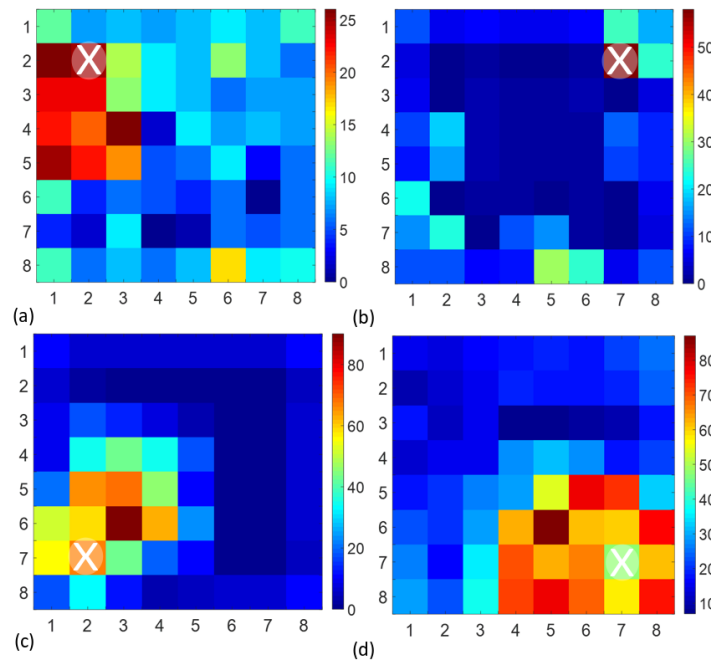
Figure 7.21: Reconstructed images of experimental results of the system response to four different Cs-137 source positions: (a) upper left, (b) upper right, (c) lower left and (d) lower right. $\otimes$ **marks the source position in the experiment relative to the imaging system.**

Experimental results reported here are comparable with MCNPv6.1.0 simulations results (section 7.6.1.2) in terms of locating the source within the right image plane corner. However, lower predicted fluence in the pixels surrounding the actual source locations in the experimental results might be due to limitations in the efficiency of the

imaging system compared to the simulation environment were all events are recorded in the PTRAC file.

7.7.1.4   Angular resolution of the Compton scattering sub-system

Two identical Cs-137 sources were used to determine the ability of the system to differentiate between two closely-spaced, gamma-ray point sources. Figure 7.22 indicates the geometry of the three experiments via plan diagrams, alongside the corresponding reconstructed images with two Cs-137 sources 40º (29 mm) apart, 15º (10.5 mm) apart and 5º (5 mm) apart. It is clear that in situations (a) and (b) the sources can be discerned from one another, whereas in situation (c) the two are indistinguishable, indicating that the angular resolution of the system is probably between 15º and 5º. Another way to look at these results is to look at the maximum value recorded compared to the lowest value between the two peaks. In these three scenarios, the lowest to highest values recorded were 4.0%, 7.4% and 100% in the 40º, 15º and 5º scenarios, respectively. Although the simulated (shown in section 7.6.1.3) and practical results are not identical, the outcomes are similar in that the system's angular resolution is in the order of 15º. The discrepancy in the results might be due to limitations in the efficiency of the imaging system.
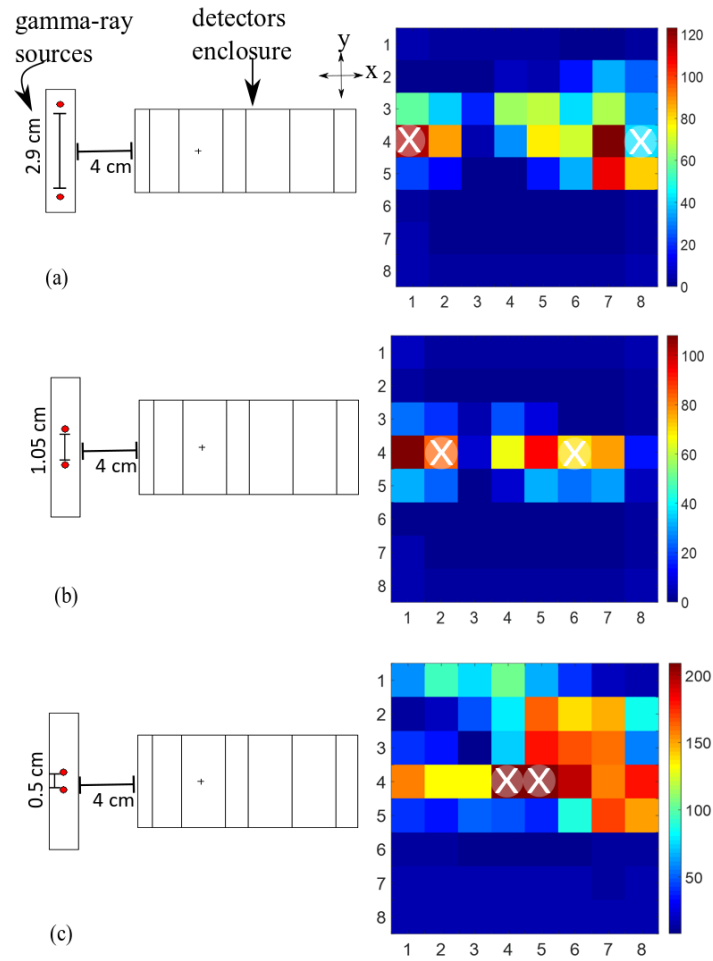
Figure 7.22: A schematic diagram of source position with respect to the detector enclosure and the reconstructed image of two gamma-ray sources 40º (29 mm) apart, 15º (10.5 mm) apart and 5º (5 mm) apart (colour map shows image intensity and $\otimes$ indicates source locations).

7.7.1.5 Gamma source within transportation devices

One of the main goals of this research is to test the capability of the design to detect and locate radiation sources in real-time in security applications. To fulfil this goal, trafficking scenarios of hidden gamma sources have been replicated using two realistic transportation devices. Initially, an IM2720 Peli® case [46] made of ABS plastic with an average thickness of 12 mm and external dimensions of 432 mm× 553 mm× 254 mm

was used as an example transportation device. These cases are toughened specifically to enable transportation of expensive and delicate items such as instrumentation equipment. Secondly, a shipping box made of cardboard with a thickness of 9 mm and external dimensions of 255 mm x 260 mm x 260 mm was used. Figure 7.23 provides some photographs of the experimental setup and the response of the system to these two scenarios using Cs-137 sources. The results indicate that the instrument can detect and locate a Cs-137 source successfully, either within a Peli® case or a cardboard box within 60 s for gamma sources of ~300 kBq. In both cases, the probability map indicates that the source is predicted to be either at its real location or within the adjacent eight pixels.
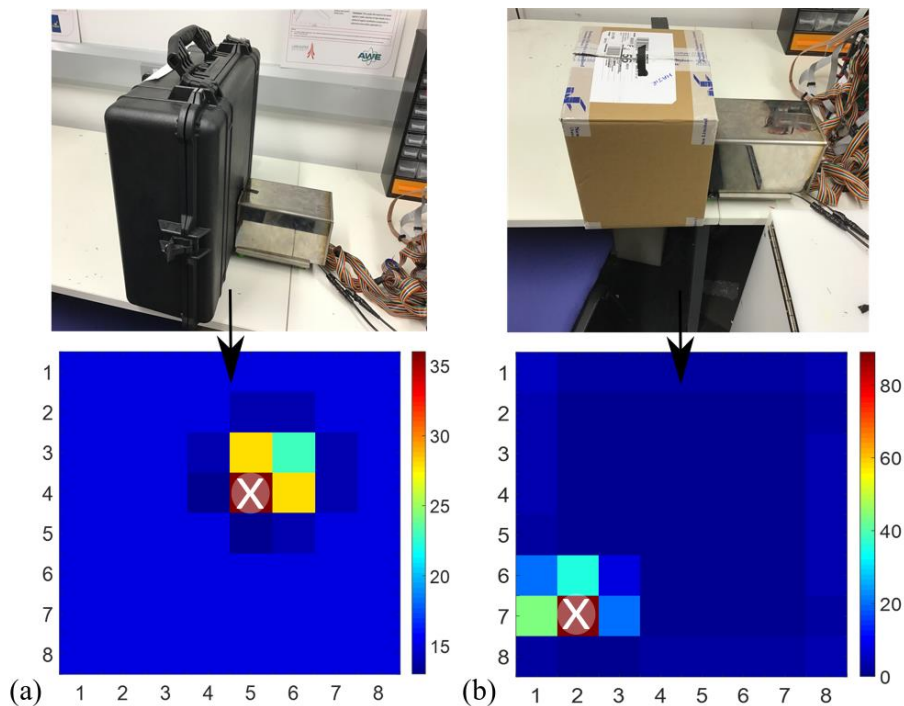
Figure 7.23: The experimental setup (top) and system response (below) to a hidden Cs-137 source in (a) Peli® transportation case and (b) cardboard shipping box with colour bars showing image intensity in arbitrary unit (⊗is the source location in the experiment setup).

7.7.1.6 The gamma-ray component of the Cf-252 source

Here, the gamma-ray Compton camera sub-system was isolated and utilised to monitor the gamma-ray component of the Cf-252 source. A 60-mm thick slab of polyethylene was placed between the instrument and the source in order to block a significant proportion of the neutron output from the source, allowing a significant gamma ray component to reach the detector with reduced neutron fluence. Figure 7.24 shows the experimental setup in the laboratory and illustrates the combination of the Cf-252 source, polyethylene slab and instrument. Figure 7.25 shows the Compton scattering sub-system response map obtained with this experimental set-up. It should be noted that, within this output, results in the upper-right corner of the instrument are shadowed by the stainless steel enclosure.
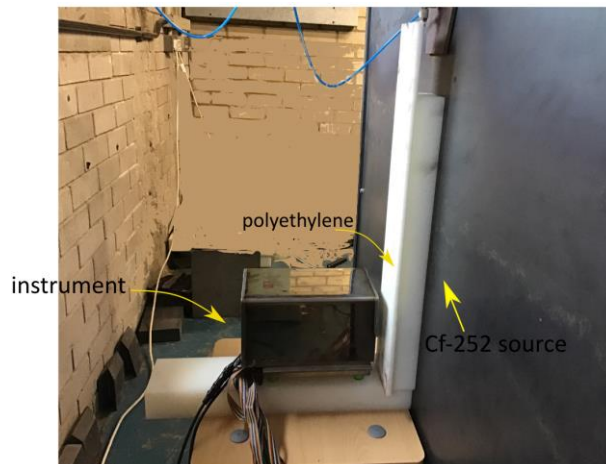
Figure 7.24: A photograph of the experimental setup for the gamma-ray experiment with the detection instrument, polyethylene slab and Cf-252 source tank.
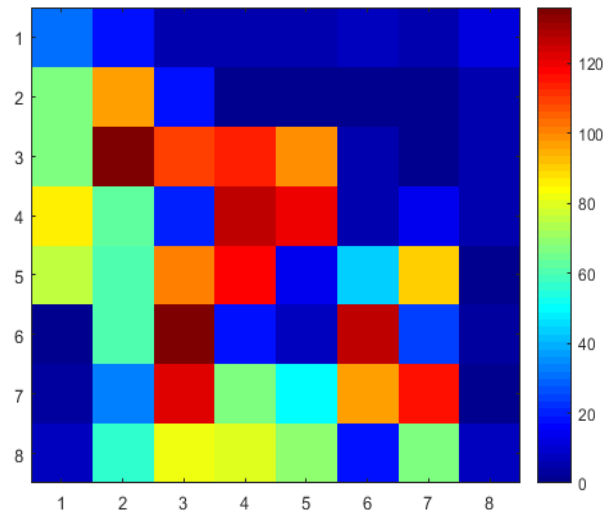
Figure 7.25: The reconstructed Compton-scattering, sub-system response to the gamma-ray component from Cf-252 with colour bars showing image intensity in arbitrary unit.

7.7.2 Thermal neutron results

To investigate the system response to thermal neutrons, an 11-mm thick polyethylene moderator was placed between the instrument and the Cf-252 source tank in order to thermalise the neutron fluence. The response of the system is shown in
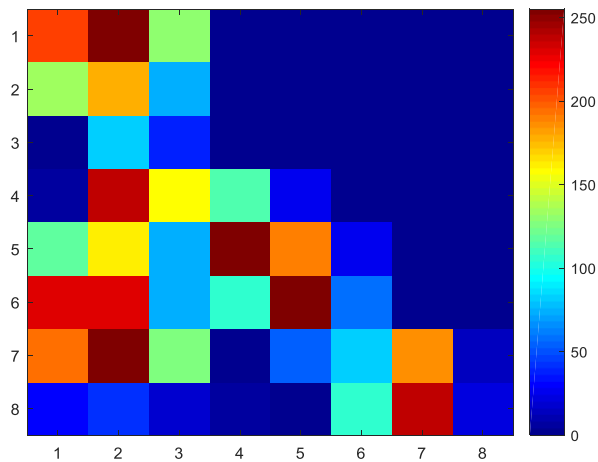
Figure 7.26. As described in section 7.6.2 above, the expected number of thermal neutrons incident on the detector as estimated via MCNPv6.1.0 simulations is 600 neutrons/s. Taking an average from five repeated experiments, the number of pulses generated in the lithium glass detector in the first layer is (460 ± 20) neutrons/s. Based on these calculations, the measured intrinsic detection efficiency is (78 ± 4) %, compared to the simulated value of (81 ± 4) % from section 7.6.2. Work by G. Ban et al [47] reports a comparable detection efficiency of (80.6 ± 2.3) % in GS10 for low energy neutrons in the ultra-cold region.
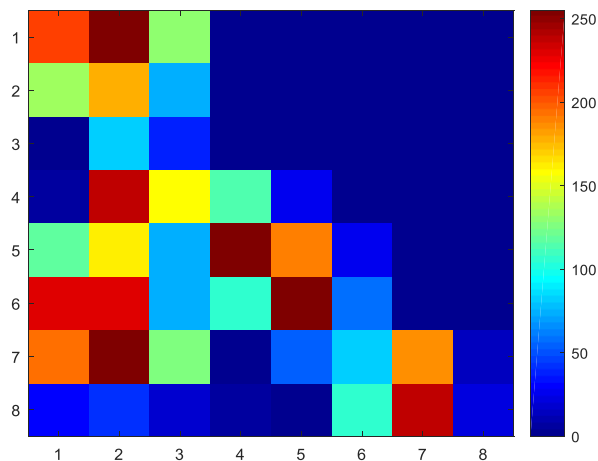
Figure 7.26: Reconstructed system's response to thermal neutrons from Cf -252 with colour bars showing image intensity in arbitrary unit.

7.7.3 Fast neutron results

7.7.3.1 The response to fast neutrons

The response of the neutron scattering sub-system was investigated by measuring the number of fast-neutron scattering events as a function of time at 50 mm from the Cf-252

source. Figure 7.27 indicates the number of fast-neutron scattering events in the first two layers as a function of time with the number of events increasing linearly as expected. 2.18×10^6 neutrons produced per second by the source multiplied by the calculated geometrical efficiency of 0.00258 indicates an expected 5,600 neutrons/s incident on the active area of the detector. Figure 7.27 indicates that an average of (4.2 ± 0.1) scattering events are being recorded per second, a figure that equates to an intrinsic efficiency of $(7.49 \pm 0.2) \times 10^{-4}$. This number roughly compares with the detection efficiency reported by Poitrasson-Rivier et al. [22], which was of the order of 10^{-4}.
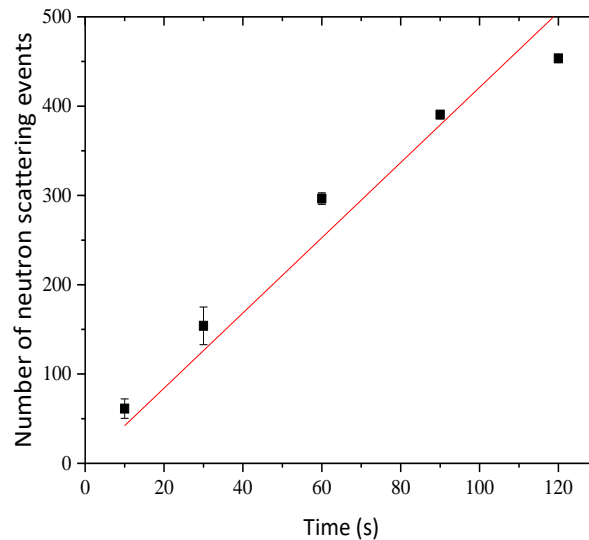
Figure 7.27: Neutron scattering events as function of time in the neutron scattering sub-system. The fit of the points indicates a linear relationship between the number of neutron scattering events and time with slope of (4.2 ± 0.1) counts per second and R^2 value of 0.99.

7.7.3.2 Collimated and un-collimated neutron beams

The response of the system was further investigated using alternate source geometry. Figure 7.28 shows a comparison of the system response between the standard non-

collimated Cf-252 source and a collimated pencil beam, with 50 mm between source and detection plane. The collimated version was formed using a 50 mm thick polyethylene slab with an 8 mm diameter hole. Results achieved indicate quite clearly through simple visual inspection the change in the system's response to the source geometries. As expected, the counts when collimation is not used are generally far higher than in the collimated version. The result for the un-collimated source, indicate that 26.3% of the predicted radiological source is correctly assigned within one pixel of the real source location. This compares to the collimated source where 55.0% of the predicted radiological source is assigned correctly to within one pixel of the real source. An alternative way to report this is to say that in Figure 7.28(a) the peak to average figure is 3.99 where as in Figure 7.28 (b) the figure is 8.56. This indicates the ability of the neutron detecting sub-system to detect both a point source (emitting neutrons over 4π) and a beam-like source geometry.
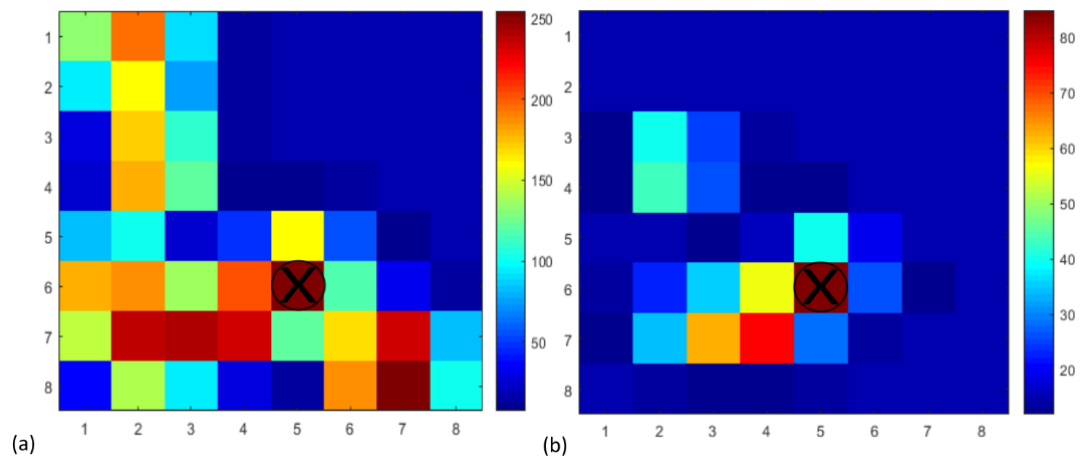
Figure 7.28: Reconstruction images of neutron scattering sub-system response to (a) non-collimated and (b) collimated Cf-252 source (colour bars shows image intensity).

7.8 Discussions and Future Work

For gamma-ray photons at energy of 662 keV, MCNP6 simulations indicated intrinsic detection efficiency in the order of 10^{-3}, whereas experimental results showed detection efficiency in the order of 10^{-4}. Similarly, for neutrons emitted from Cf-252 source, MCNP6 simulations indicated intrinsic detection efficiency in the order of 10^{-3}, whereas experimental results indicated intrinsic detection efficiency of 10^{-4}. In both cases, the differences between simulation results and experimental results are anticipated to be due to the limited speed of the DAQ. For thermal neutrons, simulation results indicated intrinsic detection efficiency of (81 ± 4) % compared to the experimental results demonstrating detection efficiency of (78 ± 4) %. In here, the experimental result falls within the range of the MCNP6 simulation result. The prototype instrument fulfils the criteria of detecting both gamma rays and neutrons within a relatively short time period of 60 seconds for gamma sources of ~300 kBq and neutron sources of 10^6 neutrons per second in close proximity of <300 mm. However, there are some significant issues and limitations: the testing that has been undertaken has involved source locations close to the detection plane. If the sources were located at a more realistic distance from the instrument, it would be expected that the statistics would be reduced significantly. The efficiency that has been recorded in both the gamma-ray and neutron cases is of the order 10^{-4}, which is comparable to efficiencies reported in other multi-layered Compton scattering imaging systems. Spatial resolution of the instrument has been estimated at <15% and more >5%, although the exact figure is difficult to ascertain due to the digitisation of the visual results achieved. So where does this instrument sit in comparison to other neutron and gamma localising instrumentation? The Germanium Gamma Ray Imager [9] has been developed at the Lawrence Livermore National laboratory, with dimensions of 300 mm x 150 mm x 230 mm and a mass of 15 kg. The

sensitive range is reported as between 30 keV and several MeV, with Compton scattering techniques also used within the instrument at higher energies (>150 keV). Spectral resolution is reported at being 2.1 keV (at 662 keV) with spatial resolution reported as being at 6 % [9]. The Gampix [6-8] is another gamma camera (known commercially as ipix) created at CERN and based on a coded mask and cadmium telluride sensor attached to a medipix 2 segmented photon counter. The instrument only weighs 1 kg and, dependent on rank of coded aperture chosen, offers spatial resolution of between 1.5 % and 2 %, and an energy range between 59 keV (i.e. the Am-241 peak) and 1.25 MeV (i.e. the Co-60 mean peak). The Advanced Portable Neutron Imaging System (APNIS) was developed at Oak Ridge National Laboratory in order to initially detect and locate 14.1 MeV neutrons generated by a D-T source. The neutron detection part of the system consists of an 8×4 array of fast plastic scintillators segmented into 100 pixels that are read by four photomultipliers whose shared response determines the pixel of interaction [48]. The Radscan 2 system developed by Whitney et al. [5], involves the use of a coded aperture and a CLYC scintillator. Although numerical results are limited, visually the work presents very impressive images when either gammas or neutrons are solely utilised. Goldsmith et al. [49] report a 40 kg instrument which utilises Compton scattering to localise gamma rays and the time of flight between two layers of EJ-309 liquid scintillators to localise neutrons, and present an efficiency of 45%. The work of Gamage et al. [50] also presents some visually impressive images although values for parameters such as spatial or spectral resolution are not readily available in the literature. The paucity of comparable numerical data within the literature thus renders it difficult to perform a thorough comparison of individual instruments.

There are several improvements, which may benefit the instrument in its current state. A larger detection plane than the current 27 mm x 27 mm may be an obvious

implementation to improve efficiency. The current photon sensor in a 2 x 2 configuration would suggest a geometrical efficiency improvement of a factor of 4 times, although there will always be a trade-off between portability and detection efficiency. Utilisation of longer scan times would obviously improve statistics whilst diminishing significantly one of the strengths of the device. Use of an Application Specific Integrated Circuit (ASIC) could allow integration of all of the circuits within one PCB that could in turn be integrated within the system enclosure, thus minimising the overall footprint of the system and enhancing the mobility. However, such a solution can be financially restrictive in an instrument designed to be cost effective.

The TOF circuit currently presents a problem when false-positive scattering events occur. Currently, the process involves a start signal generated in layer 1 and an independent stop signal generated in layer 2. Therefore, if a neutron passes through layer 1 without interaction and then interacts in layer 2, an orphan stop signal is generated and thus false-positive events are recorded. With the probability of successful neutron scattering events estimated to be of the order of 10^{-4}, this can have significant impact on the performance of the system. A proposed solution to this shortcoming is in the addition of a trigger circuit such that a stop pulse is only generated if a pulse is first recorded in layer 1, and if a pulse exceeds the threshold voltage set by the comparator board. Another potentially significant area of improvement is in the increase in the measurement range of the TOF. The TDC7200EVM module has a measurement range between 12 ns and 500 ns where, based on Table 7.2, scattered fast neutrons with scattering energies of around 0.1 MeV and above may fall outside of this range. A wider TOF measurement range can greatly improve the energy range of detected fast neutrons by the system.

Further, instead of interrogating each individual pixel, pulses could be integrated over each row and column of the SiPM array. This alteration to the current configuration could reduce power consumption in the overall circuit while maintaining the pixelated integrity of the system. In addition, because more current is allowed in each integrated row or column, the response of the circuit to deposited energy will show enhanced linearity. The signal from each row/column can be then sent to a reduced number of 16 filter and amplifier circuits for each layer of the design, reducing current consumption by a factor of four. Currently, four PCBs are utilised per layer with 64 channels filtered and amplified simultaneously, which can result in large and unbalanced currents drawn from the voltage supply. This sometimes causes an unbalanced current problem which can have a significant impact in the amplitude of the resultant signals and hence the energy resolution of the detected pulses.

The means of discriminating neutron and gamma pulses represents the most significant future work in this dual particle imaging system. The Pulse Shape Discrimination (PSD) principle [51, 52] is based on the differences in shape between the pulses from the scintillation process that are produced due to the interaction between the target radiation field and detection medium; an area of research well investigated in literature [53-58]. The shape and the height of the pulses depend on the interaction mechanism between the radiation and the detection medium, the energy of the incident radiation field and the light production mechanism in the medium [53]. Figure 7.29 shows time dependent differences for gamma-ray and neutron pulses in lithium glass as an example.
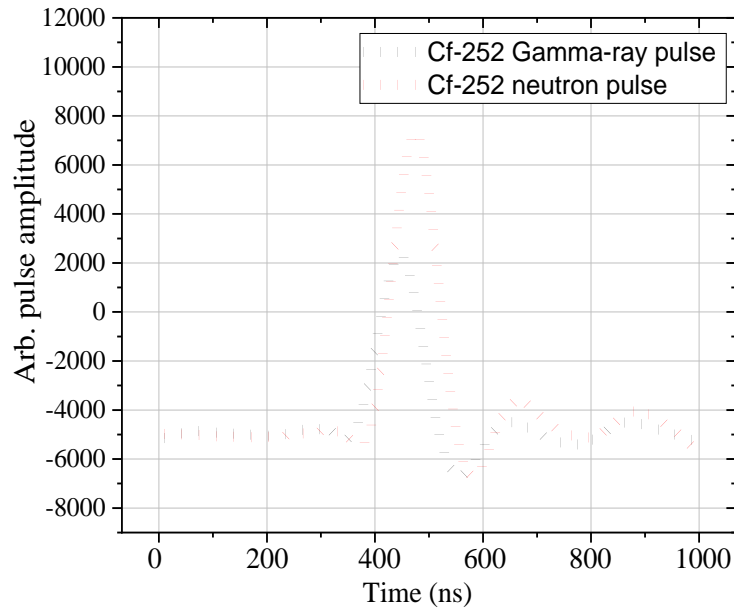
Figure 7.29: Raw gamma-ray and neutron pulses from Lithium glass crystal (GS10).

EJ-204 was utilised within this system to scatter fast neutrons, as it is a general-use plastic scintillator, although it is somewhat sensitive to low-energy gamma rays, and thus more sophisticated pulse-shape analysis may be necessary if this scintillator is retained. The very short 2.2 ns pulse from the EJ-204 would further require an ultra-fast analysis ASRC. An investigation into alternative scintillators with more favourable gamma/neutron discrimination abilities such as EJ-276, may be advisable. An implemented coded aperture system [59], could also greatly enhance the spatial accuracy of the imaging system and improve its resistance to background radiation, although detrimentally, the overall sensitivity and the field of view is typically reduced. Active electronic collimation techniques have been proposed in the literature as practical alternatives that offer higher signal-to-noise rejection and a wider field of view [60].

7.9 Conclusions

Within this extensive study, a compact imaging system capable of real-time simultaneous detection and localisation of gamma rays, thermal neutrons and fast neutrons has been investigated both theoretically and experimentally. The three layered imaging system features several scintillating materials including GS10 lithium glass, EJ-204 plastic scintillator and CsI(Tl) inorganic scintillator, in which Compton and neutron scattering techniques are utilised in parallel. Within all of these three layers, an 8 x 8 silicon photomultiplier array has been used as a compact method of capturing the scintillation protons produced within the detection layers. The 192 signals from the SiPMs are investigated individually, a process which requires a large volume of back end electronics and some high-speed components. Furthermore, algorithms have been produced in order to process the signals produced and produce in real-time a graphical output representing the radiological component of the incident field. Monte Carlo software was used to optimise and verify the design through comparison with experimental results gained subsequently with the instrument using Cs-137 as a gamma ray source and Cf-252 as a neutron and gamma source. Outcomes were that the instrument operates successfully within optimised scenarios – i.e. when single mode sources have been placed a few cm from the instrument. Within these limits, the instrument operates successfully with intrinsic efficiency of typically in the order of 10^{-4} and with spatial resolution of between 5% and 15%.

7.10 References

1. *Detection of radioactive materials at borders* 2002, Radiation Safety Section, International Atomic Energy Agency , Jointly sponsored by IAEA, WCO,EUROPOL and INTERPOL: Vienna, Austria.

2. IAEA, *IAEA Inicdents and Trafficking Database (ITDB) Incidents of nuclear and other radioactive material out of regulatory control*, in *2018 Fact Sheet*. 2018, International Atomic Energy Agency Vienna, Austria.

3. *Safeguards Techniques and Equipment*. 2011, International Atomic Energy Agency, IAEA.

4. Al Hamrashdi, H., S.D. Monk, and D. Cheneler, *Passive Gamma-Ray and Neutron Imaging Systems for National Security and Nuclear Non-Proliferation in Controlled and Uncontrolled Detection Areas: Review of Past and Current Status.* Sensors, 2019. **19**(11): p. 2638.

5. Whitney, C.M., et al., *Gamma-neutron imaging system utilizing pulse shape discrimination with CLYC.* Nuclear Instruments & Methods in Physics Research Section A: Accelerators, Spectrometers, Detectors and Associated Equipment, 2015. **784**: p. 346-351.

6. Gmar, M., et al., *GAMPIX: A new generation of gamma camera.* Nuclear Instruments & Methods in Physics Research Section a-Accelerators Spectrometers Detectors and Associated Equipment, 2011. **652**(1): p. 638-640.

7. Carrel, F., et al. *GAMPIX: A new gamma imaging system for radiological safety and Homeland Security Purposes*. in *2011 IEEE Nuclear Science Symposium Conference Record*. 2011.

8. Amoyal, G., et al., *Metrological characterization of the GAMPIX gamma camera.* Nuclear Instruments and Methods in Physics Research Section A: Accelerators, Spectrometers, Detectors and Associated Equipment, 2019. **944**: p. 162568.

9. Dreyer, J.G., M. T. Burks, and E. L. Hull, *Next generation germanium systems for safeguards applications*. 2014: Lawrence Livermore National Lab.(LLNL), Livermore, CA (United States).

10. Gal, O., et al., *CARTOGAM – a portable gamma camera for remote localisation of radioactive sources in nuclear facilities.* Nuclear Instruments and Methods in

Physics Research Section A: Accelerators, Spectrometers, Detectors and Associated Equipment, 2001. **460**(1): p. 138-145.

11. Aryaeinejad, R. and D.F. Spencer, *Pocket dual neutron/gamma radiation detector.* IEEE Transactions on Nuclear Science, 2004. **51**(4): p. 1667-1671.

12. Runkle, R.C., et al., *Lynx: An unattended sensor system for detection of gamma-ray and neutron emissions from special nuclear materials.* Nuclear Instruments and Methods in Physics Research Section A: Accelerators, Spectrometers, Detectors and Associated Equipment, 2009. **598**(3): p. 815-825.

13. Ayaz-Maierhafer, B., et al., *Angular resolution study of a combined gamma-neutron coded aperture imager for standoff detection.* Nuclear Instruments and Methods in Physics Research Section A: Accelerators, Spectrometers, Detectors and Associated Equipment, 2013. **712**: p. 120-125.

14. Soundara-Pandian, L., et al. *CLYC in gamma -Neutron imaging system.* in *IEEE Nuclear Science Symposium Conference Record.* 2012. Honolulu, HI, USA.

15. Enqvis, A., Flaska, M. and Pozzi, S., *Measurement and simulation of neutron/gamma-ray cross-correlation functions from spontaneous fission.* Nuclear Instruments and Methods in Physics Research Section A: Accelerators, Spectrometers, Detectors and Associated Equipment, 2008. **595**(2): p. 426-430.

16. Todd, R.W., Nighting.J. M, and Everett, D.B., *Proposed Gamma Camera.* Nature, 1974. **251**(5471): p. 132-134.

17. Everett, D.B., et al. *Gamma-radiation imaging system based on the Compton effect.* in *Proceedings of the Institution of Electrical Engineers-London.* 1977. IET Digital Library: London, UK.

18. Singh, M. and R.R. Brechner, *Experimental Test-Object Study Of Electronically Collimated SPECT.* Journal of Nuclear Medicine, 1990. **31**(2): p. 178-186.

19. Peterson, S.W., D. Robertson, and J. Polf, *Optimizing a three-stage Compton camera for measuring prompt gamma rays emitted during proton radiotherapy.* Physics in Medicine and Biology, 2010. **55**(22): p. 6841-6856.

20. Du, Y.F., et al., *Evaluation of a Compton scattering camera using 3-D position sensitive CdZnTe detectors.* Nuclear Instruments and Methods in Physics Research, Section A: Accelerators, Spectrometers, Detectors and Associated Equipment, 2001. **457**(1-2): p. 203-211.

21.   Polack, J.K., et al. *Dual-particle imager for standoff detection of special nuclear material*. in *2011 IEEE Nuclear Science Symposium Conference Record*. 2011. Valencia, Spain.

22.   Poitrasson-Riviere, A., et al., *Dual-particle imaging system based on simultaneous detection of photon and neutron collision events.* Nuclear Instruments & Methods in Physics Research Section a-Accelerators Spectrometers Detectors and Associated Equipment, 2014. **760**: p. 40-45.

23.   H. Al Hamrashdi, D. Cheneler, and S.D. Monk, *Material optimization in dual particle detectors by comparing advanced scintillating materials using two Monte Carlo codes.* Nuclear Instruments and Methods in Physics Research Section A: Accelerators, Spectrometers, Detectors and Associated Equipment, 2017. **869**(Supplement C): p. 163-171.

24.   H. Al Hamrashdi, S.D.Monk, D. Cheneler. *Design and Optimisation of a Three Layers Thermal Neutron, Fast Neutron and Gamma-Ray Imaging System*. in *Nuclear instrumentation and measurement methods in nuclear environments*. 2019. EPJ Web of Conferences.

25.   Knoll, G.F., *Radiation detection and measurment*. Fourth ed. 2010, New York, NY, USA: John Wiley and Sons.

26.   *6-lithium glass bespoke to your application*. [cited 2018; Available from: https://scintacor.com/products/6-lithium-glass/.

27.   *General Purpose Plastic Scintillators EJ-200, EJ-204, EJ-208, EJ-212*. 25/07/2019]; Available from: https://eljentechnology.com/images/products/data_sheets/EJ-200_EJ-204_EJ-208_EJ-212.pdf.

28.   *Csl(Tl) a rugged, non-hygroscopic alternative to NaI*. [cited 25/07/2019; Available from: https://johncaunt.com/materials/csl-tl/.

29.   *Stopping-Power & Range Tables for Electrons, Protons, and Helium Ions*. 02/08/2019]; Available from: https://www.nist.gov/pml/stopping-power-range-tables-electrons-protons-and-helium-ions.

30.   Bravar, U., et al. *Development of the fast neutron imaging telescope*. in *IEEE Nuclear Science Symposium Conference Record, 2005*. 2005.

31.   Mascarenhas, N., et al. *Development of a Neutron Scatter Camera for Fission Neutrons*. in *2006 IEEE Nuclear Science Symposium Conference Record*. 2006.

32. *J-SERIES SIPM: Silicon Photomultiplier Sensors, J-Series (SiPM)*. [cited 2019 15/05/2019]; Available from: https://www.onsemi.com/PowerSolutions/product.do?id=J-SERIES%20SIPM.

33. Spinelli, A. and A.L. Lacaita, *Physics and numerical simulation of single photon avalanche diodes*. IEEE Transactions on Electron Devices, 1997. **44**(11): p. 1931-1943.

34. Turchetta, R., *Analog electronics for radiation detection*. 2016.

35. van Eijk, C.W.E., *Inorganic Scintillators for Thermal Neutron Detection*. Ieee Transactions on Nuclear Science, 2012. **59**(5): p. 2242-2247.

36. *USB-2633 User's Guide*. [cited 2017 05/05/2017]; Available from: https://www.mccdaq.com/pdfs/manuals/USB-2633.pdf.

37. *LMx19 High Speed Dual Comparator*. [cited 2019 23/09/2019]; Available from: http://www.ti.com/lit/ds/symlink/lm319-n.pdf.

38. *mcculw 0.9.7*. Sep 5, 2017 [cited 2018 01/07/2018]; Available from: https://pypi.org/project/mcculw/.

39. Elliott, C., et al., *National Instruments LabVIEW: A Programming Environment for Laboratory Automation and Measurement*. JALA: Journal of the Association for Laboratory Automation, 2007. **12**(1): p. 17-24.

40. *MATLAB and Statistics Toolbox Release 2017b*. The MathWorks, Inc.: Natick, Massachusetts, United States.

41. NEA, O. *Java-based nuclear data information system*. 16/01/2016 [cited 2016 10/02/2016]; Available from: http://www.oecd-nea.org/janis/.

42. Martin, R.C., J.B. Knauer, and P.A. Balo, *Production, distribution and applications of californium-252 neutron sources*. Applied Radiation and Isotopes, 2000. **53**(4): p. 785-792.

43. Billnert, R., et al., *New prompt spectral γ-ray data from the reaction 252Cf(sf) and its implication on present evaluated nuclear data files*. Physical Review C - Nuclear Physics, 2013. **87**(2).

44. Goorley, J.T.J., Michael R.; Booth, Thomas E.; Brown, Forrest, et al., *Initial MCNP6 Release Overview - MCNP6 version 1.0*. 2012.

45. *MCNP6^{TM} User's Manual*. Los Alamos National Laboratory

46. *iM2720 Storm Case*. [cited 2019; Available from: https://peliproducts.co.uk/im2720-storm-

case.html?gclid=EAIaIQobChMIis3hyIKF5AIVhbHtCh2olgESEAAYAiAAE
gKOyfD_BwE.

47.   Ban, G., et al., *Ultracold neutron detection with 6Li-doped glass scintillators.*
        The European Physical Journal A, 2016. **52**(10): p. 326.

48.   Hausladen, P., et al. *Induced-Fission Imaging of Nuclear Material*. in *51 Annual
        Meeting of the Institute of Nuclear Materials Management*. 2010. United States.

49.   Goldsmith, J.E.M., M.D. Gerling, and J.S. Brennan, *A compact neutron scatter
        camera for field deployment.* Review of Scientific Instruments, 2016. **87**(8).

50.   Gamage, K.A.A., M.J. Joyce, and G.C. Taylor, *Investigation of three-
        dimensional localisation of radioactive sources using a fast organic liquid
        scintillator detector.* Nuclear Instruments and Methods in Physics Research
        Section A: Accelerators, Spectrometers, Detectors and Associated Equipment,
        2013. **707**: p. 123-126.

51.   Brooks, F.D., *A scintillation counter with neutron and gamma-ray
        discriminators.* Nuclear Instruments and Methods, 1959. **4**(3): p. 151-163.

52.   Brooks, F.D., R.W. Pringle, and B.L. Funt, *Pulse Shape Discrimination in a
        Plastic Scintillator.* IRE Transactions on Nuclear Science, 1960. **NS-7**(2-3): p.
        35-38.

53.   Owen, R.B., *The Decay Times of Organic Scintillators and Their Application to
        the Discrimination Between Particles of Differing Specific Ionization.* IRE
        Transactions on Nuclear Science, 1958. **5**(3): p. 198-201.

54.   Marrone, S., et al., *Pulse shape analysis of liquid scintillators for neutron
        studies.* Nuclear Instruments and Methods in Physics Research Section A:
        Accelerators, Spectrometers, Detectors and Associated Equipment, 2002.
        490(1–2): p. 299-307.

55.   D'Mellow, B., et al., *Digital discrimination of neutrons and γ-rays in liquid
        scintillators using pulse gradient analysis.* Nuclear Instruments and Methods in
        Physics Research, Section A: Accelerators, Spectrometers, Detectors and
        Associated Equipment, 2007. **578**(1): p. 191-197.

56.   Aspinall, M.D., et al., *The empirical characterization of organic liquid
        scintillation detectors by the normalized average of digitized pulse shapes.*
        Nuclear Instruments and Methods in Physics Research, Section A: Accelerators,
        Spectrometers, Detectors and Associated Equipment, 2007. **578**(1): p. 261-266.

57.   Liu, G., et al., *A digital method for the discrimination of neutrons and γ rays with organic scintillation detectors using frequency gradient analysis.* IEEE Transactions on Nuclear Science, 2010. **57**(3 PART 3): p. 1682-1691.

58.   Joyce, M.J., et al., *Real-time, digital pulse-shape discrimination in non-hazardous fast liquid scintillation detectors: Prospects for safety and security.* IEEE Transactions on Nuclear Science, 2012. **59**(4 PART 2): p. 1245-1251.

59.   Oda, M., *High-Resolution X-Ray Collimator with Broad Field of View for Astronomical Use.* Applied Optics, 1965. **4**(1): p. 143-143.

60.   Byrd, R.C., et al., *Nuclear detection to prevent or defeat clandestine nuclear attack.* IEEE Sensors Journal, 2005. **5**(4): p. 593-609.

8 Neutron/Gamma Pulse discrimination analysis of GS10 Lithium glass and EJ-204 plastic scintillators

H. Al Hamrashdi, S. D. Monk and D. Cheneler

8.1 Abstract

Two radiation sensitive scintillators known for their dual sensitivity to neutron and gamma-ray fields are investigated for their pulse discrimination abilities; a lithium glass GS10 inorganic scintillator and a fast organic plastic scintillator EJ-204. Each of these scintillators are optically coupled with an 8 x 8-silicon photomultiplier array to act as a photodetector. Pulse height analysis, the charge comparison method and pulse gradient analysis have all been applied here on neutron and gamma-ray events generated by a

Cf-252 source. The three discrimination methods were evaluated based on the figure of merit of the probability density plots generated. Within a GS10 crystal, it has been deduced that pulse height analysis and pulse gradient analysis possess greater abilities to discriminate between the two radiation fields compared to the charge comparison method with both showing a figure of merit of over one. The charge comparison method indicated a lower discrimination ability with a figure of merit around 0.3. When the EJ-204 detector was used, it was deduced that only pulse height analysis exhibits discrimination abilities with a figure of merit around 0.6, while the other two discrimination methods presented no distinction between the two radiation fields.

8.2   Introduction

Applications in which mixed neutron and gamma-ray radiation fields are involved have gained steady interest through the years, especially in the areas of non-proliferation [1-3], radiography and tomography [4-8] and medical imaging [9]. Two approaches made it possible for these applications to succeed: scintillation materials sensitive to both radiation fields and multi-detector systems. The field of scintillation materials sensitive to both radiation fields has gone through significant evolvement since the 1950s. It started with the practical investigation of organic scintillators with dual sensitivity in the late 1950s [10-12] to organic plastic scintillators and glass scintillators in the 1960s [12-14] to semiconductor detectors in the 2000s [15, 16] and recently to the new era of elpasolite family scintillators and new generation scintillators [17, 18]. Research on multi-detector systems aimed at investigating both radiation fields has exhibited a slow but steady increase through the years with the first reported multi-detector system described by Aryaeinejad and Spencer in 2004 in which side-by-side lithium isotope

loaded glass scintillators were used [19]. This was a handheld detection device with no imaging capabilities. In addition, the system was sensitive to background radiation with no direct means of collimation to eliminate background noise. Another dual neutron and gamma-ray imaging concept involves the use of organic and sometimes inorganic scintillator arrays arranged in parallel layers. Examples of this array-based design are the multi-layered electronic collimation based approach investigated by Polack et al. [20, 21] and the multi-layered coded-aperture based approach investigated by Ayaz-Maierhafer et al.[22]. A noticeable drawback in these designs are that the scintillators are integrated with PMTs that can be bulky and heavy. In addition, liquid organic scintillators (mainly EJ-309) and inorganic scintillators (usually NaI(Tl) and CsI(Tl)) are the most utilised scintillators in the majority of multiple detectors/multi-layered designs [20-22]. The next step forward from these instruments involves compact and fast scintillation materials that are sensitive to either or both radiation fields.

In this work, two scintillators with different properties are investigated for their abilities to be integrated in a highly compact, very fast (near real-time scale), dual particle, multi-layered imaging system. These two scintillation material are natural Lithium glass GS10 from Scintacor [23] (6.6 % total lithium content of which 7.59 % Li-6 and 92.41 % Li-7) and fast plastic scintillator EJ-204 from Eljen Technology [24] (commercial equivalents BC-404 and NE-104). In terms of neutron detection abilities, the GS10 detector possesses a thermal neutron capture efficiency of 90 % at a 20 mm thickness. In addition, GS10 possesses distinctively higher fast neutron backscattering and forward scattering abilities compared to other scintillation detectors including CLYC from the elpasolite scintillators family and EJ-309 from the liquid scintillator category [25]. Moreover, being a glass-based scintillator, GS10 boasts enhanced durability in harsh radiation environments. Among other commercial glass scintillators, GS10

possess moderate lithium content, which allows GS10 to be effectively more sensitive to both neutrons and gamma rays compared to other lithium glass detectors in the same commercial category [23]. On the other hand, EJ-204 is a multipurpose Polyvinyl toluene (PVT) organic plastic scintillator with 5.15 x 10^{22} hydrogen atoms/cm^3. It is characterised by a high-speed response with a 2.2 ns pulse width and 1.8 ns decay time. In addition, EJ-204 has the highest scintillation efficiency among other plastic scintillators with 10,400 photons/MeV.e- [24]. This collection of desirable characteristics ensures that EJ-204 is strongly favoured within neutron scattering applications, especially when compact designs and a fast Time-of-Flight (TOF) are major requirements [26].

8.3 Pulse discrimination analysis

Pulse discrimination analysis was reported in the literature as early as the 1950s [10, 11]. The most common technique of pulse discrimination analysis is known as Pulse Shape Discrimination (PSD), which takes advantage of the differences in the time constants of the scintillation pulses generated by gammas and neutrons. In inorganic scintillators, absorption of radiation energy excites electrons within the energy levels of the crystal or glass lattice. Impurities are key components in the scintillation process of inorganic scintillators via which self-absorption of emitted light is minimised [27], although pure crystal cases such as diamond are exceptions to this [27]. Commonly, within inorganic impurity-activated scintillators such as Ce–activated glass detectors and Tl-activated alkali detectors, the energy bands have impurity sites in which electrons might emigrate and eventually de-excite resulting in the emission of scintillation light [27]. A discussion on the difference in the response of inorganic

scintillators including glass scintillators is discussed widely in literature [27-30]. The outcome of these discussions suggest that different ionising radiations have different energy loss rates and therefore the scintillation process is different for different radiation fields. Similarly, organic scintillators are widely employed due to the nature of the scintillation process adopted in them [11, 31, 32]. As described by Brooks et al. [33], the innate molecular characteristics of organic scintillators is responsible for the luminescence process. Within the π-electronic energy levels of the unsaturated aromatic or heterocyclic molecules, there are the singlet states (S0, S1, S2 …) and triplet states (T0, T1, T2 …). Excitation or ionisation of electrons due to energy absorption to singlet states and then de-excitation to singlet states results in the prompt emission of scintillation light known as fluorescence. Fluorescence is characterised by a short lifetime between 1 ns and 10 ns (S1 level de-excitation). On the other hand, excitation from singlet states and de-excitation from triplet states results in a delayed and slower emission of scintillation known as phosphorescence. This type of emission is characterised by a longer wavelength and decay time and appears to be the predominant recombination process (~75% of the time) [27]. Scintillation luminescence varies with the energy loss rate in organic scintillators including plastic scintillators. Therefore, ionising radiations have varying energy loss rates and the scintillation process is thus different for each radiation field type [27]. More specifically protons generated via neutron scattering reactions in organic scintillators result in a higher number of triplet state based phosphorescence photons and more excited electrons compared to gamma rays. This gives neutron-generated pulses a longer decay time compared to other radiation fields [34]. There are two main PSD approaches for scintillators with PSD potentials: the analogue approach and the digital approach. Table 8.1 shows the most common PSD techniques based on these two approaches in the literature.

Table 8.1: Common PSD techniques in the literature.

Analogue approach	Digital approach
Pulse height analysis	Pulse height analysis
Zero-crossing	Zero crossing
Charge comparison	Charge comparison
	Optimal linear filter
	Pulse gradient analysis
	Frequency gradient analysis
	Artificial neural network
	Triangular filter
	Power spectrum analysis

The Pulse Height Analysis method (PHA) is based on comparing the total scintillation light generated by the radiation field. It is highly recommended for scintillation detectors in which the scintillation photon generation process shows no major difference when either heavy charged particle ionisation events and electron ionisation events occur [35]. In the zero-crossing technique, the pulse is converted into a bipolar pulse with the time interval between the starting point of the pulse and the point at which the pulse crosses zero measured. The Charge Comparison Method (CCM) is a well-established method in the field of PSD. Applied in both analogue and digital approaches, this method is based on comparing the integrals of the charge over two time intervals commonly known as the short integral and the long integral [12, 34]. The time intervals are selected based on the pulse characteristics of the detector under investigation. This method has been shown to be very successful within organic scintillators where a long decay time is commonly observed for scintillation photons generated by the ionisation caused by heavily charged particles.

Digital methods such as the optimal linear filter technique require the use of model data and labelled data template sets of expected neutron/gamma pulse shapes. Normalised gamma-ray and neutron pulses are the compared to the template sets to discriminate neutron from gamma-ray pulses [36]. The optimal linear filter process is lengthy and requires a substantial training data set. In addition, this method might not be applicable for very fast pulses where accurate digitisation needs an ultra-high speed digitiser (> GSa/s). Pure digital PSD techniques thrived after advances in semiconductor technologies, surface mount electrical circuit components and analogue-to-digital converters (ADCs). Data acquiring systems and Field Programmable Gate Arrays (FPGAs), in particular, allowed fast digitisation and analysis of data, which greatly enhanced the performance of these techniques. Within the field of organic scintillation detectors, these techniques have proven to be highly efficient [37-41]. Pulse gradient analysis (PGA), successfully first discussed by D'Mellow et al. [37], compares the gradient of a normalised pulse at a fixed point on the peak (known as the first integral) to a second gradient at a second point located at a fixed time interval from the first integral, and known as the second integral. Another digitally based method is Frequency Gradient Analysis (FGA) [39] where the pulse is transformed into the frequency domain. When a discrete Fourier transformation is utilised in the conversion method, PSD is performed by comparing the point at zero frequency to the point of the first frequency component in the discrete Fourier transform. A more comprehensive method is the artificial neural network method which compares the results to data sets [41]; the system being trained artificially or compared to previously approved data sets. However, the method requires substantial data sets, which might not be applicable to all scintillation detectors. The triangular filter method transforms the pulses using passive and active triangular shaping circuits with pulses compared to each other [42].

Power spectrum analysis is very similar to frequency gradient analysis where the pulse is transferred to the frequency domain [43].

To the knowledge of the authors, GS10 and EJ-204 scintillators have never been directly investigated for their neutron and gamma-ray discrimination abilities and with the rise of dual particle detection applications along with the previously outlined characteristics of these two detectors, this work offers a preparatory foundation for applications involving these two scintillation materials. The discrimination method criteria should fit the application intended in this research where a fast and low processing power digital technique is required for a dual-particle multi-layered design in which fast pulses from GS10 and EJ-204 are investigated. Three of the previously outlined methods follow these criteria, the PHA method, the CCM and the PGA method.

8.4 Experimental setup

The GS10 crystal used in this experiment had dimensions of 27 mm x 27 mm x 15 mm, whereas the EJ-204 plastic scintillator had dimensions of 27 mm x 27 mm x 20 mm. A Cf-252 source was utilised throughout the experiment to generate the required neutron particles and gamma-ray photons. Cf-252 is a spontaneous fission source with a half-life of 965 days and a branching ratio of 3.09% [44]. The energy spectrum of Cf-252 fission neutrons follow the Watt spectrum fit with an average neutron energy of 2.1 MeV, most probable energy of 0.7 MeV and a yield of 3.759 per spontaneous fission decay [45]. The average energy of associated gamma-ray component is 0.8 MeV with average prompt fission multiplicity of 8.3 gamma-ray photons per fission event [46]. The scintillation detectors assembly arranges the scintillators in series, with the GS10 scintillator located 3 cm behind the EJ-204 scintillator. The photodetector utilised in the

experiment is the 8×8 SiPM (ArrayJ-30035-64P-PCB 8 x 8 SiPM, SensL, Cork, Ireland [28]). These detection arrays are placed in optical contact with the scintillators within each layer, and are mounted on ARRAYJ-BOB3-64P (SensL) breakout boards. Each SiPM pixel has a designated simple current-to-voltage converter consisting of a 47 Ω resistor in series with the diode. A dual benchtop power supply was used to provide 29.4 V of reverse bias, which was applied across the resistor and diode. The assembly was placed 10 cm way from the water tank housing the Cf-252 source. Figure 8.1 illustrates the arrangement of the source and the detectors assembly in the experiment.
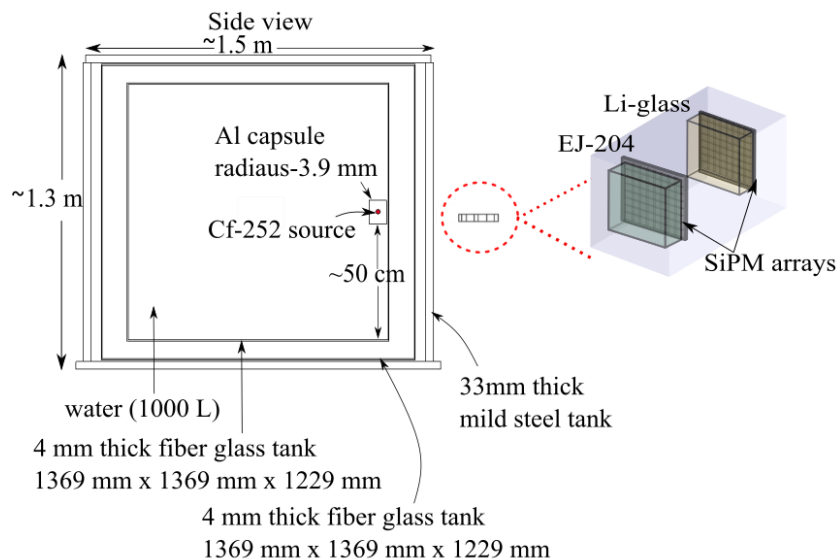
Figure 8.1. The Cf-252 source housing used in studying the response of the scintillation detectors along with the scintillation detectors assembly located in front of the tank. The GS10 scintillator is located 3 cm behind the EJ-204 scintillator.

In general, the response of the scintillators and SiPM arrays depends on a number of geometrical factors (such as the size and the shape of the scintillators, the optical coupling and the SiPM array geometry), and their physical characteristics (the dark pulses and electrical noise for this photodetector at ~1.1 μA at 29.4V). A simple

integration circuit was created with a 1 nF capacitor across the ports where the pulses are acquired using an Agilent 54845A Infiniium Oscilloscope with a sampling speed of 8 GSa/s and bandwidth of 1.5 GHz. Two dedicated MATLAB® programs (described in [47]) were used while conducting the experiment and subsequent analysis of the pulses. The first program mediated the pulses from the oscilloscope to the PC while the second program analysed the data. Over 10,000 pulses from the GS10 and EJ-204 scintillators were acquired and analysed in this work. Figure 8.2 shows a block diagram of the experimental setup. The pulses are sent to the Agilent 54845A Infiniium Oscilloscope via ribbon cables. The acquired data are then sent via an Ethernet cable to the control area.
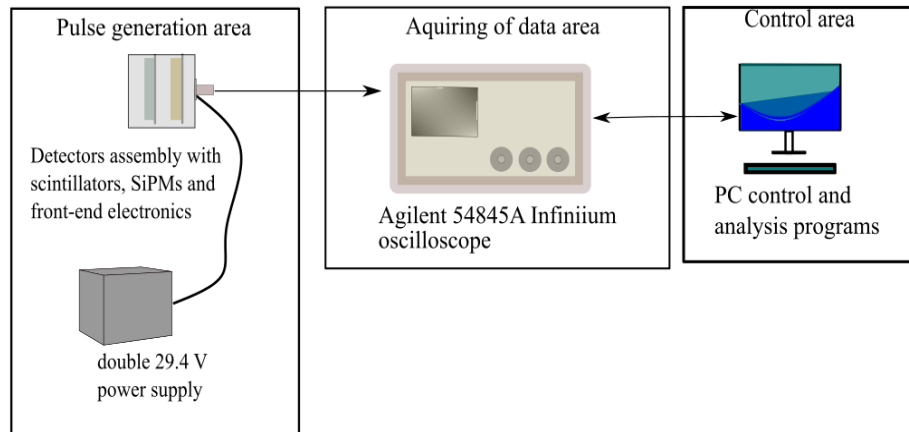
Figure 8.2. The main components in the experimental setup; (L-R): The pulse generation area with EJ-204 and GS10 scintillators and SiPM arrays, the data acquisition area comprised of Infiniium Oscilloscope and finally the PC control area.

The raw pulses acquired from the GS10 glass varied in amplitude and shape. Figure 8.3 shows examples of neutron and gamma-ray pulses directly generated from GS10 and visually digitised by the Agilent 54845A Infiniium Oscilloscope.
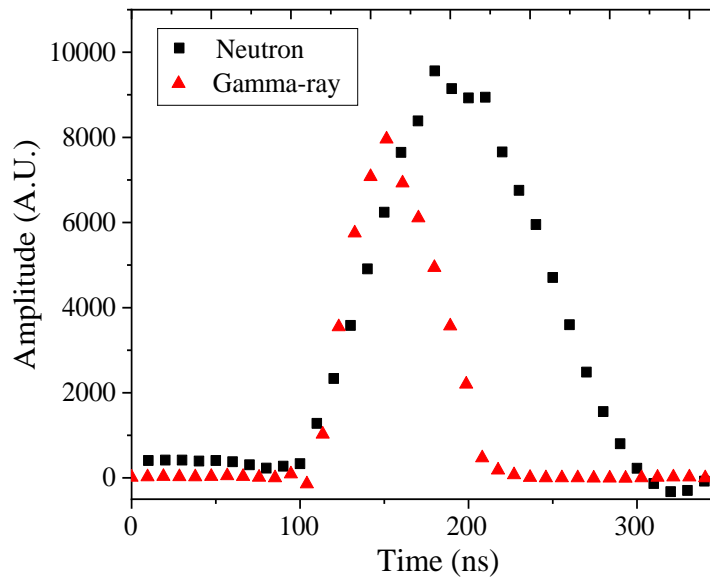
Figure 8.3. Examples of Cf-252 neutron and gamma-ray raw pulses acquired directly from the GS10 scintillator.

EJ-204 is characterised by its fast response and hence short scintillation pulse width, estimated to be 2.2 ns [24]. The high sampling speed of the Agilent 54845A Infiniium Oscilloscope allows the digitising of EJ-204 pulses with a rate of 1 sample every ~1/4 ns (taken by 8 GSa/s acquiring instrument but downed to 4 GSa/s) and hence the plotting and acquiring of the pulses as shown in Figure 8.4. However, the finite sampling rate of the acquisition system will affect the CCM and PGA methods where higher resolution representation of the pulses is essential for the success of these methods.
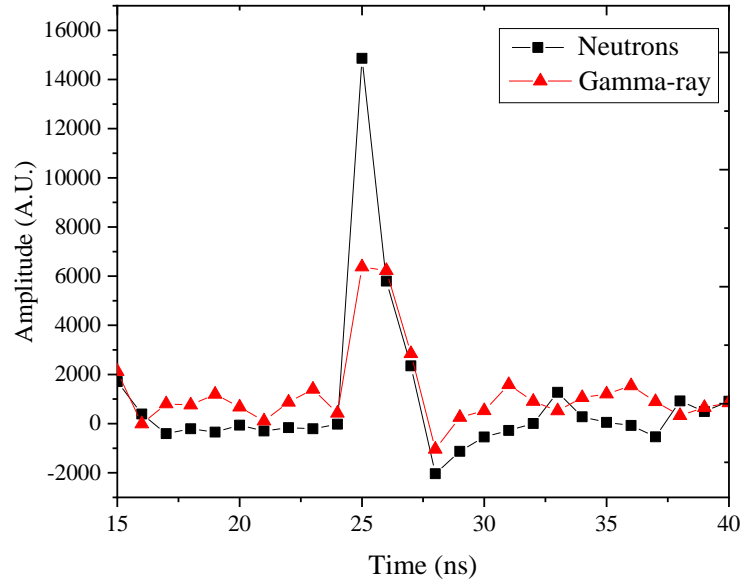
Figure 8.4. Examples of Cf-252 neutron and gamma-ray photon pulses acquired directly from EJ-204 scintillation detector (the line joining the data points are added for clarity).

8.5 Results

8.5.1 Pulse height analysis method (PHA)

Both neutron and gamma-ray events result in the generation of scintillation light in GS10 and EJ-204. However, the integrated intensity of scintillation photons per unit length depends on the charge of the secondary particles generating primary excitations in the scintillation material [27, 34]. Therefore, scintillation light generated from gamma-ray photon interaction in these two scintillators is usually less than the scintillation light generated by neutron interaction. As a result, direct measurement and comparison of the magnitude of generated electrical pulses allows the discrimination of gamma-ray events from neutron events. Figure 8.5 shows the relative frequency of

events representing the normalised number of pulses as function of integrated charges (i.e. pulse height) for gamma-ray photons and neutrons within a GS10 scintillator. The figure shows how a Gaussian fit of neutron generated pulses have a higher pulse amplitude compared to the Gaussian fit to the gamma-ray pulses, allowing a clear and a comfortable discrimination between events generated by these two radiation fields. Based on the results in Figure 8.5 neutrons generated pulses have an average pulse height of (94000 ± 1000) ADC units with a Full Width at Half Maximum (FWHM) = (21000 ± 3000) ADC units and a spectrum resolution of 0.49, whereas gamma-ray generated pulses have an average pulse height of (47620 ± 20) ADC units with a spread of FWHM = (3610 ± 40) ADC units and a spectrum resolution of 0.076. This method can be implemented directly within the readout circuit of the scintillation detector by setting a voltage threshold level using the pulse height peak level and the associated confidence level for the two events.
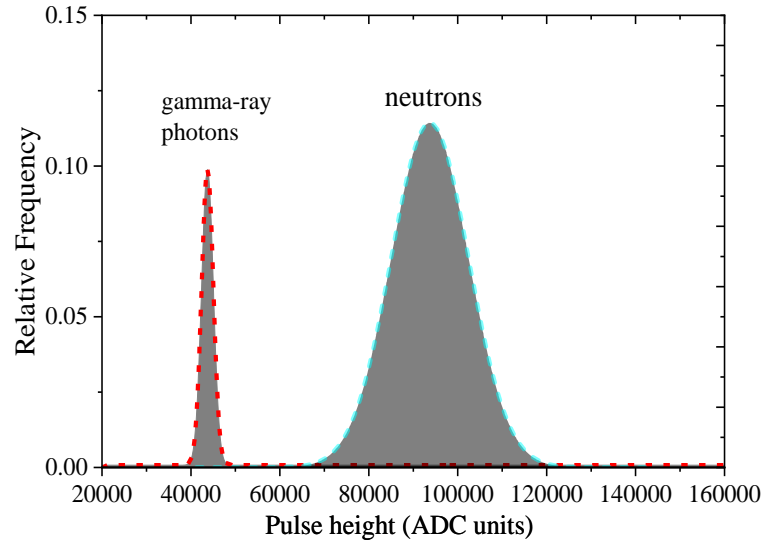
Figure 8.5. Relative frequency of events as function of pulse height for neutron and gamma-ray pulses from the Cf-252 source in the GS10 detector. Gamma-ray photons generated pulses (left) and neutron generated pulses (right) are distinctly separated.

For the EJ-204 scintillation detector, the total integrated charge generated by neutron events and gamma-ray photons are measured and normalised to the total number of pulses. The relative frequency of pulses are presented as a function of pulse height in a probability density plot shown in Figure 8.6. The figure shows two clear peaks for neutron and gamma-ray photons, however, intersection between the distributions is clear in the figure. This indicates an ambiguity of ~8% of neutron events and ~15% of gamma-ray events. This can lead to significant loss in efficiency for scattering based imaging systems. In addition, the results in Figure 8.6 show that neutron generated pulses have an average pulse height of (20000 ± 800) ADC units with FWHM = (6100 ± 2000) ADC units and a spectrum resolution of 0.30, whereas gamma-ray generated pulses have an average pulse height of (11000 ± 2000) ADC units with FWHM = (10000 ± 4000) ADC units and a spectrum resolution of 0.9. The wide spread in the

relative frequency counts of pulse heights for EJ-204 resulted on high uncertainty in the average pulse height values and FWHM values for both radiation fields.
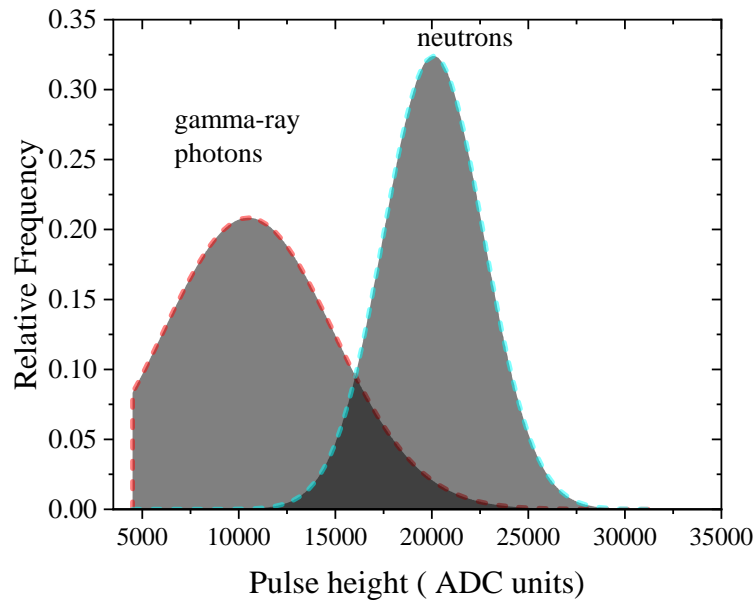
Figure 8.6. Relative frequency of events as function of pulse height for neutron and gamma-ray pulses from the Cf-252 source in the EJ-204 detector. Gamma-ray generated pulses (left) and neutron generated pulses (right) are intersecting over an area of 10,000 ADC units.

8.5.2   Charge comparison method (CCM)

The charge comparison method evaluates the integrated charges in a pulse over two periods of time commonly known as the long integral and the short integral. In here, the long integral corresponds to the area of the entire pulse whereas the short integral corresponds to the area covering part of the pulse commonly set at an optimised sample time on the decaying part of pulse For a GS10 detector, the charge comparison method was applied to the acquired pulses with a short integral set to start at 50 ns after the peak. A scatter plot of the short integral against the long integral was created as illustrated in Figure 8.7. The figure shows a cross-reference area where the events

overlap. However, the majority of gamma-ray events are located below the diagonal

line crossing the zero reference point in the figure.
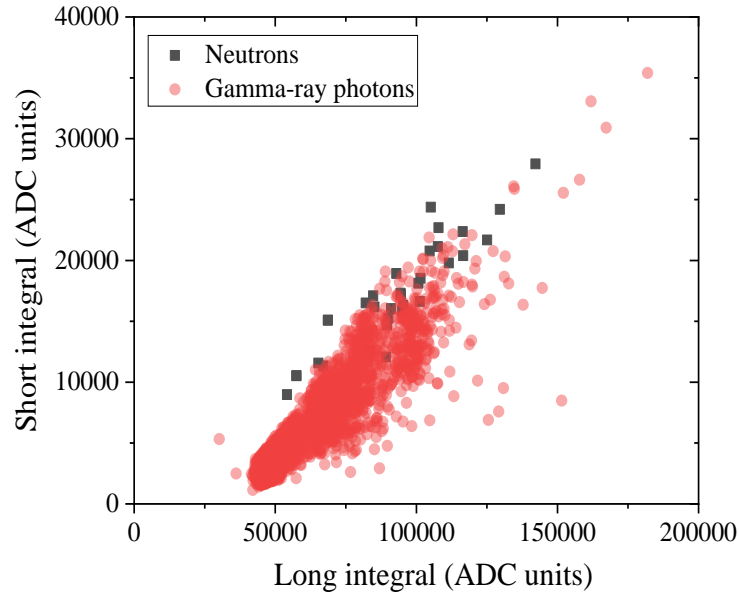
Figure 8.7. A scatter plot of short integrals against long integrals for the events

from the Cf-252 source in the GS10 detector.

The pulses in Figure 8.7 were normalised to the total number of events in the

corresponding radiation group and a probability distribution plot with the relative

frequency against the ratio of short integral to long integral was generated. Figure 8.8

shows the two Gaussian fits of the probability distribution plot of the total events. The

neutron events have an average short integral to long integral ratio of (0.35 ± 0.01) with

a spread of $\sigma = (0.11 \pm 0.07)$. The gamma-ray events have an average short integral to

long integral ratio of (0.80 ± 0.06) with spread $\sigma = (0.45 \pm 0.07)$. Events clearly overlap

in the probability distribution plot suggesting low discrimination efficiency.
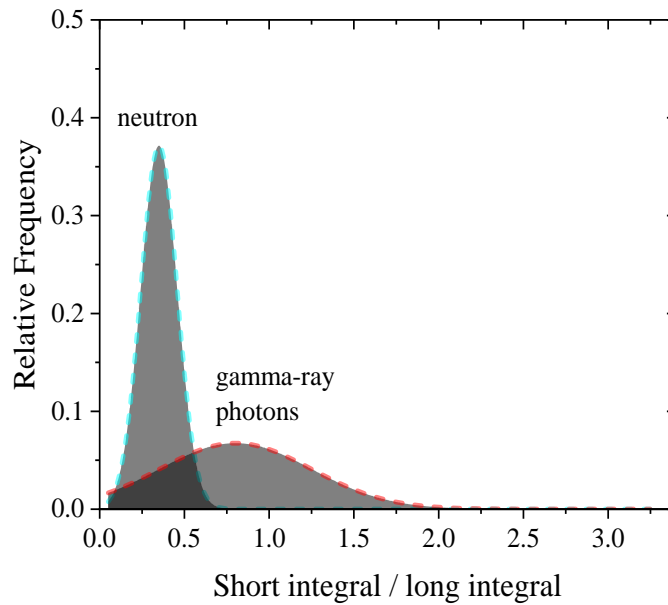
Figure 8.8. Relative frequency of events against short integral to long integral

ratio of all events generated by gamma-ray photons (centre left) and neutrons

(far left) from the Cf-252 source using the GS10 detector.

Attempts were made to generate a discrimination platform for an EJ-204 detector using charge comparison discrimination methods. However, as shown in Figure 8.9 there were no clear discrimination levels between the neutron and gamma-ray events.
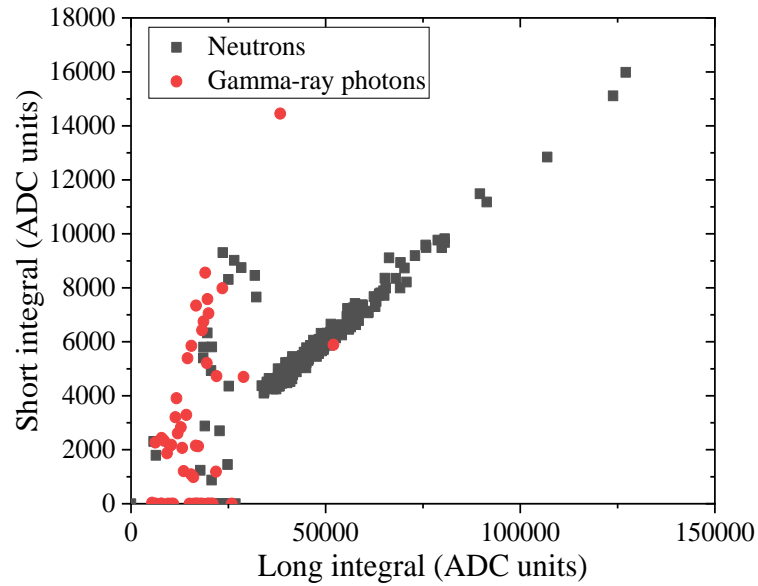
Figure 8.9. A scatter plot of short integrals against long integrals for the events from the Cf-252 source in the EJ-204 detector.

8.5.3 Pulse gradient analysis (PGA)

The PGA method uses the differences in the time domain over the decaying interval of the pulses generated by gamma-ray photons and neutrons. The main advantage of this method is that it compares parameters that are sensitive to any changes in the production mechanism of scintillation photons allowing subtle deduction of pulse variations. For a GS10 crystal, the time constant at which the sample amplitude was investigated against peak amplitude was optimised at 50 ns after the peak amplitude. Figure 8.10 illustrates the sample amplitude as the function of the peak amplitude for combined neutron and gamma-ray events.
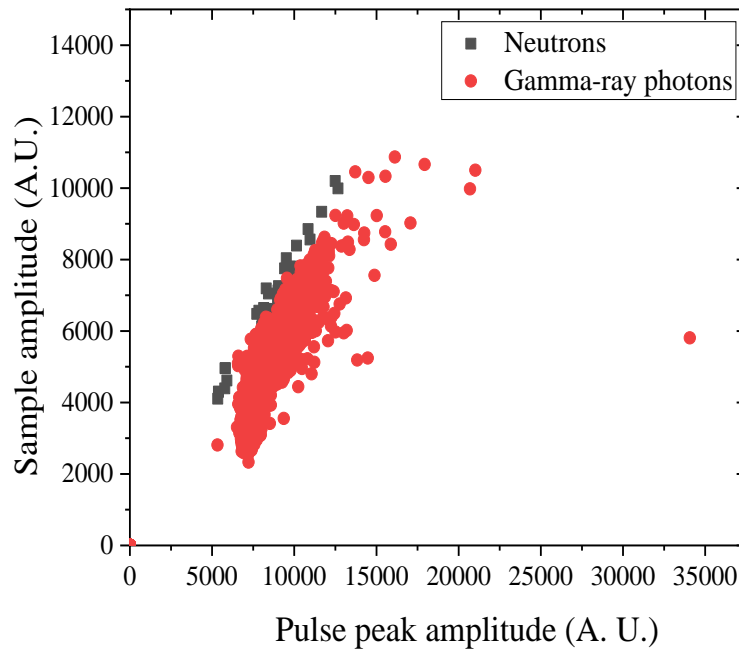
Figure 8.10. A scatter plot of the sample amplitudes against the peak amplitude of the events from the Cf-252 source in the GS10 detector.

The pulses in Figure 8.10 were normalised to the total number of pulses in the corresponding radiation type and a probability distribution plot with the relative frequency against the ratio of sample amplitude to peak amplitude was generated. Figure 8.11 shows two Gaussian fits of the probability distribution plot of neutron events and gamma-ray events. The neutron events have an average PGA ratio of (0.788 ± 0.001) with a spread of σ = (0.018 ± 0.001). The gamma-ray events had an average PGA ratio of (0.510 ± 0.004) with a spread of σ = (0.085 ± 0.005).
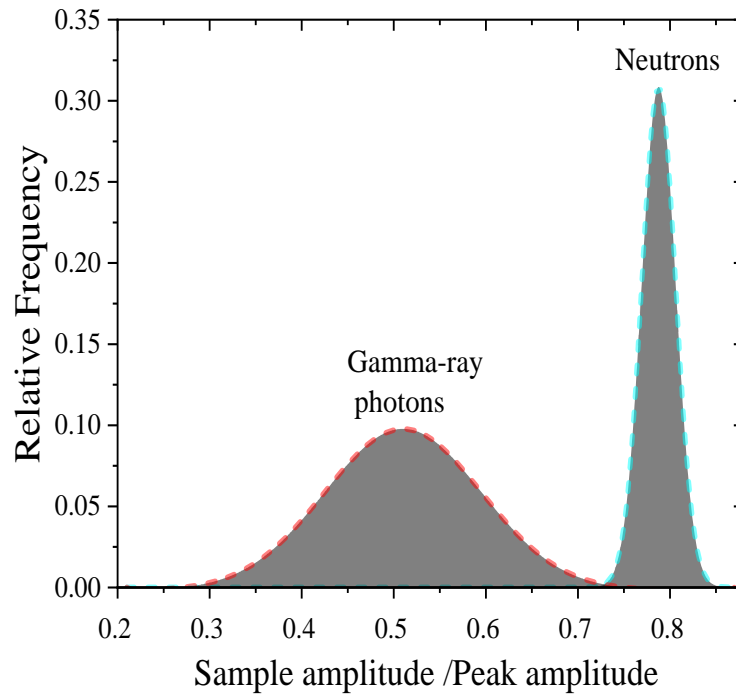
Figure 8.11: Relative frequency of events as function of PGA ratio by gamma-ray photons (centre) and neutrons (left) from a Cf-252 source using a GS10 detector.

For EJ-204 the sample amplitude was attempted at different peak lag times. However, there was no clear discrimination level between the two events and they completely overlapped. This can be clearly seen in Figure 8.12 where a scatter plot of the sample amplitude against peak amplitude at 1 ns after the peak amplitude show complete overlapping of events from the two radiation fields.
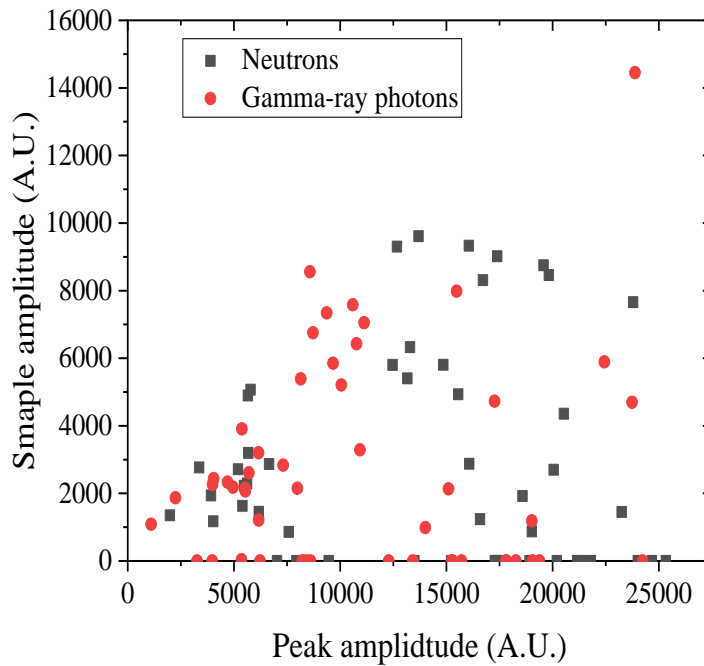
Figure 8.12. A scatter plot of the sample amplitudes against the peak amplitude of the events from the Cf-252 source in the EJ-204 detector.

8.6 Discussion and conclusion

Three different pulse discrimination methods, PHA, CCM and PGA, were used to discriminate neutron and gamma-ray events in GS10 and EJ-204 scintillation detectors. One common technique applied in evaluating and comparing the quality of discrimination methods is the figure-of-merit, FOM. Commonly, the FOM is obtained from the probability distribution plot of the discrimination method under review. The FOM in a probability distribution plot can be expressed as [28]

$$F \, OM = \frac{|Peak_\gamma - Peak_n|}{FWHM_\gamma + FWHM_n} \tag{8.1}$$

Where $Peak_\gamma$ is the gamma-ray events peak position, $Peak_n$ is neutron events peak position, $FWHM_\gamma$ is gamma rays peak full width at half maximum value and $FWHM_n$

neutrons peak full width at half maximum value. For example, in Figure 8.11, $Peak_\gamma =$ 0.51, $Peak_n = 0.79$, $FWHM_\gamma = 0.2$ and $FWHM_n = 0.04$, based on equation (8.1), FOM in this case is 1.1. The statistics characterising three discrimination methods applied in this work along with FOM values based on figures 8.5, 8.6, 8.8 and 8.10 are summarised in Table 8.2.

Table 8.2: Summary of the average values and the FOMs of the three pulse discrimination methods applied on GS10 and EJ-204 neutron and gamma-ray pulses from Cf-252 source.

	GS10			EJ-204		
Pulse discrimination method	Neutrons average	Gamma-ray average	*FOM*	Neutrons average	Gamma-ray average	*FOM*
PHA (ADC units for average values)	(92 ± 2)x 10^5	(53 ± 1)x 10^5	1.00	(22 ± 4) x 10^5	(13 ± 6) x 10^5	0.682
short integral to long integral ratio	0.35 ± 0.10	1.1 ± 0.5	0.383	1.000 ± 0.002	1.00 ± 0.001	NA
PGA ratio	3.1 ± 0.9	2.05 ± 0.05	1.10	0.21 ± 0.21	0.30 ± 0.21	NA

In the case of the GS10 scintillation detector, neutron pulses have a distinctly higher pulse amplitude compared to gamma-ray pulses. Similarly, PGA analysis on GS10 shows that neutron pulses generally have a higher sample amplitude to peak amplitude ratio (defined in Table 8.2 as PGA ratio). Reflecting on the FOM values in Table 8.2, neutron and gamma-ray pulses discrimination is applicable for a GS10 scintillation detector via the PHA and PGA method with both showing FOM values around 1. In contrast, the charge comparison method shows poor discrimination abilities between neutron and gamma-ray pulses in a GS10 scintillation detector with a FOM value of around 0.383. In the case of the EJ-204 scintillation detector, neutron pulses acquire a

higher pulse amplitude compared to gamma-ray pulses with a FOM equal to 0.682 suggesting the possibility of successful PHA in a mixed radiation field measurement. However, loss in counts from both radiation fields will occur as a result. Both the CCM and PGA methods suggests pulse shape discrimination is not applicable for EJ-204 in this work. One major reason for this outcome is the poor presentation of EJ-204 pulses acquired by the oscilloscope. The pulses generated by EJ-204 are very fast with a 2.2 ns pulse width. The oscilloscope digitises the pulse with sampling speed of 8 GSa/s, a sampling speed that is sufficiently fast enough to acquire the pulse. However, a higher sampling speed is required to acquire more samples per pulse allowing higher accuracy in recreating the shape of the pulses later in the analysis stage. There are a number of oscilloscopes with a higher sampling rate than the one utilised within this study. However, the aim within this work is to utilise a sampling speed comparable to the best data acquisition systems currently available for integration in portable radiation detection systems. In addition, this work is intended to create a platform for further investigation into the pulse discrimination abilities of two detectors, which possess great potential in the field of dual-particles detection but yet are currently understudied in the literature.

8.7 References

1. Polack, J.K., et al., *Image Reconstruction Using a Three-Plane, Dual-Particle Imager for Standoff Detection of Special Nuclear Material*, in *2012 IEEENuclear Science Symposium and Medical Imaging Conference Record*, B. Yu, Editor. 2012. p. 118-121.

2. Ayaz-Maierhafer, B., et al., *Transmission and signal loss in mask designs for a dual neutron and gamma imager applied to mobile standoff detection.* Nuclear

Instruments & Methods in Physics Research Section a-Accelerators Spectrometers Detectors and Associated Equipment, 2013. **712**: p. 1-8.

3. Cester, D., et al., *A novel detector assembly for detecting thermal neutrons, fast neutrons and gamma rays.* Nuclear Instruments and Methods in Physics Research Section A: Accelerators, Spectrometers, Detectors and Associated Equipment, 2016. **830**: p. 191-196.

4. Devolpi, A. and E.A. Rhodes, *Neutron and gamma-ray tomographic imaging of LMFBR SAREF-program safety-test fuel assemblies.* MATER EVAL, 1982. **V 40**(N 12): p. 1273-1279.

5. Chaouki, J., F. Larachi, and M.P. Duduković, *Noninvasive Tomographic and Velocimetric Monitoring of Multiphase Flows.* Industrial and Engineering Chemistry Research, 1997. **36**(11): p. 4476-4503.

6. Gozani, T., *The role of neutron based inspection techniques in the post 9/11/01 era.* Nuclear Instruments and Methods in Physics Research, Section B: Beam Interactions with Materials and Atoms, 2004. **213**: p. 460-463.

7. Kapadia, A.J., et al. *GEANT4 simulation of an NSECT system for iron overload detection.* in *IEEE Nuclear Science Symposium Conference Record.* 2007.

8. Sowerby, B.D., et al. *Recent developments in fast neutron radiography for the interrogation of air cargo containers.* in *International Topical Meeting on Nuclear Research Applications and Utilization of Accelerators.* 2009.

9. Biegun, A.K., et al., *Time-of-flight neutron rejection to improve prompt gamma imaging for proton range verification: a simulation study.* Physics in Medicine and Biology, 2012. **57**(20): p. 6429-6444.

10.   Owen, R.B., *The Decay Times of Organic Scintillators and Their Application to the Discrimination Between Particles of Differing Specific Ionization.* IRE Transactions on Nuclear Science, 1958. **5**(3): p. 198-201.

11.   Brooks, F.D., *A scintillation counter with neutron and gamma-ray discriminators.* Nuclear Instruments and Methods, 1959. **4**(3): p. 151-163.

12.   Brooks, F.D., R.W. Pringle, and B.L. Funt, *Pulse Shape Discrimination in a Plastic Scintillator.* IRE Transactions on Nuclear Science, 1960. **NS-7**(2-3): p. 35-38.

13.   Coceva, C., *Pulse-shape discrimination with a glass scintillator.* Nuclear Instruments and Methods, 1963. **21**(C): p. 93-96.

14.   Smith, D.L., R.G. Polk, and T.G. Miller, *Measurement of the response of several organic scintillators to electrons, protons and deuterons.* Nuclear Instruments and Methods, 1968. **64**(2): p. 157-166.

15.   Martín-Martín, A., et al., *Evaluation of CdZnTe as neutron detector around medical accelerators.* Radiation Protection Dosimetry, 2009. **133**(4): p. 193-199.

16.   Tupitsyn, E., et al., *Single crystal of LiInSe$_2$ semiconductor for neutron detector.* Applied Physics Letters, 2012. **101**(20).

17.   Glodo, J., et al. *Cs$_2$LiYCl$_6$: Ce Neutron gamma detection system.* in *2007 IEEE Nuclear Science Symposium Conference Record.* 2007. Honolulu, HI, USA.

18.   Glodo, J., et al., *Selected Properties of Cs2LiYCl6, Cs2LiLaCl6, and Cs2LiLaYBr6 Scintillators.* Ieee Transactions on Nuclear Science, 2011. **58**(1): p. 333-338.

19.   Aryaeinejad, R. and D.F. Spencer, *Pocket dual neutron/gamma radiation detector.* IEEE Transactions on Nuclear Science, 2004. **51**(4): p. 1667-1671.

20. Polack, J.K., et al. *Dual-particle imager for standoff detection of special nuclear material*. in *2011 IEEE Nuclear Science Symposium Conference Record*. 2011. Valencia, Spain.

21. Poitrasson-Riviere, A., et al., *Dual-particle imaging system based on simultaneous detection of photon and neutron collision events.* Nuclear Instruments & Methods in Physics Research Section a-Accelerators Spectrometers Detectors and Associated Equipment, 2014. **760**: p. 40-45.

22. Ayaz-Maierhafer, B., et al., *Angular resolution study of a combined gamma-neutron coded aperture imager for standoff detection.* Nuclear Instruments and Methods in Physics Research Section A: Accelerators, Spectrometers, Detectors and Associated Equipment, 2013. **712**: p. 120-125.

23. *6-lithium glass bespoke to your application*. [cited 2018; Available from: https://scintacor.com/products/6-lithium-glass/.

24. *General Purpose Plastic Scintillators EJ-200, EJ-204, EJ-208, EJ-212*. 25/07/2019]; Available from: https://eljentechnology.com/images/products/data_sheets/EJ-200_EJ-204_EJ-208_EJ-212.pdf.

25. Al Hamrashdi, H., D. Cheneler, and S.D. Monk, *Material optimization in dual particle detectors by comparing advanced scintillating materials using two Monte Carlo codes.* Nuclear Instruments and Methods in Physics Research Section A: Accelerators, Spectrometers, Detectors and Associated Equipment, 2017. **869**(Supplement C): p. 163-171.

26. Mascarenhas, N., et al. *Development of a neutron scatter camera for fission neutrons*. in *IEEE Nuclear Science Symposium Conference Record*. 2007. San Diego, CA, USA.

27.   Birks, J.B., *The theory and practice of scintillation counting*. 1964: Pergamon Press, Macmillan, New York.

28.   Winyard, R.A., J.E. Lutkin, and G.W. McBeth, *Pulse shape discrimination in inorganic and organic scintillators. I.* Nuclear Instruments and Methods, 1971. **95**(1): p. 141-153.

29.   Ranucci, G., *An analytical approach to the evaluation of the pulse shape discrimination properties of scintillators.* Nuclear Instruments and Methods in Physics Research Section A: Accelerators, Spectrometers, Detectors and Associated Equipment, 1995. **354**(2): p. 389-399.

30.   Spowart, A.R., *Energy transfer in cerium-activated silicate glasses.* Journal of Physics C: Solid State Physics, 1979. **12**(16): p. 3369-3374.

31.   Phillips, H.B. and R.K. Swank, *Measurements of Scintillation Lifetimes.* Review of Scientific Instruments, 1953. **24**(8): p. 611-616.

32.   Wright, G.T., *Scintillation decay Times of organic crystals.* Proceedings of the Physical Society. Section B, 1956. **69**(3): p. 358-372.

33.   Brooks, F.D., *Development of organic scintillators.* Nuclear Instruments and Methods, 1979. **162**(1): p. 477-505.

34.   Brooks, F.D., *Development of organic scintillators.* Nuclear Instruments and Methods, 1979. **162**(1-3): p. 477-505.

35.   Emmerich, W.S., *A fast neutron scintillator.* Review of Scientific Instruments, 1954. **25**(1): p. 69-70.

36.   Gatti, E. and F.D. Martini, *A new linear method of discrimination between elementary particles in scintillation counters*. 1962, International Atomic Energy Agency (IAEA): Brueder Rosenbaum.

37. D'Mellow, B., et al., *Digital discrimination of neutrons and γ-rays in liquid scintillators using pulse gradient analysis.* Nuclear Instruments and Methods in Physics Research, Section A: Accelerators, Spectrometers, Detectors and Associated Equipment, 2007. **578**(1): p. 191-197.

38. Aspinall, M.D., et al., *The empirical characterization of organic liquid scintillation detectors by the normalized average of digitized pulse shapes.* Nuclear Instruments and Methods in Physics Research, Section A: Accelerators, Spectrometers, Detectors and Associated Equipment, 2007. **578**(1): p. 261-266.

39. Liu, G., et al., *A digital method for the discrimination of neutrons and γ rays with organic scintillation detectors using frequency gradient analysis.* IEEE Transactions on Nuclear Science, 2010. **57**(3 PART 3): p. 1682-1691.

40. Marrone, S., et al., *Pulse shape analysis of liquid scintillators for neutron studies.* Nuclear Instruments and Methods in Physics Research Section A: Accelerators, Spectrometers, Detectors and Associated Equipment, 2002. **490**(1–2): p. 299-307.

41. Kangas, L.J., et al., *The use of artificial neural networks in PVT-based radiation portal monitors.* Nuclear Instruments and Methods in Physics Research Section A: Accelerators, Spectrometers, Detectors and Associated Equipment, 2008. **587**(2): p. 398-412.

42. Nakhostin, M., *A new digital method for high precision neutron-gamma discrimination with liquid scintillation detectors.* Journal of Instrumentation, 2013. **8**(05): p. P05023-P05023.

43. Luo, X.L., et al., *Neutron/gamma discrimination employing the power spectrum analysis of the signal from the liquid scintillator BC501A.* Nuclear

Instruments and Methods in Physics Research Section A: Accelerators, Spectrometers, Detectors and Associated Equipment, 2013. **717**: p. 44-50.

44.   NEA, O. *Java-based nuclear data information system*. 16/01/2016 [cited 2016 10/02/2016]; Available from: http://www.oecd-nea.org/janis/.

45.   Martin, R.C., J.B. Knauer, and P.A. Balo, *Production, distribution and applications of californium-252 neutron sources.* Applied Radiation and Isotopes, 2000. **53**(4): p. 785-792.

46.   Billnert, R., et al., *New prompt spectral γ-ray data from the reaction 252Cf(sf) and its implication on present evaluated nuclear data files.* Physical Review C - Nuclear Physics, 2013. **87**(2).

47.   *MATLAB and Statistics Toolbox Release 2017b*. The MathWorks, Inc.: Natick, Massachusetts, United States.

9 Conclusions and Recommendations

This final chapter presents the conclusions of the thesis. It gives a general summary of the work discussed in the thesis before reviewing the main advantages and drawbacks in the proposed design. In addition, it outlines the intended applications of the design followed by a list of recommended future work for enhancing this prototype design.

9.1 Thesis conclusion

In this thesis a novel gamma-ray and neutron imaging system has been designed, built and experimentally tested. The system delivers these capabilities while maintaining its highly portable size as a result of combining the advantages of Compton scattering technique and neutron scattering technique. In addition, the imaging system offers low energy consumption via a pixelated array of silicon photomultipliers as photodetectors of scintillation light.

Prior work in the field of dual-particle imaging systems proved the feasibility of the simultaneous detection of gamma rays and neutrons; however, these studies have either restricted the energy range of targeted particles or suffered from limited portability. In this work, a proof-of-concept design is investigated in which three layers of scintillators (all with active detection area of 27 mm x 27 mm) are combined in one single configuration. Each layer of scintillator is coupled with an 8 x 8-pixelated photodetectors array. The scintillators in the design are arranged in a novel configuration in the following order: layer 1 comprises of a 10 mm thick lithium glass GS10 detector followed by a 20 mm thick EJ-204 plastic scintillator, layer 2 comprises of a 15 mm thick lithium glass GS10 detector and layer 3 comprises of a 30 mm thick CsI(Tl) scintillator. The feasibility of this design was proved computationally via MCNP6 and Geant4 simulations and experimentally via testing the design with sealed radioactive sources, namely Cs-137 and Cf-252. These findings overcome the drawbacks of large and bulky designs by Poitrasson-Riviere et al. [1] and Ayaz-Maierhafer et al. [2]. In addition, unlike the aforementioned studies and a number of other reported dual-particle imaging systems [3, 4], the results show the possibility of covering a wider neutron energy range from thermal to fast neutrons. This design, however, offers most notably of all, a real-time response optimised to 60 s acquisition time and approximately 60 s data analysis time for gamma sources of ~300 kBq and neutron sources of 10^6 neutrons per second (total) in close proximity (< 300 mm). The detection efficiency of the system was measured to be in the order of 10^{-4} per incident radiation field for both gamma rays and fast neutrons and 0.78 detection efficiency for thermal neutrons.

The aim of proving the feasibility of the porotype design went through stages. The first stage featured an intensive review of documented work on gamma-ray and neutron

detection imaging systems utilised in safeguard applications. The review outlined the techniques reported in the literature and showed the gaps in this field where real-time, highly portable and dual-particle imaging systems are absent. The second stage in the research featured an investigation into suitable scintillators that fulfil the requirements of a highly portable multi-layered imaging system using MCNP6 and Geant4 simulations. This investigation involved simulations of four different scintillators from different scintillation material families including a lithium glass inorganic scintillator GS10, two different versions of Cs_2LiYCl_6:Ce elpasolite scintillator widely known as CLYC6 and CLYC, and an EJ-309 organic liquid scintillator. The results indicated that the lithium glass scintillator possess an thermal neutron detection efficiency of (80.6 ± 2.3) %, superior fast neutron scattering abilities and adequate gamma-ray attenuation abilities, implying that lithium glass would be the best candidate as the central detection material in the prototype design. The third stage in the research was to design an optimum configuration of scintillators using MCNP6 and Geant4 simulations. In this stage, the overall detection materials for the prototype design were finalised and the prototype design configuration was established. The investigation methodology and the investigation results of this stage were the subject of chapter 6. The fourth stage was the subject of chapter 7 where the feasibility of the design concept and the prototype configuration were investigated computationally and experimentally. The final stage in this research was to study the abilities of the lithium glass detector GS10 and the EJ-204 in separating gamma-ray and neutron events. The results from all these stages showed compelling evidence on the feasibility of the proposed imaging system. However, some limitations are worth noting. First, although the hypothesis of computing the TOF of scattered neutrons with the current configuration was computationally proven, during the experiments false neutron scattering events were

present leading to some miscalculations in the TOF. The ambiguity was found to be due to the independency in response of the first layer and the second layer in the design. Suggestions of ways to overcome this drawback in the electronics design are further discussed in the recommendations section of this chapter. In addition, the very short pulse of the EJ-204 plastic scintillator (~ 2.2 ns) proved to be both an advantage and a disadvantage in the design. The short pulse time of EJ-204 allowed fast detection of neutron events, hence short dead time for the scintillator, however, it showed to be too fast for the acquiring system (8 GSa/s) to fully digitise the pulses. Due to this limitation in the pulse digitising components of the system, it was impractical to apply pulse shape discrimination techniques to separate neutron scattering events from gamma-ray events. However, pulse height discrimination might be an alternative method of discriminating pulses in EJ-204 at this stage of the research.

9.2 Potential research applications

Integrating the imaging system into real-life applications is one of the aims for future work in this project. The main target application is radioactive source safeguarding and security applications. The design offers the features required for a successful imaging system in this field including its multiple functionality, its highly portable size and its real-time response. A future plan for this research is to test the system at airport security checkpoints in Oman. The foundation for this plan has already been set with researchers at Sultan Qaboos University in Oman.

Another potential application for the proposed imaging system is in the field of gauging and logging. In particular, the imaging system can be integrated in the gauging and the logging processes associated with oil and gas fields. Naturally occurring radioactive

sources, as well as artificially man made sources, are widely present in this field, especially in exploration and in pipeline monitoring applications. A plan to test the imaging system in gauging and logging operations associated with the oil fields in Oman is highly considered as a future project.

Radiography and tomography are another two possible application fields, particularly in combined industrial gamma-ray and neutron radiography and tomography [5, 8]. However, the active detection area in the current prototype design is very small and further computational investigation is required to assess and enhance the abilities of the current configuration to suit this application field.

9.3 Recommendations and future work

The prototype design of the instrument discussed in this thesis shows promising results. It showed the feasibility of this proof-of-concept study and proved the viability of the design. However, there are a number of acknowledged limitations in the current prototype. Recommendations for future work believed to be of benefit to the design are discussed in the following subsections.

9.3.1 Changes to the scintillation materials

Currently the system consists of four scintillators; GS10 glass and EJ-204 plastic in the first layer, GS10 glass scintillator in the second layer and CsI(Tl) in the third layer. The first recommendation of change is within the first layer, namely the EJ-204 plastic scintillator. EJ-204 shows limited gamma-ray and neutron discrimination abilities as discussed in chapter 8, mainly due to its short pulse width (average of 2.2 ns). This made it difficult to apply time dependent and frequency dependent pulse shape

discrimination methods such as pulse gradient analysis [9] and shape comparison methods [10] in real-time. An alternative organic plastic scintillator is EJ-276 plastic scintillator (formally known as EJ-299-33A or EJ-299-34) [11]. It has a built in ability to discriminate gamma-ray pulses from neutron pulses. A drawback might be the lower scintillation efficiency of EJ-276 (8600 photons/MeV e$^-$) compared to EJ-204 (10,400 photons/MeV e$^-$).

GS10 (6% natural Li content) was used twice in the design, firstly in the first layer as a thermal neutron detector and secondly in the second layer as a fast neutron and gamma-ray scattering layer. GS10 offered (78 $\pm$ 4) % detection efficiency of incident thermal neutrons. One would argue that G20 (95% Li-6 enrichment) [12] or KS2 [12] would offer higher thermal neutron detection efficiency compared to GS10. However, the overall configuration would require reassessment as higher Li-6 content might affect the neutron scattering sub-system and the overall cost.

9.3.2 Front-end and backend readout circuit

The first recommendation regarding the electronics associated with the imaging system is to reduce the size of the circuitry. Currently the electronics in the imaging system are divided into two main structures: front-end readout electronics and backend readout electronics (discussed in chapter 7 as the application specific readout circuit (ASRC)). The front-end electronics are placed within the detectors' enclosure on the same breakout boards as the SiPM arrays to minimise signal loss. However, the backend readout circuits, which are designed to filter and amplify the 192 SiPM pixels, compare them to a reference voltage and analyse them to extract time and location information, comprise of 15 PCBs (area of the smallest PCB equals 120 mm x 120 mm). This reflects the size of the backend readout electronics. For this proof-of-concept study, this design

served the aim of thoroughly investigating individual pulses generated from individual SiPM pixels. The recommendation here is to integrate the front-end electronics and the backend electronics in application specific integrated circuits (ASIC). This can be accomplished; first by changing the design of the filter and amplifier circuits which currently comprises of four PCBs for each layer in the system, and then minimise the size of the component into the fewest number of ASICs. One suggestion to improve the filter and amplifier circuit is to use one level 2D integration of the SiPM array as shown in Figure 9.1. This one level integration will reduce the size of the front-end electronics from 64 current-to-voltage converters to 16. As a result, only 16 filter and amplifier circuits and 16 comparator circuits will be required for each SiPM array in the design. This will significantly reduce the size of the electronics in the imaging system. In addition, this one level integration will reduce power consumption while maintaining the pixelated integrity of the system. In addition, more current will be allowed in each integrated raw or column, which will enhance the linearity in response of the ASIC. The second step towards reducing the size of the readout circuit is to integrate the overall electronics into ASICs. The optimum aim is to have all ASICs fit within the detectors enclosure, hence increasing the portability of the design.
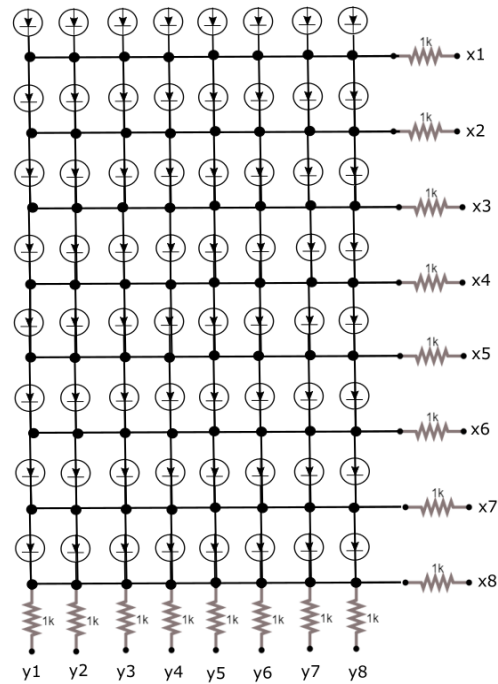
Figure 9.1: A schematic of the one level 2D current integration from the 8 x 8 SiPM photodiodes utilised in the design.

Another recommendation to enhance the performance of the readout circuit is to minimise false neutron scattering events and false Compton scattering events. The main suggestion here is to add a triggering circuit linking layers one and two to reduce false neutron scattering events and a triggering circuit linking layers two and three to reduce false Compton scattering events.

An additional recommendation here is extending the measurement range of the TOF circuit. Currently, the TOF circuit utilises the TDC7200EVM (Texas Instruments) evaluation module with a measurement range between 12 ns to 500 ns. To the knowledge of the author, this is one of the most advanced of-the-shelf circuits for TOF measurements. However, the fields of analogue and the digital electronics are wide and undergo constant improvements and innovation. Hence, the overall readout circuit in general and the TOF circuit in particular can be the subject to further improvement.

9.3.3 Pulse digitising electronics

The Data Acquisition System (DAQ) utilised in this work is the USB-2633 [13], which operate at a 1 MS/s sampling rate with 64 single ended analogue inputs and three 8-bit digital inputs. To the knowledge of the author, this is one of few DAQs with 64 input analogue channels and a sampling speed in MS/s range. This efficiently served the purpose of individually reading the SiPM array pixels in each layer in the design. However, the digitisation speed is low compared to the time components of the acquired pulses from GS10 (average measured rise time of 50.4 ns and average measured fall time of 70 ns) and from the EJ-204 (average reported rise time of 0.7 ns and average fall time of 1.8 ns [14]). Other DAQs, which utilise faster ADCs, would offer higher digitising speed. However, the condition for the applicability of this suggestion will be in reducing the number of analogue input channels from 64, which will require signals multiplexing from the SiPM array.

9.3.4 Further testing of the imaging system

The feasibility of the design was experimentally validated using Cs-137 gamma-ray source (~300 kBq) and Cf-252 spontaneous fission source (~18.8 MBq). Further experimental testing against higher activity sources, different radioactive materials and different source geometries is recommended for future work. It will allow further understanding of the imaging systems' capabilities and will allow further quantification of the angular resolution and the energy resolution of the system.

Testing the imaging system in an environment replicating real-life scenarios is also recommended future work in this project. This project is considered the first step towards building an instrument used in radioactive sources safeguard and security

applications. Hence, it will be greatly beneficial to test the system in an environment modelling airport security protocols with hidden sources in a luggage or in phantoms.

9.4 References

1. Poitrasson-Riviere, A., et al., *Dual-particle imaging system based on simultaneous detection of photon and neutron collision events.* Nuclear Instruments & Methods in Physics Research Section a-Accelerators Spectrometers Detectors and Associated Equipment, 2014. **760**: p. 40-45.

2. Ayaz-Maierhafer, B., et al., *Transmission and signal loss in mask designs for a dual neutron and gamma imager applied to mobile standoff detection.* Nuclear Instruments & Methods in Physics Research Section a-Accelerators Spectrometers Detectors and Associated Equipment, 2013. **712**: p. 1-8.

3. Aryaeinejad, R., E.L. Reber, and D.F. Spencer, *Development of a handheld device for simultaneous monitoring of fast neutrons and gamma rays.* IEEE Transactions on Nuclear Science, 2002. **49**(4): p. 1909-1913.

4. Runkle, R.C., et al., *Lynx: An unattended sensor system for detection of gamma-ray and neutron emissions from special nuclear materials.* Nuclear Instruments and Methods in Physics Research Section A: Accelerators, Spectrometers, Detectors and Associated Equipment, 2009. **598**(3): p. 815-825.

5. *CRP Report: Fast Neutron and Gamma-Ray Interrogation of Air Cargo Containers.* [cited 2019 14/11/2019]; Available from: http://www-naweb.iaea.org/napc/physics/meetings/3rd-rcm-nbt/presentations/sowerby.pdf.

6. Byrd, R.C., et al., *Nuclear detection to prevent or defeat clandestine nuclear attack.* IEEE Sensors Journal, 2005. **5**(4): p. 593-609.

7. Voitovetskii, V.K., N.S. Tolmacheva, and M.I. Arsaev, *Scintillating glass for the detection of slow neutrons.* The Soviet Journal of Atomic Energy, 1960. **6**(3): p. 203-207.

8. Rynes, J., et al., *Gamma-ray and neutron radiography as part of a pulsed fast neutron analysis inspection system11This work was partially supported by both the Federal Aviation Administration (Contract no. DTFA03-87-C-00043) and the Department of Defense (Contract no. DAAD05-97-C-0018).* Nuclear

Instruments and Methods in Physics Research Section A: Accelerators, Spectrometers, Detectors and Associated Equipment, 1999. **422**(1): p. 895-899.

9. D'Mellow, B., et al., *Digital discrimination of neutrons and γ-rays in liquid scintillators using pulse gradient analysis.* Nuclear Instruments and Methods in Physics Research, Section A: Accelerators, Spectrometers, Detectors and Associated Equipment, 2007. **578**(1): p. 191-197.

10. Marrone, S., et al., *Pulse shape analysis of liquid scintillators for neutron studies.* Nuclear Instruments and Methods in Physics Research Section A: Accelerators, Spectrometers, Detectors and Associated Equipment, 2002. **490**(1–2): p. 299-307.

11. *Pulse Shape Discrimination EJ-276 & EJ-276G.* [cited 2019 06/11/2019]; Available from: https://eljentechnology.com/products/plastic-scintillators/ej-276.

12. *6-lithium glass bespoke to your application.* [cited 2018; Available from: https://scintacor.com/products/6-lithium-glass/.

13. *USB-2633 User's Guide.* [cited 2017 05/05/2017]; Available from: https://www.mccdaq.com/pdfs/manuals/USB-2633.pdf.

14. *General Purpose Plastic Scintillators EJ-200, EJ-204, EJ-208, EJ-212.* 25/07/2019]; Available from: https://eljentechnology.com/images/products/data_sheets/EJ-200_EJ-204_EJ-208_EJ-212.pdf.

Appendix A

A.1 MCNP simulations

A.1.1 Example of MCNP code in studying Cf-252 source fluence and

spectra using EJ-309

```
-- Cf-252 fission source investigation
c     command line: mcnp6 i=Cf252_exp o=filename
c           *** CELL CARDS ***
  19    19 -2.6989 -19  $ source
  29    29       1 -49 19  $ water
  39    49   -0.23 -59 49  $FG
  49    39 -0.001255 -69 49 59  $ SPACE BETWEEN FG LAYERS
  59    49   -0.23 -79 49 59 69  $FG
  69    39 -0.001255 -89 49 59 69 79  $SPACE BETWEEN FG AND S
  79    69   -7.85 -90 49 59 69 79 89  $ STEEL BOX
  89    69   -7.85 -109  $TOP PLATE
  90    69   -7.85 -119  $BASE
  91     5 -0.964 -12  $EJ-309
c  ****** globe cell and void cell     ******
  98    39 -0.001205 -98 79 89 90 109 119 12 $air
  99     0       -99 98 79 89 90 109 119 12 $ Void cell

c       *** SURAFACE CARDS ***
c  ********** source Cf-252 **********
c Al CAPSULE WITH Cf-252 INSIDE IT
  19      rcc 52.6 0 -5 0 0 10 3.9
c WATER TANK
  49      box 57 -57 -53.55 -114.1 0 0 0 114.1 0 0 0 107.1
  59      box 57.4 -57.4 -53.95 -114.9 0 0 0 114.9 0 0 0 107.9
  69      box 68.45 -68.45 -61.45 -136.9 0 0 0 136.9 0 0 0 122.9
  79      box 68.85 -68.85 -61.85 -137.7 0 0 0 137.7 0 0 0 123.7
  89      box 73.5 -69.4 -62.5 -147 0 0 0 138.8 0 0 0 125
  90      box 76.8 -72.7 -62.5 -153.6 0 0 0 145.4 0 0 0 125
c TOP PLATE
```

```
   109      box 75.8 -75 62.5 -151.6 0 0 0 150 0 0 0 3.3
c BOTTOM PLATE
   119      box 80 -80 -62.5 -160 0 0 0 160 0 0 0 -3.3
c EJ-309 block
   12       box 82.5 -5 -5 10 0 0 0 10 0 0 0 11.8
c ********** Globe cell and Viod cell surf.s **********
   98       sph 0 0 0 300
   99       sph 0 0 0 400


c                **** Source card ***
c     *** MODE CARD ***
mode  n p h t a  $ n: neutron, p: photon, h: proton, t: triton and a: alpha
c     **** MATERIAL CARDS ***
c the data  library is .80c
m19   13027.        1 $ Al
m29   1001.       -0.111    8016.       -0.889  $ WATER, negative sign is for mass fraction, m39   7014.
   -0.8      8016.       -0.2  $ air, 80% nitrogen, 20% oxygen by mass
      gas=1
m49   8016.           -0.467  $fiber glass by mass (O, Si, Ca, Al, Mg, Na)
      14028.       -0.336 20040.       -0.071 13027.       -0.003
      12024.       -0.015 11023.       -0.105 16032.       -0.003
m69   6012.          -0.0022  $ Mild steel with Mo
      29064.       -0.0019 26056.       -0.97517 25055.       -0.0122
      14028.       -0.0021 16032.       -0.00027 15031.       -0.00016
      13000.       -0.0002 42000.       -0.0049 24000.       -0.0007
      28000.       -0.0002
m5    1001.       -0.09434     6012.        -0.90566  $EJ-309
imp:n   1 10r      0        $ 19, 99
imp:p   1 10r      0        $ 19, 99
c     *** PHYS and cutoff ***
phys:n J 10 4J 1 $ invoking analogue capture
phys:h J 10 J J J J J 3J J
cut:n  2J 0 0 J    $ ---------/
cut:h J 1e-3 3J
cut:t J 1e-3 3J
cut:a J 1e-3 3J
c   SOURCE DEFINITION
sdef POS=52.6 0 0 PAR=D1 ERG=FPAR=D2
si1 L n p
sp1 1 1
ds2 S 3 4
si3
sp3 -3 1.025 2.926
si4 A 0.085 0.09 0.1 0.11 0.12 0.13 0.14 0.15 0.16 0.17 0.18 0.19 0.2 0.21 &
  0.22 0.23 0.24 0.25 0.26 0.27 0.28 0.29 0.3 0.35 0.4 0.45 0.5 0.55 0.6 &
  0.65 0.70 0.75 0.80 0.85 0.90 0.95 1.0 1.05 1.1 1.15 1.2 1.25 1.3 1.35 &
  1.4 1.45 1.5 1.55 1.6 1.65 1.7 1.75 1.8 1.85 1.9 1.95 2 2.05 2.1 2.15 &
  2.2 2.25 2.3 2.35 2.4 2.45 2.5 2.55 2.6 2.65 2.7 2.75 2.8 2.85 2.9 2.95 &
  3 3.05 3.1 3.15 3.2 3.25 3.3 3.35 3.4 3.45 3.5 3.55 3.6 3.65 3.7 3.75 &
  3.8 3.85 3.9 3.95 4 4.05 4.1 4.15 4.2 4.25 4.3 4.35 4.4 4.45 4.5 4.55 &
  4.6 4.65 4.7 4.75 4.8 4.85 4.9 4.95 5 5.05 5.1 5.15 5.2 5.25 5.3 5.35 &
  5.4 5.45 5.5 5.55 5.6 5.65 5.7 5.75 5.8 5.85 5.9 5.95 6 6.05 6.1 6.15 &
  6.2 6.25 6.3 6.35 6.4 6.45 6.5 6.55 6.6 6.65 6.7 6.75 6.8 6.85 6.9 6.95 &
  7 7.05 7.1 7.15 7.2 7.25 7.3 7.35 7.4 7.45 7.5 7.55 7.6 7.65 7.7 7.75 &
  7.8 7.85 7.9 7.95 8 8.05
sp4 0.0 0.000182468 0.000556455 0.000942761 0.001341689 0.001753553 0.00217867 &
  0.002617366 0.003069975 0.003536836 0.004018297 0.004514714 0.005026448 &
  0.005553871 0.006097362 0.006657308 0.007234104 0.007828155 0.008439874 &
  0.009069682 0.009718011 0.010385300 0.011099912 0.009894086 0.008819253 &
```

0.007861184 0.007007193 0.006245974 0.005567450 0.004962637 0.004423526 &
0.003942982 0.003514640 0.003132831 0.002792500 0.002489140 0.002218735 &
0.002081267 0.001969888 0.001864470 0.001764693 0.001670256 0.001580872 &
0.001496272 0.001416199 0.001340412 0.001268680 0.001200787 0.001136527 &
0.001075706 0.001018139 0.000963654 0.000912084 0.000863274 0.000817076 &
0.000773350 0.000731965 0.000692794 0.000655719 0.000620628 0.000587415 &
0.000555980 0.000526227 0.000498066 0.000471412 0.000446184 0.000422307 &
0.000399707 0.000378317 0.000358071 0.000338909 0.000320772 0.000303606 &
0.000287359 0.000271981 0.000257426 0.000243650 0.000230611 0.000218270 &
0.000206589 0.000195534 0.000185070 0.000175166 0.000165792 0.000156919 &
0.000148522 0.000140574 0.000133051 0.000125931 0.000119192 0.000112813 &
0.000106776 0.000101062 0.000095653 0.000090535 0.000085690 0.000081104 &
0.000076764 0.000072656 0.000068768 0.000065087 0.000061604 0.000058308 &
0.000055187 0.000052234 0.000049439 0.000046793 0.000044289 0.000041919 &
0.000039675 0.000037552 0.000035543 0.000033641 0.000031840 0.000030136 &
0.000028524 0.000026997 0.000025552 0.000024185 0.000022891 0.000021657 &
0.000020506 0.000019409 0.000018370 0.000017387 0.000016457 0.000015576 &
0.000014742 0.000013954 0.000013207 0.000012500 0.000011831 0.000011198 &
0.000010599 0.000010032 0.000009495 0.000008987 0.000008506 0.000008050 &
0.000007620 0.000007212 0.000006826 0.000006461 0.000006115 0.000005788 &
0.000005478 0.000005185 0.000004907 0.000004645 0.000004396 0.000004161 &
0.000003938 0.000003727 0.000003528 0.000003339 0.000003161 0.000002991 &
0.000002831 0.000002680 0.000002536 0.000002401 0.000002272 0.000002151 &
0.000002035 0.000001927 0.000001823 0.000001726 0.000001634 0.000001546 &
0.000001463 0.000001385 0.000001311 0.000001241 0.000001174 0.000001112 &
0.000001052 0.000000996 0.000000942
c Number of Particles
nps 3000000

A.2 Geant4 simulations

A.2.1 Example of Geant4 code in Detection materials investigation (Detector Constructor.cc file)

```cpp
/// \file hadronic/Hadr03/src/DetectorConstruction.cc
/// \brief Implementation of the DetectorConstruction class
// $Id: DetectorConstruction.cc 70755 2013-06-05 12:17:48Z ihrivnac $
#include "DetectorConstruction.hh"
#include "DetectorMessenger.hh"
#include "G4Material.hh"
#include "G4NistManager.hh"
#include "G4Element.hh"
#include "G4Box.hh"
#include "G4Orb.hh"
#include "G4LogicalVolume.hh"
#include "G4PVPlacement.hh"
#include "G4GeometryManager.hh"
#include "G4PhysicalVolumeStore.hh"
#include "G4LogicalVolumeStore.hh"
#include "G4SolidStore.hh"
#include "G4RunManager.hh"
#include "G4UnitsTable.hh"
#include "G4SystemOfUnits.hh"
DetectorConstruction::DetectorConstruction()
:G4VUserDetectorConstruction(),
 fPBox(0), fLBox(0), fMaterial(0)
 //, fDetectorMessenger(0)
{
  fBoxSize = 1*m;
}
DetectorConstruction::~DetectorConstruction(){;}
G4VPhysicalVolume* DetectorConstruction::Construct()
{
// ------------- Materials -------------
  G4double a, z, density;
  G4int nelements;
//CLYC7
  G4Element* Cl = new G4Element("Clorine", "Cl", z=17 , a=35.45*g/mole);
  G4Element* Y = new G4Element("Yttrium" , "Y", z=39 , a=88.91*g/mole);
  G4Element* Cs = new G4Element("Caesium", "Cs", z=55 , a=132.91*g/mole);
  G4Element* Li = new G4Element("Lithium" , "Li", z=3 , a=6.94*g/mole);
  G4Material* CLYC7 = new G4Material("Cs2LiYCl5", density=3.31*g/cm3, nelements=4);
  CLYC7->AddElement(Cl, 5);
  CLYC7->AddElement(Y, 1);
  CLYC7->AddElement(Cs, 2);
  CLYC7->AddElement(Li, 1);
// Air
  G4Element* N = new G4Element("Nitrogen", "N", z=7 , a=14.01*g/mole);
  G4Element* O = new G4Element("Oxygen" , "O", z=8 , a=16.00*g/mole);
  G4Material* air = new G4Material("Air", density=1.29*mg/cm3, nelements=2);
  air->AddElement(N, 70.*perCent);
  air->AddElement(O, 30.*perCent);
```

```
// Water
  G4Element* H = new G4Element("Hydrogen", "H", z=1 , a=1.01*g/mole);
  G4Material* water = new G4Material("Water", density= 1.0*g/cm3, nelements=2);
  water->AddElement(H, 2);
  water->AddElement(O, 1);
G4cout << *(G4Material::GetMaterialTable()) << G4endl;
// ------------- Volumes --------------
// The experimental Hall
  G4Box* expHall_box = new G4Box("World",30.0*cm,30.0*cm,30.0*cm);
  G4LogicalVolume* expHall_log
    = new G4LogicalVolume(expHall_box,air,"World",0,0,0);
  G4VPhysicalVolume* expHall_phys
    = new G4PVPlacement(0,G4ThreeVector(),expHall_log,"World",0,false,0);
//The CLYC7 Detector
  G4Orb*  CrystDetector = new G4Orb("Crystal", 1.0*cm);
  G4LogicalVolume* crysdetector_log
    = new G4LogicalVolume(CrystDetector,CLYC7,"Crystal",0,0,0);
  G4VPhysicalVolume* crysdetector_phys
    = new G4PVPlacement(0,
              G4ThreeVector(),
              crysdetector_log,
              "Crystal",
               expHall_log,
               false,
               0);
//always return the physical World
  return expHall_phys;
}
```

A.2.2 Example of Geant4 code: Macro file (Detection materials investigation)

Example 1: Gamma-ray

```
# Macro file for gamma-ray photons transport investigation in detection materials candidates (1 keV
photon)
# Macro file for "TestEm14.cc"
/run/initialize
/process/list
#/control/verbose 2
/tracking/verbose 2
/gps/particle gamma
/gps/pos/type Point
/gps/pos/centre 0. 0. 0. cm
/gps/ang/type iso
/gps/ene/mono 0.001 MeV
/run/beamOn 1000000
```

Example 2: Fast neutron

```
/control/verbose 2
/run/verbose 2
/run/initialize
/process/list
```

```
/gun/particle neutron
/gun/energy 2 MeV
/run/beamOn 1000000
```

A.2.3 Example of Geant4 code: Detector Constructor (Configuration optimisation)

```cpp
#include "OpNoviceDetectorConstruction.hh"
#include "G4Material.hh"
#include "G4Element.hh"
#include "G4LogicalBorderSurface.hh"
#include "G4LogicalSkinSurface.hh"
#include "G4OpticalSurface.hh"
#include "G4Box.hh"
#include "G4LogicalVolume.hh"
#include "G4ThreeVector.hh"
#include "G4PVPlacement.hh"
#include "G4SystemOfUnits.hh"
OpNoviceDetectorConstruction::OpNoviceDetectorConstruction()
 : G4VUserDetectorConstruction()
{
  fExpHall_x = fExpHall_y = fExpHall_z = 10.0*m;
  fTank_x   = fTank_y   = fTank_z   = 5.0*m;
  fBubble_x  = fBubble_y  = fBubble_z  = 0.5*m;
}
OpNoviceDetectorConstruction::~OpNoviceDetectorConstruction(){;}
G4VPhysicalVolume* OpNoviceDetectorConstruction::Construct()
{
// ------------- Materials -------------
  G4double a, z, density;
  G4int nelements;
//Liglass
  G4Element* O = new G4Element("Oxygen", "O", z=8 , a=16.00*g/mole);
  G4Element* Mg = new G4Element("Magnesium"  , "Mg", z=12 , a=24.31*g/mole);
  G4Element* Al = new G4Element("Aluminium", "Al", z=13, a=26.98*g/mole);
  G4Element* Li = new G4Element("Lithium"  , "Li", z=3 , a=6.94*g/mole);
  G4Element* Si = new G4Element("Silicon"  , "Si", z=14 , a=28.09*g/mole);
  G4Element* Ce = new G4Element("Cerium"  , "Ce", z=58 , a=140.12*g/mole);
  G4Material* Liglass = new G4Material("LiGlass", density=2.50*g/cm3, nelements=6);
  Liglass->AddElement(O,  50.11*perCent);
  Liglass->AddElement(Mg, 2.41*perCent);
  Liglass->AddElement(Al, 9.53*perCent);
  Liglass->AddElement(Li, 8.36*perCent);
  Liglass->AddElement(Si, 26.18*perCent);
  Liglass->AddElement(Ce, 3.42*perCent);
// Air
  G4Element* N = new G4Element("Nitrogen", "N", z=7 , a=14.01*g/mole);
  G4Material* air = new G4Material("Air", density=1.29*mg/cm3, nelements=2);
  air->AddElement(N, 70.*perCent);
  air->AddElement(O, 30.*perCent);
//EJ204
  G4Element* C = new G4Element("Carbon"  , "C", z=6 , a=12.01*g/mole);
  G4Element* H = new G4Element("Hydrogen"  , "H", z=1 , a=1.01*g/mole);
  G4Material* EJ204 = new G4Material("EJ204", density=1.023*g/cm3, nelements=2);
  EJ204->AddElement(C, 91.55*perCent);
  EJ204->AddElement(H, 8.45*perCent);
```

```cpp
//CsI(Tl)
  G4Element* Cs = new G4Element("Caesium"   , "Cs", z=55 , a=132.91*g/mole);
  G4Element* I= new G4Element("Iodine"   , "I", z=53 , a=126.9*g/mole);
  G4Element* Tl= new G4Element("Thallium"   , "Tl", z=81 , a=204.38*g/mole);
  G4Material* CsI = new G4Material("CsI", density=4.51*g/cm3, nelements=3);
  CsI->AddElement(Cs, 48.08*perCent);
  CsI->AddElement(I, 45.92*perCent);
  CsI->AddElement(Tl, 6.0*perCent);
// ------------- Volumes --------------
// The experimental Hall
  G4Box* expHall_box = new G4Box("World",70.0*cm,70.0*cm,70.0*cm);
  G4LogicalVolume* expHall_log
    = new G4LogicalVolume(expHall_box,air,"World",0,0,0);
  G4VPhysicalVolume* expHall_phys
    = new G4PVPlacement(0,G4ThreeVector(),expHall_log,"World",0,false,0);
//The first Li-glass detector (1 cm X 2.7 cm X 2.7 cm)
G4Box*  CrystDetector_1= new G4Box("Crystal1",0.5*cm,1.35*cm,1.35*cm);
  G4LogicalVolume* crysdetector_1log
    = new G4LogicalVolume(CrystDetector_1,Liglass,"Crystal1");
  G4VPhysicalVolume* crysdetector_phys1
  = new G4PVPlacement(0,
              G4ThreeVector(0.501*cm, 0*cm, 0*cm),
              crysdetector_1log,
              "Crystal1",
               expHall_log,
               false,
               0);
//The plastic glass detector (2.0 cm X 2.7 cm X 2.7 cm)
 G4Box* CrystDetector_2= new G4Box("Crystal2",1.0*cm,1.35*cm,1.35* cm);
  G4LogicalVolume* crysdetector_2log
    = new G4LogicalVolume(CrystDetector_2,EJ204,"Crystal2");
  G4VPhysicalVolume* crysdetector_phys2
  = new G4PVPlacement(0,
              G4ThreeVector(2.001*cm, 0*cm, 0*cm),
              crysdetector_2log,
              "Crystal2",
               expHall_log,
               false,
               0);
//The second Li-glass detector (1.5 cm X 2.7 cm X 2.7 cm)
 G4Box* CrystDetector_3= new G4Box("Crystal3",0.75*cm,1.35*cm,1.35* cm);
  G4LogicalVolume* crysdetector_3log
    = new G4LogicalVolume(CrystDetector_3,Liglass,"Crystal3");
  G4VPhysicalVolume* crysdetector_phys3
  = new G4PVPlacement(0,
              G4ThreeVector(6.751*cm, 0*cm, 0*cm),
              crysdetector_3log,
              "Crystal3",
               expHall_log,
               false,
               0);
//The CsI detector (3.0 cm X 2.7 cm X 2.7 cm)
 G4Box* CrystDetector_4= new G4Box("Crystal4",1.5*cm,1.35*cm,1.35* cm);
  G4LogicalVolume* crysdetector_4log
    = new G4LogicalVolume(CrystDetector_4,CsI,"Crystal4");
  G4VPhysicalVolume* crysdetector_phys4
  = new G4PVPlacement(0,
              G4ThreeVector(11.5*cm, 0*cm, 0*cm),
              crysdetector_4log,
              "Crystal4",
```

```
            expHall_log,
            false,
            0);
```

//always return the physical World
```
  return expHall_phys;
}
```

A.2.4 Examples of Geant4 code Macro file (Configuration optimisation)

```
# Co-60 point source simulations with two gamma-ray energy peaks
/run/initialize
/process/list
/tracking/verbose 1
/gps/source/intensity 1
/gps/particle gamma
/gps/pos/type Plane
/gps/pos/shape Circle
/gps/pos/centre -30 0.1333 0.1333 cm
/gps/pos/rot1  0 1 0
/gps/pos/rot2  0 0 1
/gps/pos/radius 0.1 cm
/gps/direction 1 0 0
/gps/ene/mono 1.17 MeV
/gps/source/intensity 1
/gps/source/add 1
/gps/particle gamma
/gps/pos/type Plane
/gps/pos/shape Circle
/gps/pos/centre -30 -0.1333 -0.1333 cm
/gps/pos/rot1  0 1 0
/gps/pos/rot2  0 0 1
/gps/pos/radius 0.01 cm
/gps/direction 1 0 0
/gps/ene/mono 1.33 MeV
/run/beamOn 40000
```

A.3 MATLAB® analysis programs

A.3.1 Example of MATLAB program used in analysing MCNP6

PTRAC output file (investigation of detection materials)

```matlab
% Main program for investigating detectors characteristics with incident fast neutrons
% Open the file and skip the first 10 lines
fID=fopen('filename');
n=linecount(fID);
frewind(fID);
for k=1:11
    tline=fgets(fID);
end
% initiating matrices
n=n-10;
O=zeros(n,10);
i=1;
k=0;
% Reading from PTRAC file and save data
while ischar(tline)
    M=tline;
    N=str2num(M);
    N(10)=0;
    O(i,:)=N;
    i=i+1;
    tline=fgets(fID);
end
i=1;
Q=zeros(n,15);
count=0;
for j=1:n
    test=check(O,i);              % checking if its NPS
    if test==1
     count=count+1;
     s=scatter(O,i,n);
      if s==1
      k=k+1;
      Q=matrix(O,i,k,Q);
      end
     end
    i=i+1;
end
count=count
Q(k+1:n,:)=[];
[theta_d,x_max,x_mean]=scattering_angle(Q);
[bss,fss,ms,no,no_event]=event_counter(O,n)
ss_percentage=(ss/count)*100;
 % closing the file
fclose(fID);
_____
% A function to caount the 1. single scattering, 2. multiple scattering,
% 3. no interaction events
function [bss,fss,ms,no,not_event]=event_counter(O,n)
bss=0;  % Single backscattering events
fss=0;  % single forward scattering events
```

```matlab
ms=0;    % multiple scattering events
no=0;    % no interaction
not_event=0; % not an event
for i=1:n
if (i+7)<n && (O(i+1,1)==3000) && (O(i+3,1)==4000) && (O(i+5,1)==3000)...
     && (O(i+3,3)==1.3) && (O(i+7,3)==1.3)
   bss=bss+1;
elseif (i+7)<n && (O(i+1,1)==3000) && (O(i+3,1)==4000) && (O(i+5,1)==3000)...
     && (O(i+3,3)==1.3) && (O(i+7,3)==1.2)
   fss=fss+1;
elseif (i+7)<n && (O(i+1,1)==3000) && (O(i+3,1)==4000) && (O(i+5,1)==4000)
   ms=ms+1;
elseif (i+7)<n && (O(i+1,1)==3000) && (O(i+3,1)==3000) && ...
     (O(i+5,1)==3000) && (O(i+7,1)==5000)
   no=no+1;
else
   not_event=not_event+1;
end
end
_____
% This function will find the scattering angle around the x-axis as the n's leave the 1st scatter detector.
function [theta_d,x_max,x_mean]=scattering_angle(Q)
[m,~]=size(Q);
cos_theta=zeros(m,1);
theta=zeros(m,1);
x_mean=0;
for i=1:m
cos_theta(i,1)=Q(i,13);
theta(i,1)=acos(cos_theta(i,1));
x_mean=x_mean+abs(theta(i,1));
end
x_min=min(abs(theta));
r_min=sin(x_min);
x_max=max(abs(theta));
r_max=sin(x_max);
x_mean=x_mean/m;
theta_d=zeros(m,2);
for i=1:m
theta_d(i,1)=theta(i,1);
theta_d(i,2)=theta(i,1)*(180/pi);
end
end
```

A.3.2 Examples of MATLAB program used in analysing MCNP6 PTRAC output file (optimum configuration investigation)

Example 1: Gamma-ray analysis

```matlab
% Open the file and skip the first 10 lines
fID=fopen('filename');
n=0;
tline=fgets(fID);
while ischar(tline)
   tline=fgets(fID);
   n=n+1;
```

```matlab
end
frewind(fID);
for k=1:11
    tline=fgets(fID);
end
n=n-11;
O=zeros(n,10);
i=1;
while ischar(tline)
    M=tline;
    N=str2num(M);
    N(10)=0;
    O(i,:)=N;
    i=i+1;
    tline=fgets(fID);
end
k=1;
Q=zeros(n,2);     %A matrix to register all the NPS
for i=1:n       % NPS heading
    heading=check(O,i);
    if heading==1
        Q=heading_matrix(O,i,k,Q);
        k=k+1;
    end
end
Q(k:n,:)=[];    % All NPS are registered and their location
[QL,~]=size(Q);
t_thn=zeros(n,5);
c=1;
% registering n's events
compton_g=zeros(n,10); % Compton scattering in srystal 3 events
photo_g=zeros(n,15);   % Photoelectric events
% intiating counters
k=1;
counter_events=1;               %Comtpon scattering events
c_sur=1;                %g sur crossing
c_compton=1;             %g compton
c_photo=1;              %g photo
for i=1:QL
    if i+1<QL
        for j=Q(i,2)+1:Q(i+1,2)
        if (i+20<n) && (O(j,1)==4000) && (O(j,3)==3.2)&& (O(j+6,1)==4000)...
            && (O(j+6,3)==4.2)
        compton_g(c,1)=Q(i,1);
        compton_g(c,2:4)=O(j+3,1:3);
        compton_g(c,5)=O(j+3,7);
        compton_g(c,6:8)=O(j+9,1:3);
        compton_g(c,9)=O(j+9,7);
        compton_g(c,10)=O(j+1,7);
        c=c+1;
        end
        end
    end
end
compton_g(c:n,:)=[];
photo_g(c:n,:)=[];
[Comp_counter,~]=size(compton_g);
Data_Compton=zeros(Comp_counter,6);
for i=1:Comp_counter
    Data_Compton(i,1)=compton_g(i,10);
```

```matlab
    Data_Compton(i,2)=1-(0.511*((1/compton_g(i,5))-...
        (1/compton_g(i,10))));
    Data_Compton(i,3)=acos(Data_Compton(i,2));
    Data_Compton(i,4)=Data_Compton(i,3)*180/pi;
    %Data_Compton(i,5:6)=compton_g(i,3:4)/10;
end
d=0.5;
X1=zeros(c,101);        %to store the points of each circle
Y1=zeros(c,101);
r=zeros(c,1);
for i=1:(c-1)
    r(i,1)=tan(Data_Compton(i,3))*d;
    t=[0;r(i,1)];
    [X,Y,Z]=cylinder(t);
    Data=[X,Y,Z];
    %plotting the ellipses
    figure(1);
    surf(X+compton_g(i,3),Y+compton_g(i,4),Z,'EdgeColor',...
        'none','LineStyle','none','FaceColor','black');
        alpha 0.3;
    %xlim([-1.35 1.35])
    %ylim([-1.35 1.35])
    alpha 0.3;
    hold on
    figure(2)
    th = 0:pi/50:2*pi;
    xunit = r(i,1) * cos(th) + (compton_g(i,3));
    yunit = r (i,1)* sin(th) +(compton_g(i,4));
    h = plot(xunit, yunit,'Color','black');
    %fill(xunit, yunit,'black')
    xlim([-1.35 1.35])
    ylim([-1.35 1.35])
    alpha 0.2;
    hold on
    X1(i,:)=xunit;
    Y1(i,:)=yunit;
end
    F=getframe;
    axis off
    imwrite(F.cdata,'I.jpg');        %Saving Figure 3 as an image
    RGB=imread('I.jpg');
    Igray=rgb2gray(RGB);            %Reading the number of pixeles in I.jpg
    [IgrayY,IgrayX]=size(Igray);
    pixel_min=min(min(Igray));     % Finding the mainimum value of the pixeles in I.jpg (the pixel with
the darkest shade (maximum interactions)
    [pixel_minX, pixel_minY]=find(Igray==pixel_min);   %Finding the X and Y position of that pixel
    X_w=((2.7/IgrayX)*pixel_minY);   %Converting it into the size of the SiPM.
    Y_w=((2.7/IgrayY)*pixel_minX);
    figure(3)
    J_image = imresize(Igray,[8 8]); %resize the image
    pixelJ_min=min(min(J_image))
    result=find(J_image==pixelJ_min)
    inverseGrayImage = uint8(255) - Igray;  % inverse the colours of pixels
    J_image2 = imresize(inverseGrayImage,[128 128]);
    imagesc(J_image2)
% closing the file
fclose(fID);
```

Example 2: Thermal neutrons

```matlab
% Open the file and skip the first 10 lines
fID=fopen('filename');
n=0;
tline=fgets(fID);
while ischar(tline)
    tline=fgets(fID);
    n=n+1;
end
frewind(fID);
for k=1:11
    tline=fgets(fID);
end
n=n-11;
O=zeros(n,10);
i=1;
while ischar(tline)
    M=tline;
    N=str2num(M);
    N(10)=0;
    O(i,:)=N;
    i=i+1;
    tline=fgets(fID);
end
k=1;
Q=zeros(n,2);      %A matrix to register all the NPS
for i=1:n        % NPS heading
    heading=check(O,i);
    if heading==1
        Q=heading_matrix(O,i,k,Q);
        k=k+1;
    end
end
Q(k:n,:)=[];    % All NPS are registered and their location
[QL,~]=size(Q);
t_thn=zeros(n,5);
c=1;
for i=1:QL
    if i+1<QL
    for j=Q(i,2)+1:Q(i+1,2)
    if (i+20<n) && (O(j,1)==3000) && (O(i+2,3)==1.2)&& (O(i+4,3)==3006)
    t_thn(c,1)=Q(i,1);
    t_thn(c,2:4)=O(i+5,1:3);
    c=c+1;
    end
    end
    end
end
    t_thn(c:n,:)=[];
    scatter(t_thn(:,3),t_thn(:,4),80,'filled','black')
    % set(gca,'visible','off')
    F=getframe;
    imwrite(F.cdata,'I.jpg');      %Saving Figure 3 as an image
    RGB=imread('I.jpg');
    Igray=rgb2gray(RGB);          %Reading the number of pixeles in I.jpg
    [IgrayY,IgrayX]=size(Igray);
    figure(2)
    J_image = imresize(Igray,[8 8]); %resize the image
    pixelJ_min=min(min(J_image));
    result=find(J_image==pixelJ_min);
```

```
    inverseGrayImage = uint8(255) - Igray;  % inverse the colors of pixels
    J_image2 = imresize(inverseGrayImage,[8 8]);
    %heatmap(J_image)
    imagesc(J_image2)
% closing the file
fclose(fID);
```
_____
Example 3: Fast neutrons
```
% Open the file and skip the first 10 lines
fID=fopen('filename');
n=0;
tline=fgets(fID);
while ischar(tline)
    tline=fgets(fID);
    n=n+1;
end
frewind(fID);
for k=1:11
    tline=fgets(fID);
end
n=n-11;
O=zeros(n,10);
i=1;
while ischar(tline)
    M=tline;
    N=str2num(M);
    N(10)=0;
    O(i,:)=N;
    i=i+1;
    tline=fgets(fID);
end
k=1;
Q=zeros(n,2);     %A matrix to register all the NPS
for i=1:n        % NPS heading
    heading=check(O,i);
    if heading==1;
        Q=heading_matrix(O,i,k,Q);
        k=k+1;
    end
end
Q(k:n,:)=[];    % All NPS are registered and their location
[QL,~]=size(Q);
t_thn=zeros(n,15);
c=1;
for i=1:QL    % registering any capturing events
    if i+1<QL
    for j=Q(i,2)+1:Q(i+1,2)
    if (i+20<n) && (O(j,1)==3000) && (O(i+2,3)==1.2)&& (O(i+4,3)==3006)
    t_thn(c,1)=Q(i,1);
    t_thn(c,2:4)=O(i+5,1:3);
    c=c+1;
    end
    end
    end
end
t_thn(c:n,:)=[];
n_elastic_info=zeros(n,15);
% intiating counters
k=1;
```

```matlab
for i=1:QL
    if i+1<QL
        for j=Q(i,2)+1:Q(i+1,2)
        if (i+20<n) && (O(j,1)==4000) && (O(j,3)==1.1)&& (O(j+6,1)==4000)...
            && (O(j+6,3)==3.2)
        n_elastic_info(k,1)=Q(i,1);
        n_elastic_info(k,2:4)=O(j+3,1:3);
        n_elastic_info(k,5)=O(j+3,7);
        n_elastic_info(k,10)=O(j+3,9);
        n_elastic_info(k,6:8)=O(j+9,1:3);
        n_elastic_info(k,9)=O(j+9,7);
        n_elastic_info(k,11)=O(j+9,9);
        k=k+1;
        end
        end
    end
end
n_elastic_info(k:end,:)=[];
%plotting probability cones
[a,b]=size(n_elastic_info);
Theta=zeros(a,1);
k=1;
X1=zeros(a,101); %to store the points of each circle
Y1=zeros(a,101);
distance=1;
r=zeros(a,1);
for i=1:a
    TOF=1e-8*(n_elastic_info(i,11)-n_elastic_info(i,10));
    TOF2=TOF^2;
    d2=(n_elastic_info(i,6)-n_elastic_info(i,2))^2;
    En2=0.5*1.675E-27*d2*(0.0001)/TOF2/1.6E-19/1000000;
    Theta(k,1)=atan(sqrt(n_elastic_info(i,5)/En2))*180/3.141592654;
    r=tan(Theta(k,1))*1;
    t=[0;r];
    [X,Y,Z]=cylinder(t);
    Data=[X,Y,Z];
    figure(1);
    surf(X+n_elastic_info(i,3),Y+n_elastic_info(i,4),Z);
    alpha 0.3;
    hold on
    figure(3)
    th = 0:pi/50:2*pi;
    xunit = r * cos(th) + n_elastic_info(i,3);
    yunit = r * sin(th) + n_elastic_info(i,4);
    h = plot(xunit, yunit);
    fill(xunit, yunit,'white')
    alpha 0.1;
    xlim([-1.35 1.35])
    ylim([-1.35 1.35])
    hold on
    X1(k,:)=xunit;
    Y1(k,:)=yunit;
    k=k+1;
end
    F=getframe;
    imwrite(F.cdata,'I.jpg');       %Saving Figure 3 as an image
    RGB=imread('I.jpg');
    Igray=rgb2gray(RGB);            %Reading the number of pixels in I.jpg
    [IgrayY,IgrayX]=size(Igray);
```

```
  pixel_min=min(min(Igray));   % Finding the minimum value of the pixels in I.jpg (the pixel with the
darkest shade (maximum interactions)
  [pixel_minX, pixel_minY]=find(Igray==pixel_min);   %Finding the X and Y position of that pixel
  X_w=((2.7/IgrayX)*pixel_minY);   %Converting it into the size of the SiPM.
  Y_w=((2.7/IgrayY)*pixel_minX);
  figure(4)
  J_image = imresize(Igray,[8 8]); %resize the image
  pixelJ_min=min(min(J_image))
  result=find(J_image==pixelJ_min)
  inverseGrayImage = 255 - J_image;  % inverse the colours of pixels
  J_image2 = imresize(Igray,[8 8]);
  imagesc(J_image2)
  figure(5)
  imagesc(inverseGrayImage)
% closing the file
fclose(fID);
```

A.1.3 Example of MATLAB program for Geant4 code output file (investigation of detection materials)

Example 1: Thermal and fast neutrons

```
% This program is for Geant 4 output files analysis for neutrons. It calculates the efficiency of Elastic
scattering (both
% backward and forwards, non-elastic scattering, escaping probabilities and capturing probability
% Open the file
fID=fopen('t6.out');
x1 = 30.1;
x2 = 0.1;
% creating a function to count the number of lines in a text file
n=0;
tline=fgets(fID);
while ischar(tline)
    tline=fgets(fID);
    n=n+1;
end
frewind(fID);
for k=1:59
    tline=fgets(fID);
end
A = cell(n-115,1);
i = 1;
for k=60:n
  tline=fgets(fID);
  M =(tline);
  N = cellstr(M);
  A (i,1) = (N);
  i=i+1;
end
% Initializing counters
s0='TransportationCrystal';
s1='nCapture';
s2='hadElastic';
s3='neutronInelastic';
ElasticCounter = 0;
```

```matlab
SElasticCounter = 0;
% Capture Counter
L2= find(ismember(A,s1));
[a,~]=size(L2);
CaptureCounter = a;
%InElastic scattering counter
L3 = find(ismember(A,s3));
[b,~]=size(L3);
InElasticCounter = b;
CaptureCounter = a+b;
% Escape counter
L1= find(ismember(A,s0));
[a,~]=size(L1);
EscapeCounter = a;
% Elasticcounter counter
L4= find(ismember(A,s2));
[c,~]=size(L4);
L44=zeros(c,1);      %to differentiate multiple scattering events from single scattering events
for k=1:c         % a loop to differentiate mult scattering from singele scattering
if k+1 <= c && k-1~=0
   if L4(k+1)-L4(k) == 2 || L4(k)-L4(k-1) == 2
      L44(k,1)=L4(k,1);
   end
elseif k == c
   if L4(k)-L4(k-1) == 2
      L44(k,1)=L4(k,1);
   end
end
end
c=find(ismember(L44,0));
L4=L4(c);
[j,~]=size(L44);
[c,~] =size(L4);
for k=1:j         % a loop to count multiple scattering events
    [i,~]=find(L1 == L44(k)+2);
         if i~=0
             ElasticCounter = ElasticCounter +1;
         end
end
j=1;
O = zeros(c,1);
C = zeros(c,1);     %For alocating hadElastic scattering positions
CB = cell(c,1);     %/-- --        --        --       --
B = zeros(c,1);     %For alocating Escaping  positions
BB = cell(c,1);     %/-- --        --       --
for k=1:c
    [i,~]=find(L1 == L4(k)+2);
         if i~=0
             O(j,1)=i;
             C(j,1)=L4(k)+1;
             CB(j,1)=A(C(j,1));
             B(j,1)=L1(i)+1;
             BB(j,1)=A(B(j,1));
             j=j+1;
             SElasticCounter = SElasticCounter +1;
         end
end
%Redefining Escape counter after counting how many elastic+escape events
EscapeCounter = a-SElasticCounter-ElasticCounter;
%finding scattering angles
```

```matlab
j=j-1;
O((j+1):c,:)=[];
C((j+1):c,:)=[];
B((j+1):c,:)=[];
CB((j+1):c,:)=[];
CD = zeros(j,3);          % CD: A matrix to register scattering positions
BB((j+1):c,:)=[];
BD = zeros(j,3);          % BD: A matrix to register Escaping positions
BE = zeros(j,1);
a_vec = zeros(j,3);
a_angle=zeros(j,1);
backward_counter=0;
forward_counter=0;
for k=1:j
   CC=cell2mat(CB(k));    % created to convert cell format of the positions into matrix format
   CC=str2num(CC);
   CD(k,:)=CC;
   BC=cell2mat(BB(k));    % created to convert cell format of the positions into matrix format
   BC=str2num(BC);
   BD(k,:)=BC;
   a_vec(k,1)=(BD(k,1)-CD(k,1));
   a_vec(k,2)=(BD(k,2)-CD(k,2));
   a_vec(k,3)=(BD(k,3)-CD(k,3));
   z_vec = [0,0,1];
   a_angle(k,1)= 180*acos(dot(a_vec(k,:),z_vec)/(norm(a_vec(k,:))*norm(z_vec)))/pi;
   if (BD(k,3) == x2 && a_angle(k,1) > 90 && a_angle(k,1) < 270 )
    backward_counter= backward_counter + 1;
   elseif  (BD(k,3) == x1 && a_angle(k,1) > 0 && a_angle(k,1) < 360 )
    forward_counter=forward_counter + 1;
   end
end

Total_number_of_event=EscapeCounter+CaptureCounter+SElasticCounter+ElasticCounter;
EscapeCounter_per=100*EscapeCounter/Total_number_of_event
CaptureCounter_per=100*CaptureCounter/Total_number_of_event
backward_counter_per=100*backward_counter/Total_number_of_event
forward_counter_per=100*forward_counter/Total_number_of_event
 % closing the file
fclose(fID);
```

Example 2: Gamma-ray

```matlab
% This program is for Geant 4 output files analysis of detection materials for gamma rays. It calculates
the efficiency of CC, PE and transportation
% Open the file
fID=fopen('t1e-2.out');
% creating a function to count the number of lines in a text file
n=0;
tline=fgets(fID);
while ischar(tline)
   tline=fgets(fID);
   n=n+1;
end
frewind(fID);
for k=1:183
   tline=fgets(fID);
end
A = cell(n-183,1);
i = 1;
```

```matlab
for k=184:n
  tline=fgets(fID);
  M =(tline);
  N = cellstr(M);
  A (i,1) = (N);
  i=i+1;
end
% Initializing counters
s0='Transportation';
s1='compt';
s2='phot';
s3='conv';
mfp = 0;
% Compton Counter
%Step I: Allocating and counting CS
L1= find(ismember(A,s1));
[a,~]=size(L1);
Compton_Counter = a
%Step II: Finding the position, energy and track length
j=1;
CS = zeros(a,5);
for k=1:a
    CC=A(L1(k)+1);
    CC=cell2mat(CC);   % created to convert cell format of the positions into matrix format
    CC=str2num(CC);
    CS(k,:)=CC;
    mfp=mfp + CS(k,4);
end
 mfp=mfp + sum(CS(1:a,4));
%PP scattering counter
%Step I: Alocating and counting PP interaction
L2 = find(ismember(A,s3));
[b,~]=size(L2);
PairProduction_Counter = b
%Step II: Finding the position, energy and track length
j=1;
PP = zeros(b,5);
for k=1:b
    CC=A(L2(k)+1);
    CC=cell2mat(CC);   % created to convert cell format of the positions into matrix format
    CC=str2num(CC);
    PP(k,:)=CC;
end
mfp=mfp + sum(PP(1:b,4));
% Escape counter
%Step I: Alocating and counting Escape
L3= find(ismember(A,s0));
[c,~]=size(L3);
EscapeCounter = c
%Step II: Finding the position, energy and track length
j=1;
ES = zeros(b,5);
for k=1:c
    CC=A(L3(k)+1);
    CC=cell2mat(CC);   % created to convert cell format of the positions into matrix format
    CC=str2num(CC);
    ES(k,:)=CC;
end
% Photoelctric counter
%Step I: Alocating and counting PE interaction
```

```matlab
L4= find(ismember(A,s2));
[d,~]=size(L4);
PhotoElectric_Counter = d
%Step II: Finding the position, energy and track length
j=1;
PE = zeros(d,5);
for k=1:d
   CC=A(L4(k)+1);
   CC=cell2mat(CC);   % created to convert cell format of the positions into matrix format
   CC=str2num(CC);
   PE(k,:)=CC;
end
mfp=mfp + sum(PE(1:d,4));
mfp = mfp /(a+b+d)
 % closing the file
fclose(fID);
```

A.1.4 Example of MATLAB program for analysing Geant4 code output files (optimum configuration investigation)

Example 1: design optimisation for gamma rays.

```matlab
% Open the file (geant4)
fID=fopen('position_1');
% creating a function to count the number of lines in a text file
n=0;
tline=fgets(fID);
while ischar(tline)
   tline=fgets(fID);
   n=n+1;
end
frewind(fID);
for k=1:313
   tline=fgets(fID);
end
%Matrices initialisation
n=n-313;
A = cell(n,1);
O=zeros(n,5);
i=1;
%Creating and saving matrices
while ischar(tline)         %reading the data from the file
   M=tline;
   N=str2num(M);
   N(6)=0;
   O(i,:)=N(1,1:5);             %The matrix with all the numbers
   A (i,1) =cellstr (M);     %The matrix with all the info
   i=i+1;
   tline=fgets(fID);
end
%Variables intiation
E0='Transportation';
E1='compt';
E2='phot';
C1='Crystal1';
C2='Crystal2';
```

```matlab
C3='Crystal3';
C4='Crystal4';
W='World';
Photo_counter = 0;
Photo_Matrix=zeros(n,5);
Comp_counter = 0;
Comp_Matrix=zeros(2*n,5);
L1= find(ismember(A,'End'));
[Number_events,~]=size(L1);
for i=1:n
    if  strcmp(cell2mat(A(i)),'End')==1 && ...
        strcmp(cell2mat(A(i+8)),E0)==1 && strcmp(cell2mat(A(i+9)),W)==1 && ...
        strcmp(cell2mat(A(i+12)),E0)==1 && strcmp(cell2mat(A(i+13)),C1)==1 && ...
        strcmp(cell2mat(A(i+16)),E0)==1 && strcmp(cell2mat(A(i+17)),C2)==1 && ...
        strcmp(cell2mat(A(i+20)),E0)==1 && strcmp(cell2mat(A(i+21)),W)==1 && ...
        strcmp(cell2mat(A(i+24)),E1)==1 && strcmp(cell2mat(A(i+25)),C3)==1 && ...
        strcmp(cell2mat(A(i+28)),E0)==1 && strcmp(cell2mat(A(i+29)),C3)==1 && ...
        strcmp(cell2mat(A(i+32)),E0)==1 && strcmp(cell2mat(A(i+33)),W)==1 && ...
        strcmp(cell2mat(A(i+36)),E2)==1 && strcmp(cell2mat(A(i+37)),C4)==1
    Comp_counter = Comp_counter +1;
    Comp_Matrix(Comp_counter,1) = i;
    Comp_Matrix(Comp_counter,2:4) = O(i+25,1:3);    %Reading from the output file
    Comp_Matrix(Comp_counter,5) = O(i+13,4)-O(i+25,4);
    Comp_Matrix(Comp_counter+1,1) = i;
    Comp_Matrix(Comp_counter+1,2:4) = O(i+21,1:3);
    Comp_Matrix(Comp_counter+1,5) = O(i+21,4);
    Comp_counter = Comp_counter +1;
    elseif  strcmp(A(i),E2)==1 && strcmp(A(i+1),C4)==1
        Photo_counter = Photo_counter +1;
        Photo_Matrix(Photo_counter,1) = i;
        Photo_Matrix(Photo_counter,2:4) = O(i+2,1:3);
        Photo_Matrix(Photo_counter,5) = O(i-1,4);
    end
end
%Comp_countere=Comp_counter/2;
Photo_Matrix(Photo_counter+1:n,:) =[];
Comp_Matrix(Comp_counter+1:2*n,:) =[];
%building the data matrix for Compton events
c=1;
Data_Compton=zeros(Comp_counter,6); % 1:Energy 2:cos(theta) 3:theta in rad 4:theta in degree 5&6:
X and Y interaction in first Compton detector
for i=1:2:Comp_counter
    Data_Compton(c,1)=Comp_Matrix(i,5)+Comp_Matrix(i+1,5);
    Data_Compton(c,2)=1-(0.511/Comp_Matrix(i+1,5))+...
    (0.511/Data_Compton(c,1));
    Data_Compton(c,3)=acos(Data_Compton(c,2));
    Data_Compton(c,4)=Data_Compton(c,3)*180/pi;
    Data_Compton(c,5:6)=Comp_Matrix(i,3:4)/10;
    c=c+1;
end
Data_Compton(c:Comp_counter,:)=[];

%Finding location
%prompt = 'What is the distance to the image plane (in cm)? ';
%d = input(prompt);        %Distance to source
d=1;
X1=zeros(c,101);          %to store the points of each circle
Y1=zeros(c,101);
r=zeros(c,1);
```

```matlab
for i=1:(c-1)
    r(i,1)=tan(Data_Compton(i,3))*d;
    t=[0;r(i,1)];
    [X,Y,Z]=cylinder(t);
    Data=[X,Y,Z];
    %plotting the ellipses
    figure(1);
    surf(X+(Data_Compton(i,5)/10),Y+(Data_Compton(i,6)/10),Z);
    alpha 0.3;
    xlim([-1.35 1.35])
    ylim([-1.35 1.35])
    hold on
    figure(2)
    th = 0:pi/50:2*pi;
    xunit = r(i,1) * cos(th) + (Data_Compton(i,5)/10);
    yunit = r (i,1)* sin(th) +(Data_Compton(i,6)/10);
    h = plot(xunit, yunit,'Color','black');
    xlim([-1.35 1.35])
    ylim([-1.35 1.35])
    hold on
    X1(i,:)=xunit;
    Y1(i,:)=yunit;
end

    F=getframe;
    imwrite(F.cdata,'I.jpg');        %Saving Figure 3 as an image
    RGB=imread('I.jpg');
    Igray=rgb2gray(RGB);            %Reading the number of pixels in I.jpg
    figure(4)
    J_image = imresize(Igray,[8 8]); %resize the image
    imagesc(J_image)
    inverseGrayImage = 255 - J_image;  % inverse the colours of pixels
    J_image2 = imresize(Igray,[8 8]);
    figure(5)
    imagesc(inverseGrayImage)
 % closing the file
fclose(fID);
```

Appendix B

Scintillators calibration using Cs-137 source

Lithium glass scintillator and CsI(Tl) scintillator were calibrated using a Cs-137 source (energy 0.667 MeV). The number of counts were plotted against the voltage as shown in Figure B.1. A Gaussian fit was then applied to find the photo-peak and subsequently calibrate the detectors (i.e. the scintillators and the SiPM array optically coupled to each scintillator). As discussed in chapter 7, the 662 keV gamma-ray photo-peak was detected in the lithium glass at 0.36 V and resolution in terms of a FWHM of (0.23 ± 0.02) V. Similarly within CsI(Tl), the 662 keV gamma-ray photo-peak was detected at 0.44 V and resolution in terms of a FWHM of (0.37 ± 0.01) V.
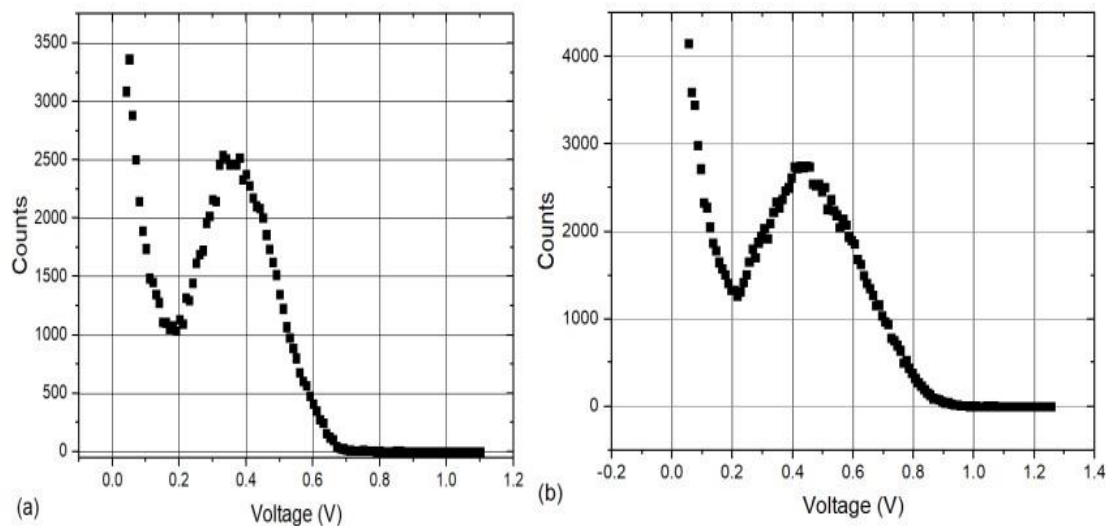

Figure B.1: Counts vs voltage for (a) Lithium glass GS10 and (b) CsI(Tl) scintillators using Cs-137 source.

Hajir Al Hamrashdi - February 2020